Time Reversal techniques applied to wire fault detection and location in wire networks

Layane Abboud

N° d'ordre : 2012-02-TH

THÈSE DE DOCTORAT

SPECIALITE : PHYSIQUE

Ecole Doctorale « Sciences et Technologies de l'Information des Télécommunications et des Systèmes »

Présentée par :

Layane ABBOUD

Sujet :

Application des techniques de retournement temporel au diagnostic filaire automobile et avionique

Soutenue le 19 Mars 2012 devant les membres du jury :

M. Andrea COZZA	Supélec	Encadrant
M. Mauro FELIZIANI	Université L'Aquila Italie	Rapporteur
Mme Françoise PALADIAN	Université Blaise Pascal	Président du jury
M. Marc PETIT	Supélec	Examinateur
M. Lionel PICHON	CNRS – Supélec	Directeur de thèse
M. Christian PICHOT	Université de Nice Sophia-Antipolis	Rapporteur
M. Odile PICON	Université Paris Est – Marne la vallée	Examinateur
M. Laurent SOMMERVOGEL	CEA	invité

REMERCIEMENTS

C'est un moment très fort en émotion, fermer ce long chapitre de ma vie en remerciant toutes les personnes qui m'ont accompagnée pendant.

Je remercie mon directeur de thèse, Monsieur Lionel Pichon, de m'avoir confié ce travail de recherche. Merci pour ton aide et tes remarques précieuses, merci pour ta disponibilité et ta gentillesse inégalée.

Je tiens à exprimer ma profonde gratitude à Monsieur Andrea Cozza, mon encadrant de thèse. Merci d'avoir consacré de ton temps pour me guider pendant ces trois années. Merci pour tes précieux conseils et ton aide permanente, au niveau intellectuel et humain. J'ai eu un très grand honneur de travailler avec un chercheur aussi brillant que toi.

Je remercie aussi Monsieur Mauro Feliziani, Professeur à L'Université de l'Aquila en Italie, et Monsieur Christian Pichot, professeur à l'Université de Nice Sophia-Antipolis, d'avoir accepté de rapporter mon travail de thèse. Je remercie aussi Madame Françoise Paladian, Professeur à L'Université Blaise Pascal, Monsieur Marc Petit professeur à Supélec, Madame Odile Picon, professeur à L'Université Paris Est Marne la vallée et Monsieur Laurent Sommervogel du CEA d'avoir accepté de juger mon travail de thèse.

Je souhaite aussi remercier Monsieur Dominique Lecointe, responsable du département Electromagnétisme de Supélec, et Monsieur Bernard Duchêne, responsable de la division ondes du LSS, de m'avoir accueilli au sein de leurs équipes avec une hospitalité aussi remarquable. Merci de m'avoir assuré les meilleures conditions de travail.

Un grand merci à Laurence, Vincent, Raul, Alain, François, Marc, Florian, Mohammed, pour tous les moments agréables que nous avons passé ensemble. Merci à tous mes collègues de Supélec, bb Lana, Aya, Ali, Younan, Mahmoud, Jacques, Diego, Victor, Jose Luis, Philippe, merci pour tous les moments inoubliables, les séances de rire et de sourire que nous avons passé ensemble... Je pense aussi à tous mes amis qui ont déjà fini leur thèse, Reine, Carine, Michael, Houmam, en espérant que la vie vous réservera le meilleur.

Un immense merci à une amie spéciale et une collègue qui m'a accompagnée pendant les derniers mois de ma thèse. Merci Najett pour tous les moments inoubliables, pour les fous rires, pour ta présence permanente et ton soutien. Ça y est la thèse est finie, une nouvelle étape de nos vies commence !

Je n'aurai pas pu continuer ce long chemin sans le soutien et la présence permanente de ma chère amie Reine, merci de m'avoir montré que l'on peut toujours rire face aux difficultés, de m'avoir soutenue dans les moments où j'avais vraiment besoin de bons conseils pour pouvoir me relever et continuer, merci pour ton amour et ta patience inégalées. Bientôt c'est ta soutenance !

Un grand merci à tous les amis de Notre Dame du Liban, Père Elie, Elias, Josiane Saleh, Jamil, Racha, Jo, Josiane Maalouf, Chadi, Georges, Samar, d'avoir été pour moi une deuxième famille durant mon séjour en France. Merci à Fadi, Sandy, Georges et Nicole mes amis du Liban, Merci pour votre amitié, si chère à moi, merci pour votre solidarité, merci pour ces magnifiques années de que nous avons passé ensemble, merci pour tous ces moments inoubliables !

Tout cela, ce petit rêve, n'aurait jamais pu se réaliser sans l'amour, la confiance, le soutien de ma famille. Je remercie mon très cher papa Samir et ma très chère maman Hana pour leur immense amour et encouragement, merci d'avoir embrassé toutes mes réussites et mes échecs sans distinction, merci de m'avoir donné tellement de joie et de chaleur de vivre, merci d'avoir été toujours là pour moi. A vous, ma très chère sœur Loubna et mon très cher frère Samer, je dis merci. De m'avoir appris que la vie est une chanson qu'il faut chanter à chaque instant, De m'avoir tellement aimé et apprécié. Merci de m'avoir appris à ne jamais baisser les bras.

Finalement, je remercie le Seigneur qui m'a comblé de ses dons, qui m'a donné une famille magnifique et des amis extraordinaires ! Dans les plus grandes tempêtes j'ai toujours pu jeter l'ancre dans Ses bras ! Merci !

« Les racines de l'éducation sont amères, mais ses fruits sont doux »
Aristote

Abstract

In this thesis we present new approaches in the domains of soft fault detection and location in complex wire networks, based on the properties of time reversal. When addressing the detection of soft faults, the idea is to adapt the testing signal to the network under test, instead of being predefined for all the tested networks, as opposed to standard reflectometry techniques. We prove that this approach, which we name the Matched Pulse approach (MP), is beneficial whenever the system complexity increases, i.e., its response is richer in echoes. The MP analysis is conducted via a formal mathematical study, followed by simulation and experimental results validating the proposed approach.

In the domain of soft fault location, we derive a distributed non-iterative method capable of synthesizing signals focusing on the fault position, based on the DORT properties. Through a statistical study we analyze some of the influencing parameters on the performance of the method, and then simulation and experimental results prove that the method is able to synthesize signals directly focalizing on the soft fault position, without the need for iterations.

Résumé

Dans ce mémoire de thèse, nous présentons de nouvelles approches dans le domaine de la détection et de la localisation des défauts non-francs dans les réseaux filaires. Dans le domaine de la détection, l'idée est d'adapter le signal de test au réseau sous test. Par conséquent, celui-là dépendra de la configuration du système sans devoir être prédéfini, comme c'est le cas des méthodes standard de réflectométrie. Nous prouvons que cette approche, que nous nommons Matched Pulse (MP), est plus performante lorsque le système est plus complexe, c'est-à-dire lorsque sa réponse est plus riche en échos. L'étude de la MP est menée à travers une étude mathématique, et des résultats de simulation et d'expérimentation valident l'approche proposée.

Dans le domaine de la localisation de défauts, nous développons une méthode distribuée non-itérative capable de synthétiser des signaux de test se focalisant directement sur la position du défaut, en se basant sur les propriétés de la méthode DORT. Une étude statistique nous permet d'analyser quelques-uns des paramètres les plus influents sur la performance de la méthode, puis les résultats de simulation et expérimentaux montrent la capacité de la méthode à synthétiser des signaux se focalisant directement sur la position du défaut non-franc, sans le recours aux algorithmes itératifs.

Contents

Introduction

Electrical cables are present in almost all modern systems, where energy and information flow between different parts in the system. From transportation systems, to industrial machinery and nuclear power plants, not to forget electricity transmission networks, cables have become one of the most important components of an electrical system, that must guarantee the reliable transmission of information within the system.

However, these cables are subject to different internal and external conditions, such as local heating, corrosion, humidity and mechanical aggressions, that increase the probability of the appearance of faults, and might lead to the system disfunction. These faults are generally classified into two main categories: hard faults, which are open and short circuits, and soft faults, which represent all minor faults, such as insulation damage, cracks, etc.

A faulty wiring might have severe consequences: e.g., it was held responsible for the crash of the Trans World Airlines-800 (1996) and Swiss air-111 (1998) flights, leading to hundred of deaths. Faulty and improperly installed electrical wiring is a leading cause of fires in homes and commercial buildings: in 2005, almost $400,000$ fires occurred within the united states leading to over 3000 deaths and almost $14,000$ injuries, not to mention the economical impact, where the statistics show that these fires costed 703 million dollar in property damage.

The safety issues related to faulty electrical wiring encouraged governmental and industrial funding of research projects aiming at finding novel solutions and techniques to accurately detect and localize faults in cables. Among the most promising methods that exist are reflectometry methods, which are divided into two main families: Time Domain Reflectometry (TDR) and Frequency Domain Reflectometry. These methods share the same general principle: the injection of a testing signal into the wire network under test, and the analysis of the reflected signal searching for the signature of an eventual fault. Generally, these methods are able to detect hard faults in relatively simple network configurations, because they result in a larger reflection than soft faults. In this case, and when dealing with complex configurations, reflectometry methods start to fail as multiple echoes in the reflected signal, resulting from the presence of junctions and impedance discontinuities in the network, mask the signature of an eventual fault. Whence the need to find novel approaches that are able to detect and localize soft faults in complex configurations, where conventional methods start to fail, a point that motivated the present study.

The objective of this thesis is to propose new approaches for fault detection and localization, to improve these processes when dealing with soft faults and complex networks. We can com-

pare this problem to that of radar target detection in a cluttered environment, where multiple scattering in the propagation medium can mask a weak target signature, jeopardizing its eventual detection. In this domain, the solution was to adapt the testing signal to the medium, resulting in an optimal efficiency; this was done by using the principles of Time Reversal (TR), first introduced in acoustics in the early 1990s, which transforms the traditionally 'hostile' multipath components to performance-boosting elements, especially in cluttered environments. Based on this principle, we developed an approach we named Matched Pulse approach (MP), able to synthesize testing signals that are adapted to the network being tested, thus depending on the configuration of the latter, as opposed to standard reflectometry techniques where testing signals are predefined for all the tested networks. This approach is shown to result in an optimal efficiency as the TR principle is equivalent to the idea of matched filter encountered in telecommunications.

Through a mathematical analysis, the advantages of the MP are quantified, and it is shown that the MP is more beneficial when the network is more complex, as opposed to common understanding based on the properties of reflectometry techniques. Simulation and experimental validation also show that the MP approach provides a complimentary testing solution with major advantages in critical configurations where standard reflectometry techniques may be no more reliable, thus ensuring a higher sensitivity to the presence of soft faults.

Since the MP approach cannot lead to the localization of an eventual fault, we dealt with this problem in the second part of our study. Generally, when it comes to complex networks, distributive and iterative methods are used for a possible fault localization. However, when dealing with soft faults, distributive methods may be insufficient, and iterative ones can be time consuming and result in a solution not corresponding to the true position of the fault. Whence our decision to deal with this kind of faults, and apply the ideas of TR earlier introduced. In fact, time reversal allows the SNR maximization at the fault position, an idea that has been exploited when dealing with fault detection. When addressing fault localization, the same ideas remain applicable, because time reversal also allows maximizing the energy at the fault position. This idea was exploited in medical imaging, radar and sonar communications, sensing of buried objects, etc. In these domains, the properties of iterative time reversal have been taken into account through the DORT (Décomposition de l'Opérateur de Retournement Temporel) method, originally developed in acoustics to deal with the problem of focusing on one of several scatterers present in a homogeneous medium: it has been demonstrated that this method is capable of synthesizing signals that focus selectively on the desired scatterer. Hence, it seemed interesting to study the contribution of this method in our domain of fault localization. After adapting the method to the case of guided propagation, we show how this new approach in the domain of wire fault location allows synthesizing signals directly focusing on the fault, without the need for iterations. Through a statistical study, we show the most influencing parameters on the new method's performance, and then an experimental study involving soft faults in complex networks validates the important advantages of the method over the usual iterative methods,

concerning the direct location of the soft fault in the complex network.

The thesis is organized as follows: Chapter 1 presents an overview of the context of our study, the problem of faulty electrical wiring, and the most common methods used for investigating the wire health, among which reflectometry techniques; we present the general principle of these methods, along with their major advantages and limitations. Next Chapter 2 describes the concepts and tools we used to model and simulate the guided propagation. We recall the transmission line theory tools that are going to be needed in our study, and also multiport modeling using the S-parameter matrices, used to define our simulator. Space-time diagrams are also introduced; they represent the tool we adopted to observe voltage propagation in the tested networks thus facilitating the development of the fault localization method. Finally in this chapter the use of the 'difference' system in the case of soft faults is discussed, after establishing a comparison between the free-space propagation and the guided propagation case.

Chapter 3 addresses the first part of our work, that deals with fault detection. In this part, we discuss the use of the TR principle and introduce the MP approach, followed by a formal mathematical analysis that compares the MP to standard TDR methods, where we deduce the scenarios where the MP presents major advantages over the existing methods. Parametric and experimental validations also support our conclusions, showing the important benefits of the MP approach in critical scenarios dealing with soft faults and complex networks.

Chapter 4 deals with the fault localization problem, where we derive a distributive non-iterative approach for fault location in wire networks, based on the DORT method. We establish a heuristic location criterion that will permit us to conduct a statistical study allowing to evaluate the most influencing parameters on the new method's performance. An experimental study shows the important benefit of the method over iterative methods, as it permits to directly locate soft faults in complex networks.

Chapter 1

State of the art

1.1 Introduction

This chapter is devoted to the presentation of the most common methods used nowadays to inspect the wire health in an electrical system. After a brief introduction to the growing need for electrical cables in today's modern systems, we present the fault types usually encountered in these systems, that can pose significant safety issues, as well as an important economical impact. Several methods aiming at detecting and locating cable faults are next presented, and their advantages and limitations are discussed. We highlight reflectometry methods, most commonly used today, and the base of our present work, to finally position the latter based on the need that currently exist in the domain of wire health inspection.

1.2 Electrical cables

1.2.1 Introduction

Since the emergence of electrical systems, the use of electrical cables became primordial. Electrical cables are widely used in almost all the modern systems, where the energy and information flow from one part to another in the system. We can cite several examples, such as transportation systems [1], nuclear power plants [2], industrial machinery [3], electricity transmission networks [4], etc. The cable types can vary depending on the nature of the transmitted signals, and the environment in which the cable is placed (see Fig. 1.1 for illustration): the transmitted signals can be either analog or digital [5], have low or high power, at low, medium or high frequencies. The environments vary widely, and cables can be placed in the air, such as for power transmission networks, also in the sea or in the ground for underwater and underground connections [6], etc. Fig 1.1 shows an example of the diversity of electrical cables used in power transmission, where we can find medium and high-voltage cables for energy transmission, low-voltage and underground cables for plant application and subscriber distribution.

Another example is computer networks, which may use two different types of cables: coaxial cables [8] and twisted pair [9]. With this increasing use of electrical cables, the length of the wires in some systems have also increased during the past few years. Aircraft and watercraft are examples where the cumulative length of cables might reach several hundred kilometers, such is the case of an Airbus A380 (500 Km) or the 'Queen Mary 2' boat (2500 Km). Fig. 1.2 shows the evolution of the cumulative length of the wiring in the aircraft industry, for three main manufacturers: Airbus, Boeing and McDonald-Douglas. Also an example of a eurocopter HH-65 circuitry is shown in Fig. 1.3.

The several examples we discussed earlier allow to introduce the three most used cable types: coaxial, twisted pair, and power cables.

1.2.2 Coaxial cables

Coaxial cables conduct electrical power using an inner conductor (usually a flexible solid or braided copper wire) surrounded by an insulating layer and all enclosed by a shield layer, typically a woven metallic braid, as seen in Fig. 1.4, for an RG-59 coaxial cable [11]. The cable is often protected by an outer insulating jacket. Normally, the shield is kept at ground potential and a voltage is applied to the center conductor to carry electrical power. The advantage of coaxial design is that the electric and magnetic fields are confined to the dielectric with little leakage outside the shield. Conversely, electric and magnetic fields outside the cable are largely kept from causing interference to signals inside the cable. This property makes coaxial cable a good choice for carrying weak signals that cannot tolerate interference from the environment or for higher power signals that must not be allowed to radiate or couple into adjacent structures or circuits [12].

Common applications of coaxial cable include video and CATV distribution, RF and microwave transmission, and computer and instrumentation data connections [13].

1.2.3 Twisted pair

Twisted pair (TP) cabling (see Fig. 1.5) is a type of wiring in which two conductors (the forward and return conductors of a single circuit) are twisted together for the purposes of canceling out electromagnetic interference from external sources; for instance, electromagnetic radiation from unshielded twisted pair (UTP) cables, and crosstalk between neighboring pairs. Two main categories exist: Shielded Twisted Pair (STP) and Unshielded Twisted Pair (UTP). In computer networking environments that use twisted-pair cabling, one pair of wires is typically used for transmitting data while another pair receives data. Twisted-pair cabling used in Ethernet networking is usually unshielded twisted-pair (UTP) cabling, while shielded twisted-pair (STP) cabling is typically used in Token Ring networks.

In our work, we developed our own simulator, and considered the case of uniform two-wire transmission lines, as the starting point to validate our new methods (in the detection and

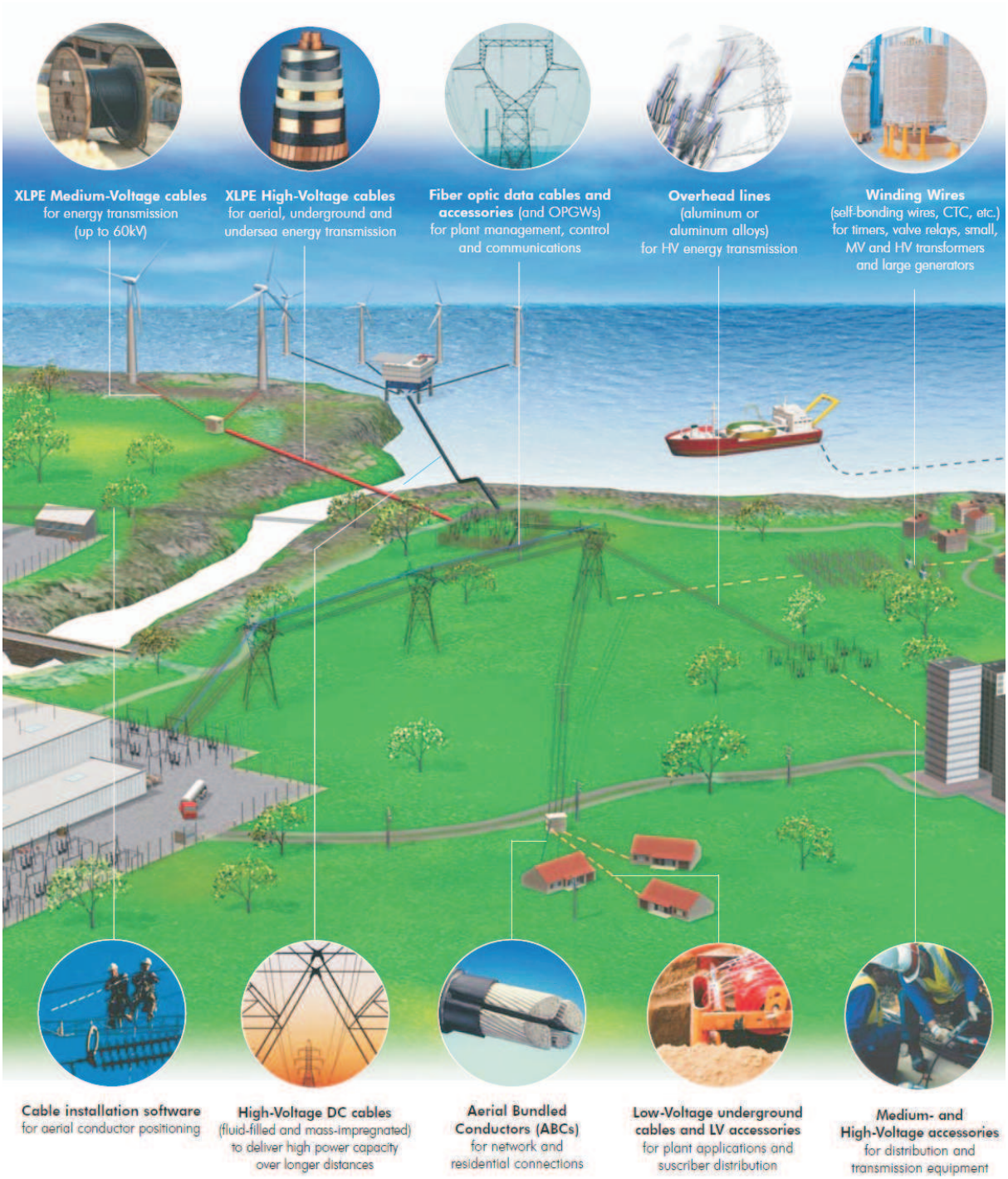

Figure 1.1: Different cables and their areas of application. *Source: [7].*

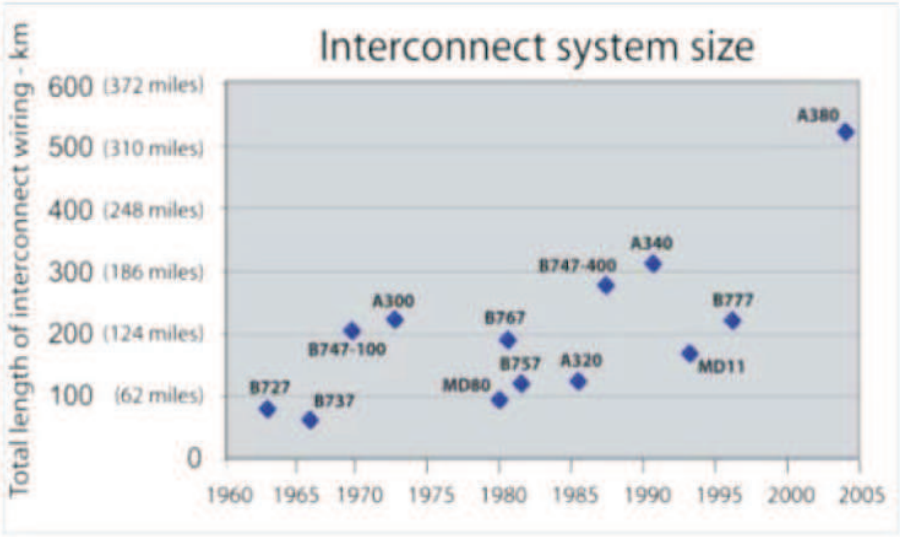

Figure 1.2: The evolution of the cumulative length of the wiring in the aircraft industry [10], for three main manufacturers: Airbus, Boeing and McDonald-Douglas.

Figure 1.3: The backbone and circuitry of a eurocopter HH-65.

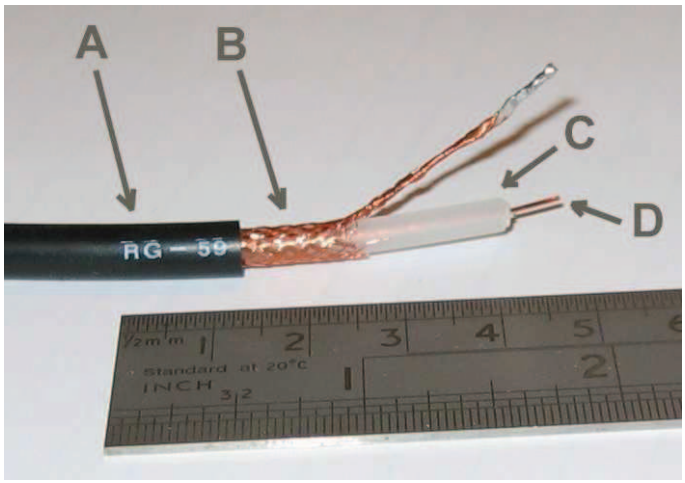

Figure 1.4: Example of an RG-59 coaxial cable showing its components: **A**: plastic outer insulation, **B**: dopper-clad aluminium braid shield conductor, **C**: dielectric, and **D**: central conductor (copper-clad steel). *Source: wikipedia.*

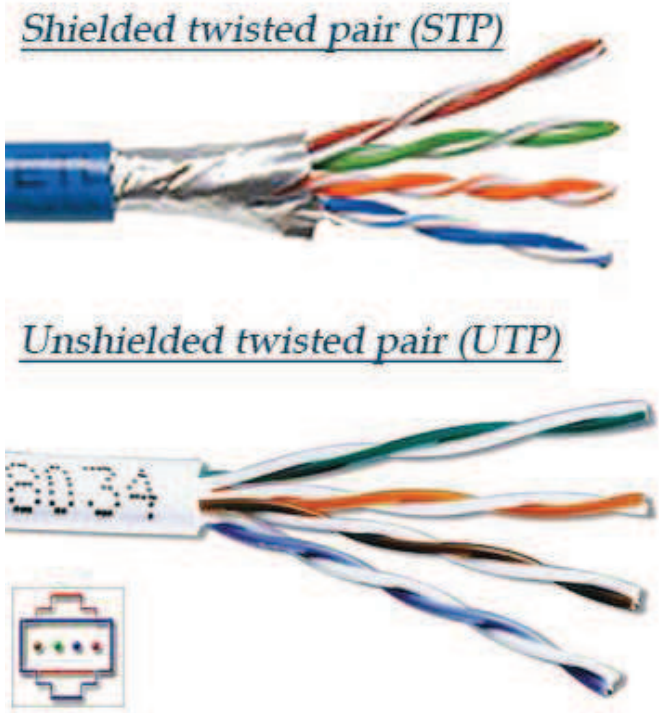

Figure 1.5: Example of STP and UTP cables.

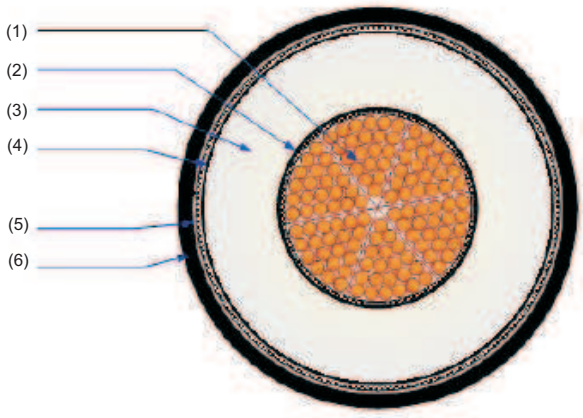

Figure 1.6: Example of a power cable cross section, showing 7 different parts: (1): Conductor, (2): internal semi-conductor, (3): insulation, (4): external semi-conductor, (5) : metallic screen, and (6): outer protective sheath. *Source: [14].*

location of faults). In a following stage, we conducted experimental measurements, and chose to use coaxial cables: on one hand this permits to compare the simulated data to the measured one, on the other hand we needed the simulator to model our circuit when deriving the fault location method (see Chapter 4). That is why it seemed adequate to consider coaxial cables.

1.2.4 Power cables

This type of cables is used to transmit electrical power at high voltage, whether it be AC or DC power transmission, ignition systems (in rocket engines for example), instruments, etc. In all applications, one aspect when conceiving these cables is that the insulation be able to support high voltage stress. A high voltage cable has a metallic shield layer over the insulation, connected to earth ground and designed to equalize the dielectric stress on the insulation layer. Fig. 1.6 shows a cross section through a high voltage power cable, showing its main parts. The inner conductor must withstand pulling stresses during cable laying, and the metallic screen also contributes to the mechanical protection of the cable. The outer protective sheath also contributes to the protection, along with insulating the metallic screen from the surrounding medium and protecting it from the corrosion [7]. Fig. 1.7 shows an example of submarine cables used for power transmission.

Having introduced some cable types along with their areas of application, we now proceed to introducing the main fault types that might affect a certain cable and the main reasons behind their appearance.

Figure 1.7: Underwater power transmission cables. *Source: [15].*

1.3 Wire faults

A 'healthy wire is the simplest yet most important element in an electrical system' [1]. Due to several causes, one or several anomalies might appear affecting the performance of the cable, and disturbing the reliable information or energy transmission. Depending on the application areas, the consequence of such a performance degradation might have catastrophic consequences: faults in aircraft wiring have been implicated in a number of severe aircraft accidents including the Swiss Air-111, TWA-800, and UAL-811 flights [16]. According to Captain Jim Shaw, manager of the in-flight fire project for the United States Air Line Pilots Association (ALPA), there are on average three fire and smoke events in jet transport aircraft each day in the USA and Canada alone, and the vast majority are electrical [17]. Faulty and improperly installed electrical wiring is a leading cause of fires in homes and commercial buildings : in 2005, almost $400,000$ fires occurred within the United States leading to over 3000 deaths and almost $14,000$ injuries [18, 19]. Using updated average statistics from the American NFPA (National Fire Protection Association), about $65,000$ of these fires were ignited by some sort of electrical fault. The data shows that these electrical faults costed about 703 million dollars in property damage [20].

The safety issues related to the faulty electrical wiring, as well as the high maintenance cost, have encouraged the governmental and industrial funding of the studies aiming to find novel wire fault detection and location methods that are able to spot any abnormality on the tested wires.

Generally, faults are classified into two main categories:

- hard faults: open and short circuits.
- soft faults: the other types of faults, such as insulation damage, cracks, frays, etc. A more formal definition based on the reflection coefficient from the fault will be addressed in the

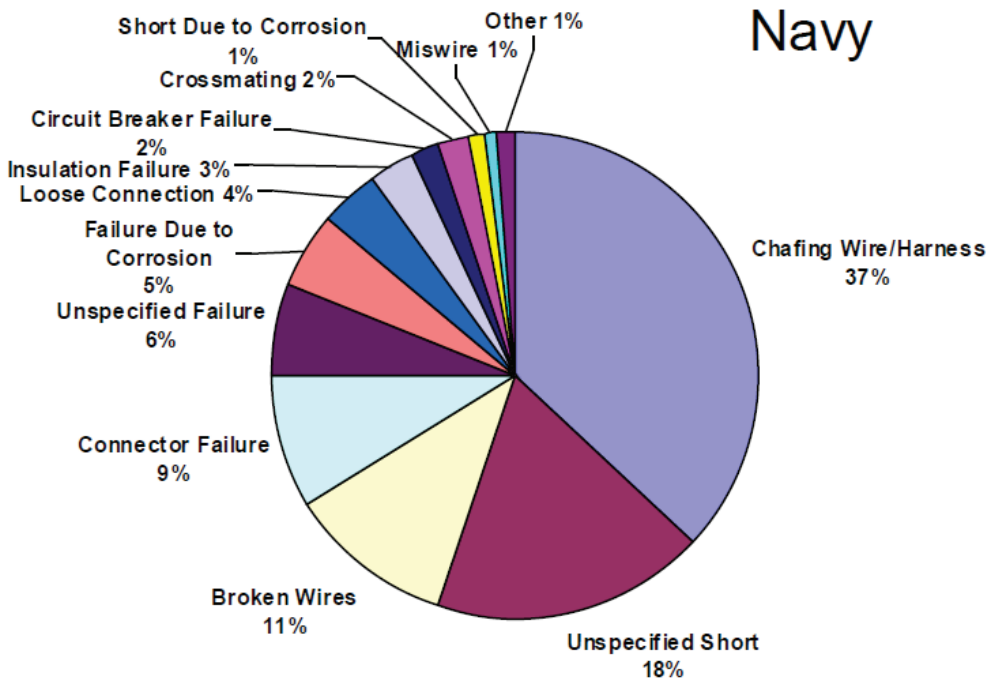

Figure 1.8: Wire fault types in the American Navy and their percentage [17].

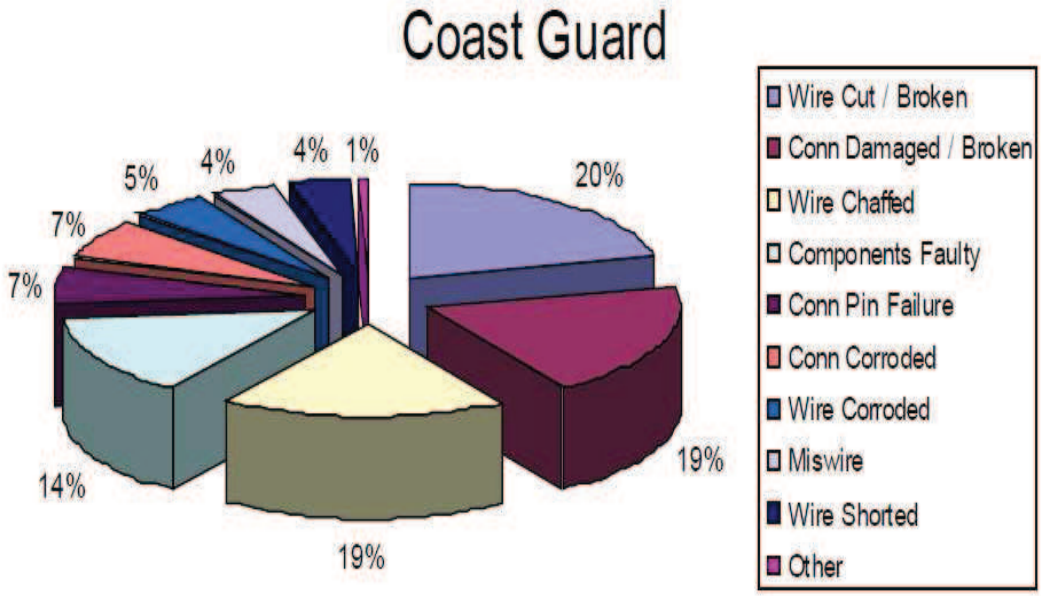

Figure 1.9: Wire fault types (Coast Guards) and their percentage [17].

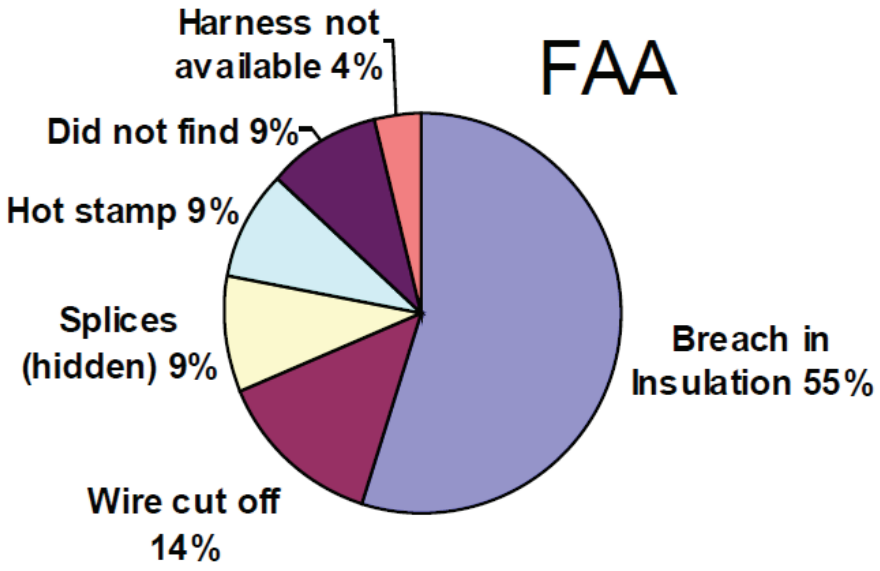

Figure 1.10: Wire fault types in the Federal Aviation Agency (FAA) and their percentage [17].

next chapter.

For a two-wire line, a short circuit occurs between the two conductors. In the domain of energy transportation (three-phase network), a short circuit [21] might occur between a phase and the ground, between two phases (with or without grounding), or between the three phases (with or without grounding). It is called two-phase short circuit and three-phase short circuit respectively. The same idea applies for polyphase circuits.

Figures 1.8, 1.9 and 1.10 show fault statistics conducted by the American navy, coast guards and the Federal Aviation Administration (FAA), showing the different fault types that occur in the equipments of the three administrations. The three diagrams show different types of soft faults, as well as a non negligible percentage of occurrence compared to hard faults. We are going to see, later in this chapter and in the next chapter, that this type of faults is generally the hardest to detect and locate using current techniques.

Since soft faults might develop into hard ones, they might jeopardize the well-functioning of a whole system: it is the case of cables that are exposed to moisture for example, and which already contain cracks in the insulator. The moisture can penetrate many types of insulation, causing it to break down [22], and electrical arcing might occur endangering the whole system. Thus, the need to find accurate methods able to detect and locate soft faults is crucial.

Wire faults occur for several reasons, that can be either internal or external to the cable.

- Internal causes, mainly due to:
  - A manufacturing defect that was not detected during factory tests (presence of impu-

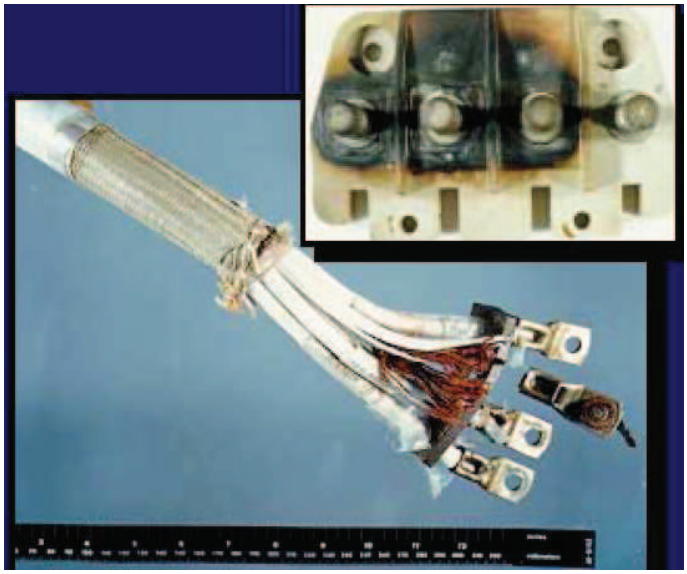

Figure 1.11: Wires and connections damaged due to long-term high temperature exposure and excessive power.

rities creating partial discharges leading to the progressive degradation of the insulation); however this type of faults is rare as the cables undergo extensive qualification tests before being delivered to the users.

  - An important local heating
  - long-term aging of the dielectric (the case of the cables with impregnated paper insulation).

- External causes:
  - Mechanical external aggressions: sod or Backhoe (in this case easily detectable), hanging by a anchor or trawl in the case of submarine cables;
  - Assembly defects, such as human intervention in the maintenance process.
  - Corrosion, oxidation, environmental effects (temperature, humidity, etc.)

Several photos show different fault types: in Fig. 1.11 we see a damaged cable because of long term high temperature exposure and excessive power. In Fig. 1.12 the damage is caused by the cable's presence in a high moisture environment. Fig. 1.13 points examples of cracks in aircraft cables, that can be found by the thousand in a typical aircraft [1].

1.4 Fault Detection and localization methods

In previous sections we have seen the variety of the existing cable types, as well as the faults that may occur and affect the cable performance. Thus, several methods emerged to inspect the

Figure 1.12: A damaged cable due to its presence in a high moisture environment.

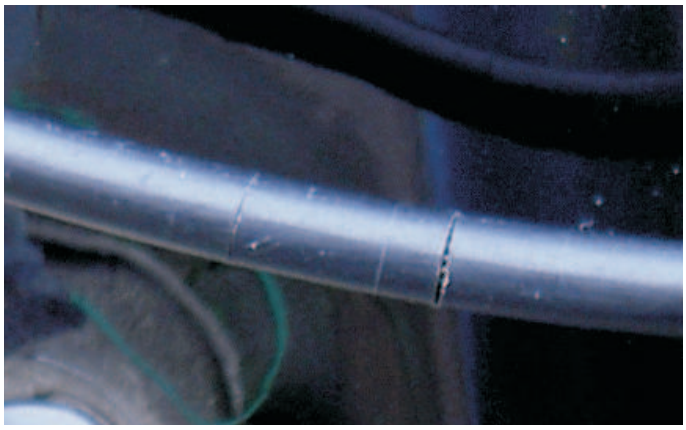

Figure 1.13: Example of cracks in aircraft cables.

presence of a damage in the cable, and a vast majority focused on the hard faults that may exist, because they are generally at the origin of the incidents that occur, such as fires and data breaks, and are also easier to detect and locate [23] as we will be seeing in the next chapter. However, the importance of soft faults should not be under-estimated, as a soft fault might develop into a hard one [24] [25] and might also cause the appearance of electrical arcing while the damaged cable is in use, thus threatening the safety of the system.

We begin by exposing the most common methods used today for the detection and location of cable faults, and their major limitations.

1.4.1 Visual inspection

It is a classic and common way to inspect the presence of anomalies in the tested cables, such as the case in the domain of aircraft [26, 27]. Visual inspection means inspecting the cable's health using 'raw' human senses; it entails accessing the cables and then carefully checking the insulation for holes and cracks, often no larger than the head of a pin. However, whole sections of wiring might never get inspected: chafed insulation can be hidden under clamps or around corners, or within multiwire bundles, which makes accessing the inspected wires very difficult. Also, the quality of the inspection is often subjective, and depends on the 'eye quality' of the inspector.

1.4.2 Radiographic inspections

X-Rays and other radiographic techniques have been successfully used to find problems in electrical wiring [16]. The advantage of these techniques is that they allow inspection through the insulation, thus allowing the technicians to see the conductors inside the insulation. However, this method presents the same inconvenience as the visual inspection method: it requires a human intervention, as well as an X-ray generator and detector that have to be placed near the cable under test. Thus, this imaging technique cannot be applied to cables that are not easily accessible.

1.4.3 Low frequency and DC methods

These methods require having a 'healthy' cable with the same characteristics as the tested cable. Among the most common methods are the 'three-wire' fault location method and the loop method.

1.4.3.1 Three-wire fault location method

A first approach is to try to estimate the location of an insulation fault, by applying a direct voltage (or current), as represented in Fig. 1.14. This studied circuit is modeled in Fig. 1.15, where every conductor can be modeled as a resistance, whose value depends on the cable length.

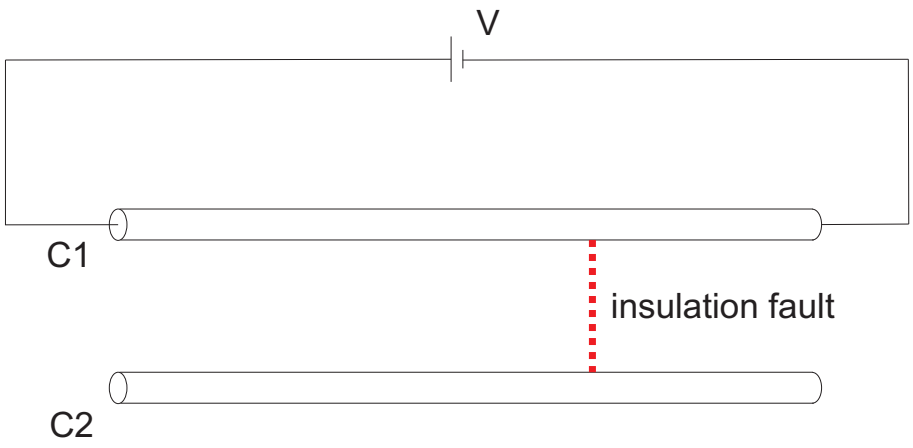

Figure 1.14: Wire Testing using DC methods. The damaged wire is connected to the voltage source.

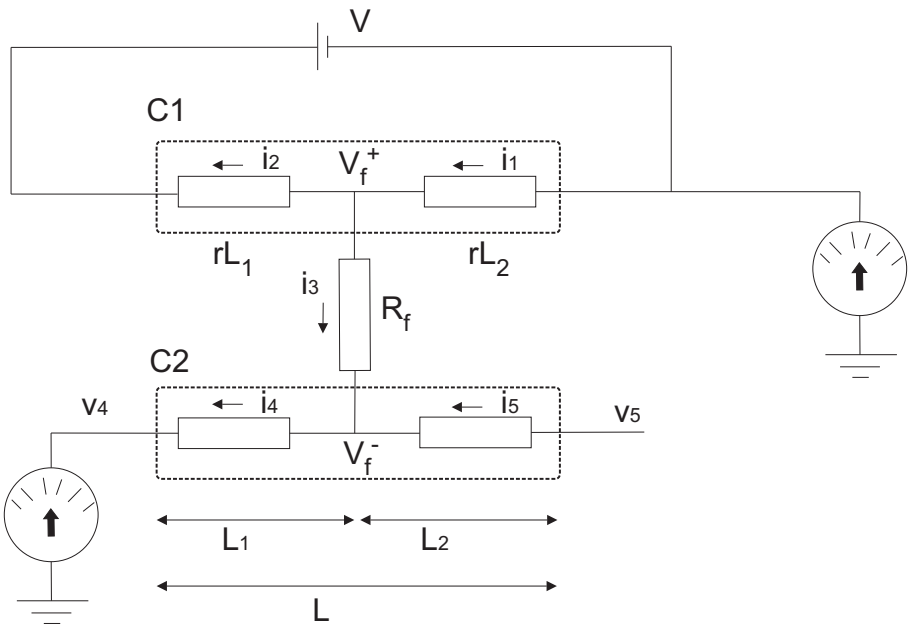

Figure 1.15: Three-wire fault location method. Currents i_3, i_4 and i_5 are all assumed to be zero, so $V_4 = V_3 = V_5 = V$.

We denote by r the resistance per meter of the tested cables, whose unit is Ω/m, whilst R_f models the short circuit (created by the insulating damage) between the cables which length is referred to as L.

We suppose that R_f is equal to zero, and consequently the current i_3 is null. The same applies for the currents i_4 and i_5 because the cable C_2 is idle. Under these assumptions, we can calculate the position of the short circuit by calculating the length L_1, based on the following equations

$$V_5 = V_4 = V_f^- = V_f^+ = \frac{rL_1}{rL_1 + rL_2}V = \frac{L_1}{L_1 + L_2}V \tag{1.1}$$

since $L = L_1 + L_2$, we can conclude

$$V_f^+ = \frac{L_1}{L}V \tag{1.2}$$

and consequently

$$L_1 = \frac{V_f^+}{V}L \tag{1.3}$$

V_f^+ can be determined by measuring V_4 or V_5 according to Equation (1.1), and the position of the damage can be found. This method is generally used for electric power cables [28]. In order to be able to apply this method, the cables must be disconnected from their electrical circuit to avoid a potential damage of the latter when injecting the DC voltage, which can have high values depending on the amplitude of the insulating fault we are trying to locate.

Other methods in this category are the loop methods [29].

1.4.3.2 Loop methods

Generally, these methods are based on the principle of the Wheatstone bridge [30], illustrated in Fig. 1.16. At the point of balance, i.e., when the galvanometer G indicates a null value, we have the following equation

$$R_1 R_x = R_2 R_3 \tag{1.4}$$

The values of the three resistances R_1, R_2 and R_3 are known, so the value of R_x can be determined.

When applied to fault location on cables, the method is known as the Murray loop bridge [31]. It is the Wheatstone bridge principle, as shown in Fig. 1.17: At the point of balance, we have,

$$R_1 rd = R_2 r(2D - d) \tag{1.5}$$

with r being the resistance per unit length of the conductor, and considering the case where the healthy conductor and the faulty one are identical. This brings us to the following

$$d = \frac{2R_2}{R_1 + R_2}D \tag{1.6}$$

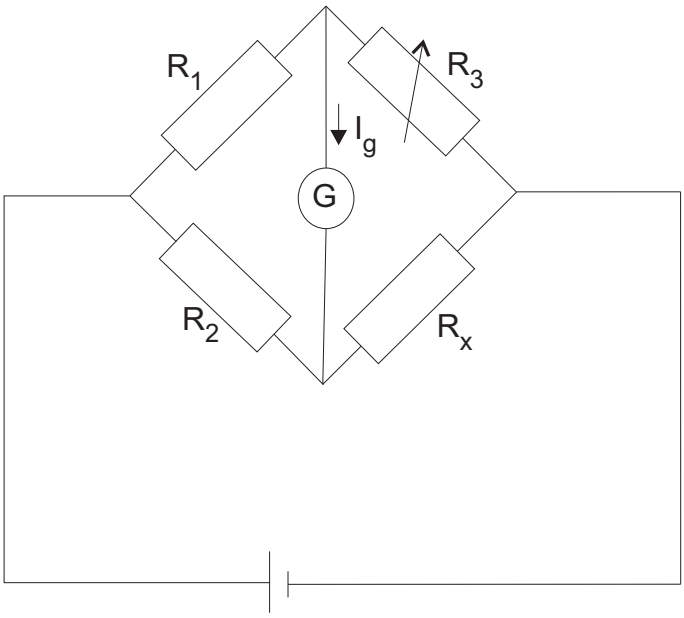

Figure 1.16: The Wheatstone bridge, used to calculate an unknown resistance R_x. When the bridge is balanced, $I_g = 0$ and consequently $\frac{R_1}{R_3} = \frac{R_2}{R_x}$.

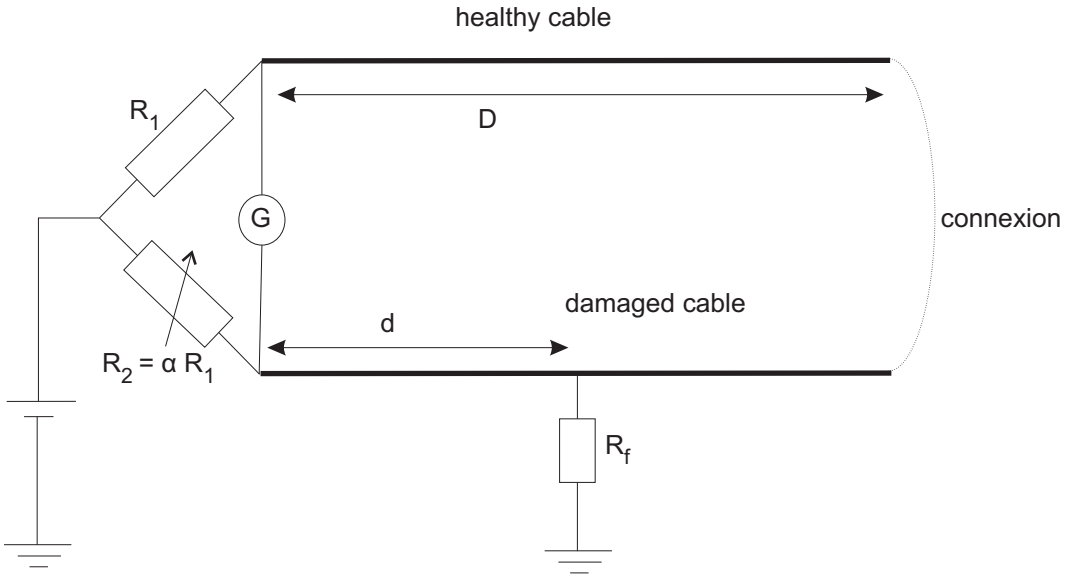

Figure 1.17: Fault location using the loop method. d is the distance to the fault of value R_f.

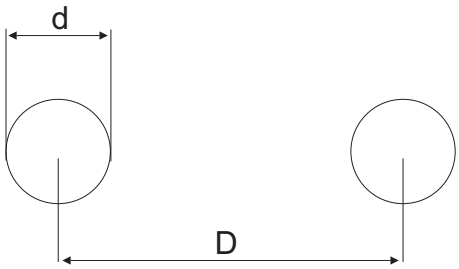

Figure 1.18: Symmetrical two-wire line.

in general, the two resistors R_1 and R_2 are chosen such that we have $R_2 = \alpha R_1$, with α a potentiometer that can be adjusted so as to have a null value of the voltage indicated by G. Under this condition the distance d can be determined by the relation

$$d = \frac{2\alpha}{1+\alpha} D \tag{1.7}$$

This method is easy to implement but the inconvenience is that it only locates hard faults, and it is usually better to disconnect the cables from the electronic system in order to carry out the measurements, which means a human intervention. Also these methods are not used when it comes to complex networks configurations, but are rather used for single cable configurations.

1.4.4 Capacitive and inductive methods

Other methods to determine the position of a hard fault are capacitive and inductive methods [32]. Capacitance measurement tend to locate an open circuit while induction measurement is used to locate a short circuit. These methods are also used for single cable configurations and cannot be applied to more complex network configurations, including one or several junctions and discontinuities, such as a single junction network, equivalently pointed to as a Y-network.

An example will help us illustrate the principle of these methods: let us consider a symmetrical two-wire line, as shown in Fig. 1.18. D denotes the distance between the two conductors, d the diameter of the conductors, ε the permittivity of the dielectric separating the conductors, and μ the magnetic permeability of the insulator between the two conductors. For a symmetrical two-wire line, the capacitance and inductance per unit length are given by

$$C = \frac{\pi\varepsilon}{\cosh^{-1}\left(\frac{D}{d}\right)} \tag{1.8}$$

and

$$L = \frac{\mu}{\pi} \cosh^{-1}\left(\frac{D}{d}\right) \tag{1.9}$$

where C is expressed in F/m and L in H/m. The values of C and L for each type of cables are known, and consequently by measuring the global capacitance and inductance of the cable under

test, it is possible to determine the distance to the open or short circuit. To be able to do this measurement, we can use voltage dividers, loop methods (as we already saw), oscillators or any other device that can measure the impedance. Note that the capacitive and inductive methods are simple methods, but are not adapted to test wire networks because we cannot locate a fault situated on one of the network branches.

1.4.5 Medium frequency techniques

1.4.5.1 Tone injection

This technique usually allows a technician to locate a hard fault. A voltage and/or current is injected onto a wire and the technician walks along a cable while carrying an electric or magnetic field sensing probe. The voltage and/or current is modulated with one or more AC signals (60 Hz - 450 kHz) that creates an electric or magnetic field that can be detected by the sensing probe. This probe produces a tone when the electric or magnetic field is detected.

Both electric and magnetic field probes are routinely used for finding faults and tracing wiring routes in household wiring. However, electric field tests cannot be used on shielded wiring or wiring passed through a conductive conduit because the electric field does not penetrate the shield. Magnetic field tests have similar limitations. This limits the applicability of this technique.

1.4.5.2 Radio Frequency (RF) radiation

RF shield testing is a method for locating damage to shields used in coax or STP wires [16]. A radio frequency source is applied to a shielded wire. Any place along the wire where the grounded shield is not complete will radiate, and that radiation can be picked up and its source located with a radio receiver. But in domains such as the aircraft, the majority of the wiring is not shielded, and therefore cannot be tested using this technique, because the wire radiates along its entire length, giving no information other than the routing of the wire.

1.4.6 High frequency techniques

High frequency techniques are defined as the techniques that use frequencies with wavelengths shorter than two times the length of the cable being tested. They include impedance spectroscopy and reflectometry methods.

1.4.6.1 Impedance spectroscopy

This method consists of analyzing the insulation characteristics of the cable at various frequencies [16] [33] [34]. It can be accomplished using a network analyzer to inject a sine wave into one end of the cable and monitor the impedance of the cable with respect to the airframe or

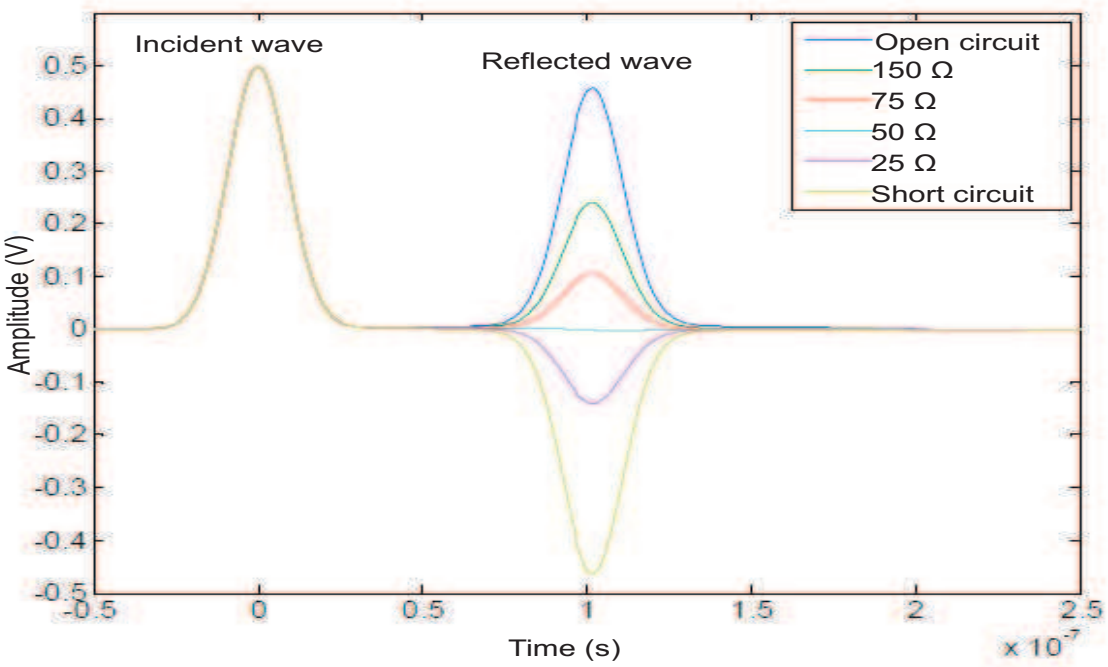

Figure 1.19: Example of standard TDR applied to a 50 Ω coaxial cable, for different values of the terminal charge.

adjacent wires. The technique requires that the other cable end be disconnected from any other devices. The frequency is swept over a predetermined range, and the impedance is recorded for each frequency injected. The data collected is analyzed by comparing frequency-dependent impedance data sampled from healthy wires. Soft faults are difficult to detect using this method, adding the fact that this method requires the access to both ends of the cables.

1.4.6.2 Reflectometry methods

Reflectometry methods [35] are the most common methods used today for fault detection and location in wire networks. Since the middle of the twentieth century, reflectometry was used to detect and locate faults in electrical cables, as well as in telecommunication networks [36]; not to forget other applications, such as geotechnology [37], hydrology [38], construction [39], aircraft wire health inspection [1, 40], etc.

In the domain of wire fault detection and location, there are several reflectometry methods, divided into two main categories, based on the analysis domain: Time Domain Reflectometry (TDR) [41] and Frequency Domain Reflectometry (FDR) [42]. The general principle of the different methods is however the same: they rely on the propagation of an electromagnetic waveform in the wire network to be tested, and the analysis of the reflected wave (caused by the presence of impedance discontinuities, junctions, etc. in the network) trying to detect and locate an eventual fault.

The different reflectometry methods differ in the form of the injected wave, or in the post processing techniques used to extract information from the reflected wave. For example, in the TDR family, standard TDR injects a step or a pulse [43] into the wire network to be tested, hereafter referred to as the Network Under Test (NUT), and relies on the analysis of the reflected wave in the temporal domain in order to extract the fault's signature, whilst Sequence TDR (STDR) [43, 44] and Spread Spectrum TDR (SSTDR) [44, 43, 45, 24] inject a numerical pseudo-noise sequence, and when the reflected wave is received, a correlation operation of this wave with the initially injected template is performed to try to determine the position of an eventual fault.

In the Frequency domain, we inject stepped frequency sine waves into the NUT, and can distinguish three main methods, depending on the parameter that is to be measured in order to determine the fault location: Frequency Modulated Continuous Wave (FMCW) [46] which is based on the frequency measurement, Phase Detection FDR (PDFDR) [42, 47] based on the phase measurement, and Standing Wave Reflectometry (SWR) [48] based on the measurement of the amplitude of the stationary wave (superposition of the incident and reflected waves).

There is also a third type of methods that has been recently developed called the Noise domain Reflectometry (NDR) [49]. It also uses correlation-based analysis to try to determine the position of an eventual fault, but differs from spread spectrum techniques in the fact that it uses the signals already present on the cable, and thus requires that the tested cable be in usage.

To better illustrate the basic principle of these methods, we chose the simple example of a $50\ \Omega$ coaxial cable, where we have a testing port connected to the line to be tested. This testing port is both the emitter of the incident voltage wave (i.e., the testing signal) and the receiver of the reflected wave.

We consider standard TDR, because it is going to be the method we chose in our study to compare its performances to the new method we developed. In guided wave propagation, a wave travels down the wire until it encounters an impedance discontinuity: then a part of this wave is reflected back and the other part is transmitted through the discontinuity. The reflected part relates to the incident one through a reflection coefficient, which depends on the characteristic impedance of the line [50], as well as the impedance of the discontinuity situated on the line (for a detailed explanation refer to chapter 2).

Consequently, the reflected wave contains information about the nature of the fault, and the time (in standard TDR) required for the fault-related echo (in the reflected wave) to reach the testing port position gives information about the position of the fault. In the example we considered above, several resistive charges have been connected to the end of the cable, and the reflected wave compared to the injected one have been shown on Fig. 1.19. We clearly notice the large reflections in the case of hard faults (see chapter 2 for demonstration) and weak reflections in the case of soft faults. Consequently, a soft fault is generally less easier to detect than a hard fault, because it results in a weaker reflection, and because usual detection techniques rely on the peak detection [51, 43] to asses the presence of an eventual fault.

Moreover, the detection becomes more complicated in complex networks, where several reflections from the network discontinuities (junctions, mismatched loads, impedance variations, etc.) occur and can mask an eventual fault's reflection, especially if this fault is soft, and separated from the testing port by one or several discontinuities (i.e., the fault is embedded in the network). Generally, reflectometry methods work well for simple cases on single transmission lines [23, 42, 44, 49, 52, 53, 54], but start to be insufficient as soon as the network structure becomes more complex, or the faults becomes 'softer', so that the reflected wave amplitude caused by these faults becomes comparable to the noise level [23].

In order to ameliorate the detection and location processes, other post processing techniques have been proposed. For example, in the case of time domain measurements, iterative algorithms such as the Clean deconvolution Algorithm (CA)[51] were proposed to detect several faults on a coaxial cable. However, the utilization of this algorithm assumes the propagating medium to be non-dispersive, which is not the case in real fault cases, as we will be seeing when we analyze several types of faults in the experimental section in the third chapter.

Also, other correlation-based techniques, such as the Time-Frequency Domain Reflectometry (TFDR) [53, 55] were proven experimentally to work well in the case of a single coaxial cables, but more complex networks have not been addressed yet. Other methods for fault location, such as the iterative ones, will be addressed in details in the fourth chapter, when analyzing the most common fault location methods and their limitations.

Based on the literature, we can resume the main advantages and inconveniences of the different reflectometry methods in Table 1.1, where we can see that the choice of a certain test method depends on the application type, the material cost, the desired resolution, etc. As seen in the table, the main advantages of the TDR methods are their implementation simplicity relatively to FDR techniques, their higher noise immunity, especially for STDR and SSTDR, and also the minimal interference with the existing signals on live wires that the S/SSTDR provide [43]. However, TDR methods include using more complex electronics than FDR and are thus more expensive, also the interpretation of the results is often difficult for complex networks [27]. As for the FDR architectures, they are less expensive and more compact than the TDR ones, but not ideal to be used on live wires, although they can be used for some applications [56]. Both TDR and FDR methods start to fail as soon as we start to deal with soft faults, which result in weak reflections that might be comparable to the noise level. Network complexity is also another factor that limits the performance of both methods, given that the multiple reflections that occur within these structures mask the fault response, and consequently faults become harder to detect and locate. These facts will be further illustrated in the following chapters.

1.5 Conclusion

In this chapter, we presented an overview of the different electrical cables types that exist in today's modern systems, along with the major fault causes that affect the performances of these

	Advantages	**Inconveniences**
TDR methods	• Most effective for live wire testing (S/SSTDR) • Better resolution than FDR • Higher noise immunity (S/SSTDR) • Simpler architecture than FDR	• More expensive than FDR • Results interpretation is hard • Start to fail when dealing with soft faults and complex networks
FDR methods	• More compact architecture than TDR • MSR and PDFDR are less expensive than TDR	• Not ideal for live wire testing • Resolution depends on the sweeping frequency • FMCW is more expensive than the other FDR methods • Start to fail when dealing with soft faults and complex networks
NDR	• No interference with the existing signals on the tested wire • Reduction of the global architecture of a reflectometer	• Start to fail when dealing with soft faults and complex networks

Table 1.1: Evaluation of the advantages and inconveniences of the different reflectometry methods.

cables, threatening the well-functioning of the system. After viewing the two major fault families, hard faults and soft faults, we highlighted the different wire fault detection and location methods; capacitive and inductive methods are the simplest and least expensive methods, yet they can only locate hard faults on single cable configurations, and cannot be used on live wires. Loop methods are also less expensive than reflectometry methods, but with larger response times than these methods. Reflectometry methods present the advantage of being 'automated' methods, unlike the loop methods for example, and thus can be considered for embedded applications. Notice that a common inconvenience for all the methods is that they start to fail as soon as the fault becomes 'softer', that is when the fault's response becomes weak compared to that of a hard fault. Complexity also arises when we deal with complex networks, involving the presence of one or several junction, discontinuities, mismatched loads, etc. Hence the motivation of our work to deal with soft faults in complex networks.

Chapter 2

Guided Wave Propagation: Concepts and Tools

2.1 Introduction

In the previous chapter, we saw that cables in modern electronic systems, such as aircraft, ships and vehicles serve to transmit information and energy between the different components of the system. Some of these cables consist of a large number of individual wires, which are packed into bundles for neatness and space conservation. These cables are referred to as Multi-conductor Transmission Lines (MTLs) [50], and their analysis is somewhat more complex than that of a two-conductor transmission line. For example, the transmission-line equations for a two conductor line will be a coupled set of two partial differential equations for the line voltage $V(z,t)$, and line current $I(z,t)$, where the line conductors are parallel to the z axis, and time is denoted as t. Solution of these coupled, scalar equations is straightforward . In the case of a MTL consisting in $(n+1)$ conductors parallel to the z axis, the corresponding governing equations are a coupled set of $2n$, matrix partial differential equations relating the n line voltages, $V_i(z,t)$, and n line currents, $I_i(z,t)$, for $i = 1, 2, \cdots, n$. the number of conductors might be quite large, e.g., $(n+1) = 100$, in which case efficiency of solution of the $2n$ equation becomes an important consideration.

In our study, we introduce new concepts into the domain of fault detection and location in wire networks, that, to the best of our knowledge, have not been proposed before. We begin with the case of two-conductor transmission lines, considered by the majority of researchers [23, 25, 27, 42, 51, 52, 54], and do not address MTLs in the present work. Moreover, for the sake of simplicity, we consider uniform lines (such as for coaxial cables for example), which means that the conductors are parallel to each other and the z-axis, also that they have uniform cross sections along the line axis.

This chapter is devoted to presenting an overview of the concepts and tools we used in the present work. The explanation concerning the tools we considered shows the methods we

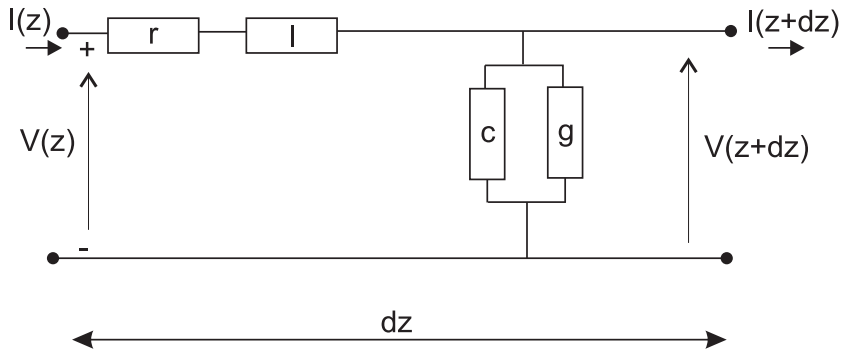

Figure 2.1: Equivalent circuit of a small section of a transmission line, showing the per-unit-length parameters r, l, c and g.

adopted to build our transmission lines simulator, and observe the voltage propagation in these lines. As for the concepts, we introduce the idea of the 'difference system', after a justified approach explaining the reasons behind this choice.

We begin by introducing the transmission line theory, which we used to model guided propagation in our study.

2.2 Guided Propagation Modeling

A simple way to describe the propagation of voltage and current waves along a two conductor transmission line is the transmission line theory, as presented in [50]. The fundamental assumption for all transmission-line formulations and analysis, whether it be for a two-conductor line or a MTL, is that the field distribution surrounding the conductors obeys a Transverse ElectroMagnetic (TEM) distribution. For our case of a two-conductor transmission line, this assumption results in a set of coupled partial differential equations, referred to as the transmission-line equations (see Section 2.2.1). The solution of these equations can be obtained via a time-domain or frequency-domain analysis [57]. Frequency domain analysis is however easier to implement, that is why we chose to use it when developing our simulator. Consequently, time-domain responses are obtained from frequency responses via an inverse Fourier Transform [58].

2.2.1 Two conductor transmission line

We consider conductors with a uniform cross section, whose dimensions are considered negligible when compared to the wavelength. All cross sectional information about a particular line is contained in the per-unit-length parameters, i.e., inductance l, capacitance c, conductance g and resistance r for the given line [50], as shown in Fig. 2.1, for a small section of a transmission line with length dz.

Let $V(z)$ and $I(z)$ denote the voltage and current at any position z of a transmission line,

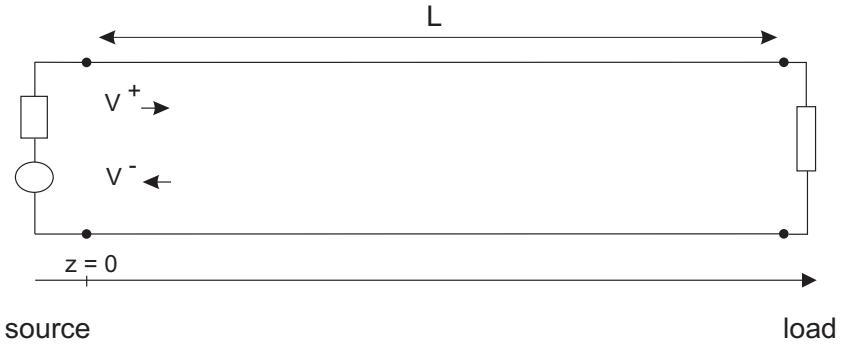

Figure 2.2: A two conductor transmission line.

in their phasor notation [59], which means that the line voltage and current in the time domain, $V(z,t)$ and $I(z,t)$, can be written as

$$V(z,t) = Re\{V(z)e^{j\omega t}\} \tag{2.1}$$

$$I(z,t) = Re\{I(z)e^{j\omega t}\}, \tag{2.2}$$

ω is the radian frequency of excitation, i.e., $\omega = 2\pi f$ where f is the cyclic frequency of excitation, and $Re\{\}$ denotes the real part of the enclosed complex quantity. Note that for the phasor notation, we use peak voltages and currents. The voltage and current at the position z can be found by solving the two wave equations

$$\frac{\partial^2 V(z)}{\partial z^2} - \gamma^2 V(z) = 0 \tag{2.3}$$

$$\frac{\partial^2 I(z)}{\partial z^2} - \gamma^2 I(z) = 0 \tag{2.4}$$

where γ is the complex propagation constant given by

$$\gamma = \sqrt{(r + j\omega l)(g + j\omega c)} = \alpha + j\beta \tag{2.5}$$

j is the imaginary unit, α is the attenuation constant whose units are nepers/m and β is the phase constant whose units are radians/m.

Let us consider the example of Fig. 2.2, illustrating a two-conductor transmission line. $V(z)$ and $I(z)$ can be determined from the solution to the wave equations as follows

$$V(z) = V^+ e^{-\gamma z} + V^- e^{\gamma z} \tag{2.6}$$

$$I(z) = I^+ e^{-\gamma z} + I^- e^{\gamma z} \tag{2.7}$$

where $V^+ e^{-\gamma z}$ and $I^+ e^{-\gamma z}$ are the forward propagating voltage and current waves, $V^- e^{\gamma z}$ and $I^- e^{\gamma z}$ are the backward propagating waves. The terms V^+, V^-, I^+ and I^- are complex-valued, undetermined constants, which will be determined when we incorporate the terminal conditions

at the two ends of the line, i.e., at the source and load positions. These constants are connected by the characteristic impedance of the line, Z_c, as follows

$$Z_c = \frac{V^+}{I^+} = \frac{-V^-}{I^-} = \sqrt{\frac{r + j\omega l}{g + j\omega c}} = \sqrt{\frac{Z}{Y}} \tag{2.8}$$

where $Z = r + j\omega l$ and $Y = g + j\omega c$. The ratio of backward-traveling and forward-traveling voltage waves at any point of the line is referred to as the reflection coefficient $\Gamma(z)$ at that point

$$\Gamma(z) = \frac{V^- e^{\gamma z}}{V^+ e^{-\gamma z}} \tag{2.9}$$

at the load, this reflection coefficient is

$$\Gamma(L) = \frac{Z_L - Z_c}{Z_L + Z_c} \tag{2.10}$$

In the previous chapter, we pointed out that a hard fault (open and short circuit) results in a large reflection at the fault position. Indeed, in the case of an open circuit, the reflection coefficient of (2.10) is equal to $+1$, and in the case of a short circuit it is equal to -1. The definition of a hard fault points the fact that the absolute value of the reflection coefficient is equal to 1, whilst for the soft faults, it is always inferior to 1. The more this value is close to zero, the more the fault is said to be 'soft', and the more difficult its detection and location become, due to the weak reflection caused by this fault. The inferior limit of the absolute value of $\gamma(z)$ is reached when $Z_L = Z_c$, i.e., when the load is matched to the transmission line. In this case we have no reflection occurring from the load.

So far we have been considering a uniform two-conductor transmission line where the two conductors are parallel to each other. In our work we will consider complex networks with discontinuities and junctions with 3 and 4 branches. The way to model these networks and discontinuities will be presented in the next sections.

2.2.2 Multiport modeling: Scattering parameter matrix

The network model we are going to use in our simulations contains junctions and discontinuities. A way to represent these blocks is the use of the S-parameter matrix, denoted as S [60]. To begin our discussion, we consider the example illustrated in Fig. 2.3. Each transmission line is characterized by a characteristic impedance Z_{c_i}, a length L_i, and a propagation constant γ_i. The discontinuity (a 2-port for instance) is represented with a black box, referred to as (B). Note that the length of this block is null.

Let us consider the first line of length L_1, the voltage $V_1(z)$ and current $I_1(z)$ at any point of this line can be written as follows

$$V_1(z) = V_1^+ e^{-\gamma_1 z} + V_1^- e^{\gamma_1 z} \tag{2.11}$$

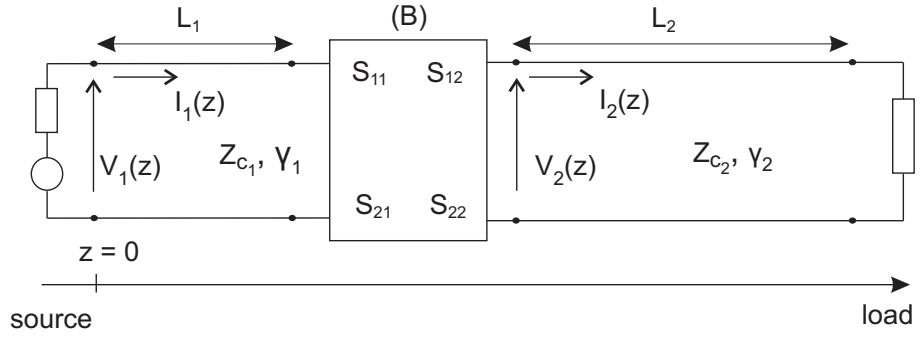

Figure 2.3: A two-conductor transmission line containing a discontinuity represented as a block (B) whose length is null.

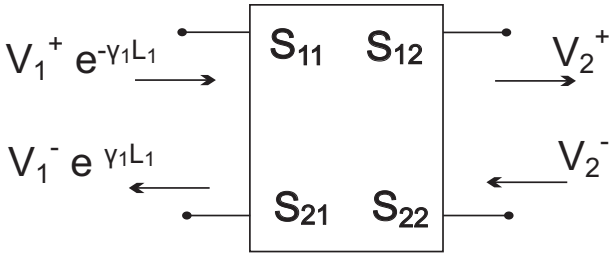

Figure 2.4: S-parameters of a 2-port system

$$I_1(z) = \frac{V_1^+}{Z_{c_1}} e^{-\gamma_1 z} - \frac{V_1^-}{Z_{c_1}} e^{\gamma_1 z} \tag{2.12}$$

Similarly, the voltage $V_2(z)$ and current $I_2(z)$ for any point situated on the second branch which length is L_2 are

$$V_2(z) = V_2^+ e^{-\gamma_2 (z - L_1)} + V_2^- e^{\gamma_2 (z - L_1)} \tag{2.13}$$

$$I_2(z) = \frac{V_2^+}{Z_{c_2}} e^{-\gamma_2 (z - L_1)} - \frac{V_2^-}{Z_{c_2}} e^{\gamma_2 (z - L_1)} \tag{2.14}$$

The discontinuity (B) can be characterized with a voltage scattering parameter matrix (i.e., S-parameter matrix), relating the incident and reflected waves at that point, as shown in Fig. 2.4. The incident waves are portions of Equations (2.11) and (2.13) incoming at the junction, i.e., $V_1^+ e^{-\gamma_1 L_1}$ and V_2^-. The reflected waves, $V_1^- e^{\gamma_1 L_1}$ and V_2^+, are outgoing from the junction. So we can write

$$\begin{bmatrix} V_1^- e^{\gamma_1 L_1} \\ V_2^+ \end{bmatrix} = S \begin{bmatrix} V_1^+ e^{-\gamma_1 L_1} \\ V_2^- \end{bmatrix} \tag{2.15}$$

with

$$S = \begin{bmatrix} S_{11} & S_{12} \\ S_{21} & S_{22} \end{bmatrix} \tag{2.16}$$

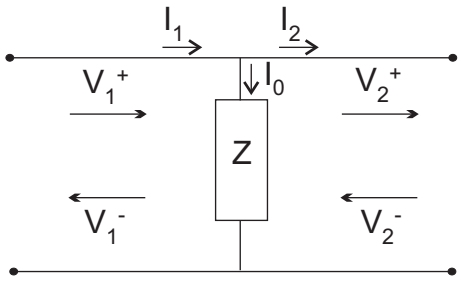

Figure 2.5: A 2-port system formed of a parallel load. Incident and reflected voltage waves are illustrated.

In this case, the parameters S_{ii} are the voltage reflection coefficients, and S_{ij} are the transmission coefficients. The transmission coefficient S_{21} describes the part of the wave that has been transmitted through the discontinuity from the first section (line 1) to the second section (line 2). In this case, it is equal to

$$S_{21} = \frac{V_2^+}{V_1^+ e^{-\gamma_1 L_1}} \tag{2.17}$$

Considering the fact that the multiports we study contain passive components, we assume that they are reciprocal; consequently, in this case we have $S_{12} = S_{21}$ and thus S is symmetrical.

The determination of the reflection and transmission coefficients allows determining the S-parameter matrix of a certain discontinuity, thus characterizing the latter. Next we give a few examples we used in our simulator.

2.2.2.1 S-parameter matrix of a parallel load

In [29], the author investigated fault types in electrical cables, and showed that some of these faults can be modeled as parallel resistive loads. As we developed our simulator before addressing a specific type of faults (whether it be hard or soft) we considered a parallel load for modeling the faults in the networks, and were interested in the local reflection coefficient from the fault as an indicator of the 'softness' of the fault.

This type of discontinuities is illustrated in Fig. 2.5. We consider the same characteristic impedance for the line upstream and downstream the discontinuity, denoted as Z_c. The impedance of the parallel load (discontinuity) is Z. We note the incident voltage waves as V_1^+ and V_2^-, the reflected ones as V_1^- and V_2^+.

The S-parameter matrix satisfies the following equation

$$\begin{bmatrix} V_1^- \\ V_2^+ \end{bmatrix} = S \begin{bmatrix} V_1^+ \\ V_2^- \end{bmatrix} \tag{2.18}$$

It is found by calculating the corresponding reflection and transmission coefficients, or equivalently by imposing the continuity conditions of the voltages and currents across the discontinu-

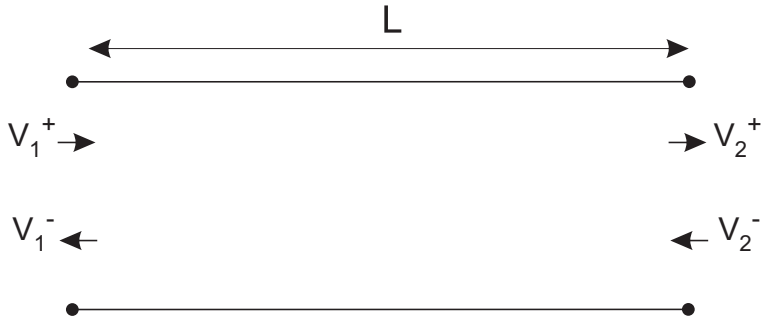

Figure 2.6: Example of a uniform two-conductor transmission line showing the forward and backward propagating voltage waves.

ity, i.e.,

$$V_1^+ + V_1^- = V_2^+ + V_2^- \tag{2.19}$$

$$I_1 = I_0 + I_2 \tag{2.20}$$

so as to find

$$S = \begin{bmatrix} \frac{-Z_c}{2Z+Z_c} & \frac{2Z}{2Z+Z_c} \\ \\ \frac{2Z}{2Z+Z_c} & \frac{-Z_c}{2Z+Z_c} \end{bmatrix} \tag{2.21}$$

So far we have two equations and four unknown constants to be determined. The remaining two equations are determined when imposing the continuity conditions at the two ends of this block, which for example might be connected to a source from one side, and to a load or another block from the other side.

2.2.2.2 S-parameter matrix of a two-conductor transmission line

An example of a uniform two-conductor transmission line is given in Fig. 2.6. Let L be the length of the transmission line, and γ the propagation constant defined in (2.5). In the particular case of uniform lossless transmission lines, the attenuation constant $\alpha = 0$, and consequently $\gamma = j\beta$; this means that the difference between the forward propagating waves V_1^+ and V_2^+ is the phase delay, because no attenuation or dispersion affects these propagating waves. This is also the case of the backward propagating waves V_1^- and V_2^-. The S-matrix in the case of a two-conductor transmission line is:

$$S = \begin{bmatrix} 0 & e^{-\gamma L} \\ \\ e^{-\gamma L} & 0 \end{bmatrix} \tag{2.22}$$

2.2.2.3 S-parameter matrix of an n-branch junction

In our simulations we consider perfect lossless junctions, which means that the capacitive and inductive parasitic effects [61] are not taken into account. The case of a 3-branch junction is

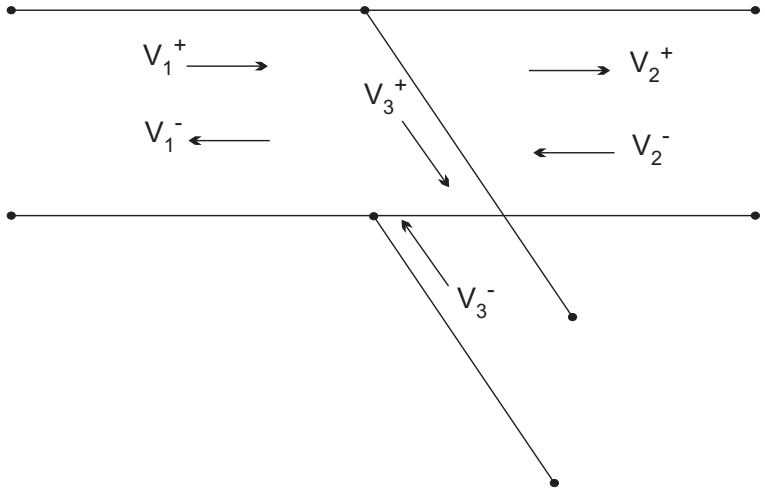

Figure 2.7: A 3-branch perfect junction.

illustrated in Fig. 2.7. In the general case of an n-branch junction, the continuity of the voltage allows to form $(n-1)$ equations, and the current continuity 1 equation. The other n equations are obtained by imposing the continuity conditions at the extremities of the port, as invoked earlier. For the case of Fig. 2.7, where we considered that the three branches have the same characteristic impedance Z_c for simplification purposes, the voltage continuity conditions at the junction are

$$V_1^+ + V_1^- = V_2^+ + V_2^- \tag{2.23}$$

and

$$V_1^+ + V_1^- = V_3^+ + V_3^-. \tag{2.24}$$

The current continuity condition at the junction, or Kirchhoff's nodal law [62], implies that the sum of the currents flowing into the junction is equal to the sum of currents flowing out of the junction. If expressed in terms of the voltage waves, the condition is

$$\frac{V_1^+}{Z_c} - \frac{V_1^-}{Z_c} = \frac{V_2^+}{Z_c} - \frac{V_2^-}{Z_c} + \frac{V_3^+}{Z_c} - \frac{V_3^-}{Z_c} \tag{2.25}$$

(2.23), (2.24) and (2.25) allow calculating S, which must satisfy the following equation

$$\begin{bmatrix} V_1^- \\ V_2^+ \\ V_3^+ \end{bmatrix} = S \begin{bmatrix} V_1^+ \\ V_2^- \\ V_3^- \end{bmatrix} \tag{2.26}$$

the calculation of S leads to the following

$$S = \begin{bmatrix} -\frac{1}{3} & \frac{2}{3} & \frac{2}{3} \\ \frac{2}{3} & -\frac{1}{3} & \frac{2}{3} \\ \frac{2}{3} & \frac{2}{3} & -\frac{1}{3} \end{bmatrix} \tag{2.27}$$

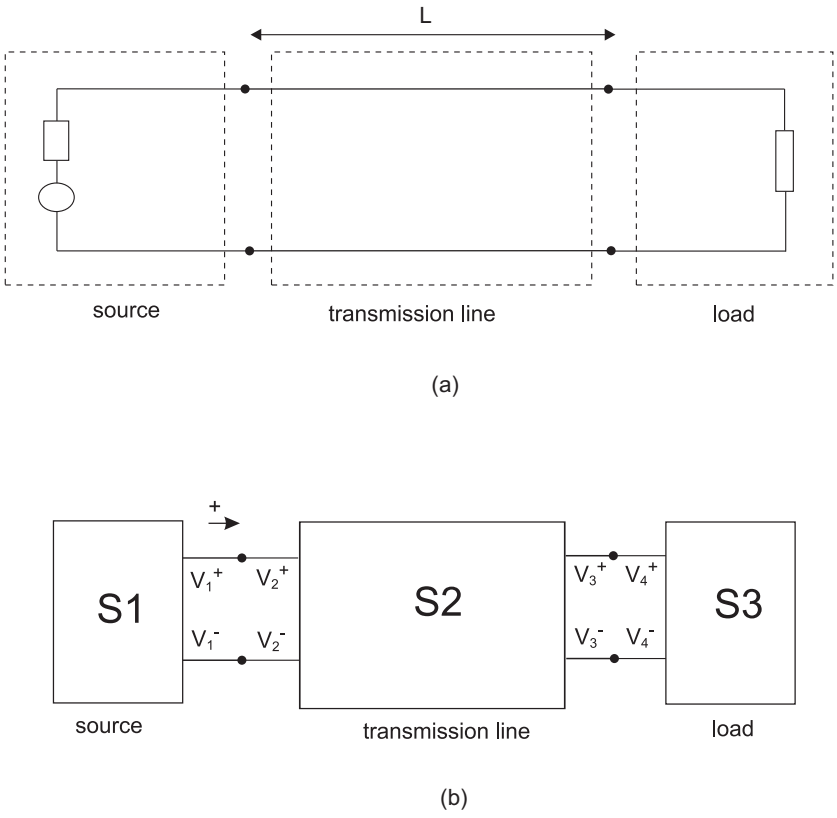

Figure 2.8: A two-conductor transmission line (a), and its representation using the S matrices of its different elements (b). Note that the blocks represented by $S1$ and $S3$ have a length equal to zero.

The diagonal elements of S are the reflection coefficients at the junction; when a wave arrives at this position, it 'sees' two infinite lines, each can be represented by a parallel load whose value is Z_c. The equivalent impedance seen by this same wave is thus the equivalent of two parallel loads which values are Z_c: its value is $Z_c/2$. Replacing the value of the load impedance Z_L in (2.10) by $Z_c/2$ leads to the reflection coefficient value already found.

2.2.2.4 Simulation of complex networks using the S-parameter matrices

Several existing software permit to simulate wire networks, such as SPICE [63], CST [64]; these software use different types of circuit analysis methods, such as matrix formulations, state variables [65], etc. In our work, we opted for the matrix formulation, because it is easy to implement and developed our own simulation tool: this was necessary to simplify the access to the modal variables, and also to facilitate the interaction between the simulator and the post processing using Matlab, having everything under one software environment.

We have seen that each network element can be described with an S-parameter matrix. The interconnection of these elements to form a network can also be described by cascading the S matrices corresponding to each element, and taking the continuity conditions of the voltage

and current between these different elements into account. To illustrate the idea, we reconsider the example of a two-conductor transmission line, shown in Fig. 2.8(a). The elements of this network are the source, the transmission line, and the load. Therefore we can represent this network by the S matrices of these elements as shown in Fig. 2.8(b). $S1$, $S2$ and $S3$ are the S-parameter matrices of the source, the transmission line and the load respectively. The incident and reflected voltage waves at each port are designated with V_i^+, having $i = 1$ to 4.

Looking at these 8 undetermined voltage constants (or equivalently the current constants), we have to obtain 8 equations so as to fully determine them. If we examine the source block, we derive the first equation linking V_1^+ and V_1^-

$$V_1^+ + V_1^- = V_s - Z_s\left(\frac{V_1^+}{Z_c} - \frac{V_1^-}{Z_c}\right) \tag{2.28}$$

The continuity conditions between the blocks corresponding to the source and the transmission line are the following

$$V_1^+ = V_2^+ \tag{2.29}$$

$$V_1^- = V_2^- \tag{2.30}$$

As already seen, the S-parameter matrix of the block corresponding to the transmission line allows to obtain 2 equations, because we have

$$\begin{bmatrix} V_2^- \\ V_3^+ \end{bmatrix} = S \begin{bmatrix} V_2^+ \\ V_3^- \end{bmatrix} \tag{2.31}$$

and S is determined according to (2.22). Till now we have 5 equations. The remaining 3 equations are obtained from the continuity conditions between the transmission line and the load, i.e.,

$$V_3^+ = V_4^+ \tag{2.32}$$

$$V_3^- = V_4^- \tag{2.33}$$

and the last equation links the incident and reflected voltage at the load as follows

$$V_4^+ + V_4^- = Z_L\left(\frac{V_4^+}{Z_c} - \frac{V_4^-}{Z_c}\right) \tag{2.34}$$

The equations we obtained can be written in a matrix form as follows

$$\begin{bmatrix} (1+\frac{Z_s}{Z_c}) & (1-\frac{Z_s}{Z_c}) & 0 & 0 & 0 & 0 & 0 & 0 \\ 1 & 0 & -1 & 0 & 0 & 0 & 0 & 0 \\ 0 & 1 & 0 & -1 & 0 & 0 & 0 & 0 \\ 0 & 0 & 0 & 1 & 0 & -e^{-\gamma L} & 0 & 0 \\ 0 & 0 & -e^{-\gamma L} & 0 & 1 & 0 & 0 & 0 \\ 0 & 0 & 0 & 0 & 1 & 0 & -1 & 0 \\ 0 & 0 & 0 & 0 & 0 & 1 & 0 & -1 \\ 0 & 0 & 0 & 0 & 0 & 0 & (1-\frac{Z_L}{Z_c}) & (1+\frac{Z_L}{Z_c}) \end{bmatrix} \begin{bmatrix} V_1^+ \\ V_1^- \\ V_2^+ \\ V_2^- \\ V_3^+ \\ V_3^- \\ V_4^+ \\ V_4^- \end{bmatrix} = \begin{bmatrix} V_s \\ 0 \\ 0 \\ 0 \\ 0 \\ 0 \\ 0 \\ 0 \end{bmatrix} \tag{2.35}$$

In a general form

$$MV = E \tag{2.36}$$

where M is the matrix containing the coefficients multiplying the unknown voltage variables, V is the matrix containing these variables, and E is the matrix containing the source excitation. Solving these equations for each frequency allows to determine the incident and reflected voltages, and consequently obtaining the voltage and current at any position in the network. This is useful when we address the voltage propagation in the network and define the space-time diagrams (see section 2.2.4).

Note that this approach requires rewriting the global matrix each time we change the network structure, because we have to rewrite the boundary conditions between the different blocks. However, this is not a handicap in our case given that we dealt with a limited number of configurations in our study.

Based on the idea we presented in this section, we developed a simulation code which we used throughout this work. We addressed complex networks, that is why we also needed a simple way to represent these networks. The following section highlights the point.

2.2.3 Graph representation of networks

A simple but effective way to represent complex networks is to use the graph representation. Sources, discontinuities, and transmission lines are represented with special symbols, allowing to highlight the elements influencing the wave propagation in the network, while maintaining a simple representation of the latter. In our case, we chose to represent sources (i.e., testing ports where we inject and receive signals) with rectangles, discontinuities such as junctions and loads with circles; this indicates that wave propagation at the corresponding position is disturbed by the presence of the discontinuity, giving rise to a reflection and transmission coefficients. Uniform lossless transmission lines are also represented with delay lines; the latter only referring to the time delay of the wave passing through the line, and does not have any physical properties. A fault occurring in the network will be represented by two parallel lines, in order to be distinguished from other discontinuities originally present in the network.

An example of a faulty network is given in Fig. 2.9. The graph representation of this network is given in Fig. 2.10. As for the length of the branches, the value and nature of a certain impedance, whether it be a parallel or series load for example, they will be indicated on the figure or in a corresponding table where necessary.

We point out that this tool would be important when we address fault location in the fourth chapter.

2.2.4 Space-time (or ZT) diagram

In the first chapter, we saw that the reflectogram is used in standard TDR when trying to detect and locate the presence of an eventual fault. The reflectogram allows to observe the reflected

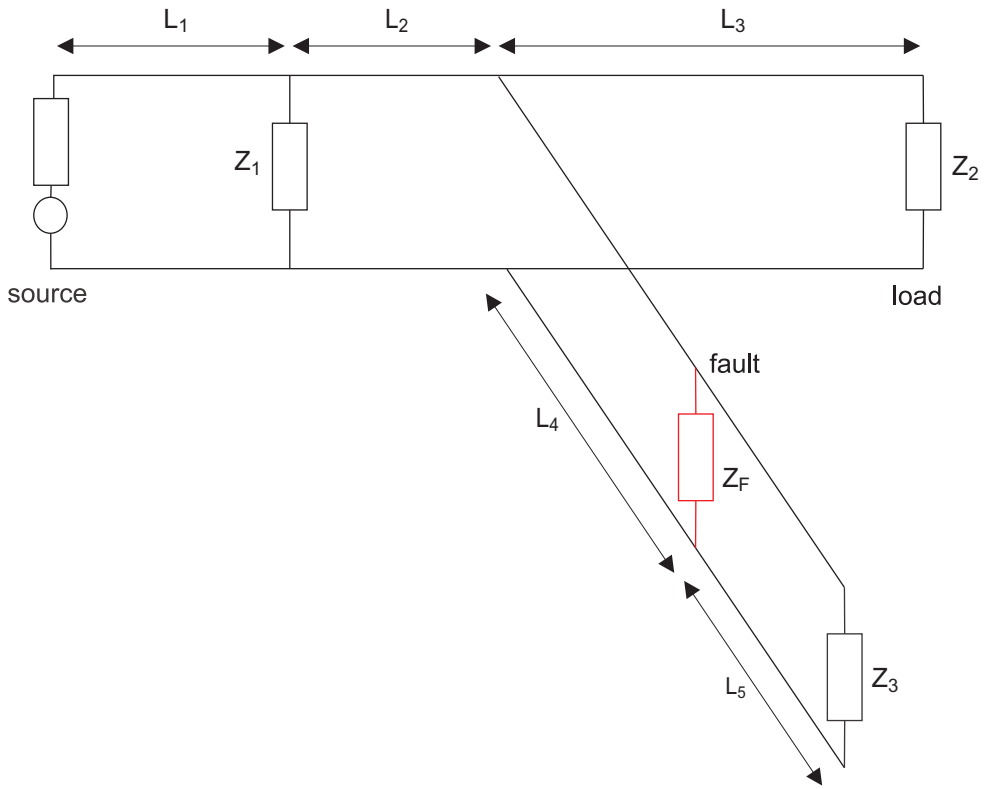

Figure 2.9: Example of a network to illustrate its graph representation in Fig. 2.10.

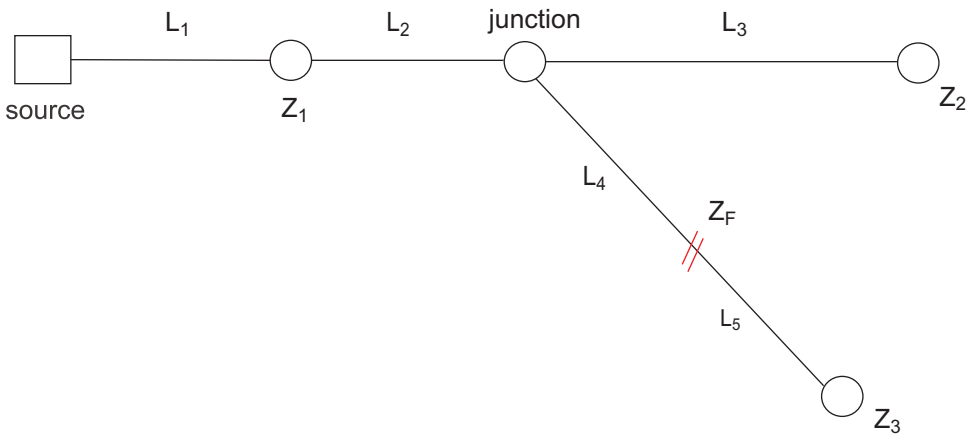

Figure 2.10: Graph representation of the network of Fig. 2.9.

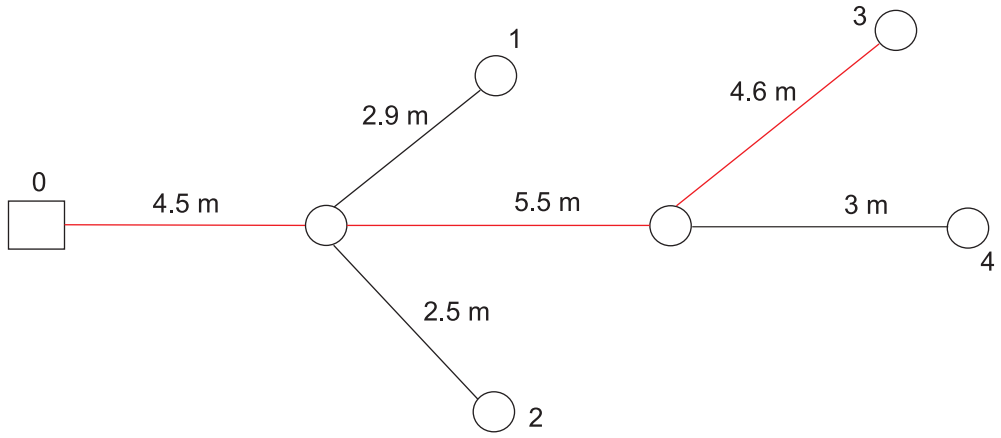

Figure 2.11: Example of a network with two junctions and matched terminations. The red line indicates the path along which we will observe the ZT diagram.

voltage wave only at the testing port position. But in some cases we need to observe the voltage propagation inside the network, i.e., at different positions, as we will do when dealing with fault location (see the fourth chapter). That is why we introduce a tool we name the space-time (or ZT) diagram.

We consider the case of the network represented in Fig. 2.11. It contains 2 junctions, located at 4.5 m and 10 m from the testing port. The lengths of the branches, indicated on the same figure, were chosen arbitrarily. For simplification purposes, we consider that the extremities of the network are matched loads, which means that no reflection occur at these endings (see Section 2.2.1).

A ZT diagram is a tool for observing the voltage propagation in the network, both in space and time. We represented this propagation between two extremities of the network, which we numbered from 0 (the testing port position) to 4. This numbering covers all the positions within the studied network. We consider that the testing port position, referred to as 0, is the origin of the position axis, so when we say we are going to observe the voltage propagation along the path number 1, we mean that we are considering the path between the two extremities 0 and 1, and so on. The path number 3 is drawn with a red line in Fig. 2.11.

Let us now introduce the ZT diagram, observed along the third path. It is represented in Fig. 2.12, where the x axis indicates the distance from the testing port, and the y axis is the time axis. We consider a total bandwidth of 500 MHz, and a frequency sampling step of 2 MHz, which will allow us to observe the evolution of the voltage propagation for a period of 0.5 μs, as observed along the time axis. The gaussian pulse we injected is normalized in amplitude and have a bandwidth of 140 MHz at -3 dB. The speed of the propagating voltage wave is considered to be equal to 0.8 times the speed of light.

At time $t = 0$, we inject this gaussian pulse into the network. A closer look to the propagation can be observed on the diagram of Fig. 2.13. The voltage propagates in space and time, as

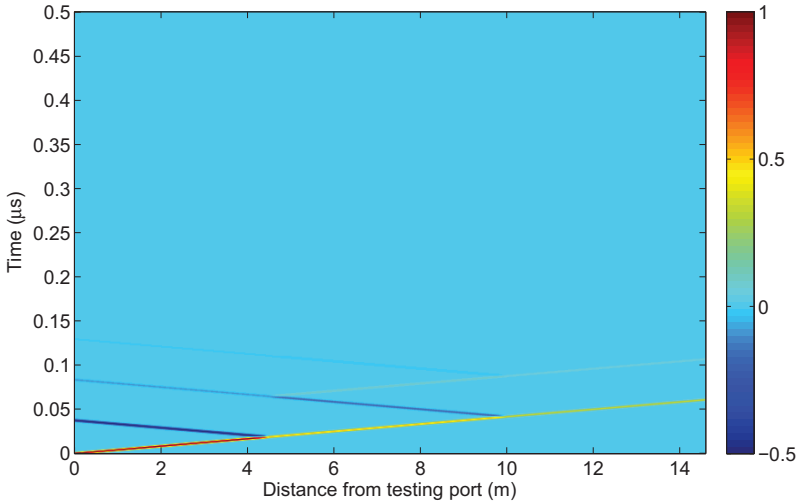

Figure 2.12: ZT diagram along the third path of the network represented in Fig. 2.11, showing the voltage propagation along this path.

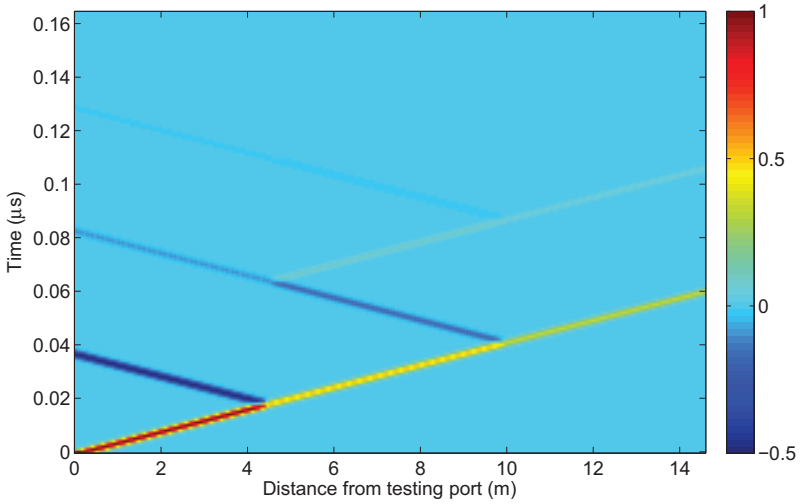

Figure 2.13: Zoom on the ZT diagram of Fig. 2.12, to better observe the voltage propagation along the third path.

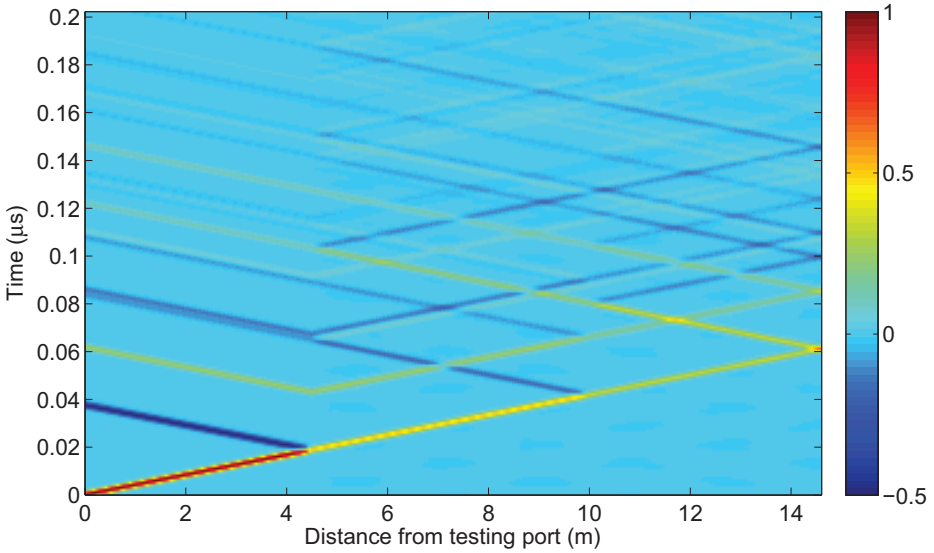

Figure 2.14: ZT diagram along the third path in the network of Fig. 2.11, where the extremities 1 and 3 are open circuits, and the extremities 2 and 4 are matched to the network.

seen on the diagram, till it encounters the first junction at a distance of $4.5\ m$ from the testing port. This discontinuity causes a part of the wave to be reflected back at the source, and another part to be transmitted, as can also be seen on the diagram. The reflected part reaches the testing port position at about $0.037\ \mu s$ from the origin. It is the round-trip time to reach this junction. Since the source is matched, no reflection occurs afterward. As for the transmitted parts, one part propagates in the path number 1 till it reaches a matched load. Of course this propagation cannot be observed on the diagram of Fig. 2.12. In the same way, a part of the transmitted wave also propagates in the second path ending with a matched load. As for the part we are observing, i.e., propagating along the third path, it continues its propagation in the network.

The example we considered illustrates a simple case of a ZT diagram involving few reflections. But what would it be like when having multiple reflections? The case of having the same network but with open circuit terminations instead of matched ones at the extremities 1 and 3, would lead to a ZT diagram represented in Fig. 2.14, where multiple reflections will not allow us to distinguish the fault's signature once present in the network, especially if the fault is embedded in the system, i.e., hidden from the testing ports by junctions and discontinuities. The echo propagation observed on the ZT diagram reminds us the problem of clutter encountered in radar.

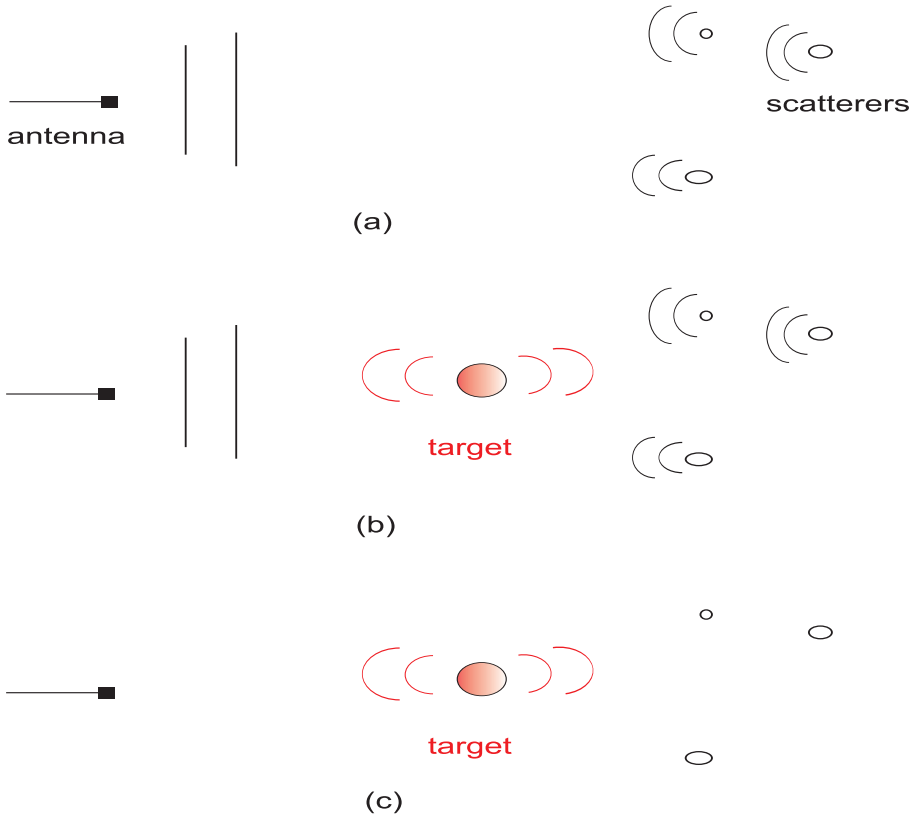

Figure 2.15: An example of free space propagation with the absence of a target (a) and with its presence (b).

2.3 Difference system

Clutter is a term generally used to point unwanted echoes in electronic systems. In radar systems, these echoes are typically returned from rain, sea, ground, objects, atmospheric turbulence, etc. If embedded in a cluttered medium, a target can be very difficult to detect. This situation is similar to our situation of wave propagation in guided structures, especially when it comes to complex networks. In such cases, as we can see in the previous example of Fig. 2.14, the echoes from different discontinuities would mask the echo from an eventual fault, especially if it is a soft fault embedded in the network. To overcome the problem of clutter in free space propagation, the basic idea was to try to minimize as much as possible the effect of the clutter, by considering what we will call the 'difference system'. To explain this concept, we begin by considering a simple scenario in free space.

2.3.1 Comparison between free space propagation and guided propagation

Let us consider a wave emitted by an antenna present in a homogeneous medium, and one scatterer present in the medium. Note that a scatterer is a non-uniformity (particle, bubble, droplet, etc.) which forces the wave to deviate from its original trajectory. The wave travels in the medium until it encounters the scatterer; The interaction of the incident wave and the scatterer gives rise to a reflected wave. In this simple case, the wave is scattered by one scatterer: it is a single scattering [66] scenario.

Imagine now the presence of two or more scatterers; in this case, the wave scatters many times and we obtain a multiple scattering scenario. If we consider a certain scatterer denoted as (R), the reflected wave from (R) can directly result from the incident wave interacting with it, or from waves which have underwent one or several reflections from other scatterers before interacting with (R). Generally, when the waves resulting from multiple scattering are negligible, we consider only the reflections occurring from the first interaction with the incident wave, i.e., the single scattering hypothesis. This hypothesis is justified when the scatterers are distant from each others. Here the effect of a certain wave reflected from (R) and interacting with the other scatterers is minimized: the amplitude of this wave decreases in terms of square of the distance separating (R) from the others, and consequently multiple scattering can be neglected.

We reconsider the example of a wave propagating in free-space, with the presence of several scatterers, as represented in Fig. 2.15(a). Initially no target is present in the medium, so the wave propagates until it interacts with the scatterers. In a second stage, a target is present in the medium, as shown in Fig. 2.15(b). When the wave is emitted, and before encountering the target, it follows the same path as was the case without this target. When it encounters the target or the scatterers, multiple scattering will occur, and reflected waves will interact with the scatterers and the target. Under the single scattering scenario, we neglect multiple scattering; consequently the most significant diffracted wave is considered to be the one caused by the first interaction of the initial incident wave with the scatterer or target. By ‘reflected wave’ we denote this most significant wave in the rest of the analysis, and by ‘total wave’ the sum of the incident and reflected waves.

Let us now consider the total waves in two cases, with and without the target, and subtract them. For the target, which was not originally present in the system, the incident wave is the same for the cases with and without the target’s presence, thus it will be eliminated; the resulting wave will be the reflected one (see Fig. 2.15(c)). For the other scatterers, which were present in both cases, the incident wave is also eliminated, and the resulting wave is the difference of the reflected waves both in the presence and absence of the target. If we assume that the perturbation brought by the target’s presence to the system is negligible, i.e., the reflected waves of the other scatterers are not affected due to its presence (the first-order Born approximation [67]), then the subtraction operation eliminates also the reflected waves and consequently the only significant

wave will be that of the target. Ideally, the 'new' system obtained by applying the difference of the systems with and without the target presence, only contains this target: it seems as the target was a secondary source, emitting isotropically in all directions. This system will be denoted as the difference system; it is the equivalent of a system whose transfer function is the result of the subtraction of two transfer function (of two linear systems): the first one is the reference system without the target, or the baseline system, and the second one is the system with the presence of the eventual target.

The earlier discussed ideas in free space propagation can be applied to the case of guided propagation. The target is considered as the fault to be detected, and the scatterers represent the different discontinuities that might be encountered in wire networks, especially the complex ones, such as junctions and mismatched loads. Single scattering in this case refers to the first interaction of the incident voltage wave with a certain impedance discontinuity in the system, whilst multiple scattering refers to the multiple reflections that occur between these discontinuities.

One may ask why we need to consider such an approach of the difference system in our study. Given that we deal with soft faults, an intuitive first reason is that considering the weak reflection from a soft fault, especially in complex networks, its signature would be more visible if we considered the difference of the reflected signals obtained with and without its presence; in fact this is done by many researchers [23, 68] when trying to find this kind of faults. The second reason is that we need to have the fault acting as a secondary source in order to derive and explain the fault location approach in the fourth chapter.

Back to our discussion, major differences exist between the cases of free-space and guided propagation. In free-space propagation, we saw that the single scattering approximation can be applied when the scatterers are distant from each others, because the amplitude of the wave will decrease in proportion to the square of the distance separating the scatterer from the others, whilst it is not the case in guided propagation. Here, in our case of uniform lossless transmission lines, the amplitude of the wave does not decrease in terms of the distance, and therefore this approximation cannot be applied directly if the fault and the discontinuities are distant; however, a fair compromise would be to consider the perturbation brought by the fault to the system weak enough so as to consider it as a local perturbation rather than global (the Born approximation), as opposed to the case of a hard fault (see Section 2.3.3). Under the assumption of a soft fault, we can ideally remove the effect of the other elements of the system after the subtraction operation, and the fault can be treated as a secondary source, as seen for the target in the case of free-space propagation.

2.3.2 Example of the difference system in the case of guided propagation

In the previous section we saw that applying the difference operation to a system's response in the presence and absence of a fault allows eliminating most of the contributions of the other

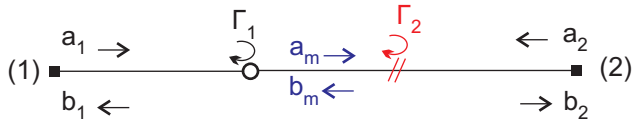

Figure 2.16: A transmission line containing an impedance discontinuity with a reflection coefficient denoted as Γ_1, and a fault with a reflection coefficient referred to as Γ_2.

elements in the system (other than the fault) that are not related to the fault's presence. However, due the presence of these elements and the multiple interactions with the fault, a residual contribution of the elements exist and appears in the difference system response.

To quantify such a contribution, we propose to consider the simple example of a uniform lossless transmission line illustrated in Fig. 2.16. For the sake of simplicity we consider that the lengths are equal to zero, and consequently no delay terms appear in the calculus. A discontinuity present in this NUT have a reflection coefficient denoted as Γ_1, whilst the fault have a reflection coefficient referred to as Γ_2. The incident voltage waves on the two extremities of the NUT, (1) and (2), are denoted as a_1 and b_1, and the reflected waves as b_1 and b_2. We assume that the system is in a steady state, and that the waves propagating in the faulty system between the discontinuity and the fault are referred to as a_m and b_m. Under these assumptions, we can write

$$a_m = a_1(1 + \Gamma_1) + a_m\Gamma_1\Gamma_2 \tag{2.37}$$

which implicates

$$\frac{a_m}{a_1} = \frac{1 + \Gamma_1}{1 - \Gamma_1\Gamma_2} \tag{2.38}$$

If we want to calculate the global reflection coefficient at the position of the first testing port, denoted as S_{11}, in the difference system , we should calculate this coefficient in both the reference and the faulty system,

$$S_{11} = \frac{b_1}{a_1}\Big|_{a_2=0} \tag{2.39}$$

In the reference system we have a reflection at the discontinuity, so as to obtain a global reflection coefficient S_{11}^0 equal to

$$S_{11}^0 = \Gamma_1. \tag{2.40}$$

In the faulty system, the reflected voltage wave b_1 can be calculated as follows

$$b_1 = \Gamma_1 a_1 + \Gamma_2(1 + \Gamma_1)a_m. \tag{2.41}$$

Using (2.38) and (2.39), the global reflection coefficient in the case of the faulty network, referred to as S_{11}^F, is

$$S_{11}^F = \Gamma_1 + \frac{\Gamma_2(1 + \Gamma_1)^2}{1 - \Gamma_1\Gamma_2}. \tag{2.42}$$

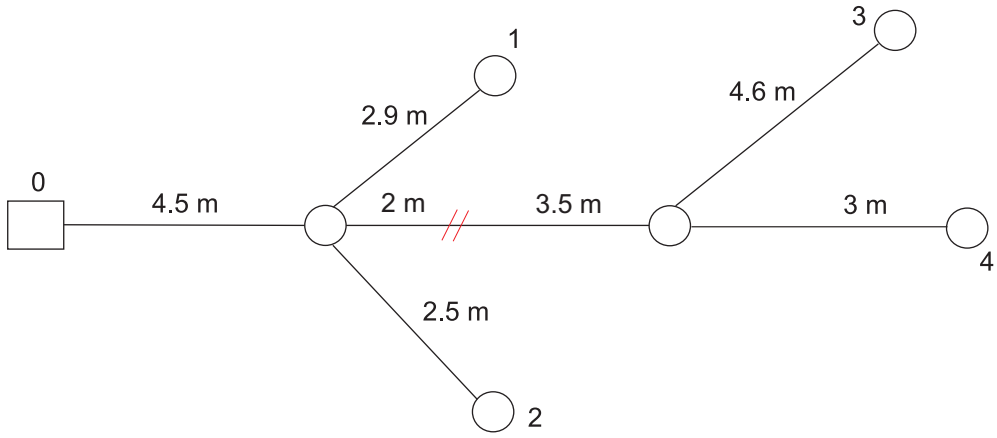

Figure 2.17: Example of a network with two junctions and matched terminations. The red line indicates the path along which we will observe the ZT diagram.

The global reflection coefficient S_{11} in the case of the difference system can now be calculated using (2.40) and (2.42):

$$S_{11} = S_{11}^F - S_{11}^0 = \frac{\Gamma_2(1+\Gamma_1)^2}{1-\Gamma_1\Gamma_2} \tag{2.43}$$

We can clearly notice that this coefficient contains contributions from the discontinuity, illustrating the fact that multiple reflections between the discontinuity and the fault in the faulty network are not completely eliminated by the difference operation. This also points out that whenever the fault is 'harder', i.e., have a higher reflection coefficient, this residual response tends to increase and consequently the perturbation brought by the fault presence to the system is more visible. That is why, to preserve the physical meaning of the difference system, and be able to apply the Born approximation invoked in the previous section, we decide to deal with soft faults in our work; this insures that a weak perturbation is caused by the fault's presence in the system. The following sections illustrate some qualitative examples.

2.3.3 Difference system in the case of a hard fault

We reconsider the example of Fig. 2.17, with a fault introduced on the third path, at a distance of $2\ m$ from the first junction, i.e., at $6.5\ m$ from the testing port. The fault is a short circuit resulting in a local reflection coefficient at the fault position equal to -1. Although we will not consider hard faults in our study, it seemed interesting to examine the case of this type of faults for a better understanding of the idea of the difference system and its physical meaning.

The ZT diagram of the system (along the third path) without the fault was already plotted in Fig. 2.12. In the presence of a short circuit, we obtain the diagram illustrated in Fig. 2.18. Notice how the presence of this hard fault eliminates the contribution of the network elements downstream of the fault, i.e., the elements situated at a distance greater than the fault's distance to the testing port. As for the contribution of the elements upstream of the fault (situated at

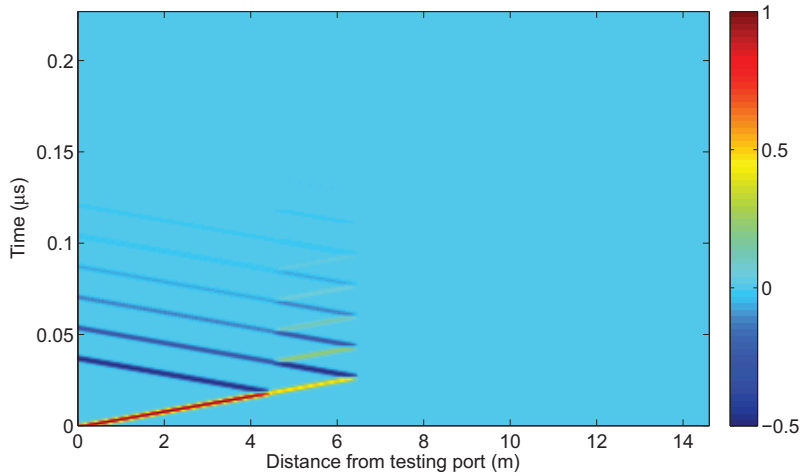

Figure 2.18: ZT diagram observed along the third path of the faulty network represented in Fig. 2.17. The fault is a short circuit situated at 6.5 m from the testing port.

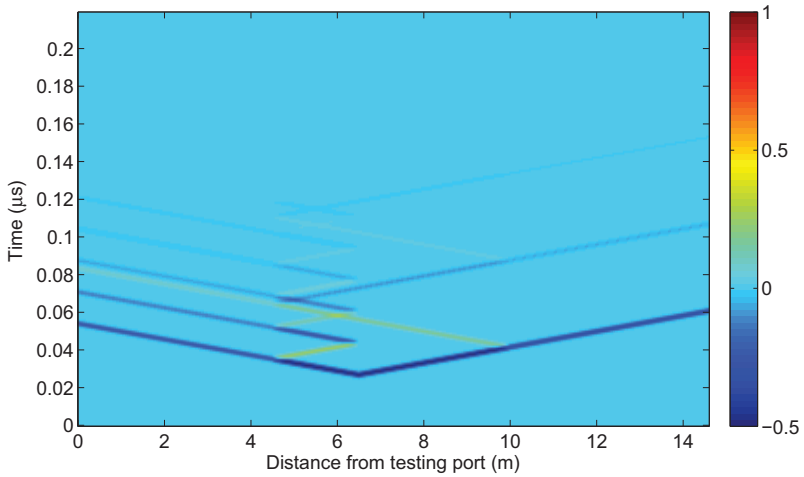

Figure 2.19: ZT diagram observed along the third path of the network represented in Fig. 2.17, for the difference system. The fault is a short circuit situated at 6.5 m from the testing port.

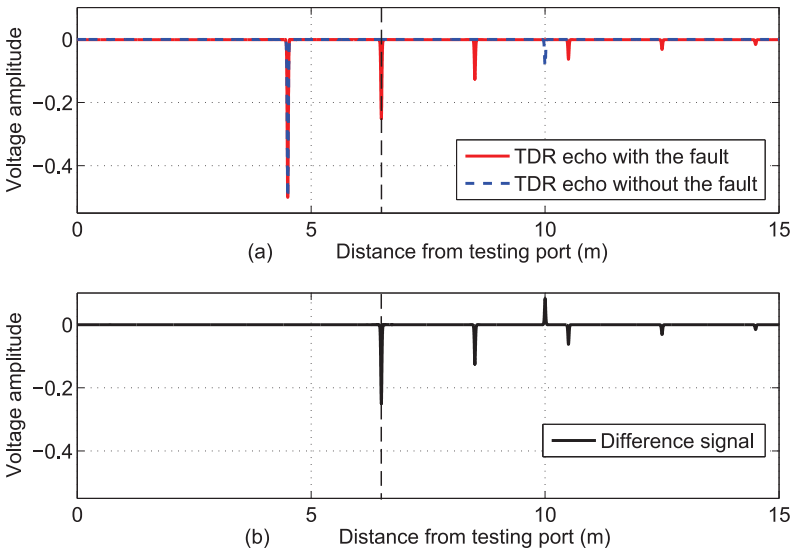

Figure 2.20: Reflectograms in the case of the network represented in Fig. 2.17. (a) shows the reflectograms of the reference and faulty systems, while (b) shows the difference signal. The fault is a short circuit situated at 6.5 m from the testing port.

a distance smaller than the distance of the fault to the testing port) it remains unchanged in both cases, with and without the fault. In free-space, the presence of this type of faults can be compared to that of an obstacle with very big dimensions (ideally infinite) that prevents the wave from interacting with other scatterers behind it, and reflect it back to the source.

Let us now consider the ZT diagram of the difference system represented in Fig. 2.19. When we look at the fault position, we notice that the fault appears as a secondary source emitting symmetrically in both directions. The diagram shows the existence of a contribution of the parts downstream of the fault. In fact, in the system without any fault, the wave continued its propagation after reaching 6.5 m from the source (later the position of the fault) and consequently interacted with the discontinuities downstream this position, giving rise to several echoes. When a hard fault appeared, the wave no longer reached the elements downstream its position, and consequently the contribution of these parts was reduced to zero. Thus the contribution we observe on the ZT difference diagram results from the mathematical subtraction operation, where the echoes initially present without the fault persist when considering the difference.

So when the fault is a hard one, with the fault acting as a secondary source on the ZT diagram, it will look like the fault is contributing to the appearance of the echoes downstream its position, which is not the case in practical, because it removes them due to the total reflection that occur at its position; the difference system in this case will not have any physical meaning.

The same analysis of the ZT diagrams applies if we observe the reflectograms, represented in Fig. 2.20(a) for the reference and faulty system, and in Fig. 2.20(b) for the difference system.

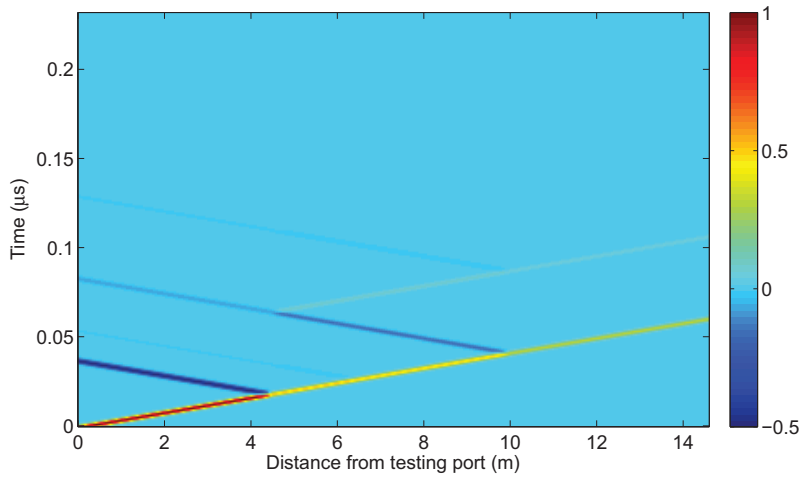

Figure 2.21: ZT diagram observed along the fourth path of the faulty network represented in Fig. 2.17. The fault is a parallel load which value is $600\ \Omega$, situated at 6.5 m from the testing port.

In the reference system, we observe a first peak at 4.5 m from the testing port, representing the first reflection on the first junction. This peak has a negative amplitude of course, since the reflection coefficient on the first junction is negative (equal to -0.5). The second peak appears at a distance of 10 m from the testing port, pointing the position of the second junction. In the faulty system, the first peak appearing in the TDR signal corresponds to the junction; the voltage wave has not 'seen' the fault yet. This wave continues its propagation till it reaches the fault; consequently, the second peak appears at a distance of 6.5 m. The reflection coefficient at the fault position is equal to -1, so a total reflection occurs at this position and the network part downstream of the fault is masked by the presence of the latter, as already seen on the ZT diagrams. In the difference system, we notice how the contribution of the elements upstream of the fault is eliminated, and the one downstream of the fault remains due to echoes in the reference system that were not eliminated by the difference. The important point to retain here is the fact that the first echo in the difference signal (without the existence of noise of course) is the one corresponding to the fault. This idea is important in the next chapter where we address fault detection in details.

2.3.4 Difference system in the case of a soft fault

A soft fault generally results in a weak local reflection coefficient compared to that of a hard fault. It is this criterion who made us chose a parallel resistive load with a corresponding value so as to obtain the desired coefficient. We consider the same example as for the hard fault in the last section, but with a parallel load instead of a short circuit. The value of the resistance is $600\ \Omega$, leading to a local reflection coefficient $\Gamma = -0.06$. The position of the fault is still the

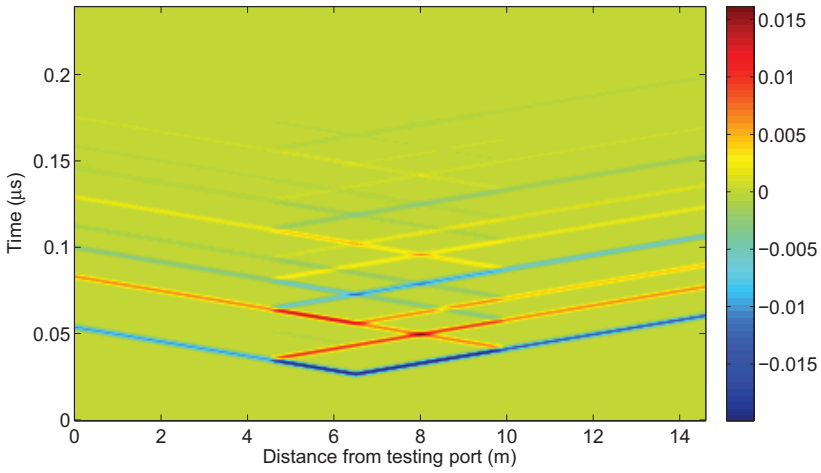

Figure 2.22: ZT diagram observed along the fourth path of the network represented in Fig. 2.17, for the difference system. The fault is a parallel load which value is $600\ \Omega$, situated at 6.5 m from the testing port.

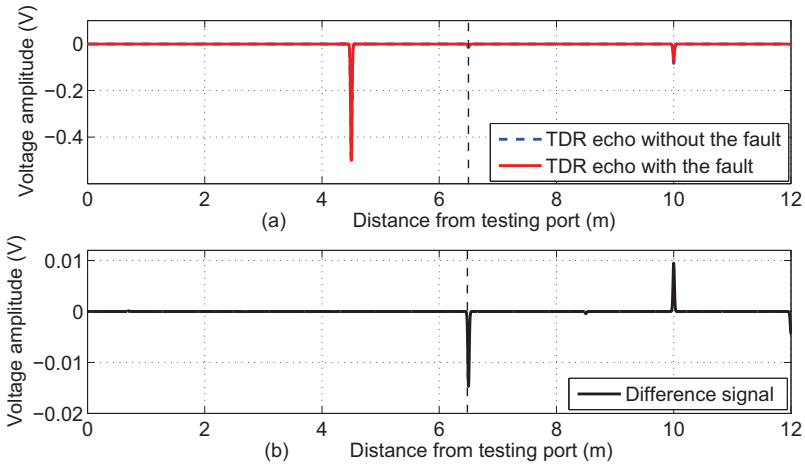

Figure 2.23: Reflectograms in the case of the network represented in Fig. 2.17. (a) shows the reflectograms of the reference and faulty systems, while (b) shows the difference signal. The fault is a parallel load which value is $600\ \Omega$, situated at 6.5 m from the testing port.

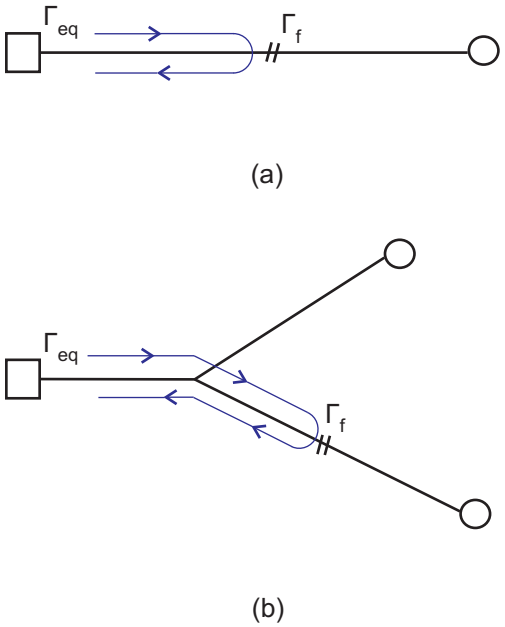

Figure 2.24: Example of two networks: a single transmission line (a), and a Y-network (b). The shortest trajectory of the voltage wave resulting in the first echo in the difference signal is traced with a purple line in both cases.

same, at $6.5\ m$ from the testing port. The ZT diagram is observed along the fourth path.

In the case of the faulty network, as we can see from the ZT diagram of Fig. 2.21, it is quite difficult to see the reflection at the fault position. The difference with the case of a hard fault is that in the latter, the network part downstream of the fault becomes invisible to the propagating wave, as if it does not exist anymore. Whereas in the case of the soft fault, there is a slight perturbation but the wave continues to propagate in the network. Thus, when considering the difference system, as we did in Fig. 2.22, the fault truly acts as a secondary source, because both propagation upstream and downstream the fault will be influenced by the fault's presence.

As for the reflectograms, they are shown in Fig. 2.23. Compared to the case of a hard fault, we notice the weak amplitude of the peak corresponding to the fault in Fig. 2.23(b) .

2.3.5 Discussion on the definition of a hard and a soft fault

To better understand the effect of the network elements on the amplitude of the fault related peak, we first propose to consider the examples of Fig. 2.24, where networks have been represented according to the graph representation earlier introduced in Section 2.2.3. The first case (Fig. 2.24(a)) deals with a simple transmission line with a matched end. We suppose that a fault is present at a certain distance from the testing port. For simplification purposes, we suppose that the testing signal (in time) is a pulse which amplitude is A, and the testing port is matched to the network. The transmission lines are assumed to be uniform and lossless, so the length of

a certain line only introduces time delay and does not affect the amplitude of the wave, thus it will not be considered here.

If we inject this pulse into the network, the wave will propagate until it reaches the fault. At the fault position, a part will be reflected back towards the testing port and another one will be transmitted. The amplitude of the reflected wave depends on the local reflection coefficient of the fault Γ_f, so the softer the fault is, the weaker Γ_f will be. In this simple case the amplitude of the reflected wave will be equal to that of the incident wave, multiplied by Γ_f, i.e., $A\Gamma_f$. So in this case it is normal to say that a hard fault is easily detectable because at the testing port the reflected pulse have an amplitude equal to A, or equivalently the global reflection coefficient Γ_{eq} as seen from the testing port position is equal to the local reflection coefficient Γ_f. This is important because the higher Γ_f is, the better the detection sensitivity is, because we have a higher Signal to Noise Ratio (SNR).

Let us now consider the second case of the Y network represented in Fig. 2.24(b), where we also have a matched testing port and two matched network terminations. Before encountering the target, the injected wave encounters the junction, and the transmitted wave through this junction will have an amplitude equal to $2A/3$. This transmitted wave will reach the fault position, and the reflected wave at this position will have an amplitude once again multiplied by the reflection coefficient Γ_f, so that its amplitude is $2A\Gamma_f/3$. This wave will once again encounter the junction while back propagating towards the testing port position, and finally arrives at the latter with an amplitude of $4A\Gamma_f/9$.

The examples above trace the shortest trajectory from the testing port to the fault. If we consider the difference system, the contribution of the parts upstream of the fault will be eliminated, and the wave that back propagates from the fault and reaches the source will cause the first fault related peak to appear in the TDR difference echo. The amplitude of this first peak will be reduced according to the number of discontinuities it has encountered as shown earlier. Here, the global reflection coefficient Γ_{eq} is no more equal to Γ_f, but rather equal to $4\Gamma_f/9$.

In the general case when we have N discontinuities, the global reflection coefficient Γ_{eq} can be written as

$$\Gamma_{eq} = \Gamma_F \left(\prod_{i=1}^{N} \tau_i \right)^2 \tag{2.44}$$

where τ_i is the transmission coefficient through the discontinuity number i. Note that the squaring operation was applied to describe the round trip trajectory, where the wave crosses the same discontinuity two times (as seen in the examples we considered).

So when it comes to complex networks, a hard fault embedded in the latter is 'seen' as a soft one from the testing port position, because the amplitude of the reflected wave will be reduced when crossing the discontinuities between the testing port and the fault. However, in this case the hypothesis of a weak perturbation does not hold anymore, as opposed to the case of a soft fault.

This section aimed at understanding the effect of the number of junctions and discontinuities

on the visibility of a fault from the testing port position, in order to asses under which conditions it is more visible (detectable). We have seen that the more complex is the network, the more difficult the detection of a fault embedded in the system, whether it be hard or soft. However, in our study, we will retain the usual definitions of hard and soft faults, based on the local reflection coefficients at the discontinuity level, because we are going to deal with the fault as being a secondary source, and thus the local reflection coefficient is considered.

2.4 Conclusion

This chapter presented the basic tools and concepts we used to model guided propagation. We adopted a frequency domain analysis to implement our simulation tool, based on the S-matrices approach, due to its simplicity and its ease of implementation. Graph representation allows us to represent the studied networks in a simple manner, while the ZT diagrams give an insight of the voltage propagation in the network. Finally, the difference system approach permit to have the soft fault acting as a secondary source; an idea that is going to be of great significance when addressing fault localization in the fourth chapter.

Chapter 3

Fault Detection

3.1 Introduction

Standard reflectometry techniques aim to detect the presence of an eventual fault by injecting a predefined testing signal in the NUT, and analyzing the reflected signal, looking for the fault's signature. However, the testing signals that are used in reflectometry are the same for all the tested networks, and thus cannot guarantee an optimal performance in all cases, especially when the fault is a soft one embedded in a complex network; under these conditions conventional reflectometry techniques become insufficient, as the multiple echoes from different impedance discontinuities in the system mask the one corresponding to the fault.

Compared to the problem of target detection in a cluttered environment encountered in radar, the same problem arises: the increasing multiple scattering in the medium poses a significant problem when the target's signature is weak compared to other scatterers, and thus the detectabiltiy of the target is put in jeopardy. To solve this problem, the idea was to adapt the testing signal to the propagating medium, so as to result in a higher efficiency; this is done by using the Time Reversal (TR) technique, introduced in the early 1990s, which transforms the traditionally 'hostile' multipath components to performance-boosting elements, especially in cluttered environments where classical techniques start to fail.

Based on this technique, we will develop an approach to fault detection in wire networks, which we will baptize the Matched Pulse (MP) approach. This approach aims at synthesizing testing signals that are matched to the NUTs, as opposed to standard reflectometry techniques. A mathematical analysis will be presented to quantify the advantages of the proposed method compared to standard reflectometry techniques. Next simulation results will highlight the impact of different network elements on the performance of the method, and an experimental validation will finally show the advantages of the method regarding soft fault detection in complex networks.

3.2 Time Reversal (TR)

3.2.1 Literature overview

Time Reversal was first introduced in acoustics by Fink *et al.* [69, 70, 71]. This technique has shown its benefits when considering cluttered environments, as it permits to transform the traditionally 'hostile' multipath to a performance-boosting element in such environments. TR involves the physical or synthetical retransmission of signals acquired by a set of transceivers in a time reversed way, i.e., like playing a tape backward. The retransmitted signals propagate backwards through the same medium and experience similar multiple scattering , reflections and refraction that they underwent during the forward propagation, resulting in energy focusing around the initial source location (see Section 3.2.2). In the frequency domain, TR corresponds to phase conjugation which has found application in optics [72, 73], as well as in electromagnetics [74, 75, 76, 77]. Fink *et al.* have conducted the first successful time-domain experiments in the early 1990s, and developed the concepts of TR cavity and TR mirrors [69, 78, 79]. TR has found many applications in different fields; in medicine for example, it has been used for the kidney stones destruction [80, 81], microwave breast cancer detection [82, 83], etc. Also, several applications in geophysics included the search for an earthquake center [84], or for buried objects [85]. TR has also found its place in non destructive testing methods, where it has been utilized for detecting defects and damages in materials and structures [86, 87, 88]. Add to this the use of TR in target detection in radar and sonar systems [89, 90, 91].

In our work, we focus on guided structures, and study the contribution brought by the TR principles to the domain of fault detection and location in wire networks. In the present chapter we are only interested in fault detection whereas in the next one fault location will be addressed separately.

3.2.2 Example of TR in acoustics

A basic example from physical acoustics to illustrate the principle of time reversal is considered in Fig. 3.1. We consider a source emitting waves in an inhomogeneous medium, and an array of piezo-electric transducers that serve to emit and receive the sound waves.

In a first step illustrated in Fig. 3.1(a), the source emits sound waves that propagate in the medium; these waves may have been distorted due to discontinuities and inhomogeneities in the medium they are propagating through, when they reach the transducers. Each transducer records the signal it detects. This is the recording step.

In a second step shown in Fig. 3.1(b), the source is removed. The recorded signals are time-reversed, and each transducer emits this signal in synchrony with the other transducers. The emitted waves travel back in time, retracing the original passage back through the medium, and refocusing on the initial source point. This is similar to playing a tape backward: the recorded signals are emitted in a reversed way, which means that the waves which were first recorded are

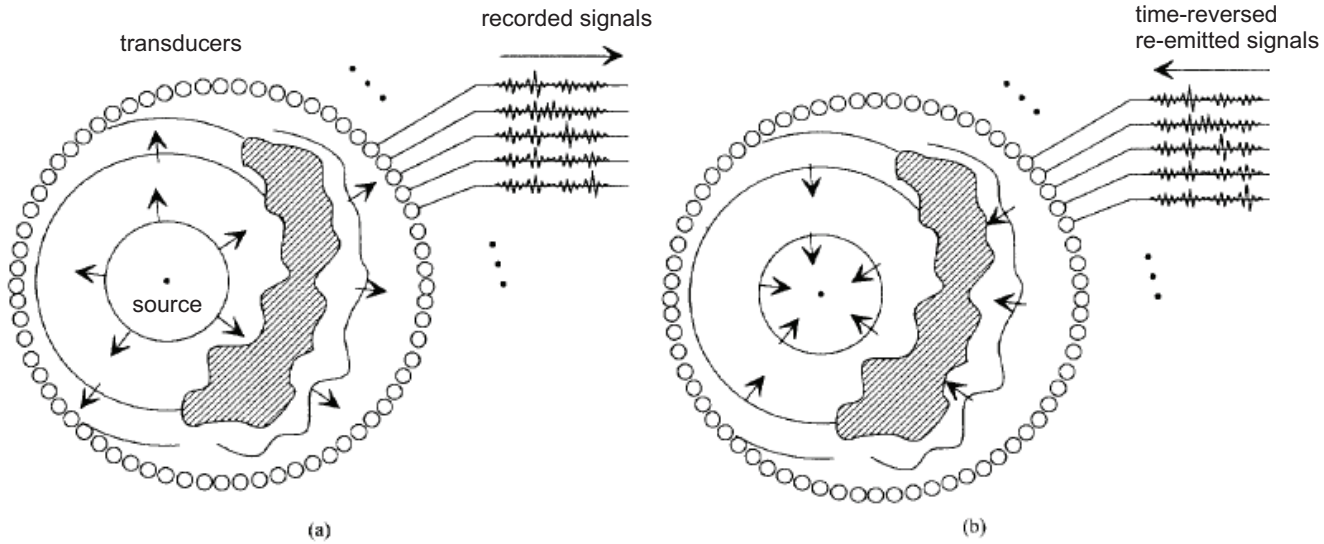

Figure 3.1: An example of a TR cavity in acoustics. In a first step, a source emits acoustic waves which are recorded by the array of transducers (a), and in a second step the recorded signals are time-reversed and re-emitted into the medium (b), focalizing on the initial source position [69].

re-emitted at the end, and so on.

Notice that the re-emitted waves contain information about the propagation medium, and depend on the latter; they are adapted to this medium. It has been demonstrated that the time-reversal process is optimal in the sense that it permits to focalize a higher amount of energy on the initial source position [92, 93], especially in cluttered environments where classical time delay methods start to fail. In the fault location process, this focalization property will be of great significance to us, but in the detection process, studied in the present chapter, the resulting maximization of the energy amount at the fault position will interest us. In fact, when detecting the fault we will be interested in maximizing the SNR at its position, that is why we are interested in a higher energy amount. In this context, the TR is optimal because its principle is equivalent to the principle of the matched filter [94], encountered in telecommunications (see Section 3.3 for further discussion).

Till now we saw that the re-emitted waves focalize on the initial active source position. In different applications, such as kidney stone destruction in medicine, we are interested in the focalization on a certain target or ‘passive source’ position, i.e., the stone in this case. Let us consider an array of transducers and a certain target in a homogeneous medium. In a first step it is the array of transducers that emit a wave into the medium this time; this wave propagates, reflects back when it encounters the target and back-propagates towards the array of transducers. The received signals are recorded. In a second step, these waves are time-reversed and re-emitted into the medium; they focalize on the source position. In fact, the reflected waves in the first step, which have interacted with the target, are seen by the transducers as if they have been

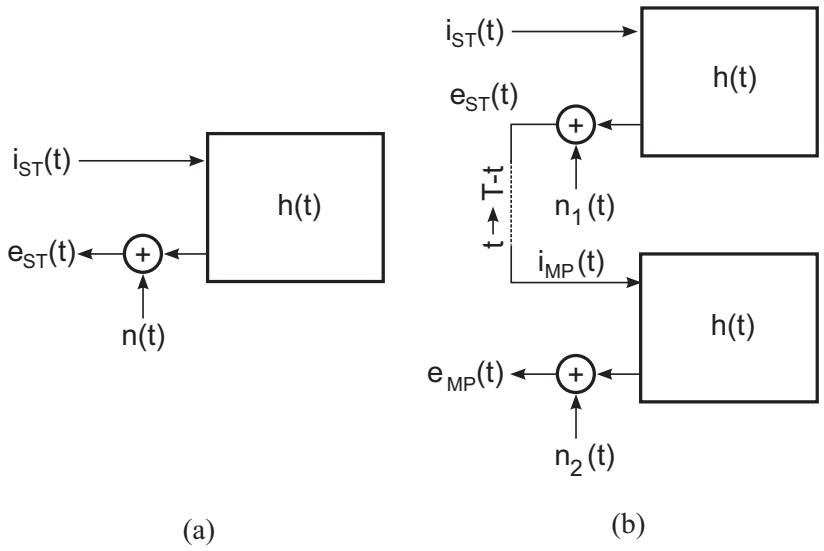

Figure 3.2: Block-diagram representations for: (a) standard TDRs and (b) MP methods. The reflectometry impulse response of the NUT is noted as $h(t)$, whereas the various $n_i(t)$ signals are equivalent additive noise sources at the output of the NUT. The time-delay T is the overall duration of the standard TDR test.

'emitted' by the target. Thus, when recorded and re-emitted, the waves focalize on the target position; the target acts as a secondary source. This will be further discussed in the next chapter when addressing fault location.

As already pointed out, time reversal allows synthesizing testing signals that are adapted to the propagation medium, rather than being predefined for all the mediums. In our case, we aim at synthesizing a signal that is adapted to the Network Under Test (NUT), in order to result in a higher energy amount at the fault position, thus improving its detectability. We baptize this adapted signal the Matched Pulse (MP).

3.2.3 Matched Pulse (MP)

In the earlier discussed example, we saw that the adapted testing signal is obtained after a first step consisting of the injection of a certain signal into the medium, and then the recording of the reflected signal; the new testing signal is the time-reversed version of the latter. In our case of fault detection in wire networks, the same ideas apply. In this section, we explain in details the procedure to obtain this testing signal which we called the Matched Pulse (MP), and compare it to the Standard reflectometry Techniques, pointed to with the acronym ST.

Fig. 3.2(a) represents the test of a network by means of a standard TDR approach: the injected signal in time domain is noted as $i_{\mathrm{ST}}(t)$. The reflected signal, i.e., the standard TDR echo, is denoted as $e_{\mathrm{ST}}(t)$. This is the signal that in any standard TDR technique, after being properly post-processed, eventually allows detecting and locating a fault, as already seen in

the second chapter. $h(t)$ denotes the impulse response of the NUT. The MP case is illustrated in Fig. 3.2(b). Here, $e_{\mathrm{ST}}(t)$ is no more the ending point of the test, but it just provides an intermediary step. In fact, we define our testing signal, or MP, as the time-reversed version of the standard TDR echo. The MP testing signal, referred to as $i_{\mathrm{MP}}(t)$, is the actual testing signal and is thus injected into the NUT so as to obtain the MP echo $e_{\mathrm{MP}}(t)$. This procedure does not require any assumption on the nature of the originally injected TDR signal $i_{\mathrm{ST}}(t)$: as a matter of fact, it could be any of the testing signals developed within the context of other TDR techniques. It is important to acknowledge that the actual shape of the MP signal depends on the system's configuration, unlike other TDR techniques. The MP is clearly still a TDR technique, but with a new definition of the testing signal. Such an approach is next proven to result in a higher efficiency compared to the original testing signal i_{ST}. But the fact that the starting point is the use of a standard TDR signal, implies that its properties are preserved when passing to the MP excitation. This could be useful when considering special excitation signals with high noise-rejection, such as spread-spectrum signals [44].

3.3 MP echo

Let us take a closer look at the MP bloc scheme earlier illustrated in Fig. 3.2. We consider the example where $i_{\mathrm{ST}}(t)$ is a Dirac function [95], so that $e_{\mathrm{ST}}(t)$ would be equal to the impulse response of the system $h(t)$. By time-reversing this signal and convolving it with $h(t)$, we will actually be obtaining the autocorrelation function [96] of $h(t)$, because we have

$$e_{\mathrm{MP}}(t) = h(T-t) * h(t) \tag{3.1}$$

where $*$ is the convolution operation, and T the recording duration, considered to be long enough so as to be dropped later. The properties of the autocorrelation function implies that this function is even, which explains the symmetry we will be observing when examining the MP echo. It also implies the existence of a maximum; we will see next that the time instant corresponding to this maximum coincides with the one corresponding to the fault. This suggests that we will be considering peak-based detection, as considered in TDR techniques. Other reflectometry methods that use pseudo-noise sequences (which is the case in STDR and SSTDR [44, 43, 24]) or any other type of signals, correlation-based post processing of the received signal allows to obtain a peak-based signal to be analyzed, which means that this case will be also reduced to the previous case of peak-based analysis.

We already mentioned that the TR principle is equivalent to the matched filter's one. In fact, if we consider the case of an emitter and a receiver encountered in telecommunications, the optimal filter which maximizes the SNR of the received signal is the one whose impulse response equals the time-reverse of the channel response. Let us apply the same ideas here, and adopt the following reverse reasoning, i.e., starting from the received signal $e_{\mathrm{MP}}(t)$. We state that we want to maximize the SNR of $e_{\mathrm{MP}}(t)$, and thus this signal must have been filtered

by a certain 'filter', whose transfer function must have been equal to the time-reverse of the injected signal $i_{\mathrm{MP}}(t)$. In this case, the 'filter' is the NUT, so its impulse response must be equal to $i_{\mathrm{MP}}(-t)$. Indeed, this is actually the case, since the signal $i_{\mathrm{MP}}(t)$ was obtained from a pre-processing step by injecting the pulse $i_{\mathrm{ST}}(t)$ into the system so as to obtain $i_{\mathrm{MP}}(t) = e_{\mathrm{ST}}(-t) = h(-t)$. Consequently the NUT itself in the second step of the injection of the MP, $i_{\mathrm{MP}}(t)$, acts as a filter that maximizes the SNR of the output signal $e_{\mathrm{MP}}(t)$, whence the optimality of the testing signal expected when using TR techniques.

Let us now begin by examining a simple example of a MP echo to discuss the possibility of detecting and locating a fault using the MP approach. We draw the reader's attention to the fact that, given we are dealing with soft faults, and based on the analysis done in the second chapter, we are going to consider the difference system of the NUT in our study. Thus, we will refer to the difference impulse response of the NUT by $h(t)$, with no further details.

3.3.1 Example of a MP echo

For illustration purposes, we suppose that $i_{\mathrm{ST}}(t)$ (Fig. 3.2) is a Dirac pulse. We also suppose that the impulse response of the difference system, $h(t)$, consists of three peaks, as represented in Fig. 3.3(a), having amplitudes denoted as a_i, for $i = 1, 2$ and 3. The time of occurrence of these echoes is also denoted t_i.

In the MP approach, the first step is to inject the testing signal $i_{ST}(t)$ into the network. In this case where $i_{\mathrm{ST}}(t)$ is a pulse, we obtain an echo $e_{\mathrm{ST}}(t)$ which is the impulse response of the system (Fig. 3.3(a)). This echo is then time-reversed (Fig. 3.3(b)), and re-injected into the network under test, so as to obtain the MP echo $e_{\mathrm{MP}}(t)$ as illustrated in Fig. 3.3(c). As earlier discussed, this MP echo is the autocorrelation function of $h(t)$. Looking at the amplitudes of the different peaks in this echo, we notice a constructive interference at the origin position (i.e., at $t = 0$), where the amplitude of the highest peak equals $\sum_{i=1}^{3} a_i^2$. This sum is always positive, regardless of the sign of the different peaks a_i. On the contrary, the cross-products $a_i a_j$ have a sign alternating between the positive and the negative, depending on the signs of a_i and a_j.

For example, if we consider the simple case of a single transmission line with a matched termination, and a fault at a certain distance of the testing port, the difference echo $e_{\mathrm{ST}}(t)$ will contain a single peak, leading to a single-peak MP echo which amplitude is a_1; it will be the same as the one obtained with standard TDR. In a more complex configuration involving junctions, we already saw in the second chapter that their existence yields negative reflection coefficients, leading to amplitudes a_i with different signs. As we will be considering complex networks, we will be dealing with configurations containing one or several junctions, thus ensuring that the signs of the amplitudes a_i would alternate between the positive and the negative. This idea will be discussed in details in Section 3.4.2, when introducing the detection Gain.

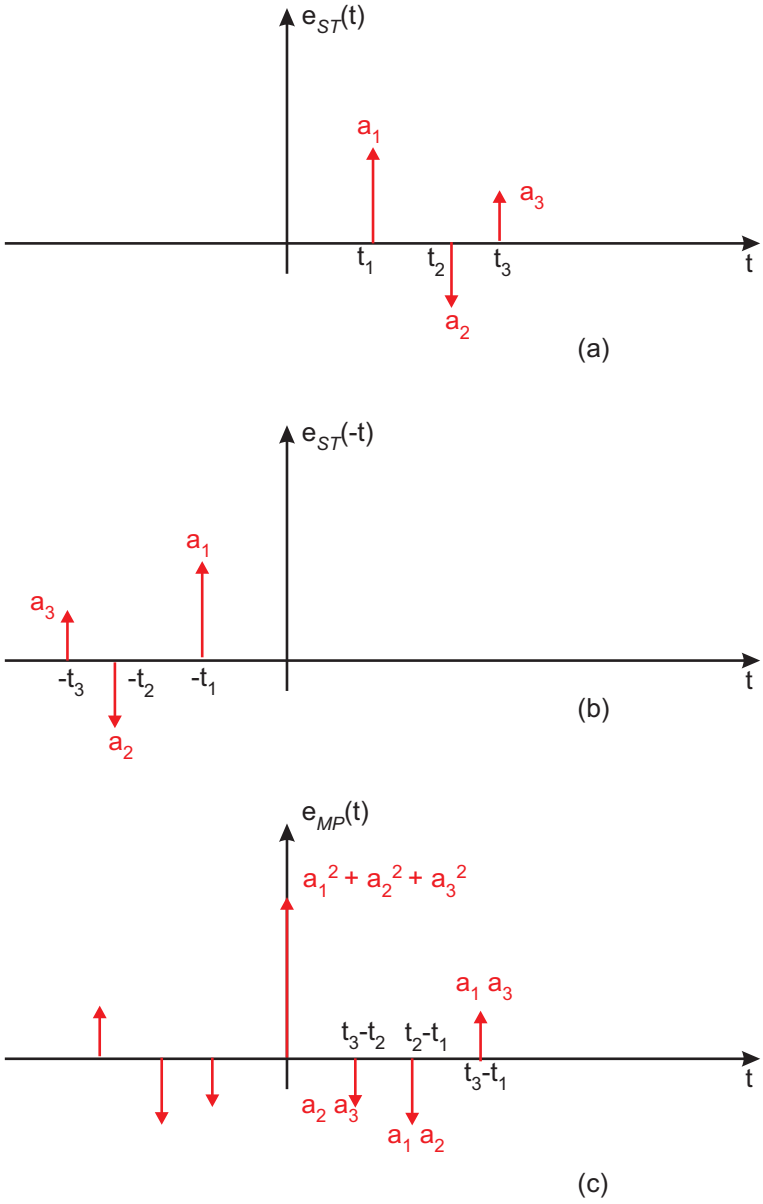

Figure 3.3: Example of obtaining a MP echo: (a) the standard TDR echo $e_{\mathrm{ST}}(t)$, (b) the time reversed TDR echo $e_{\mathrm{ST}}(-t)$, which will be reinjected into the system to give rise to (c) the MP echo $e_{\mathrm{MP}}(t)$

.

3.3.2 Localization using the MP echo

When examining the TDR echo $e_{\mathrm{ST}}(t)$, we have already pointed out in the second chapter that in the absence of noise, the first peak appearing in this difference echo corresponds to the fault. Also we have seen that this peak does not necessarily have the highest amplitude (as we will also see in the simulation and experimental results).

In the MP case, due to the lack of a time origin when injecting the time-reversed TDR echo, the maximum is situated at the origin. In fact, the time of occurrence of the fault-related peak t_1 is not known in advance, or else TDR alone would be sufficient to locate the fault. If we consider the time reversed TDR echo $e_{\mathrm{ST}}(-t)$, the fault related-echo is now situated at $-t_1$. Convolving $e_{\mathrm{ST}}(-t)$ with $h(t)$ causes the fault-related peak to appear at the origin of the time axis. This peak is due to the superposition of the constructive sum $\sum_{i=1}^{3} a_i^2$, and thus has the highest amplitude; it is also the one corresponding to the fault in the MP case. Consequently, when addressing the mathematical analysis later in this chapter, it is this peak which we will be interested in for our calculation. But since its position does not correspond to the fault's one, fault location will not be addressed using the MP approach, but rather another TR-based method explained in the next chapter.

To conclude, we will show that the MP is complementary to existing techniques, in the sense that it is useful to improve fault detection in critical scenarios, such as the case of soft faults in complex networks, as it is going to be shown later. However the MP approach cannot be used to locate the fault.

Now that we have introduced the MP approach, we proceed to a more detailed study of the latter, first through a mathematical analysis highlighting its important advantages over standard reflectometry techniques when it comes to detecting soft faults in complex network configurations.

3.4 Mathematical analysis

After Introducing the MP approach, and in order to quantify its advantages and asses the situations where it presents major benefits over existing methods, we propose to compare it to standard reflectometry techniques, as they represent the most common methods used today. The comparison will be carried in a formal way, by means of a mathematical analysis aiming to calculate a detection gain. But first of all, we need to introduce a propagation model for the signal applied to the NUT.

3.4.1 Modeling of the impulse response of the difference system

With no loss of generality, the impulse response of a typical NUT can be modeled as a superposition of time-delayed echoes, with varying amplitudes depending on the sequence of interactions between the testing signal and the discontinuities found in the NUT.

We remind that the difference system will be studied: as already explained, this procedure allows removing most of the echoes of the NUT that are not related to any fault, which constitute the clutter response preventing the detection of eventual faults: as a result, minor echoes potentially related to faults are more clearly exposed. For this approach to hold, time-invariance is an important requirement. This means that for the time between the two measurements leading to the difference response, the NUT has eventually changed only by the appearance of a fault. In some practical configurations, such as in TDR systems embedded into transportation systems, this assumption should be carefully considered, as mechanical vibrations can lead to spurious reflections due to non-perfect connections. Such a scenario is not considered in this analysis, as it only represents a part of the systems to which TDR techniques are applied. More importantly, the aim of this study is to assess whether under the same working conditions, testing signals generated through the proposed method are capable of improving the detection capabilities of TDR techniques.

The impulse response of the difference system relates the difference of the output signals reflected back by the networks (the one under test and the reference one) to the input test signal. As a result, the output signal will be made up by a series of echoes directly related to the reflectivity of the fault, hereafter referred to as $\Gamma_F(t)$.

No assumption will be formulated on the actual nature of the fault, but for the fact that it be indeed soft, i.e. when considering the fault alone, the energy it reflects back be just a fraction of the incident one, requiring

$$\Gamma_{F,\mathrm{rms}}^2 = \frac{1}{B_T} \int |\Gamma_F(\omega)|^2 \mathrm{d}\omega \ll 1. \tag{3.2}$$

where B_T is the region of Fourier spectrum occupied by the excitation signal, not necessarily a continuous region. The root-mean-square (rms) value $\Gamma_{F,\mathrm{rms}}$ of the reflectivity of the fault is required to be weak enough to regard the fault as soft, thus acting as a weak perturbation in the propagation of signals across the NUT.

As a result, the impulse response of the NUT (with respect to a baseline) can be stated as

$$h(t) = \Gamma_F(t) * \sum_{i=1}^{N} \alpha_i \delta(t - t_i), \tag{3.3}$$

where $\delta(t)$ is the Dirac pulse and the star $*$ stands for the convolution operator. The impulse response is thus modeled as a sequence of echoes of relative amplitude α_i occurring at the time t_i, representing the resulting interaction with the remaining NUT discontinuities of the energy scattered by the fault and the eventual attenuation of the echoes due to propagation losses. Subsequent interactions of these echoes with the fault can be neglected, thanks to the weak-perturbation hypothesis.

In the rest of the analysis, the sums will only be characterized by the index of summation, with no further details.

Although simplified, the model in (3.3) can actually represent the most important physical phenomena underlying the propagation of signals through a complex network. Not only the possibility of complex series of echoes is accounted for through the $\{\alpha_i\}$ sequence, but the eventual dispersive response of the fault is modeled by $\Gamma_F(t)$.

The aim of the subsequent study is twofold: 1) to support our claim of a stronger output signal reflected by the fault in increasingly complex configurations excited by means of MP signals; 2) to provide a quantitative treatment of the advantages of the MP method in terms of detection gain and detection probability in presence of a realistic NUT affected by an additive Gaussian noise.

3.4.2 Detection gain

3.4.2.1 Definition

In the following analysis, a standard TDR signal $i_{\mathrm{ST}}(t)$ will be considered, with no assumption made on its nature. As thus, the results here presented are entirely general and apply to any TDR method.

In order to compare the standard TDR and MP approaches, we are going to impose the same injected energy, the idea being of checking whether the shape of the MP signal is better suited at exciting a fault, in order to yield a higher output starting from the same amount of available injected energy.

The detection of a soft fault is usually based on the identification of the strongest signal reflected back by the NUT, after subtracting the baseline echo. In simple words, the output signal is analyzed looking for a contribution stronger than a given reference threshold suitably fixed in advance. This threshold is typically set as a compromise between the ability to detect the presence of an echo (and thus an eventual fault) and the need to provide for a robust immunity with respect to noise signals (see Section 3.4.3.3). Independently from the actual type of testing signal, the use of a threshold-detection approach implies that the quantity of interest is the maximum instantaneous power of the echo. It is defined, for the case of a standard testing signal as

$$\mathcal{P}_{\mathrm{ST}}^{\mathrm{out}} = \max_t |e_{\mathrm{ST}}(t)|^2 \tag{3.4}$$

where $e_{\mathrm{ST}}(t)$ is the echo signal generated by applying a testing signal $i_{\mathrm{ST}}(t)$, as introduced in Section 3.2.3. In simple NUT configurations, wa can expect this maximum to coincide with the first echo generated by the interaction with the fault; this allows retrieving the position of the latter. Actually, as it will be shown in the experimental results presented in Section 3.6, this assumption does not hold anymore in complex NUTs. Hence, peak-based detection schemes cannot ensure the precise localization of the fault under such circumstances. This fact is shared by any standard TDR scheme, as well as by the proposed approach.

The efficiency of the TDR scheme can thus be measured by looking at the ratio $\mathcal{P}^{\mathrm{out}}/\mathcal{E}^{\mathrm{in}}$, where $\mathcal{E}^{\mathrm{in}}$ is the energy of the testing signal applied to the NUT. Hence, the improvement

provided by the MP approach over standard TDR signals can be assessed by introducing the following definition for the detection gain

$$G = \frac{\mathcal{P}^{\text{out}}_{\text{MP}}/\mathcal{E}^{\text{in}}_{\text{MP}}}{\mathcal{P}^{\text{out}}_{\text{ST}}/\mathcal{E}^{\text{in}}_{\text{ST}}}. \tag{3.5}$$

where the quantities indexed by MP are defined as those with ST, but considering the signals generated by applying the MP test signal $i_{\text{MP}}(t)$. The gain in (3.5) assesses whether the fault is more excited by means of an MP testing signal with respect to a standard TDR one, having ensured that the same input energy is available for the test.

3.4.2.2 Calculus of the input energies

To calculate this gain, we first consider the output signal $e_{\text{ST}}(t)$ obtained in the standard TDR case

$$e_{\text{ST}}(t) = i_{\text{ST}}(t) * h(t) = \sum_i \alpha_i e^o_{\text{ST}}(t - t_i), \tag{3.6}$$

with

$$e^o_{\text{ST}}(t) = i_{\text{ST}}(t) * \Gamma_F(t), \tag{3.7}$$

the elementary response of each echo found in $e_{\text{ST}}(t)$. The input energies in (3.5) are given by

$$\mathcal{E}^{\text{in}}_{\text{ST}} = \int |i_{\text{ST}}(t)|^2 \text{d}t, \tag{3.8}$$

while for the MP approach

$$\mathcal{E}^{\text{in}}_{\text{MP}} = \int |i_{\text{MP}}(t)|^2 \text{d}t = \int |e_{\text{ST}}(T - t)|^2 \text{d}t, \tag{3.9}$$

where T is the duration of the first phase during which $i_{\text{ST}}(t)$ is applied to the NUT. For the sake of simplicity, we will drop the delay T, as it has no effect on our analysis, as pointed out in Section 3.3. An acausal formulation will thus be considered. Inserting (3.6) into (3.9) yields

$$\mathcal{E}^{\text{in}}_{\text{MP}} = \mathcal{E}_o \left[\sum_i \alpha_i^2 + \sum_{i \neq j} \alpha_i \alpha_j \phi_o(t_i - t_j) \right], \tag{3.10}$$

having introduced the energy $\mathcal{E}_o$ of the echo template $e^o_{\text{ST}}(t)$ and its peak-normalized auto-correlation function $\phi_o(t)$, i.e.,

$$\phi_o(t_i - t_j) = \frac{\int e^o_{\text{ST}}(t - t_i) e^o_{\text{ST}}(t - t_j) dt}{\mathcal{E}_o} \tag{3.11}$$

Equation (3.10) is composed of two terms: the first one is given by the sum of the energy of each individual echo, as though they were not superposed, while the second one represents the sum of the mutual energy of each couple of echoes. If we compare these two terms, we notice

that the first one is a coherent sum, more specifically a positive-term series, while the second one involves the cross-products $\alpha_i\alpha_j$, and is thus an incoherent sum based on the discussion in Section 3.3.1; as a matter of fact, in complex networks most of the echoes are generated by junctions, which have by definition a negative reflection coefficient: hence, these echoes will change sign after each interaction with any other junction in the NUT. Under these circumstances, the first term in (3.10) is bound to be much higher than the second one. The contrast between these two terms systematically increases, on average, as the number of echoes N increases, thus implying that complex networks will support the following approximation

$$\sum_{i\neq j}\alpha_i\alpha_j\phi_o(t_i-t_j) \ll \sum_i \alpha_i^2. \tag{3.12}$$

In the context of the present analysis, the above simplification will be applied, for the sake of simplicity.

3.4.2.3 Calculus of the instantaneous powers

In order to compute the detection gain, we just need to calculate the maximum instantaneous power for the two test signals; we first consider the output signal for the MP case

$$\begin{aligned} e_{\mathrm{MP}}(t) &= i_{\mathrm{ST}}(-t) * h(-t) * h(t) \\ &= \mathcal{E}_{\Gamma_F} i_{\mathrm{ST}}(-t) * \phi_{\Gamma_F}(t) * \sum_k \beta_k \delta(t-t'_k) \\ &= \mathcal{E}_{\Gamma_F} e^o_{\mathrm{MP}}(t) * \sum_k \beta_k \delta(t-t'_k), \end{aligned} \tag{3.13}$$

where $\phi_{\Gamma_F}(t)$ is the peak-normalized auto-correlation function of the fault response $\Gamma_F(t)$

$$\phi_{\Gamma_F}(t) = \frac{\Gamma_F(-t) * \Gamma_F(t)}{\mathcal{E}_{\Gamma_F}} \tag{3.14}$$

and $e^o_{\mathrm{MP}} = i_{\mathrm{ST}}(-t) * \phi_{\Gamma_F}(t)$ is the elementary response from the fault for the MP case. The term $\mathcal{E}_{\Gamma_F}$ is the energy of the $\Gamma_F(t)$ function. The Dirac's delta series based on the $\{\beta_k\}$ sequence is nothing else than the auto-correlation function of the original Dirac's delta series based on the $\{\alpha_i\}$ sequence, with

$$t'_k = t_j - t_i \tag{3.15}$$

and

$$\beta_k = \begin{cases} \sum_i \alpha_i^2 & k = 0 \\ \alpha_i\alpha_j & k \neq 0 \end{cases}. \tag{3.16}$$

All of the β_k terms (echoes) are characterized by zero-averaged weights, but for the echo β_0; this latter can be easily shown to correspond to the time of arrival of signals directly interacting with the fault and to be by definition the strongest one among the $\{\beta_k\}$.

The instantaneous output powers are then found by applying (3.4)

$$\mathcal{P}_{\mathrm{ST}}^{\mathrm{out}} \simeq \alpha_{\max}^2 \max_t |e_{\mathrm{ST}}^o(t)|^2 \tag{3.17}$$

with $\alpha_{\max} = \max_i \alpha_i$, while for the MP case

$$\mathcal{P}_{\mathrm{MP}}^{\mathrm{out}} = \max_t |e_{\mathrm{MP}}(t)|^2 \simeq \mathcal{E}_{\Gamma_F}^2 \beta_0^2 \max_t |e_{\mathrm{MP}}^o(t)|^2. \tag{3.18}$$

3.4.2.4 Calculus of the detection gain

Using (3.8), (3.10), (3.17) and (3.18), (3.5) yields

$$G = G'G'' \tag{3.19}$$

with

$$G' = \sum_i \alpha_i^2 / \alpha_{\max}^2 \tag{3.20a}$$

$$G'' = \frac{\mathcal{E}_{\Gamma_F}^2 \mathcal{E}_{\mathrm{ST}}^{\mathrm{in}}}{\mathcal{E}_o} \frac{\max_t |e_{\mathrm{MP}}^o(t)|^2}{\max_t |e_{\mathrm{ST}}^o(t)|^2} \tag{3.20b}$$

The two gain terms in (3.19) account for specific features of the NUT: G' is directly related to the complexity of the NUT, especially its topology, independently from the nature of the fault, whereas G'' depends on the fault response and the nature of the excitation signal. In order to assess whether the MP approach improves the detection of a fault, these two terms need to be studied. The first term (3.20a) is by definition greater than one, while the behavior of the second one cannot be claimed to be identically greater than one. Its actual value strongly depends on the type of signals considered, but some insight can be gained by considering two special configurations: 1) a non-dispersive fault; 2) an excitation pulse with a flat Fourier spectrum over a bandwidth B_T, that can as well be divided over a number of sub-bandwidths. In the first case,

$$\Gamma_F(t) = \Gamma_F \delta(t), \tag{3.21}$$

leading to $G'' = 1$. Conversely, in the second case,

$$\begin{aligned} G'' &= B_T \frac{\max_t \int_{B_T} |\Gamma_F(\omega)|^2 \mathrm{e}^{+\mathrm{j}\omega t} \mathrm{d}\omega}{\max_t \left| \int_{B_T} \Gamma_F(\omega) \mathrm{e}^{+\mathrm{j}\omega t} \mathrm{d}\omega \right|^2} \\ &= \left(\frac{\Gamma_{F,\mathrm{rms}}}{\max_t |\langle \Gamma_F(\omega) \mathrm{e}^{+\mathrm{j}\omega t} \rangle|} \right)^2 \end{aligned} \tag{3.22}$$

where the brackets stand for the average operator applied over the bandwidth B_T of definition of the excitation signal, and having applied Parseval's and the convolution theorems. The integral

at the numerator has its maximum value at $t = 0$, thus coinciding with $\Gamma_{F,\mathrm{rms}}$ as defined in (3.2), while an upper bound for the denominator is provided by Cauchy-Schwartz inequality

$$\max_t \left| \int_{B_T} \Gamma_F(\omega) \mathrm{e}^{+\mathrm{j}\omega t} \mathrm{d}\omega \right|^2 \leqslant B_T \int_{B_T} |\Gamma_F(\omega)|^2 \mathrm{d}\omega \tag{3.23}$$

whence the fact that $G'' \geqslant 1$. This result does not imply any assumption on the nature of the fault; it is remarkable that the lower bound for G'' is attained in what are usually regarded as the best-working conditions, i.e., for a non-dispersive fault: in this case the MP approach already provides a gain G' dependent on the complexity of the response of the NUT, as the detection gain is maximized as soon as the energy reflected back by the NUT is dispersed in a long series of echoes, rather than being concentrated into a single one. In other words, the MP approach benefits from an increased complexity in the response of the NUT, as opposed to standard reflectometry methods.

In any other condition, for an excitation with a flat spectrum, an extra gain is ensured by the fact that a fault with a response that has a higher self-resemblance (stronger dispersion) will also enable a $G'' > 1$; such a result is actually more likely when dealing with soft faults rather than hard ones. Hence, these results prove that the proposed approach can be expected to ensure a useful improvement with respect to any kind of predefined excitation signals. It is clearly not that surprising to find out such improvement, as this procedure is very closely related to the idea of matched filter as already explained in Section 3.3, hence our claim that the MP approach is optimal in the sense of maximizing the detection probability, as will be shown in the next Section.

The only configuration where $G = 1$ is what is usually regarded as the simplest and most optimistic scenario, i.e., a single echo from a non-dispersive fault, such as the case of an infinitely long (or impedance-matched) wire, with a single fault and no other discontinuities. Again, this points to the fact that the MP approach is indeed complementary to existing reflectometry techniques, and should be considered only in configurations where standard approaches fail.

These results have been derived under fairly general assumptions. Two main parameters of interest in practical scenarios are losses and a limited bandwidth. The first one is actually accounted for by the sequence $\{\alpha_i\}$: as losses increases, the time-spread of this sequence decreases, thus leading to a reduction in G'. We remind that the definition of G' does not depend on the absolute value of the $\{\alpha_i\}$, but rather on their relative distribution. The MP approach will provide a gain as long as the NUT responds with a long series of echoes.

The reduction of the excitation bandwidth has a different effect, as it will make the approximation (3.12) less precise. As the bandwidth decreases it will be no more possible to neglect the mutual energy, i.e., the overlapping of the pulses. Including this extra-term in the computation of the gain will have a broadly decreasing effect, as the echoes will be no more resolved.

3.4.3 Signal to Noise Ratio (SNR)

Real-life NUTs are always affected by some kind of background noise. Independently from its origin, the presence of noise puts a strong limit to the dynamic-range of the signals that can be properly detected. In the case of soft faults, as their echoes can be expected to be quite weak, the possibility of having fault-related echoes beneath the level of background noise is clearly a critical configuration. Within this context, the ability of the MP approach to yield a higher echo is thus a strong argument in its favor.

It is therefore important to assess how the detection gain translates into a corresponding improvement of the detection probability. As such, it is convenient to compute the SNR of the output signal at the instant of the detection, i.e., when it reaches its maximum amplitude: this is a fundamental measure of the reliability of the output signal obtained from a reflectometry measurement.

We consider an analysis based on the presence of an additive Gaussian noise. This choice does not bring any limitation to our conclusions, as the same analysis could be carried out considering other types of noise. The choice of an additive Gaussian noise is just motivate by the simplicity of the related analysis.

3.4.3.1 Standard TDR case

We start with the case of a standard TDR approach, as shown in Fig. 3.2(a). As the decision of whether a fault is present or not directly depends on the SNR at the time of arrival of what is assumed to be the fault-related echo, we focus our analysis on this quantity. In particular, we consider that the original testing signal $i_{\mathrm{ST}}(t)$ be pulse-like: in this way, the SNR can be defined as follows:

$$S_{\mathrm{ST}} = \frac{\mathcal{P}_{\mathrm{ST}}^{\mathrm{out}}}{\mathcal{P}_n}, \tag{3.24}$$

i.e., as the ratio between the peak instantaneous power of the fault-related echo (i.e., the one related to the coefficient $\alpha_{\max}$ for standard TDR techniques), and the noise average power.

- Calculus of the SNR

The instantaneous power of the fault related peak have been previously calculated in Section 3.4.2. As for the noise average power, and provided that we are considering the difference system, two noise realizations actually intervene in its measurement: the first one, $n'(t)$, in the reference system, and the second one, $n''(t)$, in the faulty system. Let their difference be denoted as $n(t)$; then the average noise power in the difference system can be written as

$$E[|n(t)|^2] = E[|n'(t) - n''(t)|^2] = E[n'^2(t)] - E[n''^2(t)] - 2E[n'(t)n''(t)] \tag{3.25}$$

Let N_0 be the average power for the noise applied to the output port of the NUT. We suppose that we start recording the signal, and consequently the noise, at the time origin $t = 0$, supposed

to be the instant of the pulse injection. Hence $n'(t)$ (or equivalently $n''(t)$) can be written as

$$n'(t) = n_0(t)u(t) \tag{3.26}$$

Where $n_0(t)$ is a Gaussian white noise process with an average noise power equal to N_0, and $u(t)$ is the step function defined as follows

$$u(t) = \begin{cases} 1 & t \geq 0 \\ 0 & t < 0 \end{cases} \tag{3.27}$$

Considering the fact that the processes $n_0(t)$ and $u(t)$ are independent, and that $E[u(t)^2] = 1$, the average power of $n'(t)$ is hereby equal to

$$E[|n'(t)|^2] = E[|n_0(t)u(t)|^2] = E[n_0(t)^2]E[u(t)^2] = N_0 \tag{3.28}$$

Based on (3.25), and since the realizations $n'(t)$ and $n''(t)$ are non-correlated, the average noise power at the output of the difference system is

$$E[|n(t)|^2] = 2N_0 \tag{3.29}$$

So that the SNR in the standard TDR case finally obtained is equal to

$$S_{\mathrm{ST}} = \frac{\mathcal{P}_{\mathrm{ST}}^{\mathrm{out}}}{2N_0}. \tag{3.30}$$

In the case of TDR techniques based on test signals shaped otherwise than pulses, particularly when the output signal is actually correlated to the injected one before proceeding to the detection analysis (e.g., spread-spectrum TDR [44] or time-frequency techniques [53]), the same definition still applies. Rather than the instantaneous power, the energy of the signals should be considered, but no major difference will be required. A similar consideration can be invoked for the noise average power: the average energy after filtering through the correlator will be considered. Indeed, in the case of correlation-based TDRs, pulse-like sequences can still be expected at the output of the correlator between the output TDR signal and the template one.

3.4.3.2 MP case

With reference to Fig. 3.2(b), we now turn our attention to the MP case. Here, the output signal from the first step of standard TDR is already corrupted by the Gaussian noise; as its time-reversed version is injected back through the NUT, the output signal for the MP will be corrupted by two noise terms, the one from the first step and then again at the output of the MP signal. Hence, the overall equivalent noise $n(t)$ can be expressed as follows

$$n(t) = n_1(-t) * h(t) + n_2(t), \tag{3.31}$$

where $n_1(t)$ and $n_2(t)$ are defined in Fig. 3.2(b). It is important to acknowledge the fact that in the MP approach the noise $n_1(t)$ is scattered back by the NUT generating a series of delayed

and scaled replicas, filtered by the fault response, acting as a number of practically uncorrelated noise sources. The following analysis aiming to calculate the average noise power will illustrate the idea.

- Calculus of the SNR

Based on the model of the impulse response of the system earlier introduced in (3.3), the equivalent noise at the output of the difference system can be written as

$$n(t) = \Gamma_F(t) * \Sigma\alpha_i n_1(-t + t_i) + n_2(t) \tag{3.32}$$

As already invoked the replicas of $n_1(t)$ are scaled by the coefficients α_i when the noisy TDR echo $e_{\mathrm{ST}}(t)$ is re-injected into the NUT, and filtered by the fault response $\Gamma_F(t)$. We denote by $n_f(t)$ the convolution product of $\Gamma_F(t)$ and $n_1(t)$, so as to have

$$n(t) = \Sigma\alpha_i n_f(-t + t_i) + n_2(t) \tag{3.33}$$

As already pointed out when calculating the SNR in the MP case, the instant when we start recording the reflected signal is supposed to be the same of the injection of the testing signal, set to the time origin. The average noise power of $n(t)$, denoted as N, is composed of three terms

$$N = E[n(t)^2] = E[(\Sigma\alpha_i n_f(-t + t_i))^2] + E[n_2^2(t)] + \Sigma E[\alpha_i n_f(-t + t_i) n_2(t)] \tag{3.34}$$

The first term in (3.34) is calculated as follows

$$E[(\Sigma\alpha_i n_f(-t + t_i))^2] = \Sigma\alpha_i^2 E[n_f^2(-t + t_i)] + \sum_{i,j} \alpha_i\alpha_j E[n_f(-t + t_i) n_f(-t + t_j)] \tag{3.35}$$

Applying Parseval's theorem leads to having

$$\Sigma E[\alpha_i^2 n_f^2(-t + t_i)] = \Sigma\alpha_i^2 \Gamma_{F,\mathrm{rms}}^2 N_0 \tag{3.36}$$

since the cross products $\alpha_i\alpha_j$ are zero-average quantities, we assume that

$$\Sigma\alpha_i^2 E[n_f^2(-t + t_i)] \gg \sum_{i,j} \alpha_i\alpha_j E[n_f(-t + t_i) n_f(-t + t_j)] \tag{3.37}$$

and consequently

$$E[(\Sigma\alpha_i n_f(-t + t_i))^2] \approx \Sigma\alpha_i^2 \Gamma_{F,\mathrm{rms}}^2 N_0. \tag{3.38}$$

The second term in (3.34) is equal to

$$E[n_2^2(t)] = N_0. \tag{3.39}$$

In the same way the third term $\Sigma E[\alpha_i n_f(-t + t_i) n_2(t)]$ can be found to be equal to zero. Consequently,

$$N \simeq N_0(1 + \Gamma_{F,\mathrm{rms}}^2 \Sigma\alpha_i^2) \tag{3.40}$$

so as to have

$$S_{\mathrm{MP}} = \frac{\mathcal{P}_{\mathrm{MP}}^{\mathrm{out}}}{2N} \tag{3.41}$$

3.4.3.3 SNR gain

Now we introduce the SNR gain R defined as the perceived increase in the output SNR while the input energy is unmodified and recalling (3.5), we obtain

$$R = \frac{S_{\mathrm{MP}}/\mathcal{E}^{\mathrm{in}}_{\mathrm{MP}}}{S_{\mathrm{ST}}/\mathcal{E}^{\mathrm{in}}_{\mathrm{ST}}} = \frac{G}{1 + \Gamma^2_{F,\mathrm{rms}} \sum_i \alpha_i^2}. \tag{3.42}$$

As we clearly notice, the sum at the denominator is expected to reduce the detection gain G, brought by the MP approach. In fact, the second term in it is about the fraction of energy reflected back by the NUT, when excited by a flat spectrum testing signal. As the fault is passive, this fraction is clearly bound to be smaller than one, hence

$$G \geq R \geq \frac{G}{2}. \tag{3.43}$$

The lower bound is only met in the trivial case of a non-dispersive hard fault with a single echo $|\alpha_1| = 1$. An example of this case is a single transmission line with a matched end, the hard fault (open or short) occurring at a certain distance of the testing port.

In all other cases, and particularly for the case of soft faults, the sequence of α_i would lead to a higher gain allowing to fully take advantage of the higher detection gain yielded by the MP approach. Some insight is provided by the special case of a NUT where neither dissipation phenomena nor dispersive ones occur, not even at the loads. This ideal case involves

$$\sum_i \alpha_i^2 \equiv 1 \tag{3.44}$$

due to energy conservation. Whence

$$R = \frac{1}{\alpha^2_{\max}(1 + \Gamma^2_{F,\mathrm{rms}})} \simeq \frac{1}{\alpha^2_{\max}}, \tag{3.45}$$

due to the hypothesis (3.2). This result implies again that the MP approach cannot lead to any advantage whenever the whole energy reflected back by the NUT is concentrated into a single echo, whereas R can be much higher than one as soon as the energy associated to the strongest echo only represents a small portion of the overall output energy, e.g., for a long sequence of echoes. This is indeed the configuration we are interested in.

3.4.4 Detection probability

3.4.4.1 True Positive probability (TP)

Having derived a relationship between the SNR in the case of a standard and an MP approach, the SNR can be easily related to the detection probability by applying standard tools from decision theory [97, 98]. We first begin by calculating the conditional probability of detection,

here referred to as the True Positive (TP) probability. If a_{max} denotes the amplitude of the maximum peak in both cases, $n(t_0)$ the value of the Gaussian noise at the peak position , and $a_{\rm th}$ the decision threshold, then the TP probability can be expressed as

$$P^{\rm TP} = Pr(a_{max} + n(t_0) > a_{\rm th} | a_{max} > a_{\rm th}) \tag{3.46}$$

which means that it is the conditional probability of having the amplitude of the highest peak a_{max}, affected by the noise $n(t_0)$, greater than the imposed detection threshold $a_{\rm th}$, under the assumption of the fault's existence, which can be translated into $a_{max} > a_{\rm th}$. As already invoked we consider the case of a white Gaussian noise process $n(t, z)$, where z denotes the spatial variable, i.e., the distance from the testing port. As we are considering the peak position, z have been omitted for the sake of simplicity, and thus the probability density function of the random variable $n(t_0)$ at the peak position would be

$$p(x) = \frac{1}{\sigma\sqrt{2\pi}} e^{-x^2/2\sigma^2} \tag{3.47}$$

where σ^2 is the variance of the noise variable.

Calculating the TP probability in (3.46) using (3.47) gives the following

$$P_{ST}^{\rm TP} = \frac{1}{2} erfc\left(\frac{a_{\rm th} - a_{max}}{2\sqrt{N}}\right) \tag{3.48}$$

$erfc(x)$ is the complementary error function [99] defined as follows

$$erfc(x) = \frac{2}{\sqrt{\pi}} \int_x^\infty e^{-t^2} dt \tag{3.49}$$

and N is the equivalent average noise power in the difference system.

Recall that in the TDR case we have

$$a_{max}^{\rm ST} = \alpha_{max} max |e_{\rm ST}^0(t)|. \tag{3.50}$$

and in the case of the MP approach,

$$a_{max}^{\rm MP} = \mathcal{E}_{\Gamma_F} \beta_0 \max_t |e_{\rm MP}^o(t)|. \tag{3.51}$$

Expressing the TP probability in terms of the SNR S previously calculated in each case, and if we consider that the detection threshold is expressed as a fraction $0 < \rho < 1$ of the peak echo, we will have the general formula

$$P^{\rm TP} = \frac{1}{2} {\rm erfc}\left((\rho - 1)\sqrt{S/2}\right). \tag{3.52}$$

3.4.4.2 False Positive probability (FP)

The same rationale applies when calculating the conditional probability of detecting a fault when no faults exists, also known as the false alarm rate. Here we formally denote it as the False Positive or FP probability.

$$P^{\mathrm{FP}} = Pr(n(t_0) > a_{\mathrm{th}}) \tag{3.53}$$

Following the same reasoning as for the TP probability calculus, the FP probability in both cases, in terms of the S and ρ can be written as

$$P^{\mathrm{FP}} = \frac{1}{2}\mathrm{erfc}\left(\rho\sqrt{S/2}\right). \tag{3.54}$$

The above expressions establish that the MP approach can ensure the same probability of detection of a standard TDR technique, but with a less stringent requirement for the SNR. More specifically, (3.42) implies that the MP approach can provide the same performance than a standard TDR technique while the noise average power is increased by a factor R. The other way round, for a given SNR, the MP can be expected to lead to a substantial improvement of the detection probability, depending on the type of response of the NUT. Remarkably, this improvement is expected to increase with the NUT complexity and the dispersiveness of the fault, a fact that is counterintuitive within the framework of standard TDR techniques.

3.5 Parametric study

In this section we validate all the discussed ideas with simulations, aiming to assess the impact of the fault position, as well as the NUT complexity on the detection gain and the detection probabilities. We first begin by introducing the network model we developed in order to simulate the studied NUTs, and next show the results we obtained when simulating two configurations, for different fault values and positions.

3.5.1 Simulation Model

Using the transmission line theory introduced in the second chapter, and the Matlab program, we simulated the model represented in Fig. 3.4. This model contains two junctions, with varying branch lengths and several discontinuities, referred to as the blocks B_i, having $i = 1, 2, ..., 6$. These blocks represent impedances that can be placed either in series or in parallel. We chose this NUT structure because it is relatively complex compared to the structures normally studied when validating reflectometry methods, the most common involving a limited number of echoes [52, 53, 42, 44, 49, 54, 23], such as single transmission lines. A maximum of 5 testing ports, denoted as P_i ($i = 1, ...5$), can be applied at the five terminations of the network, a fact that will be useful when we study fault location in the next chapter. In the present study of fault detection, we will only consider one testing port, matched to the network.

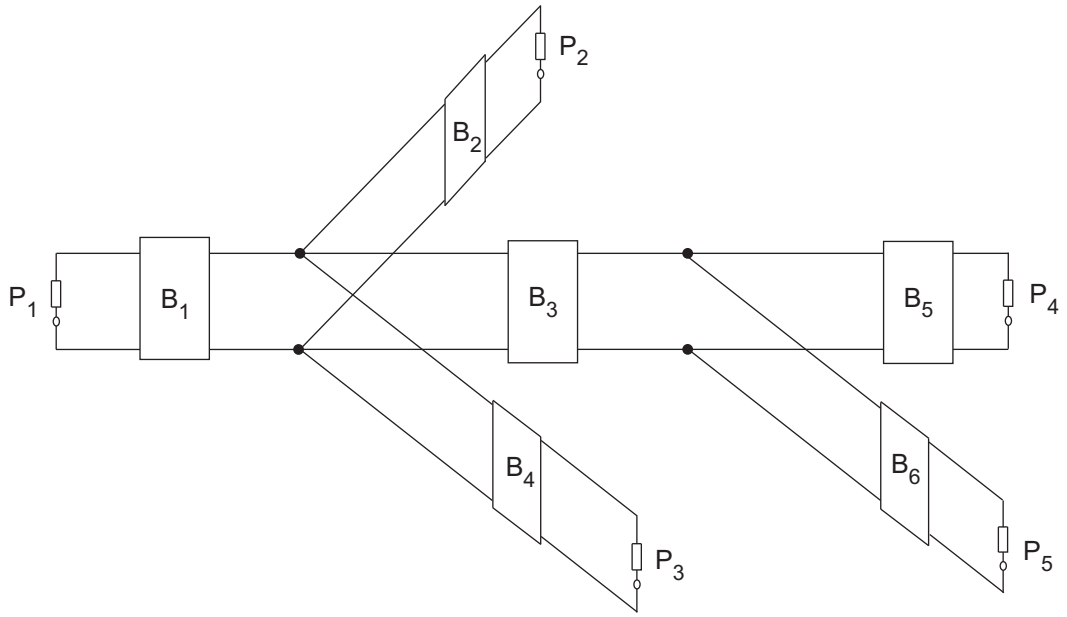

Figure 3.4: The simulation model we used in our study, showing a grand-total of five testing ports denoted as P_i ($i = 1, ..., 5$), and different impedance discontinuities referred to as B_j ($j = 1, ..., 6$).

Using the model we exposed, we simulated two different configurations: they are represented in Fig. 3.5. The first network represented in Fig. 3.5(a) is a Y network with a single junction at 0.8 m from the testing port. The second network configuration is shown in Fig. 3.5(b). It is a double-junction network, with the first one situated at 1.2 m from the testing port, and the second one at a distance of 2.6 m from the latter.

3.5.2 Single-Y network simulation

Let us begin by considering the first network structure of a single-junction NUT, as shown in Fig. 3.5(a). Two different fault positions will be considered when dealing with this configuration, as shown in figure 3.6, in order to asses how a changing fault position might affect the MP performances. Also the cases of matched and open ends will be studied, and several values of the fault impedance will be also analyzed; on one hand this will allow us to verify the impact of the number of echoes on the detection gain, and quantify the latter; on the other hand we will be able to observe the evolution of this gain with the fault 'softness'. A similar study will also be conducted on the second network of Fig. 3.7.

The first case of a fault directly 'seen' by the testing port, i.e. not separated by any discontinuity from the latter, is shown in Fig.3.6(a); here the fault is situated at a distance of 0.5 m from the testing port. In the second case of Fig. 3.6(b) the fault is hidden from the testing port by the junction, located at a distance of 0.8 m from the source.

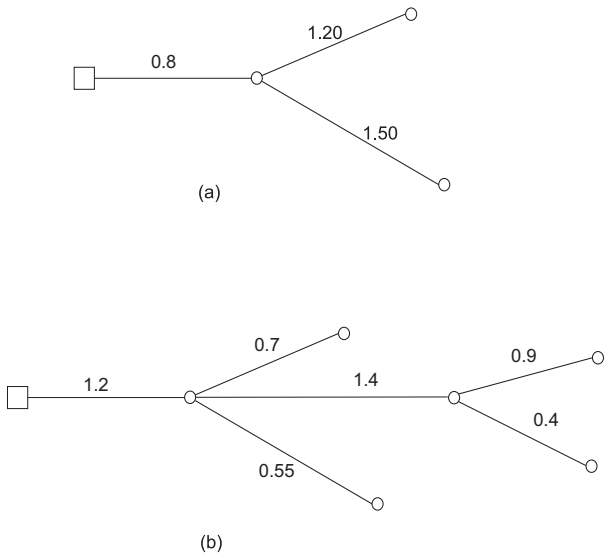

Figure 3.5: The simulated network structures. Lengths are in meters.

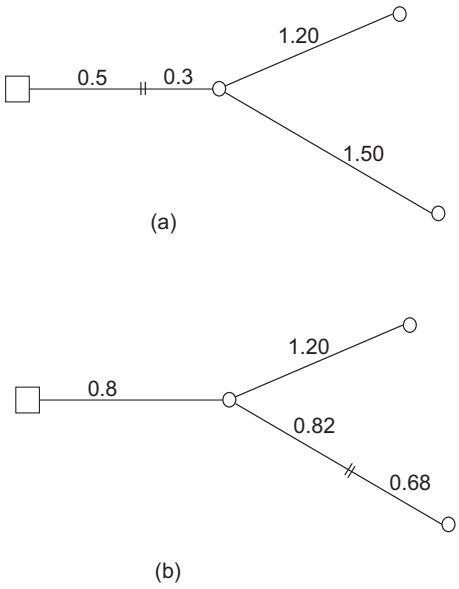

Figure 3.6: The simulated single-Y network, showing two positions of the fault: in front of the testing port (a) and on one of the branches (b). Lengths are in meters.

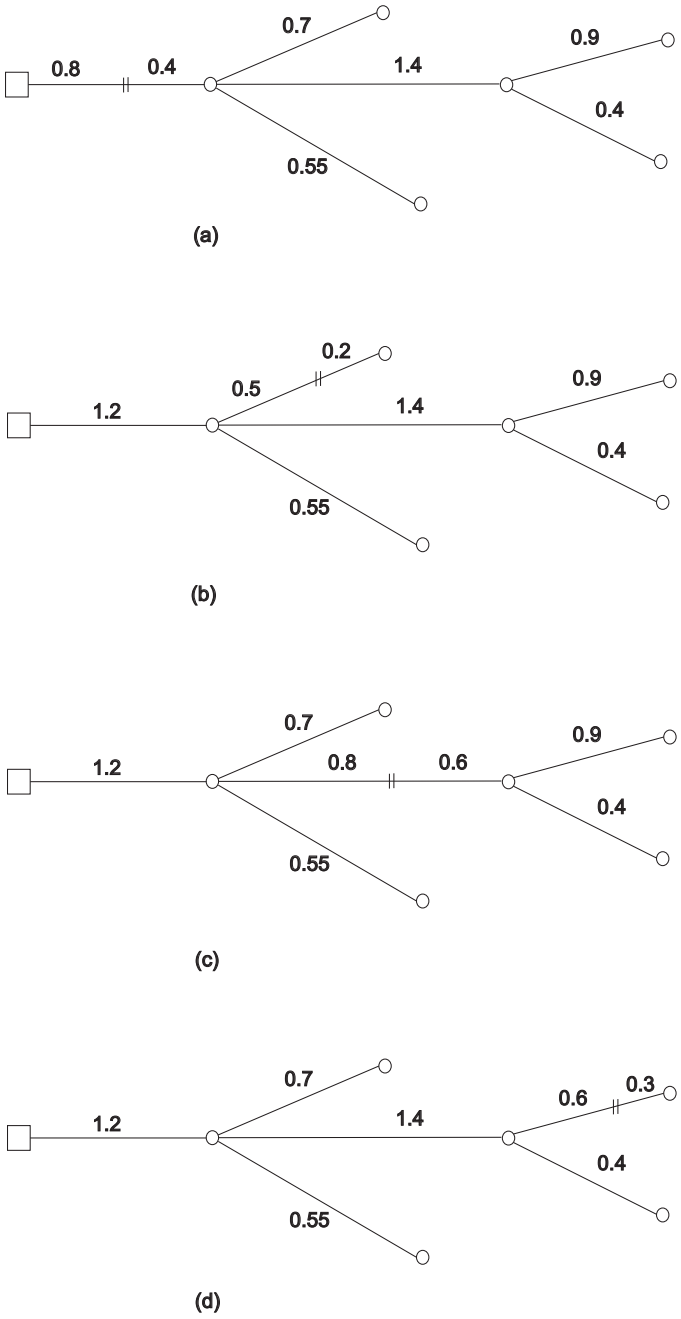

Figure 3.7: The simulated double-Y network, with the four positions of the fault. Lengths are in meters.

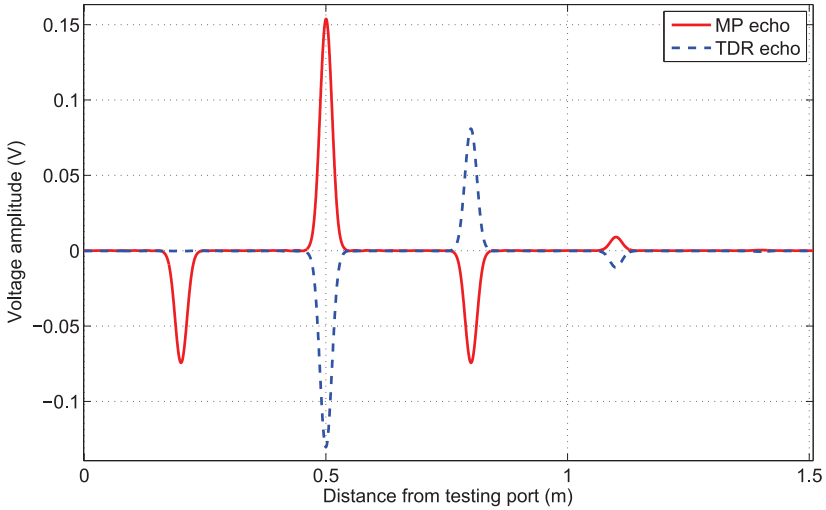

Figure 3.8: The TDR and MP echoes obtained for the case of the network in Fig. 3.6(a) with matched ends and a fault value of $250\ \Omega$.

3.5.2.1 Detection gain

We consider the first position of the fault at a distance of 0.5 m from the testing port, as shown in Fig. 3.6(a). Different impedance values were assigned to the fault, in order to asses the impact of the 'softness' of the fault (expressed by means of its local reflection coefficient) on the gain brought by the MP approach. Also, we consider the case of a short circuit as a hard fault: although hard faults have not been considered in our study, this does not prevent us from examining the results obtained with such kind of faults for the sake of comparison. We considered a total bandwidth of 500MHz, a sampling frequency step of 1 MHz, and a gaussian pulse excitation signal which bandwidth equals 135 MHz at -3 dB. The characteristic impedance of the lines is set to $75\ \Omega$. We remind that we are considering the difference system.

Let us observe the TDR and MP echoes obtained in the case of a fault of $250\ \Omega$; this fault is 'followed' by a transmission line, so the local reflection coefficient at the fault position equals -0.13. Two cases are considered: matched ends and open-circuited ends configurations.

In the case of matched ends, the MP and TDR echoes are shown in Fig. 3.8, where we notice in this simple case that the TDR fault-related peak is the maximum among the peaks (in terms of the absolute value of its amplitude), and also has a normalized amplitude equal to the local reflection coefficient. The few echoes we have due to the presence of the junction and having the network ended with matched impedances gives a detection gain $G = G' = 1.41$ dB, because we have $G'' = 1$.

We define the contrast as being the ratio of the amplitude of the first most significant peak in the echo, to the amplitude of the second most significant peak. Calculating this contrast

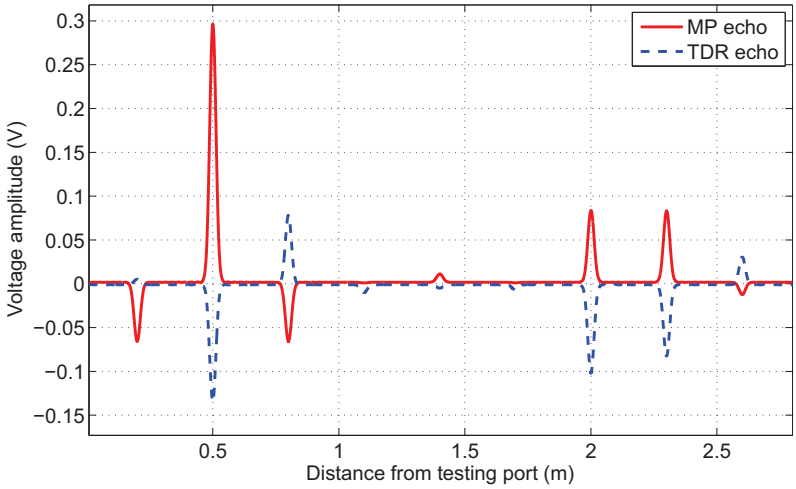

Figure 3.9: The TDR and MP echoes obtained for the case of the network in Fig. 3.6(a) with open circuit ends and a fault value of $250\ \Omega$.

Fault value (Ω)	short	150	250	600
Γ_F	-1	-0.2	-0.13	-0.06

Table 3.1: Local reflection coefficients for different fault values. The faults are represented as parallel impedances and the characteristic impedance of the line is equal to $75\ \Omega$.

for both the TDR and MP cases, we find a value of 1.62 in standard TDR, whilst in the MP case this contrast equals 2.08. Here the MP approach permits to obtain a more distinguishable fault-related echo than TDR.

If we substitute the matched ends with open circuited ends, the echoes obtained are represented in Fig. 3.9. When considering the five most significant peaks in the TDR echo, based on (3.20), we can predict a gain value $G \geq 3.46$ dB, while its actual value is 4.33 dB. Compared to the previous case, we clearly notice how the increase in the number of peaks results in an increase of the detection gain.

This simple comparison shows the benefit of the MP approach regarding complex NUT responses, where the increasing number of peaks turns out to be an advantage for this method over standard reflectometry techniques; a fact that is opposed to common sense as the increasing number of peaks usually presents a nuisance for fault detection and location. As for the contrast, the TDR approach leads to a value of 1.34, to be compared to 2.57 in the MP case. Here also, the contrast is improved with the MP approach.

Back to the general case where different fault values were considered for the NUT illustrated in Fig. 3.6(a), the local reflection coefficients were calculated and their values are shown in Table 3.1. For each fault value, the cases of matched and open-circuited terminations were

Fault value (Ω)	short	150	250	600
Matched	0.4	1.35	1.41	1.57
Open	3.046	4.75	4.33	4.34

Table 3.2: Detection gain values (in dB) in the case of the NUT represented in Fig. 3.6(a) in the case of matched and open-circuit ends.

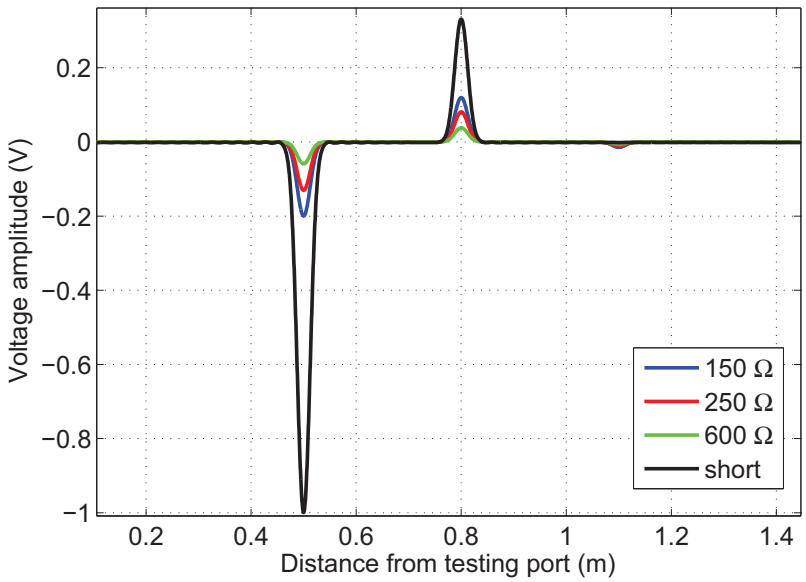

Figure 3.10: The TDR echoes in the case of the NUT illustrated in Fig. 3.6(a) with matched ends, for different fault values.

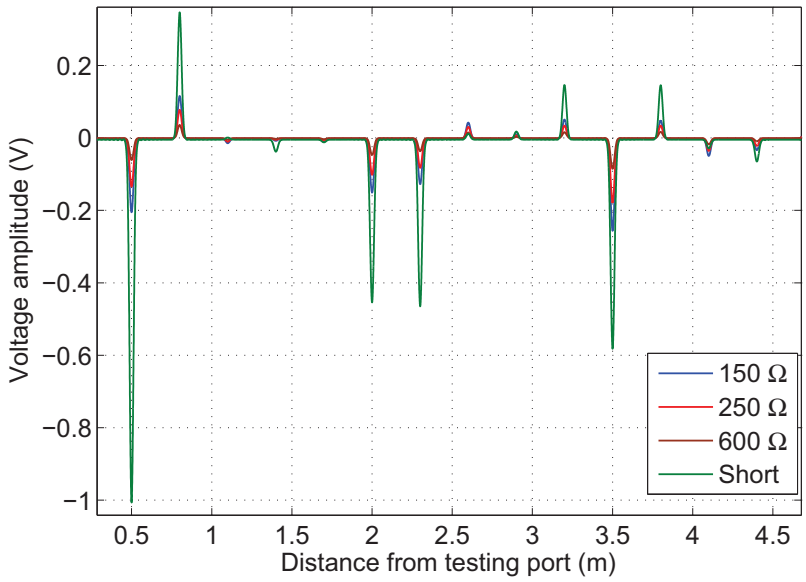

Figure 3.11: The TDR echoes in the case of the NUT illustrated in Fig. 3.6(a) with open-circuited ends, for different fault values.

Fault value (Ω)	short	150	250	600
Matched	0.54	0.02	0.045	0.05
Open	5.75	5.35	5.93	6.94

Table 3.3: Detection gain values (in dB) in the case of the NUT represented in Fig. 3.6(b) in the case of matched and open-circuit ends.

considered, leading to the detection gain values calculated in Table 3.2.

Notice the difference between the two cases: in the case of matched ends, due to the weak number of echoes (shown in Fig. 3.10 for the four fault values), the detection gain does not exceed 1.6 dB, whilst in the case of open ends, the increase in the number of peaks causes the gain to increase more than 4.3 dB. The echoes in this second case for the four fault values can be observed in Fig. 3.11. The fact of having a higher number of echoes results in the increasing of the detection gain.

We now turn our attention to the configuration of Fig. 3.6(b), where the fault is situated at a distance of 1.62 m from the testing port, masked from the latter by a perfect junction. The gain values we obtain in both matched and open-circuited ends are depicted in Table 3.3.

In the case of matched ends, the gain decreased compared to the previous case where the fault was at 0.5 m from the testing port. To understand the reason behind this difference, we choose one of the simulated fault values, 250 Ω, and observe the MP and TDR echoes of the two configurations of Fig. 3.6(a) and (b), where the terminations are matched to the network.

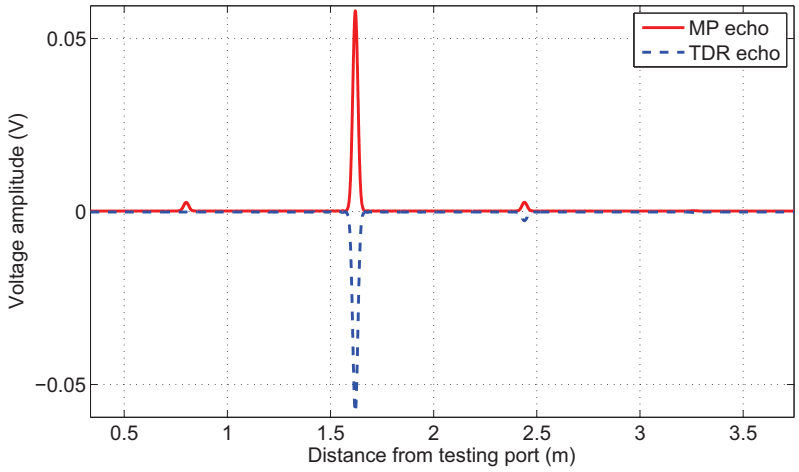

Figure 3.12: The TDR and MP echoes obtained for the case of the network in Fig. 3.6(b) with matched ends and a fault value of $250\ \Omega$.

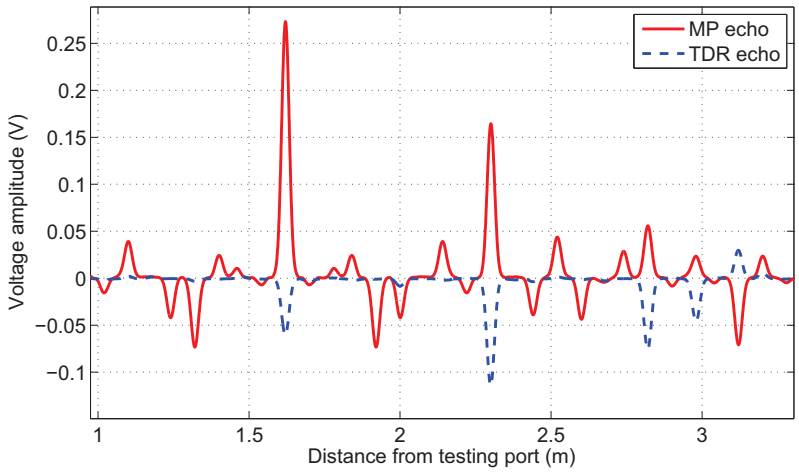

Figure 3.13: The TDR and MP echoes obtained for the case of the network in Fig. 3.6(b) with open circuit ends and a fault value of $250\ \Omega$.

We already plotted the MP and TDR echoes for the first case (Fig. 3.6(a)) in Fig. 3.8. For the second case, these echoes are shown on Fig. 3.12. When the fault was at 1.62 m from the testing port, downstream the junction (relatively to the testing port position), the difference operation allowing to obtain the TDR difference signal eliminates the junction contribution. Thus, one single peak dominates the TDR difference echo, leading to a detection gain almost equal to one, regardless of the softness of the fault. This fact can be predicted based on the mathematical analysis earlier conducted in this chapter.

Whereas when the fault is at 0.5 m from the testing port, which means upstream of the junction, the contribution of the latter in the difference echo is not eliminated. Indeed, the amplitude of the voltage wave in the faulty system arriving at the junction was affected by the presence of the fault, and thus differ from the amplitude of the corresponding wave in the reference system. Thus the subtraction operation will not eliminate the junction contribution, and a secondary peak appearing in the TDR echo will contribute to a higher detection gain compared to the previous case.

Also, when examining Table 3.3 for the case of open ends, we notice that the more the fault is soft, the more the detection gain increases; this is an important advantage for the MP approach in this case, provided that standard techniques may fail whenever the fault becomes softer, and consequently such critical scenarios show the added value of the MP method.

3.5.2.2 ROC Curves

In a Receiver Operating Characteristic curve, also known as a ROC Curve [100], the true positive rate is plotted in terms of the false positive rate for different values of a parameter. Each point on the ROC curve represents a pair corresponding to a particular decision threshold, for a given SNR. In practical cases, the choice of this decision threshold is set as a compromise between the ability to detect the presence of the maximum peak and the need to provide for a robust immunity with respect to noise signals. The ROC curve can be useful to determine this detection threshold for a given SNR. Let us consider the illustrating example of Fig. 3.6(a), with open circuited ends, and a fault value of $250\ \Omega$.

When examining the corresponding ROC curve in Fig. 3.14 for an SNR value of 0 dB, we notice that it can be divided into three regions: the first one when the TP and FP probabilities are both close to zero corresponding to a high detection threshold, the second one when both probabilities are close to 1, which means the detection threshold is set very low. The third region is the one between these two regions; it is the one we are interested in for an eventual analysis of the curve. The advantages of the MP method over standard TDR are clear in this example, where, for the same FP probability, the MP method ensures a higher true positive probability, as can be observed. For a value of FP probability equal to 0.2 for example, we obtain a TP probability in the TDR case equal to 0.56, whilst in the MP case it reaches 0.79, which means a difference (TP gain) of 0.23.

To determine the optimal detection threshold, we reconsider the same ROC curve and rep-

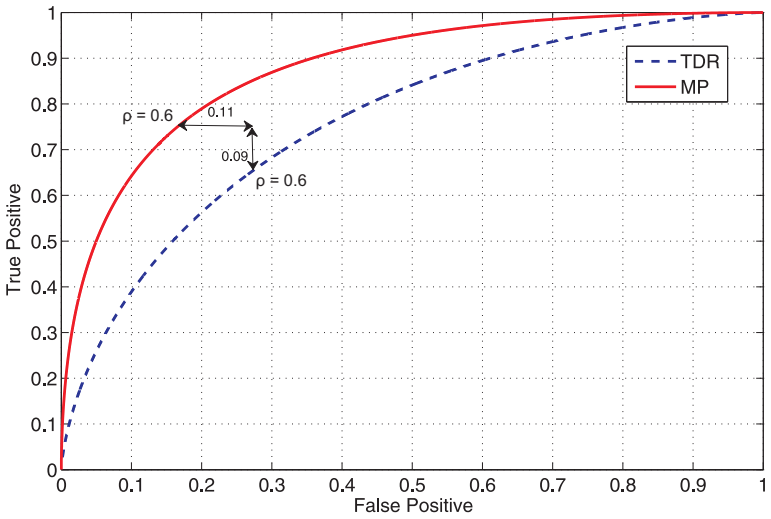

Figure 3.14: The ROC Curve corresponding to the case of the network in Fig. 3.6(a) with open circuit ends and a fault value of 250 Ω. The SNR in the TDR case is set to 0 dB. The studied parameter is the detection threshold.

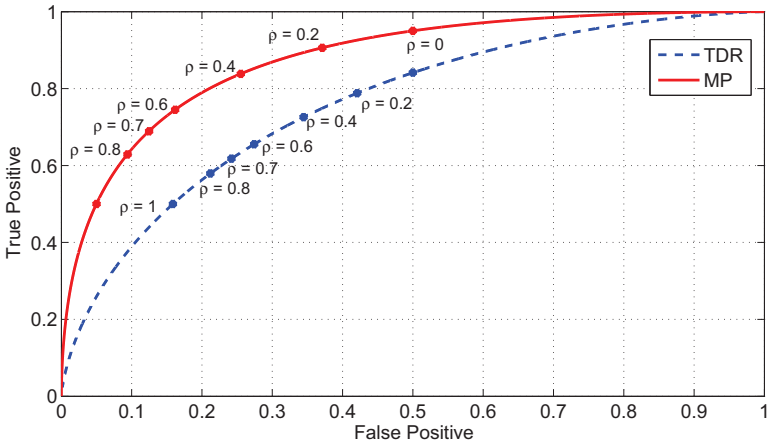

Figure 3.15: The ROC Curve corresponding to the case of the network in Fig. 3.6(a) with open circuit ends and a fault value of 250 Ω. The SNR in the TDR case is set to 0 dB. The detection thresholds for each pair of TP and FP probabilities are marked on the figure.

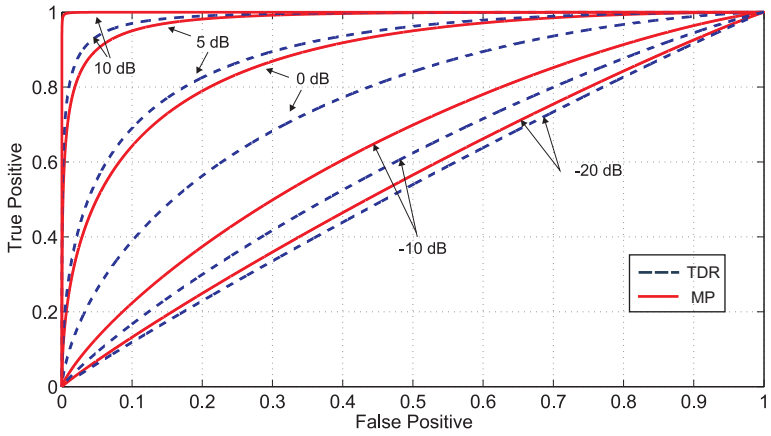

Figure 3.16: The ROC Curve corresponding to the case of the network in Fig. 3.6(a) with open circuit ends and a fault value of $250\ \Omega$. The SNR in the TDR case is set to 0 dB. Different values of the SNR are considered when plotting the curves.

resent it in Fig. 3.15, with different values of this parameter. Notice that for the values of the detection threshold set between 60% and 80% of the maximal peak value, the TP probabilities range between 0.6 and 0.8, with FP probabilities not exceeding 0.2. For a value of the threshold ρ equal to 60% the FP gain is about 0.11 and the TP gain is almost 0.09, whilst for $\rho = 70\%$, the FP gain reaches 0.12 and the TP gain 0.07. Thus, one can choose a detection threshold ranging between these values. In the following study, we choose the value $\rho = 0.6$.

The ROC Curves corresponding to several values of the SNR, for both TDR and MP cases, are plotted in Fig. 3.16. Notice how, for an increasing SNR, the curves converge towards a step function, with a faster convergence of the MP curve compared to the TDR one. Notice also that while the SNR increases, the gap between the TDR and MP curves increase, to reach its highest values for the SNRs 0 and 5 dB, which reflects the important advantage of the MP approach in such cases.

To compare this case, denoted as MP1, to the one where the fault is embedded in the NUT, we consider the example of Fig. 3.6(b), where the fault value is considered to be of the same value ($250\ \Omega$), but hidden from the testing port by a junction at a distance of 0.8 m. The NUT has open-circuited ends. This case is referred to as MP2. The ROC curves corresponding to both cases MP1 and MP2, for a SNR of 0 dB have been plotted in Fig. 3.17. The improvement in the detection gain in the case MP2 relatively to MP1 reflects on the ROC curves, where we observe that the MP performance is boosted when the fault is embedded in the system: this leads to an increasing TP and FP probability gains when compared to MP1 and thus a faster convergence towards the step function for the MP curve.

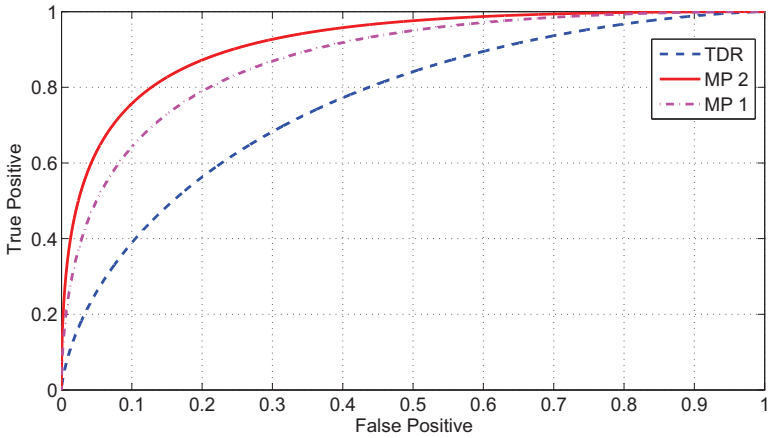

Figure 3.17: The ROC Curves corresponding to the case of the network in Fig. 3.6(a) (MP1) and Fig. 3.6(b) (MP2) with open circuit ends and a fault value of $250\ \Omega$. The SNR in the TDR case is set to 0 dB.

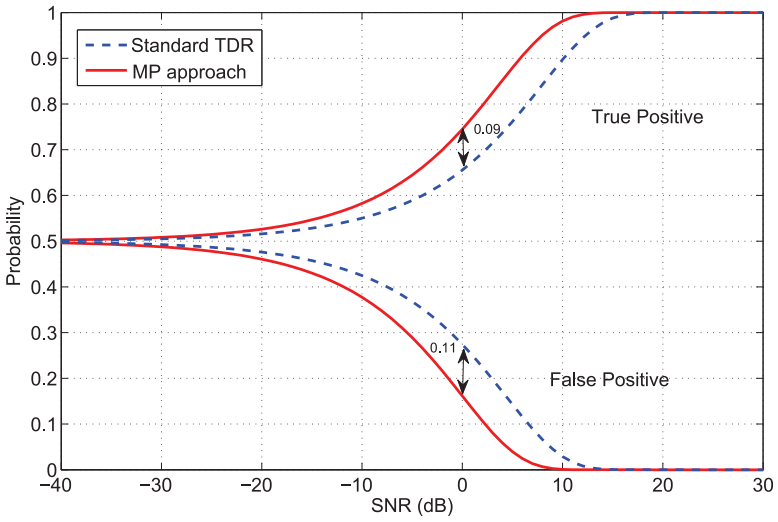

Figure 3.18: The detection probabilities corresponding to the case Fig. 3.6(a) with open circuit ends and a fault value of $250\ \Omega$. The detection threshold is set to 0.6 times the maximum peak in each case.

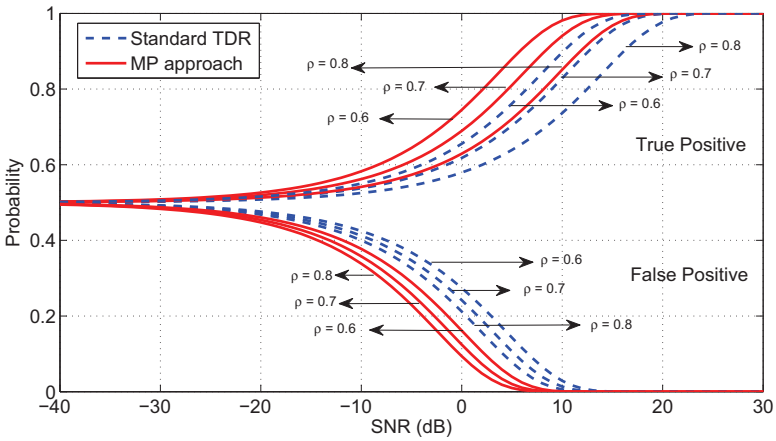

Figure 3.19: The detection probabilities corresponding to the case Fig. 3.6(a) with open circuit ends and a fault value of $250\ \Omega$. Three values of the detection threshold were considered: 0.6, 0.7 and 0.8.

3.5.2.3 Detection probabilities

Fig. 3.18 shows the detection probabilities in terms of the SNR of the TDR case, for the same previous example, and for both methods. The detection threshold was chosen to be 60% of the maximal peak, based on the discussion in the previous section. Notice how the MP approach presents more advantages over standard TDR, given that for a certain SNR value, the MP method ensures a lower FP probability and higher TP probability compared to TDR.

Examining the curves allows to observe a SNR gain R which equals 4.3 dB, whilst considering the first 5 peaks enables us to set a lower bound of R equal to 3.46 dB. These results are perfectly in line with the earlier obtained results for the detection gain, and the formula obtained in (3.42). For an SNR of 0 dB, in standard TDR, the FP probability is 0.27 and the TP probability is 0.66, whilst in the MP case these two probabilities are respectively 0.16 and 0.75, which represent a FP probability gain of 0.11 and a TP probability gain of 0.09. Note that the values of the probabilities and the probability gains in this case can also be observed on the ROC curve illustrated in Fig. 3.14, as indicated on the latter. Globally, for a SNR inferior to -20 dB, the MP approach does not present major advantages over TDR and cannot lead to a significant performance improvement. But when the SNR starts to increase, till the value of about 5 dB in the FP case and 15 dB in the TP case, we notice the probability gain offered by the MP approach, reaching as already indicated values of 0.09 for the TP gain at 10 dB, and 0.11 for the FP gain at 0 dB.

To observe the evolution of the curves in terms of the detection threshold values, we considered some examples represented in Fig. 3.19. Here three values of the threshold were chosen, based on the analysis of the ROC Curve in Section 3.5.2.2, where these values provided a fair compromise between a relatively high TP probability and a low FP probability.

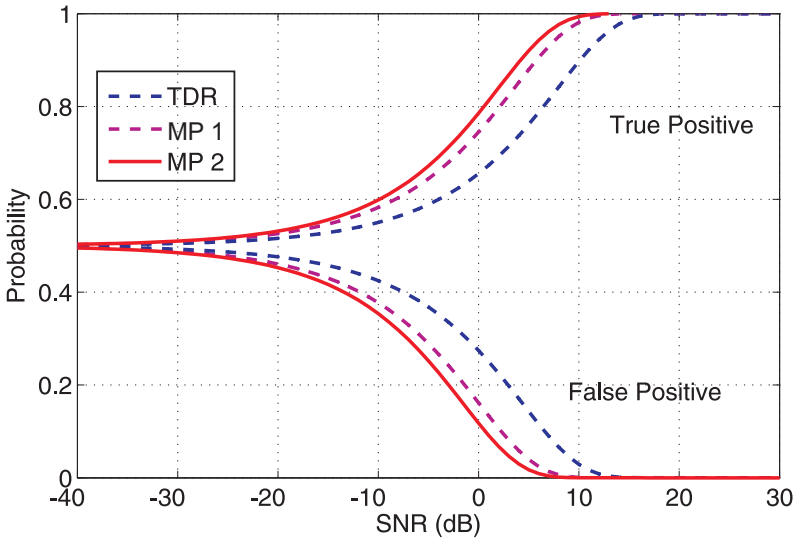

Figure 3.20: The detection probabilities corresponding to the case Fig. 3.6(a) (MP1) and Fig. 3.6(b) (MP2) with open circuit ends and a fault value of $250\ \Omega$. The detection threshold is set to 0.7 times the maximum peak in each case.

Normally when the threshold increases, a certain TP probability value is obtained with a higher value of the SNR, while it is the opposite case for the FP curves, a fact that is shown when examining the curves. Also, the probability gap between two TP curves for the same method (MP or TDR) is bigger than the gap between the FP curves of the same method. This implies that changing the threshold would result in a better improvement in the TP gain than the FP one, for both TDR and MP.

If we compare this case to the case where the fault is hidden from the testing port by a junction (Fig. 3.6(b)), and we re-plot the curves corresponding to both cases in Fig. 3.20, we notice, as can be expected, that the improvement in the detection gain when the fault is embedded in the system leads to an improvement in the TP and FP probabilities: a SNR gap of about 1.6 dB is observed between the two MP curves, which aligns with the SNR gain difference between the two cases according to (3.42), where the values of G are found in Tables 3.2 and 3.3 for the two studied cases.

3.5.3 Double-Y network simulation

We turn our attention towards a more complex network, which structure is illustrated in Fig. 3.5(b). Four positions of the fault will be studied, as earlier illustrated in Fig. 3.21, for the already considered values in the single Y-network simulation, and for both matched and open-circuited ends.

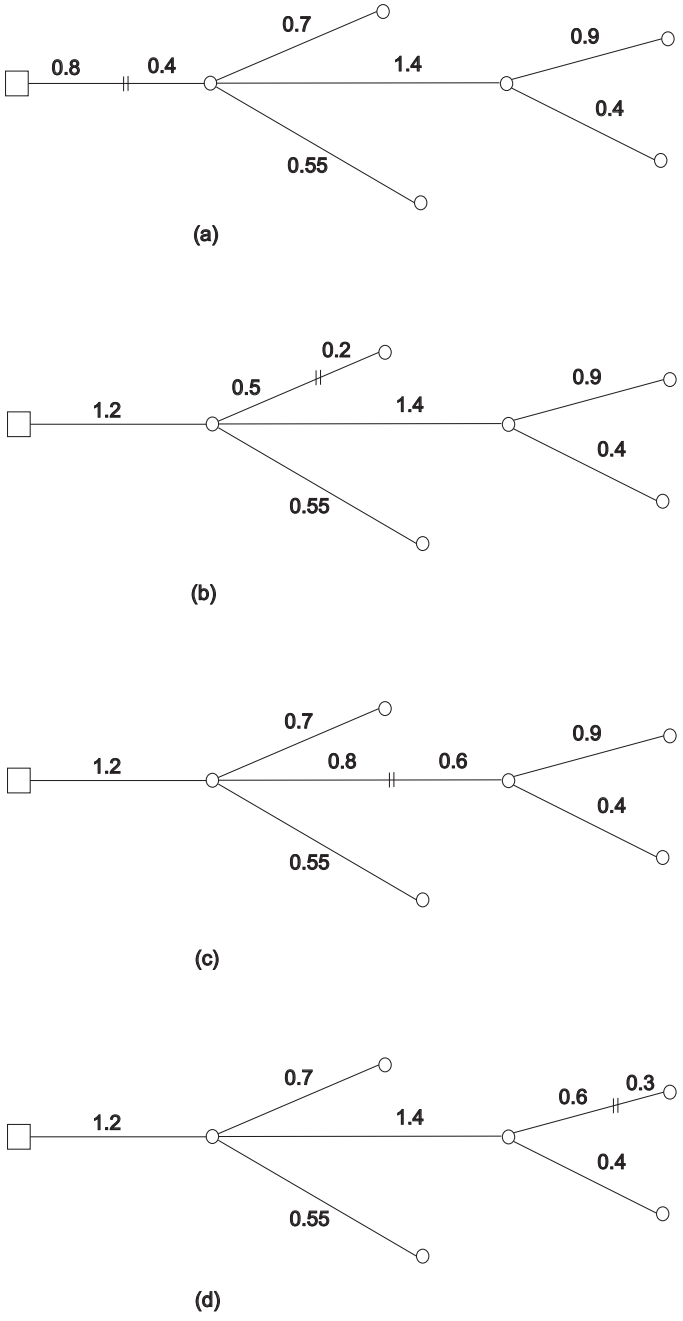

Figure 3.21: The simulated double-Y network, with the four positions of the fault.

Fault value (Ω)	short	150	250	600
Matched	0.98	2.76	2.88	3.16
Open	3	6.69	7.09	7.44

Table 3.4: Detection gain values (in dB) in the case of the NUT represented in Fig. 3.21(a) in the case of matched and open-circuit ends.

Fault value (Ω)	short	150	250	600
Matched	1.62	0.5	0.63	0.46
Open	11.26	12.34	12.33	11.26

Table 3.5: Detection gain values (in dB) in the case of the NUT represented in Fig. 3.21(b) in the case of matched and open-circuit ends.

3.5.3.1 Detection gain

As in the previous case, we considered a total bandwidth of 500MHz, a sampling frequency step of 1 MHz, and a gaussian pulse excitation signal which bandwidth equals 135 MHz at -3 dB. The first case of a fault directly 'seen' by the testing port is shown in Fig. 3.21(a). The values of the detection gain are found in Table 3.4. The three other cases of a fault embedded in the network and illustrated in Fig. 3.21(b), (c), and (d) are observed in Tables 3.5, 3.6 and 3.7 respectively. Once more, in the four cases, the open-circuited ends yield a higher detection gain compared to the matched ends case, due to the decreasing number of peaks in the latter. This can be verified by considering an example where the fault value is equal to $250\ \Omega$ for the four fault positions, and for both matched ends (Fig. 3.22) and open-circuited ends (Fig. 3.23). In both figures, the four configurations represented in Fig. 3.21(a), (b), (c) and (d) retain the same letter designation, i.e., the case of Fig. 3.21(b) is denoted as the case (b) on both Fig. 3.22 and Fig. 3.23.

We also notice that in the open end cases, the gain reaches important values, beyond 11 dB for all the soft fault cases, with an increasing value as soon as the fault becomes softer. Looking at the numeric values in Table 3.6, we notice how the gain increases from 12.87 dB in the case of a fault value equal to $150\ \Omega$ to 16.24 dB when the fault's value is equal to $600\ \Omega$, which shows

Fault value (Ω)	short	150	250	600
Matched	1.62	1.58	1.89	1.93
Open	8.3	12.87	13.9	16.24

Table 3.6: Detection gain values (in dB) in the case of the NUT represented in Fig. 3.21(c) in the case of matched and open-circuit ends.

Fault value (Ω)	short	150	250	600
Matched	1.75	0.61	0.61	0.64
Open	8.79	11.62	12.8	14.99

Table 3.7: Detection gain values (in dB) in the case of the NUT represented in Fig. 3.21(d) in the case of matched and open-circuit ends.

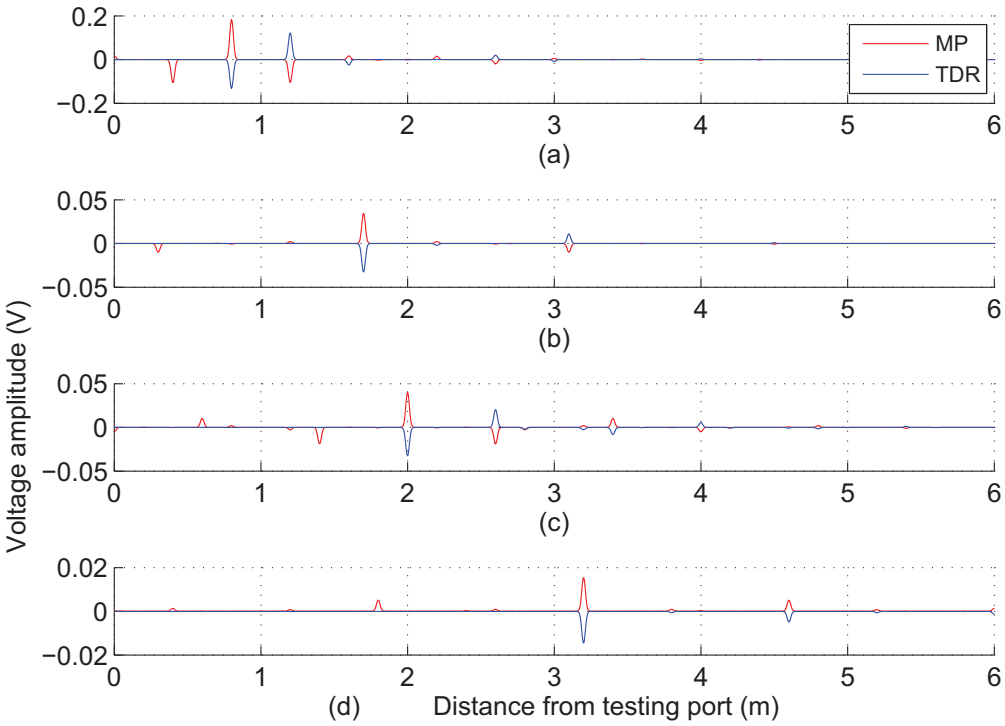

Figure 3.22: The TDR and MP echoes of the configurations represented in Fig. 3.21, with matched ends and a fault value equal to 250 Ω. The four configurations represented in Fig. 3.21(a), (b), (c) and (d) retain the same letter designation, i.e., the case of Fig. 3.21(b) is denoted here as the case (b).

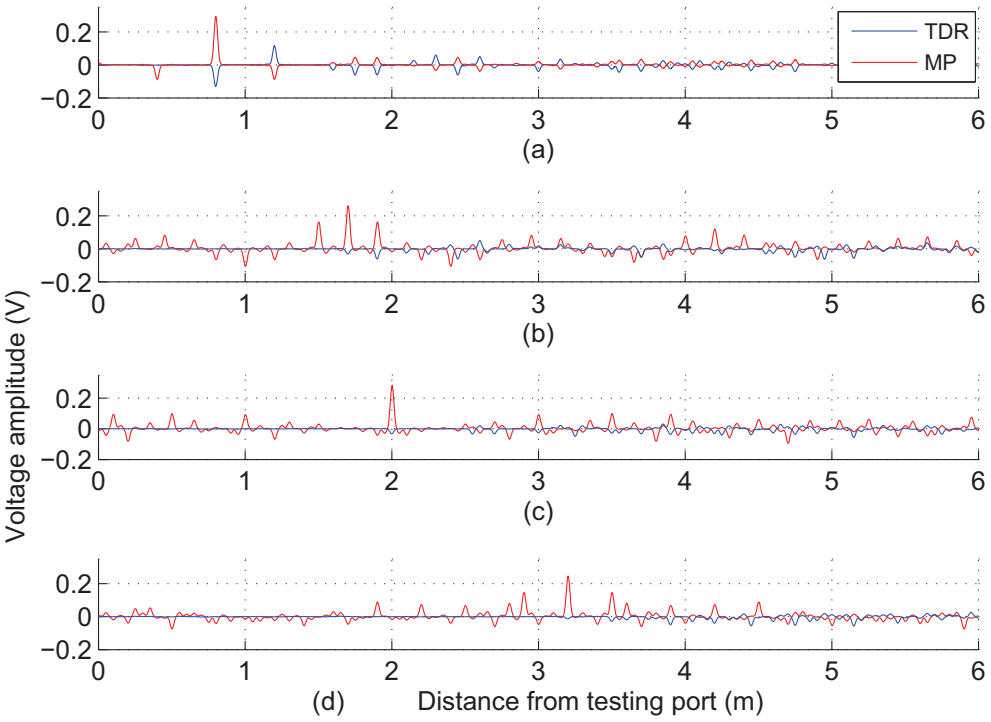

Figure 3.23: The TDR and MP echoes of the configurations represented in Fig. 3.21, with open-circuited ends and a fault value equal to 250 Ω. The four configurations represented in Fig. 3.21(a), (b), (c) and (d) retain the same letter designation, i.e., the case of Fig. 3.21(b) is denoted here as the case (b).

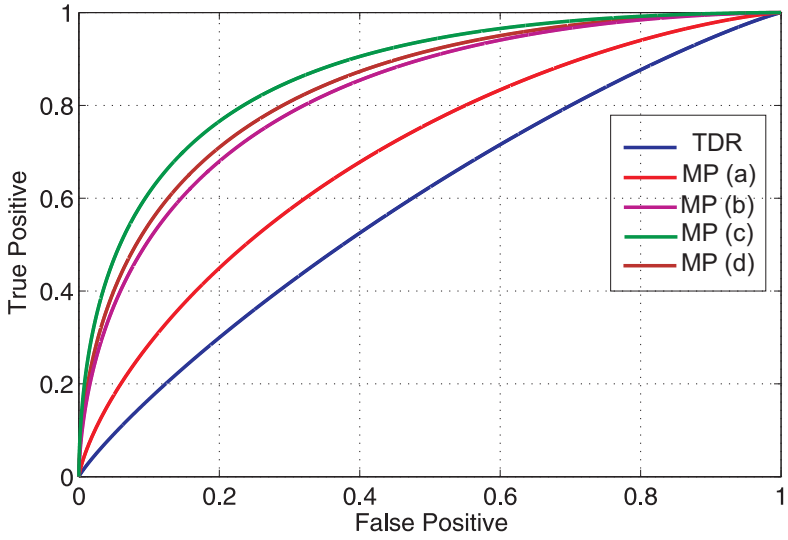

Figure 3.24: The ROC Curves of the four configurations represented in Fig. 3.21, with open-circuited ends and a fault value of $250\ \Omega$. The SNR was set to -10 dB. Note that the configurations represented in Fig. 3.21(a), (b), (c) and (d) retain the same letter designation, i.e., the case of Fig. 3.21(b) is denoted here as the case (b).

once more the important advantage of the MP approach over standard TDR when it comes to detecting soft faults in complex networks.

Looking closer at the detection gain values, if we examine the ones concerning the hard fault in Tables 3.5 and 3.6 (matched ends cases), we notice they are the same, and the reason is clear if we look back at the corresponding schemes in Fig. 3.21(b) and 3.21(c), and recall from the second chapter that, in the faulty system, a hard fault causes the contribution of the elements downstream of it to disappear. Consequently, looking back at the studied scheme with matched ends, the position of a hard fault on one of the three branches of the first junction is equivalent from the detection gain perspective: the response of the reference system is the same, and in the faulty system only the first junction and the fault contribute in the multiple reflections. However, when we have a soft fault, the reflections from the second junction interact with the fault, increasing the gain values, as can be observed on the same Tables (matched ends cases).

3.5.3.2 ROC Curves

We proceed by considering the ROC curves of the earlier considered cases, where the fault's value is $250\ \Omega$ and the terminations of the NUT are open-circuited. Fig. 3.24 shows the curves for an SNR equal to -10 dB, where we notice how the detection gain reflects on the performance of the MP relatively to the TDR one. The lowest gain among the four cases is observed for the

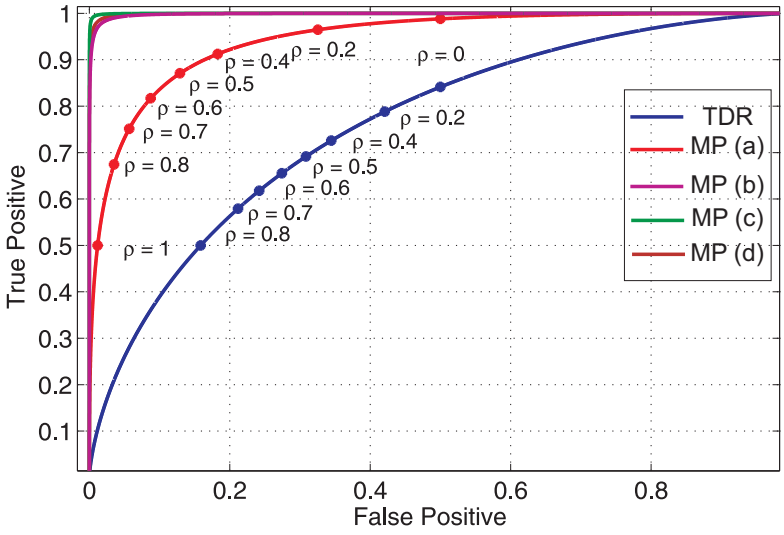

Figure 3.25: The ROC Curves of the four configurations represented in Fig. 3.21, with open-circuited ends and a fault value of $250\ \Omega$. The SNR was set to 0 dB. Note that the configurations represented in Fig. 3.21(a), (b), (c) and (d) retain the same letter designation, i.e., the case of Fig. 3.21(b) is denoted here as the case (b).

case of Fig. 3.21(a), where the fault is directly visible by the testing port, and consequently the corresponding ROC curve denoted as MP(a) is the closest to the TDR one among the other MP curves. Note however that the detection gain is notable in this case, and equal to 7.09 dB (see Table 3.4). The highest detection gain is observed for the curve with the best performance, i.e., the one corresponding to the configuration (c) (Fig. 3.21(c)). For example, for a FP probability equal to 0.2, the difference between the TP probabilities of the cases MP(a) and MP(c) equals 0.32, whilst the difference between the MP(c) and the TDR reaches a value of 0.47.

Rising the SNR to 0 dB gives the curves represented in Fig. 3.25, where we notice the faster convergence of the curves towards the step function compared to the previous case. Given that the TDR performance has improved compared to the last case, the TP gain between the last curves and the TDR one when the FP probability is 0.2 now equals 0.43.

In order to exploit these curves to determine an optimal detection threshold, as we did for the case of the Y-network, we mark several values on the curves corresponding to the TDR and the MP(a) cases. Examining these values permit us to choose a threshold equal to 60% of the maximal peak, as a fair compromise between a high TP probability and a low FP probability, for both the TDR and MP methods. Having set this threshold we now examine the detection probabilities for the four illustrated cases.

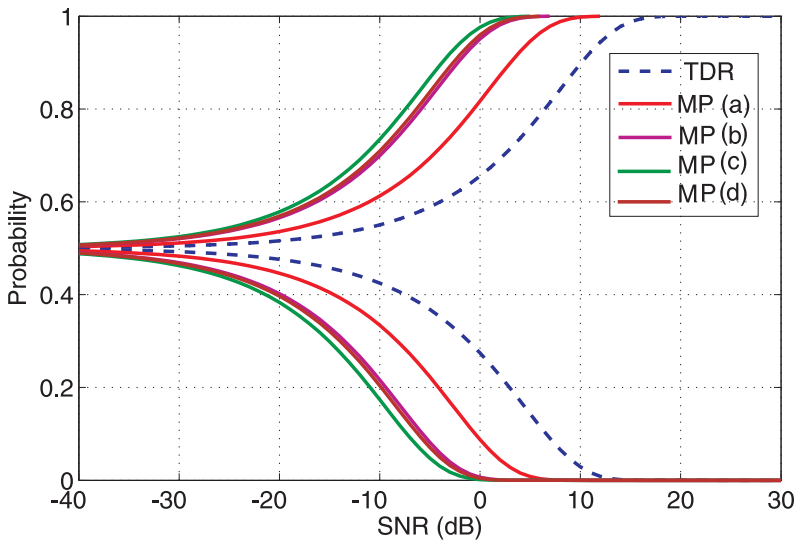

Figure 3.26: The ROC Curves of the four configurations represented in Fig. 3.21, with open-circuited ends and a fault value of $250\ \Omega$. The threshold value is $\rho = 0.6$. Note that the configurations represented in Fig. 3.21(a), (b), (c) and (d) retain the same letter designation, i.e., the case of Fig. 3.21(b) is denoted here as the case (b).

3.5.3.3 Detection probabilities

We reconsider the four configurations of Fig. 3.21, with a fault of $250\ \Omega$, and open-circuited ends. The SNR gains are observed in the gaps between the different curves, as already seen in the Y-network example, with the highest value reached when the fault is embedded in the system according to the configuration MP(c). In this example we already saw that the detection gain in Table 3.6 equals 13.9 dB, leading to a SNR gain value of 13.89 according to (3.42), as shown in Fig. 3.26.

3.5.4 Conclusion

In this section, we have simulated two networks, a single and double-Y structures, and validated the results obtained in the mathematical analysis section. We showed the important benefits of the MP over existing standard TDR methods when dealing with soft faults and complex networks, and quantified these benefits in terms of the detection gain and probabilities. The results we obtained show that MP is most beneficial in critical scenarios where the detection probability of a fault decreases, so that it becomes more likely to be mistaken in the fault detection using TDR techniques rather than MP.

3.6 Experimental validation

3.6.1 Introduction

In the previous section, we validated the mathematical analysis through simulations, aiming to asses the impact of the fault's position and the network complexity on the performance of the MP approach. A simplified fault model was thus considered, that is ideal and non-dispersive, which is not generally the case in practical cases when dealing with cable faults. That is why we have decided to conduct an experimental study, to be able first to characterize and observe some soft faults in order to propose a simplified model for them, and second to observe some practical fault detection cases with no simplifying assumptions made.

3.6.2 Experimental setup

The experimental measurements we conducted can be divided into two major parts. The first one is the fault characterization part, aiming to observe a real soft fault response and try to propose a simplified model of the latter taking into account its dispersive nature. The second part is the test of two networks: a single and double-Y configurations.

The echo-impulse responses of the different network configurations we used were measured by means of a Vector Network Analyzer (VNA) connected to the testing port, as the example shown in Fig. 3.27. The VNA we used is a Rohde & Schwarz ZVB-8 network analyzer, with

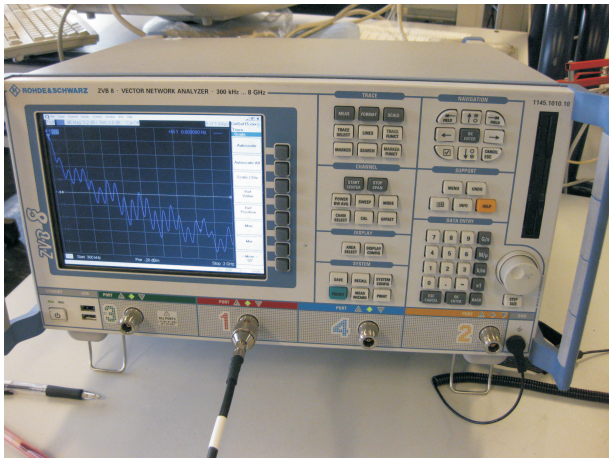

Figure 3.27: The Vector Network Analyzer (VNA) we used in our experimentations. It is a Rohde & Schwarz ZVB-8 network analyzer.

a frequency range from 300 kHz to 8 GHz, and four ports. The intermediate-frequency filter bandwidth was set to 100 kHz. The input power was set to a 0 dBm harmonic excitation signal: this ensured a strong rejection of noise, yielding very clean results that can be regarded as practically unaffected by any noise source.

Using the VNA implies accessing the Fourier-spectrum of the impulse response; for this reason, the experimental results were post-processed by applying an inverse Fourier transform. Starting with these data, all of the quantities we have introduced in the mathematical analysis section can be retrieved by means of straightforward post-processing techniques. In particular, the response of a NUT to any testing signal can be obtained by convolving the desired input signal with the experimentally measured impulse response of the NUT. This approach is clearly sound as the system under test is linear and time-invariant. Its main advantage is the simplicity with which we can obtain the responses of the NUTs to any signal, without needing a specific arbitrary waveform generator. Moreover, as we are interested in studying the SNR of the output signals, it is easier to sum a noise to the output signal than to actually apply it to the NUT. Clearly, this approach does not hinder the validity of our conclusions.

Here it is important to point out that the fact of having calibrated the VNA or not has strictly no impact on the results, as the goal here is to measure the echo-impulse response seen through the testing port. This is not affected by calibration, which aims to compensate for the presence of a cable or any device between the measuring port (on the VNA side) and the wished testing port, on the NUT side. We took our measurements directly on the testing port, so there is no reason for calibrating. And there also is no reason to connect any other device (that would have required calibration) between the VNA and the NUT.

The faults were created using 30-cm sections of semi-rigid coaxial cables terminated by two SMA connectors. In order to try to minimize the effect of the interconnections between the cable and the VNA and make the fault response more visible, the difference system was considered.

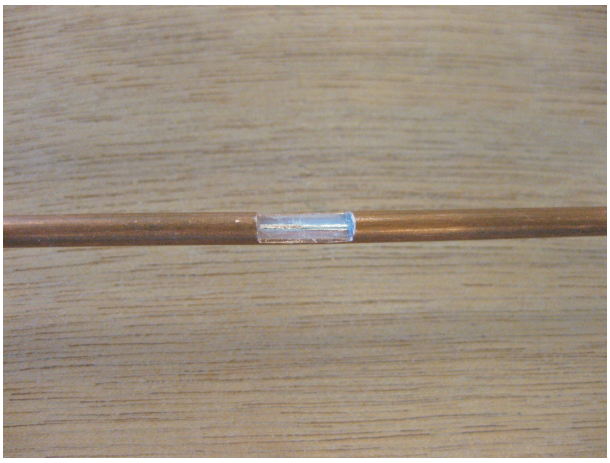

(a)

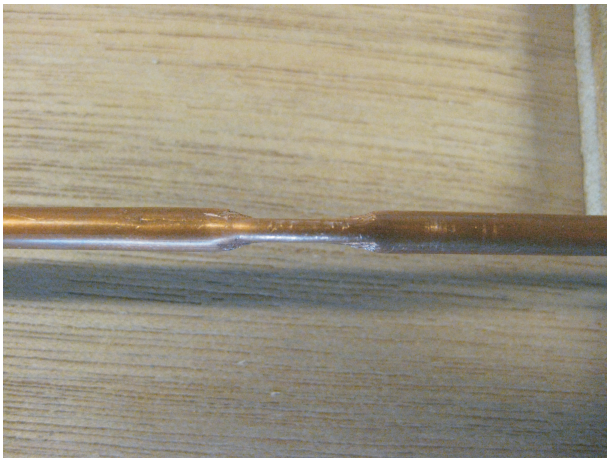

(b)

Figure 3.28: The cable fault types studied in section 3.6.3: (a) broken cable shield; (b) variation in the cable cross section.

Thus, the need for a baseline measurement was satisfied by considering an unaltered sample as the reference one, and measuring the impulse response of the NUT using this reference sample, in order to be subtracted from the response of the faulty samples later.

As the measurements were carried out in the frequency domain, post-processing using Matlab was applied to the obtained results, in order to extract the time-domain responses, using the inverse Fourier transform.

3.6.3 Fault characterization

The aim of this section is to observe a real soft fault response, and propose a simplified mathematical model of the fault taking into account the dispersive nature of the latter. We chose two soft faults types: broken shield and variation in the cable cross section, shown in Fig. 3.28, as they represent typical defects in the cable [51], and observed the evolution of the fault's

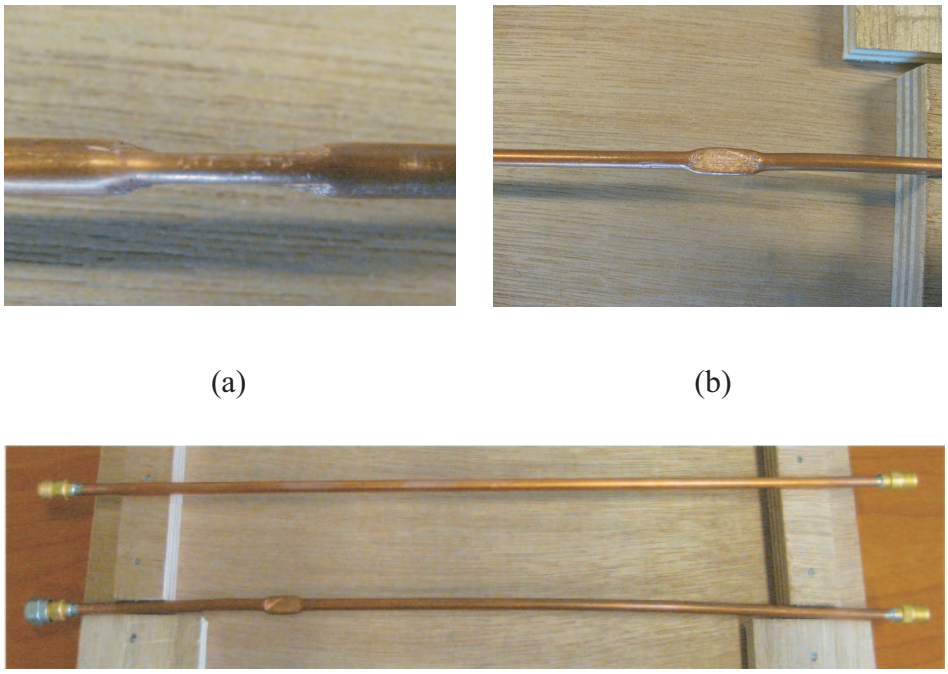

(a) (b)

(c)

Figure 3.29: The soft fault considered in the experimental validations, as obtained by crushing a 1-cm long portion of a semi-rigid cable. The three pictures present: (a) a side view of the fault, with the cable reduced to a 2 mm thickness; (b) a front view of the fault; (c) the two samples used for the measurements, i.e., the reference semi-rigid cable without fault and the one presenting the fault. They share the same dimensions and features.

response for several cases, for example several crushing thicknesses.

3.6.3.1 Variation in the cable cross section

In this section we are interested in the faults resulting from the variation of the cross section of the cable, practically performed by crushing the cable on a few millimeters.

- Fault response measurement

An example of the studied fault is illustrated in Fig. 4.40. Two cases were studied, according to the thickness of the damaged portion: we considered the case of a 2 and 2.8 mm thickness, to be compared to the initial section of the cable which is 3.4 mm. To obtain the echo-impulse responses illustrated in Fig. 3.30, we first measured the response of the damaged 30-cm semi-rigid cable, subtracted it from the baseline response, and then considered the fault signature, as illustrated in the same figure. These responses prove the weakly-reflective and dispersive nature of the fault. Indeed, this type of faults can be assimilated to a local variation in the cross section of a two-wire line, yielding a local variation in the per unit length parameters of the line.

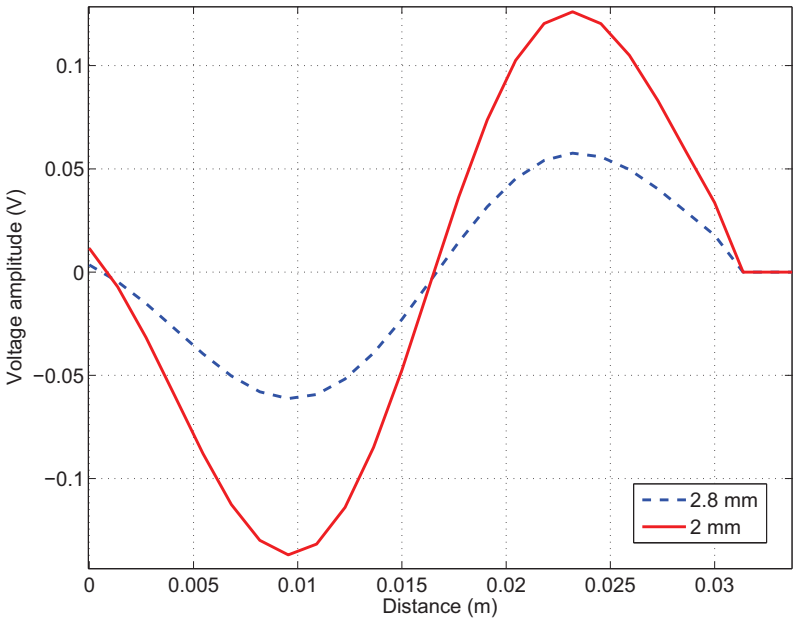

Figure 3.30: The echo-impulse response of the faults caused by crushing the cable as represented in Fig. 4.40.

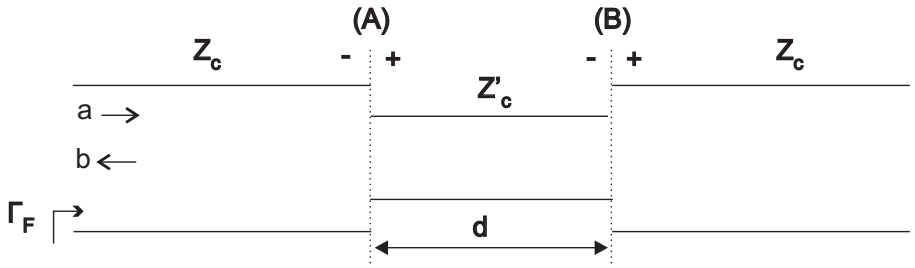

Figure 3.31: A local variation in the characteristic impedance of a transmission line, between the two orthogonal planes (A) and (B). Z_c is the characteristic impedance of the line, and Z_c' is the one corresponding to the damaged portion.

Based on this remark, we propose to calculate the response of a fault modeled as a local variation of the characteristic impedance of the line, as represented in Fig. 3.31.

- Fault model

We consider the scheme illustrated in Fig. 3.31 of a crushed transmission line, modeled as a local variation in the cable cross section. The local reflection coefficients at the interfaces (A) and (B) are respectively denoted as Γ_0 and $-\Gamma_0$. We aim at calculating the global reflection coefficient as seen at the discontinuity position, denoted as Γ_F, i.e., the ratio of the total reflected voltage wave, denoted as b, to the incident one referred to as a. We have

$$\Gamma_F = \frac{b}{a}. \tag{3.55}$$

The local reflection coefficient Γ_0 at the interface (A) can be written as

$$\Gamma_0^- = \frac{Z_c' - Z_c}{Z_c' + Z_c} \tag{3.56}$$

When the wave a arrives at (A), the part $\Gamma_0 a$ will reflect back, and the other part $(1+\Gamma_0)a$ is transmitted.

This transmitted wave arrives at the interface (B) and, likewise, a part is reflected back: this part traces the same path back to (A), and then, when arriving at (A) again, is also reflected back and a part is transmitted. We are interested in the transmitted part, which is now equal to $-a\Gamma_0(1+\Gamma_0)^2 e^{-j2Kd}$, having K the propagation constant.

The reflection process continues in the same way; here we consider the first two transmitted waves through (A) and neglect the other reflections, given that they are in the range of Γ_0^2, which we assume to be negligible given that the fault is soft.

Based on this hypothesis, the reflected wave b is the sum of the two reflected waves as follows

$$b = a\Gamma_0 - a\Gamma_0(1+\Gamma_0)^2 e^{-j2Kd} \tag{3.57}$$

Using (3.57) and (3.55)

$$\Gamma_F = \Gamma_0 - \Gamma_0(1+\Gamma_0)^2 e^{-j2Kd} \tag{3.58}$$

If we develop this expression, taking into account that the terms in the range of Γ_0^2 or higher are negligible, and considering that, for small values of d, we can write

$$e^{-j2Kd} \simeq 1 - j2Kd \tag{3.59}$$

we obtain

$$\Gamma_F = j2Kd\Gamma_0 = j2\omega d\Gamma_0/c \tag{3.60}$$

where c is the wave speed in the cable.

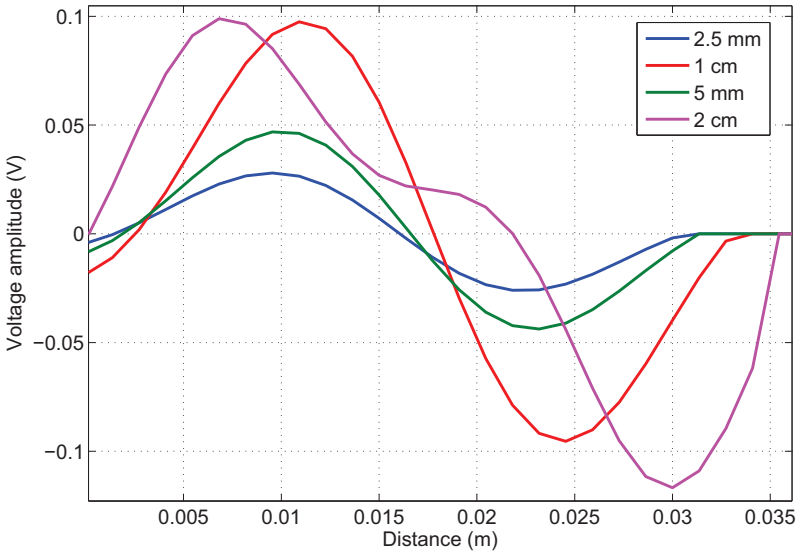

Figure 3.32: The echo-impulse response of the faults caused by removing the cable's shield as represented in Fig. 3.28(a).

This result explains the frequency-dependant behavior of the fault we earlier observed in Fig. 3.30. This also implies that we can have an approximated value of the impedance change if we consider the temporal response (Fig. 3.30), where we can deduce Γ_0 and consequently Z'_c.

For example, when we reduce the cable thickness to 2.8 mm, the local reflection coefficient Γ_0 is equal to -0.0613, and thus the value of Z'_c in this case can be deduced from the following formula

$$Z'_c = Z_c \left(\frac{1 + \Gamma_0}{1 - \Gamma_0} \right) \tag{3.61}$$

Knowing that $Z_c = 50\ \Omega$, the impedance Z'_c in this case is equal to $44.22\ \Omega$. The same calculus applies for the second case where the thickness is reduced to 2 mm; here Z'_c is about $38\ \Omega$.

3.6.3.2 Broken shield

We considered several values of the fault, shown in Fig. 3.28(b). The shield was broken by removing the external insulation and the shield of the cable at several distances, varying from 2.5 mm to 2 cm, to be compared to the minimal wavelength 2.6 cm (corresponding to the highest frequency 8 GHz).

The fault responses were plotted in Fig. 3.32. Here also, the mathematical model we already derived in the previous section applies, if we consider the fault as a local variation in the cable's cross section. The obtained result in (3.60) allows to conclude that for an increasing fault distance d, the reflection coefficient Γ_F will increase; a fact that is verified when observing the four studied cases of Fig. 3.32. Also, note that in this case Γ_0 is positive, meaning that

Z'_c is superior to Z_c. The case where d is equal to 5 mm gives $\Gamma_0 = 0.047$, and consequently $Z'_c = 55\ \Omega$.

3.6.3.3 Conclusion

This section was dedicated to observe some common soft faults responses, proving the dispersive nature of such kind of faults. The next step is to insert these faults into different network configurations, so as to validate experimentally the performances of the MP approach. That is why we adopt one of the earlier studied fault types, which is the crushed transmission line, which thickness is reduced to 2 mm. The temporal response of the fault has been earlier represented in Fig. 3.30.

3.6.4 Studied networks configurations

After characterizing different fault types, we now proceed to the validation of all the discussed ideas in the mathematical analysis section through experimentations. The parametric investigations earlier considered addressed ideal non-dispersive faults, while the previous experimental study on the fault characterization showed some examples of real faults, suggesting their dispersive nature. It is important to asses the performance of our MP approach in practical configurations, where we can also observe the impact of the non-ideality of the junctions and the terminations on the fault response, especially when a soft fault is embedded in the system.

Two NUTs were considered in our tests, as shown in Figs. 3.33 and 3.34. The rationale for our choice is the motivation to prove experimentally, for real soft fault cases, that for an increasing complexity of the NUT the MP approach ensures a better performance, particularly for the detection probability, as discussed in Section 3.4. Hence, the use of a double-Y structure for the second NUT, with the fault more deeply embedded and further away from the testing port. Scalar transmission lines were considered, as often done in the analysis of TDR schemes, since this choice provides a simple and easily repeatable setup.

3.6.5 Results

The two NUTs were considered for two different configurations: a) with their ends matched in order to avoid any reflection; b) with open-circuited ends. A grand-total of four configurations where thus tested and the resulting impulse responses are shown in Fig. 3.35. These results refer to the case of a Gaussian pulse excitation with a -3 dB bandwidth of about 2 GHz. Fig. 3.35 shows how the response of the NUT is strongly dependent not only on the topology of the NUT, but also on its electrical configuration, particularly its boundary conditions,as we already examined when studying matched and open-circuited end NUTs in the simulation section. If the number of echoes is not very different for the two NUTs in the case of matched ends, it is indeed greatly enhanced in the case of open-circuited ends: under these conditions, a more

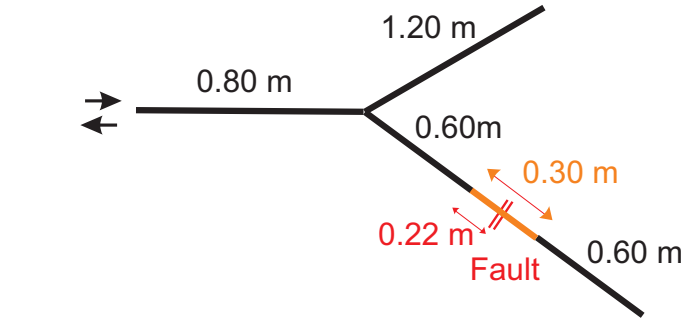

(a)

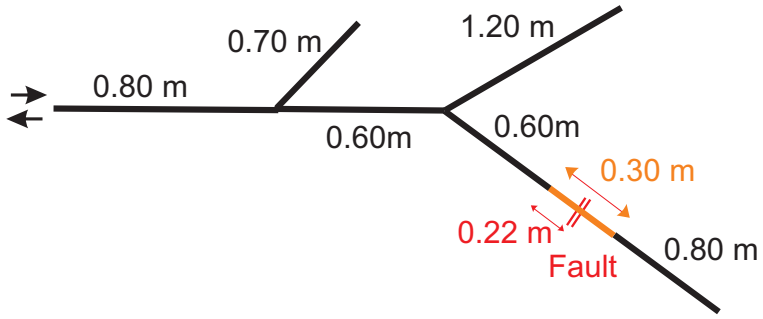

(b)

Figure 3.33: Layouts of the two NUTs considered for the experimental validation: (a) a single-Y structure; (b) a double-Y structure. Each branch of the NUTs consisted of a flexible coaxial cable with a 50 Ω characteristic impedance, while the red portions represent the samples containing the fault, as shown in Fig. 4.40. The ends of the lines were left open-circuited or matched, depending on the test configuration, while the junctions were implemented by means of BNC T-junctions. The length of each branch is shown in the figures. The double-arrow symbol stands for the port at which the testing signals are applied.

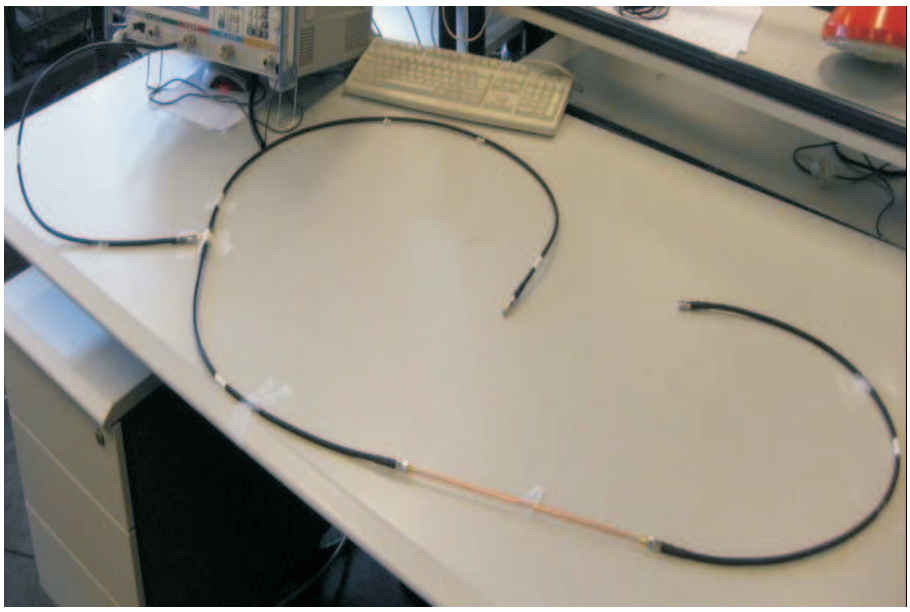

(a)

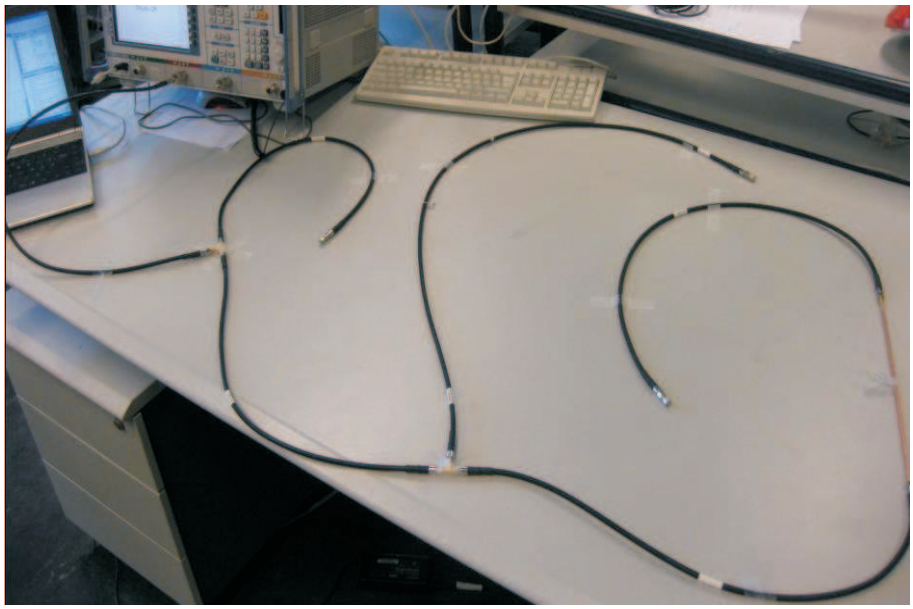

(b)

Figure 3.34: Implementations of the NUTs described in Fig. 3.33, as connected to a vector network analyzer for experimental work. The 30-cm long semi-rigid cable implementing the fault sample is clearly visible.

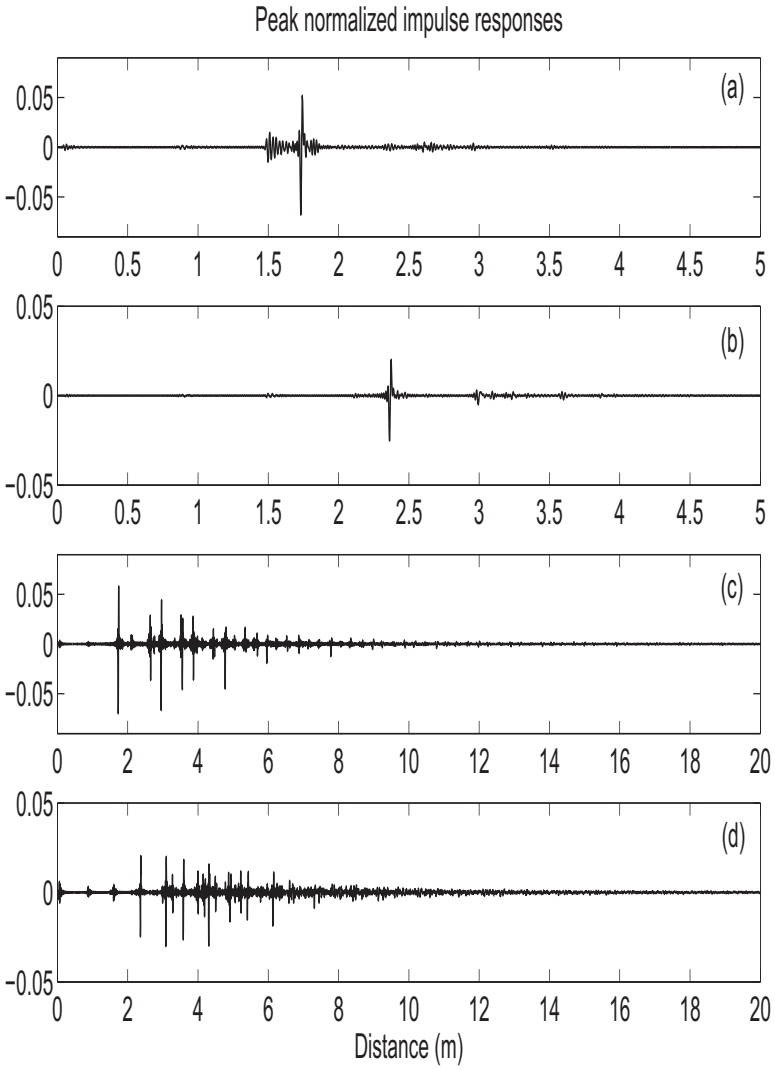

Figure 3.35: The impulse responses obtained by inverse-transforming the input reflection data for the setups shown in Fig. 3.33: (a) single-Y network, with matched ends; (b) double-Y network, with matched ends; (c) single-Y network, with open-circuit ends; (d) double-Y network, with open-circuit ends. The small echoes appearing just before the fault one are due to the inevitable positioning errors occurring during the substitution of the reference sample with the faulty one: the difference between the two responses is thus affected by these residual errors mainly due to unequal mating conditions applied to the SMA connectors.

complex network topology yields a larger number of echoes; similar results were also observed in the simulation study in Section 3.5.

3.6.5.1 Detection gain

According to (3.20), the matched-load configurations are expected to yield similar performances, with $G' \simeq 1$ and $G'' \simeq 5.5$ dB. The MP would thus only provide a detection gain due to the fact that the energy of the testing signal would be concentrated around the frequencies at which the fault will respond, rather than being uniformly distributed over a predetermined bandwidth. Conversely, in the case of open-circuited ends G' is expected to provide a stronger contribution, due to the large number of echoes shown in Fig. 3.35.

These arguments are indeed supported by the results shown in Table 3.8, where the ratio of the peak-value in the echoes obtained with a standard TDR testing signal and an MP one are summarized. The procedure described in Section 3.6.4 was applied, by post-processing the measured impulse responses with the two testing strategies. It is important to recall that the fact of having used Gaussian pulses has no major effect on these results, as we have demonstrated in Section 3.4 that the detection gain is broadly independent on the choice of the standard TDR testing signal $i_{\mathrm{ST}}(t)$. Three different bandwidths were considered in these experiments, 200 MHz, 500 MHz and 2 GHz. These differences were intended to assess how a changing bandwidth impacts on the performance of the MP approach. The results in Table 3.8 show that the bandwidth has a negligible effect on the cases of matched ends, with a typical variation of less than 1 dB on the gain, whereas for the other cases wider variations are observed. This outcome implies that the approximation (3.12) is actually valid only in configurations where the distance between the echoes is large enough as to make them distinguishable, even after having reduced the bandwidth, i.e., with a wider time-support for the excitation signal.

As predicted by the arguments introduced in Section 3.4, the gain is indeed almost independent of the network topology in the case of matched ends, where the impulse response is poor in echoes, whereas the MP ensures a strongly enhanced performance in the remaining configurations. These results are not based on a predictive model, but they are rather realized gains observed on the peak-value of the echo responses. As previously required, the energy of the testing signals was identical in all of the configurations.

It is interesting to study in more details the echo-responses obtained with a standard TDR and an MP approach. To this end, we will focus in the rest of this Section onto the two NUTs, single-Y and double-Y structures, with open-circuited ends. A bandwidth of 500 MHz will be considered, and the testing signals will be set to an energy equal to one. The impact of the detection gain will thus be considered in the case of a noisy NUT, jointly with the predicted improvement on the detection probability.

The case of the single-Y structure is first considered. Fig. 3.36(a) shows that the MP fault-related peak is about 3.4 times higher than the one obtained with the Gaussian-pulse excitation. Moreover, it also appears that the main peak of the MP approach is about 1.7 times higher

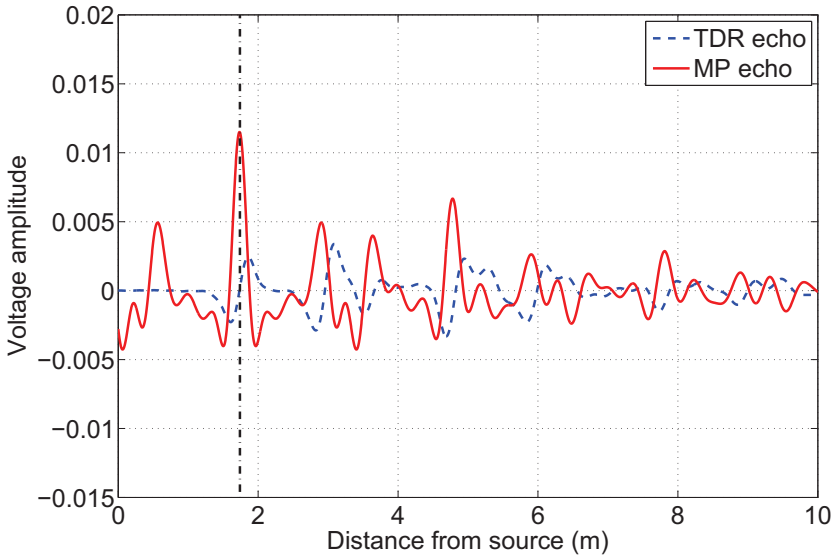

(a)

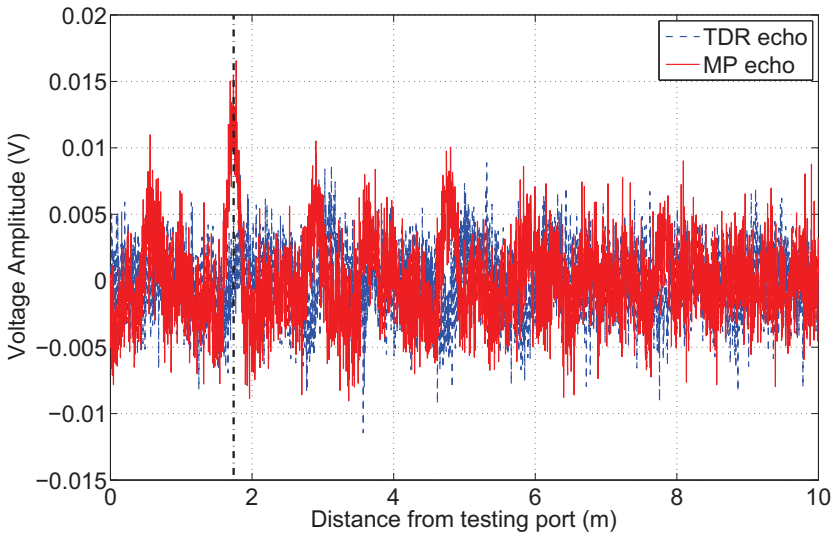

(b)

Figure 3.36: The output signals obtained when exciting the network of Fig. 3.33a with open-circuited ends by means of a Gaussian pulse or the associated MP for: (a) a noiseless configuration and (b) the presence of an additive Gaussian noise signal with a fixed average energy, resulting in an SNR of 0 dB for the Gaussian TDR case, corresponding to an SNR of 10.6 dB for the MP one. The vertical dashed line represents the position of the fault-related echo.

End loads	Bandwidth	Single Y	Double Y
Matched	200 MHz	6.1	5.1
	500 MHz	5.7	6.3
	2 GHz	6.4	6.5
Open	200 MHz	11.45	19.38
	500 MHz	10.6	12.85
	2 GHz	13.8	16.84

Table 3.8: Detection gain (expressed in dB) obtained from the four experimental configurations introduced in Section 3.6.4, for three different excitation bandwidths. The very close results obtained for the case of matched ends indicate that the gain is only due to term G'', whereas the cases of open ends attest that depending on the complexity of the impulse responses the term G' starts contributing by yielding a much greater gain.

than any other echo; conversely, the standard Gaussian TDR presents a fault-related echo that is actually 1.4 times weaker than the subsequent ones. Hence, also a standard TDR approach will not be able to correctly locate the position of the fault, as the most likely echo that will be detected is the maximum one about 3 m away from the testing port, rather than at 1.62 m. The MP approach is therefore not only providing a remarkable improvement in the echo-response with respect to a standard TDR technique, but also a clearer result to interpret, with a single dominant echo featuring a fair contrast with respect to the remaining echoes.

Having access to the impulse response of the NUT, the detection gain G can be estimated quite easily, by truncating the sum $\sum_i \alpha_i^2$. Considering just the first eleven echoes in (3.20a), we obtained a lower-bound estimate of $G' \geq 7.27$ dB. This value is consistent with the results shown in Fig. 3.36(a), thus validating the prediction capabilities of (3.20) and the analysis presented in the mathematical analysis section, particularly the approximation (3.12).

3.6.5.2 ROC Curves

Before calculating the detection probabilities, we proceed by plotting the ROC curves corresponding to the two studied configurations. The aim being to compare the performances of the two cases relatively to the TDR performance, and most importantly to asses which detection threshold insures a fair compromise between a high TP probability and a low FP probability. The case of the single-Y NUT (with open ends) illustrated in Fig. 3.34(a) is denoted to as MP1, and the second case of the double-Y NUT (with open ends) shown in Fig. 3.34(b) will be referred to as MP2.

The corresponding ROC curves are shown in Fig. 3.37, where the advantage of the MP approach is remarkable. For example, when the detection threshold $\rho = 0.8$ the FP gain between the MP methods (MP1 and MP2) and the TDR exceeds 0.2, whilst the TP gain is almost 0.17.

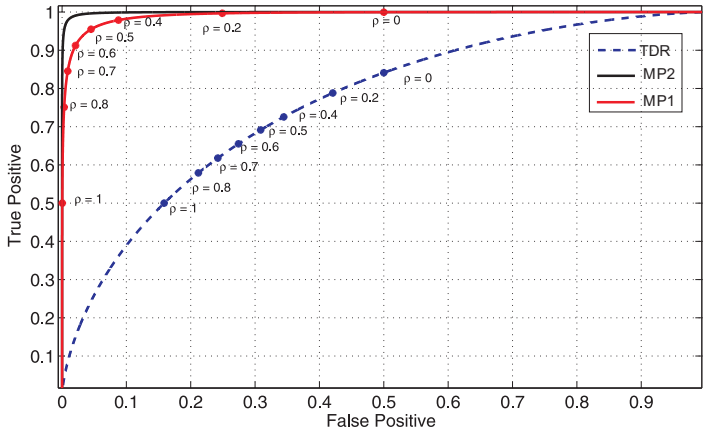

Figure 3.37: ROC curves of the two studied configurations in Fig. 3.34(a) and (b), with open-circuited ends.

Also, for a TP probability of 0.2, the TP difference between MP1 (and MP2) and the TDR is superior to 0.4. These curves show the important advantage brought by the MP in critical scenarios involving soft faults and complex networks.

Also, the detection thresholds marked on the same figure allow to deduce an optimal threshold, chosen to be $\rho = 0.5$. This threshold will be adopted for the calculus of the detection probabilities.

3.6.5.3 Detection probabilities

The results in Fig. 3.36(a) for a single-Y structure imply that for the same level of background noise, the detection probability must be expected to be substantially higher with the MP approach. This improvement can be better assessed looking at the results proposed in Fig. 3.36(b), where an additive Gaussian noise was added during the post-processing to the output signals from the two TDR techniques: as expected, the detection gain provided by the MP approach yields an output signal where the presence of a fault can be more reliably detected.

For the second configuration of Fig. 3.34, i.e., with a double-Y structure, the output signals obtained with the Gaussian-pulse TDR technique and the MP one are represented in Fig. 3.38(a). The MP fault-related peak is now about 4.4 times higher than the one obtained with the standard TDR. The contrast between the echo with the highest amplitude and the second maximum is again better in the MP case, with a margin of 1.65 to be compared to 1.62 for the Gaussian pulse excitation. However, in the TDR case, the fault-related echo is again weaker than the subsequent ones, suggesting a source of ambiguity regarding the localization of the fault, as already pointed out in Section 3.4.2. The detection gain, estimated from the first eleven echoes, is $G' \geq 5.6$ dB. The output signals obtained with a noise source are shown in Fig. 3.38(b): as the NUT complexity has increased, the MP provides even clearer results, with an easily detectable

echo well above the noisy background.

The formulas (3.52) and (3.54) earlier introduced allow studying how the increase in the output SNR leads to a higher detection probability. For the case of the single-Y NUT (MP1) and the double-Y NUT (MP2), the computed results are presented in Fig. 3.39, having set the decision threshold at 50 % of the fault-related peak (as deduced when analyzing the ROC curves). These results illustrate the non-negligible improvement of the MP approach on the likelihood of detecting an eventual fault, since it increases the detection probability while reducing the false-alarm rate without demanding any increase in the input energy.

The observed SNR gain in both cases imply a more reliable detection of the fault. It is noteworthy how standard TDR techniques would have a hard time in the second example of a double-Y structure. First of all, the localization of the fault would be put in jeopardy by the fact that the strongest echoes are not these closer to the fault-related one. Moreover, the very weak response from the fault implies that in certain configurations the output signal from a standard TDR technique could be so low as to be close to other spurious signals. In this case, not only the localization but also the detection of the fault can become critical. On the other hand, the MP approach has clearly shown that at least the detection can be improved, by using suitably defined testing signals.

These results completely support our conclusions, as derived in Section 3.4. Although the models we applied were quite simple, they are capable of reproducing the main physical phenomena underlying the use of MP reflectometry rather than standard ones and predict the trend we have experimentally observed in these results. The most important result is that indeed the use of the MP approach is justified only when dealing with NUTs with a complex response, in order to take advantage of the increased SNR. Moreover, this gain is clearly useful only when the output SNR of a standard TDR approach is deemed too low to ensure a reliable detection of faults. Therefore, the MP approach is indeed confirmed to be an interesting alternative in critical configurations where standard TDR techniques would be at the limit of their capabilities. It is important to notice that the use of the MP approach can be easily integrated into standard TDR approaches: in the case of an output TDR signal too badly corrupted by noise, this signal would just need to be time-reversed and injected back into the NUT in order to switch to an MP approach. This procedure should allow to improve the reliability of the detection, by simply requiring a further step in the usual TDR sequence shown in Fig. 3.2.

3.7 Conclusion

An alternative approach for soft-fault detection in complex wire networks was introduced, based on the properties of matched-filter signal processing. The proposed method is based on a self-adaptive definition of the testing signal, which has the peculiarity of ensuring the highest fault-related echo with respect to a given injected energy.

A mathematical analysis based on a simple yet general propagation model, as well as sim-

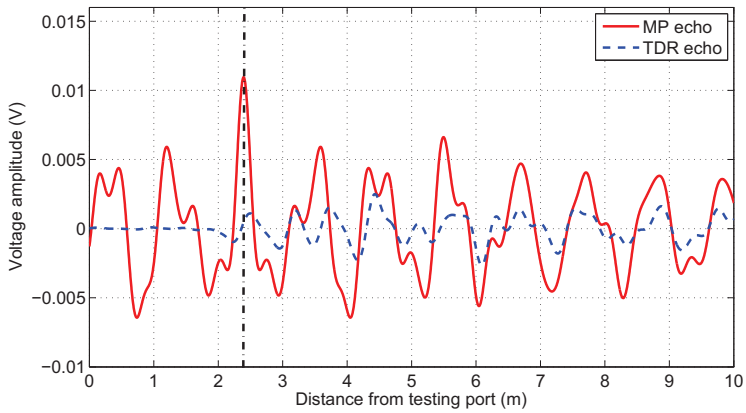

(a)

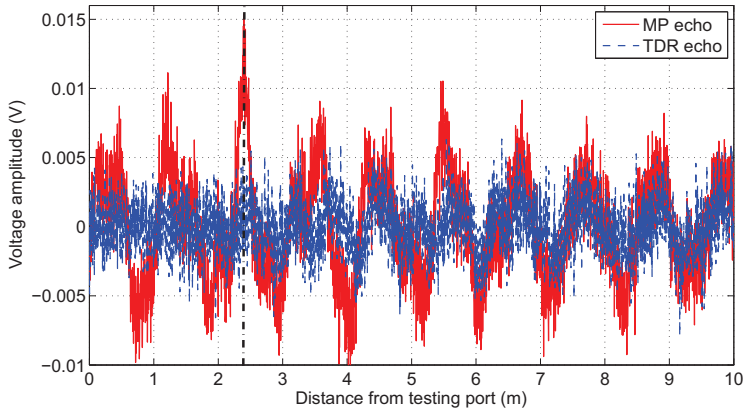

(b)

Figure 3.38: The output signals obtained when exciting the network of Fig. 3.33(b) with open-circuited ends by means of a Gaussian pulse or the associated MP for: (a) a noiseless configuration and (b) the presence of an additive Gaussian noise signal with a fixed average energy, resulting in an SNR of 0 dB for the Gaussian TDR case, corresponding to an SNR of 12.85 dB for the MP one. The vertical dashed line represents the position of the fault-related echo.

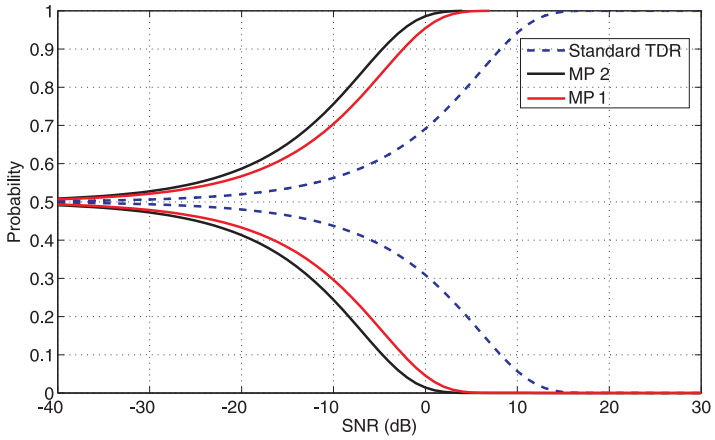

Figure 3.39: Detection probabilities of the two studied configurations in Fig. 3.34(a) and (b), with open-circuited ends, and a threshold value of 0.5.

ulation and experimental validations have proven that the MP approach outperforms standard TDR methods, as long as the detection probability is of concern. Moreover, it was shown that the complexity of the response of the NUT has a positive effect on the performance of the MP method, as an increasingly longer sequence of echoes systematically leads to a higher fraction of energy being concentrated into the peak echo. This remarkable feature is opposed to common understanding usually based on the properties of standard TDR techniques, where complex-network responses can strongly reduce the reliability of the detection criteria currently used. In a similar way, the MP approach was also shown to benefit from dispersive responses of the fault, as its matched-filter nature allows adapting the testing pulse to the frequency-spectrum of the fault.

As a consequence, the MP approach can be expected to provide a complementary testing solution with major advantages in critical configurations where standard TDR techniques are no more reliable, by ensuring a higher sensitivity to the presence of soft faults.

Chapter 4

Fault location

4.1 Introduction

In the previous chapter, we studied fault detection based on time reversal properties, introducing the MP approach. We showed that this method presents major advantages over standard TDR techniques in critical scenarios, as is the case for soft faults in complex networks. However this method does not allow us to locate the fault, hence the need to find a suitable approach to achieve this goal.

In the present chapter, we are going to study fault location in wire networks; after a brief introduction of the existing reflectometry and iterative methods and their major limitations, we present a new distributive non-iterative approach based on the DORT (Décomposition de l'Opérateur de Retournement temporel) method. The DORT is adapted to our case of guided propagation, and a location criteria is established. This empirical criterion is studied and the new method is evaluated through a statistical study aiming to asses the factors influencing its performance. This study is followed by an experimental study in order to test the methods performance in practical cases with real soft faults. Finally an example illustrates the ability of the method to locate multiple soft faults in complex networks. Note that the study presented in this chapter is a preliminary study of the method, where we assessed the ability of the DORT to locate faults in wire networks, and studied some of the influencing parameters on its performance. Thus a more extended study will be necessary in the future to fully characterize the new method and the possibility of its practical implementation.

4.2 Existing fault location methods

The aim of this section is to present a brief description of the existing fault location methods and their major limitations. We begin with the reflectometry methods introduced in the first chapter.

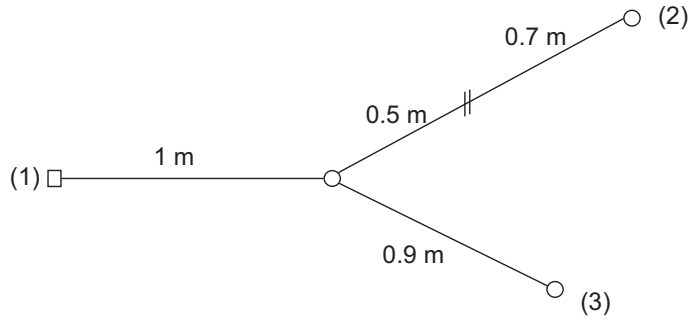

Figure 4.1: Example of a single-Y network showing the ambiguity in the location of the fault based on the information obtained from one testing port.

4.2.1 Reflectometry methods

4.2.1.1 Standard Reflectometry

Reflectometry methods are the most common methods used today for fault detection and location. In chapter one, we considered the example of a uniform lossless transmission line and examined the general principle of these methods, based on the injection of a predefined testing signal into the NUT, and then the analysis of the reflected signal searching for the position of an eventual fault. In more complex cases, such as the single-Y network with adapted ends represented in Fig. 4.1, ambiguity in the location of an eventual fault might arise, as is the case for the fault situated at 0.5 m from the junction, on the second path. When receiving the reflected signal at the position of the testing port (1), we cannot determine on which branch, (2) or (3), it is exactly situated: the same response is obtained if the fault is situated on both branches. In more complex configurations, and due to the deficiency of information obtained from the testing port, the reflectogram becomes very difficult to analyze, hence the idea of using distributed reflectometry [56].

4.2.1.2 Distributed reflectometry

Due to the ambiguity of locating an eventual fault in complex networks, the idea was, instead of using one testing port at one extremity of the NUT, to use multiple testing ports; the injected signals from these ports should have specific correlation properties in order for the location process to be accurate. We explain this by reconsidering the same network of Fig. 4.1, with three testing ports, placed on the three extremities of the network. Ravot and al. [56, 101] used pseudo-random sequences (M sequences [102]) as the testing signals: these signals are non correlated, which means practically that their intercorrelation does not produce a significant peak compared to the autocorrelation of one M sequence. The method consists of injecting simultaneously the M sequences from the testing ports, and then analyzing the correlation products of the received signals and the templates (the testing signals), in order to try to determine the

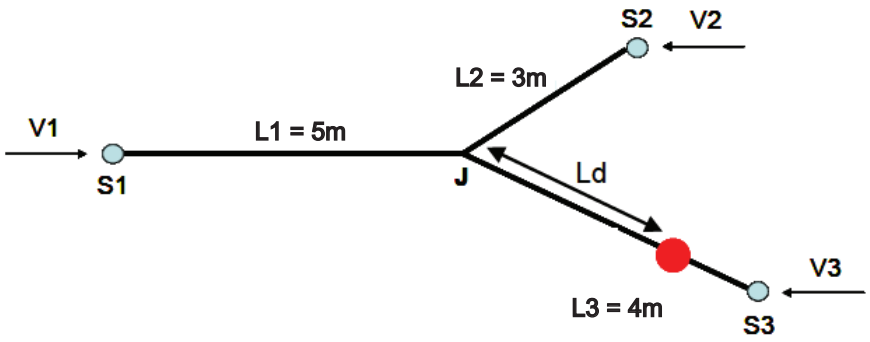

Figure 4.2: Example of a single-junction network with a short circuit representing the fault to be located. The fault is situated at a distance $L_d = 3$ m from the junction, and the cables are coaxial with a characteristic impedance equal to $50\ \Omega$. Three adapted generators are connected to the NUT extremities, and the testing signals are denoted as V_i, with i ranging from 1 to 3. *Source:* [56]

.

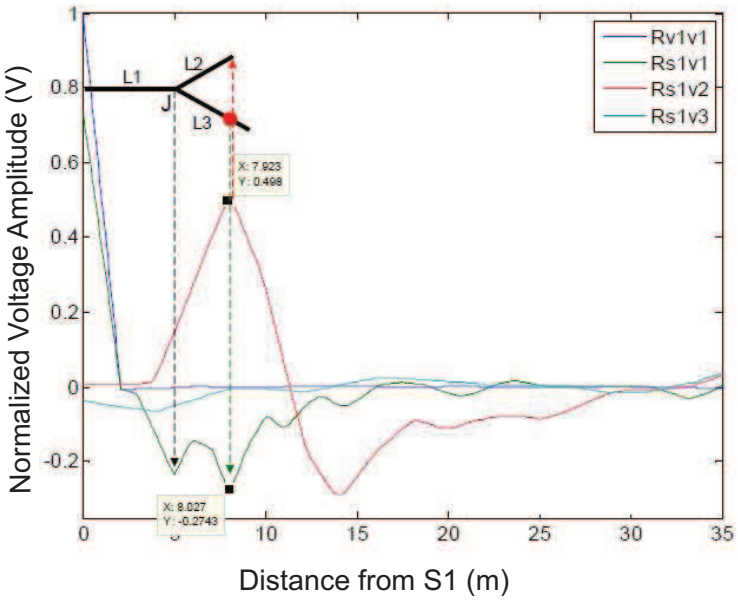

Figure 4.3: The intercorrelation functions obtained using distributive reflectometry, for the case of the single-junction NUT of Fig. 4.2. The testing signals are denoted as V_i, with i ranging from 1 to 3. *Source:* [56]

.

position of the fault. Ravot et al. addressed hard faults, and soft faults were not analyzed using this method.

An example of a case they studied is represented in Fig. 4.2. The Y-network presents a hard fault at 3 m from the junction, and if standard reflectometry methods are applied, with a single testing port at S_1, the fault cannot be exactly located on the correct branch. Thus more information is needed: it is obtained by adding two testing ports, S_1 and S_2. The signals they used are M sequences, with different primitive polynomials. The length of each sequence was 10 and the outflow 50 Mbps.

The injected signals from the testing ports are denoted as V_i, having $i = 1, 2$ or 3, and the observed signals from the corresponding positions as S_i. Let us consider the observation plane at S_1. The diagrams obtained in Fig. 4.3 show the intercorrelation products of the three testing signals V_1, V_2 and V_3, and the observed signal at this position S_1. These correlation products, denoted as $R_{S_1V_i}$, are normalized to the autocorrelation function of the injected signal V_1, R_{v1v1}.

By examining R_{s1v1}, we notice the peak corresponding to the junction at 5 m and another negative peak situated at 8 m. To be able to locate this peak on the corresponding branch, the authors calculate the correlation functions R_{s1v2} and R_{s1v3}: the function R_{s1v2} presents a positive correlation peak at about 8 m, meaning that the image of the source V_2 is visible from S_1; thus we deduce that the fault is situated on the third branch, given that the third source is not visible from S_1 due to the presence of the short circuit that totally masks its presence. A similar analysis can be conducted from the other observation planes S_2 and S_3.

As we already mentioned, hard faults were addressed when studying this method. In the case of a soft fault, the fault's response might be quite weak compared to the response of a hard fault. The distributed reflectometry cannot guarantee the location (or even the detection) of this type of faults unless his signature is quite visible, which is similar to the limitations of standard TDR techniques. Additional difficulty also arises when the network structure is more complex. In such situations, iterative methods are sometimes used to try to find an optimal solution for the inverse problem [103].

4.2.1.3 Iterative methods

The direct problem consists of obtaining the network's response from the known parameters of the fault (position and value). The inverse problem is thus obtaining the unknown fault's parameters provided that we have the fault's response; it is this problem we deal with when searching for eventual faults in wire networks. Generally, obtaining an analytical solution of the inverse problem (i.e., inverting the direct model) in complex networks is rather difficult, that is why numerical iterative methods are used most often [104, 105]. The direct model is inserted in an iterative loop, as represented in Fig. 4.4. The measured data is compared to the one provided by the direct model, and an error minimization algorithm is used to minimize the error between the two data sets. The process is iterative and continues until a certain criterion is satisfied, such as a predefined error threshold.

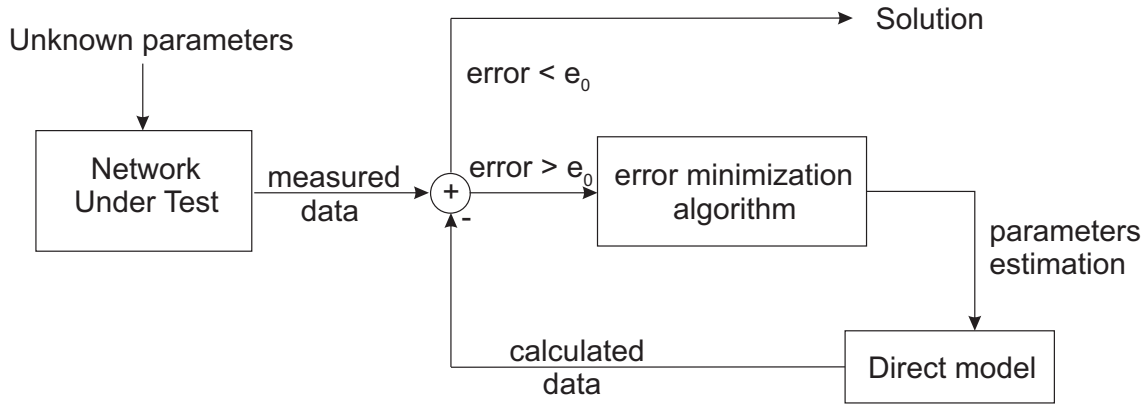

Figure 4.4: The bloc diagram of the iterative methods used in fault location. e_0 is a predefined error threshold which has not to be exceeded in order to obtain a solution.

Several iterative algorithms can be used, such as genetic algorithms [106], simulated annealing [107], the conjugate gradient [108], etc.

After reviewing the most common methods used for fault location in complex networks, we notice that these methods turn out to be insufficient when dealing with soft faults, hence the motivation of our work to find a non-iterative approach able to ameliorate the process of soft fault location in complex configurations.

4.3 The DORT method

4.3.1 Introduction

In the previous chapter, we addressed fault detection in wire networks. The information we needed in order to detect the presence of an eventual fault was the reflected voltage signal at the testing port, followed by a proper analysis of this signal to decide if a damage is present in the NUT. The NUT was considered as a black box, which means that no model of the NUT was necessary for the detection process to work, because we intervened only at the testing port. However, this is not the case when addressing fault location: in order to be able to point the location of a certain fault, a model of the NUT is necessary. The ideas encountered when studying fault detection, relating the use of the time reversal focusing properties to ensure a maximization of the fault-related echo remain applicable, because time reversal also allows maximizing the energy at the fault position.

This energy maximization property of the TR process has been exploited in imaging, whether it is medical imaging [109], radar and sonar communications [110, 111], sensing of buried objects [112, 113, 114], etc. For most of the imaging applications, analysis of the TR operator (TRO) [115] is fundamental.

In fact, given a media containing multiple discrete scatterers, the backpropagation of TR

scattered fields (standard TR) generates focal spots on all scatterers simultaneously, and more strongly on the dominant one. If we iterate this TR process, the wavefront becomes increasingly localized on the dominant scatterer [116]. The DORT method (under its french acronym, referring to Décomposition de l'Opérateur de Retournement Temporel) [115, 117, 118, 119, 120, 112, 113, 121, 122], derived from the iterative TR process isolates and classifies different scattering centers, without the need for iterations [115, 117]. To achieve this goal, the DORT utilizes the TRO, whose eigenspace structure contains valuable information about the scattering centers in the media (see next section). By propagating the corresponding signals, the DORT allows to focus on the desired scatterer as if it was the only one present in a classical TR scenario, thus providing separate images of the scatterers in the media.

When addressing the problem of fault location, soft faults are most often masked by the presence of impedance discontinuities, assimilated to the scatterers that prevent the accurate location of the fault. Taking advantage of the properties of the DORT method, we will adapt it to our case of guided propagation, and see how this method will enable us to synthesize signals intended to focus on the position of an eventual fault. But first let us begin by introducing the method through a simple example in acoustics.

4.3.2 Principle of the method : an example in acoustics

The DORT method was first developed in acoustics by Prada et al. [115], when trying to synthesize a wave focusing selectively on one of several well resolved point-like scatterers. The basic idea of the method is the following. Let us consider a set of N transducers in an inhomogeneous medium, as depicted in Fig. 4.5. We suppose we have two point-like well resolved targets, (A) and (B), where (A) is the most reflective one, i.e., (A) has a bigger reflection coefficient than (B). Both targets are supposed to have the same reflectivity in all directions, and the system is supposed to be linear and time-invariant.

We already saw in the third chapter that in the case of one scatterer, time reversal leads to a one-point focused wave. In the case of several scatterers, focal spots are generated on all the scatterers simultaneously, more strongly on the most reflective one. If the TR process is iterated, we obtain a wave focusing on the most reflective one, which in this case is (A). However, this process does not allow focusing on the 'weaker' target (B). A solution to focus on the latter might be to apply time-gating, but this technique only distinguishes temporally well-resolved scatterers and its performance is strongly influenced by the usable bandwidth [123]. Hence the importance of the DORT method, which overcomes these problems and allows selective focusing without the need for iterations.

4.3.2.1 Time Reversal Operator (TRO)

The TRO was introduced to express the received signals in terms of the transmitted ones in the description of the iterative time reversal process. Let K denote the transfer matrix of the system,

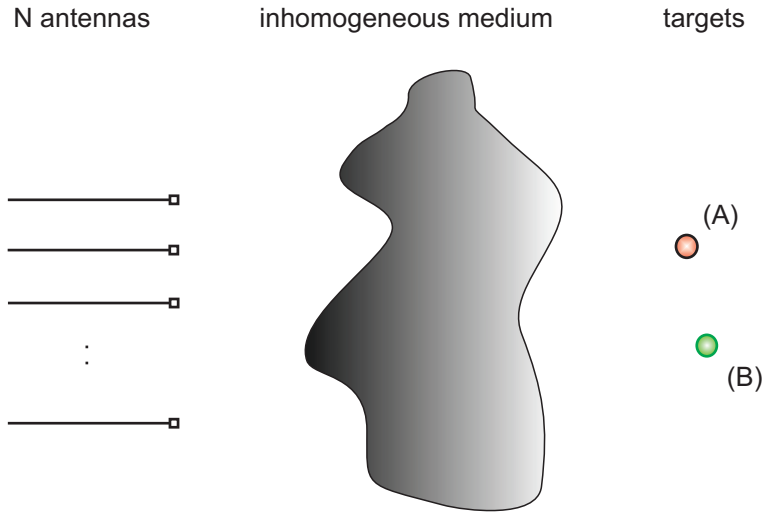

Figure 4.5: Illustration of the DORT method for two point like scatterers and a set of N antennas

linking the injected signals (the inputs) to the received signals (the outputs). Each element of K, referred to as $k_{ij}(\omega)$, is an inter element transfer function: the emitter is the element number j and the receiver is the element number i. For the set of N antennas we obtain, for each frequency, a $N \times N$ transfer matrix K, where each column j contains the N element transfer functions of the N antennas when injecting a temporal Delta function from the antenna number j. Theoretically, due to the reciprocity theorem, we have $k_{lm}(\omega) = k_{ml}(\omega)$, in other words K is symmetrical. The TRO, denoted as T, is defined as follows

$$T = K^* K \tag{4.1}$$

with the star referring to the frequency conjugation operation. The symmetry of K implies that the TRO is hermitian, and consequently can be diagonalized; its eigenvalues are real and positive. In the case of point-like targets, the number of significant eigenvalues is equal to the number of well-resolved targets. Moreover, it has been demonstrated [115] that these eigenvalues are proportional to the square of the corresponding target's reflectivity, a fact that will be further investigated in the following sections.

4.3.2.2 Description of the DORT method

The first step in the DORT method is the measurement of the matrix K. Thus we reconsider the example of Figure 4.5 for illustration. We suppose that the N transducers are the same for emitting and receiving the signals. A temporal Delta function is sent from each transducer and the received signals are recorded. This process is repeated N times, and the matrix K is stored.

The second step is the diagonalization of the TRO. This was first done at a chosen frequency, and the method was called Central-Frequency DORT. However, the diagonalization process was later extended to capture the behavior of the eigenvalues over a large frequency range, allowing

to obtain more information about the scatterers, thus facilitating data interpretation. Also super-resolution [120] was achieved using this method, the Full Time Domain DORT (FTD-DORT). In our work, we will deal with faults having reflection coefficients that depend on the frequency (as seen for real fault cases in the previous chapter) and thus we will benefit from the localization properties of the wide-band signals through the utilization of the FTD-DORT.

Back to the diagonalization operation, we already mentioned that theoretically K is symmetrical. But practically this is not the case, due to several reasons, such as noise in the system, non-ideality of the emitting and receiving antennas, etc. So we proceed by making K symmetrical, thus replacing each element k_{ij} with $\frac{1}{2}(k_{ij} + k_{ji})$. Then the TRO can be calculated and next diagonalized, in order to finally obtain the set of the eigenvalues and the corresponding eigenvectors.

The third step is now to propagate the eigenvectors. In fact, if the targets are well resolved, and under the assumption that their number is inferior to the antenna's number, each eigenvector is associated to one of the targets: it is the output vector signal that would be obtained if a source is placed at the corresponding target position.

The eigenvectors propagation process amounts to image the medium thus providing separated images of the targets. We are going to use in our experiments numerical backpropagation, which means injection of the eigenvectors into a numerical model of the reference NUT.

In the example we earlier considered in Fig. 4.5, the diagonalization of the TRO gives two significant eigenvalues corresponding to the two targets, denoted as λ_1 and λ_2 (with $\lambda_1 > \lambda_2$), and $N - 2$ eigenvalues close to zero. So if we want to focus on the weaker target (B), we consider the eigenvector corresponding to λ_2 and propagate each of its components through one of the emitting antennas. The result is a wave focusing on (B); a similar result is also obtained when we propagate the eigenvector corresponding to λ_1 in order to focus on (A), and thus selective focusing is achieved using the DORT method.

This method offers several advantages in this domain; first it allows to determine the number of scatterers by analyzing the eigenvalues and eigenvectors of the TRO. Also, since it is capable of isolating different scatterers in the domain, it can be used as a pre-processing step to improve the efficiency of the inverse scattering algorithms, by restricting the inverse problem to smaller domains considering the data provided by the method, thus leading to a faster convergence of these algorithms. The advantages of the DORT make it an interesting method to be applied in our domain of fault location in wire networks. However, fundamental differences exist between the case of 3D propagation and the one of guided propagation, which make an adaptation of the DORT method essential to benefit from its advantages.

4.3.2.3 DORT in three and one dimensional cases

A simple example to compare the case of 3D propagation to the guided wave propagation is illustrated in Fig. 4.6. Fig. 4.6(a) points the case of free space propagation, with a set of 2 transducers, and a target situated at distances L_1 and L_2 from the transducers. Fig. 4.6(b) shows the

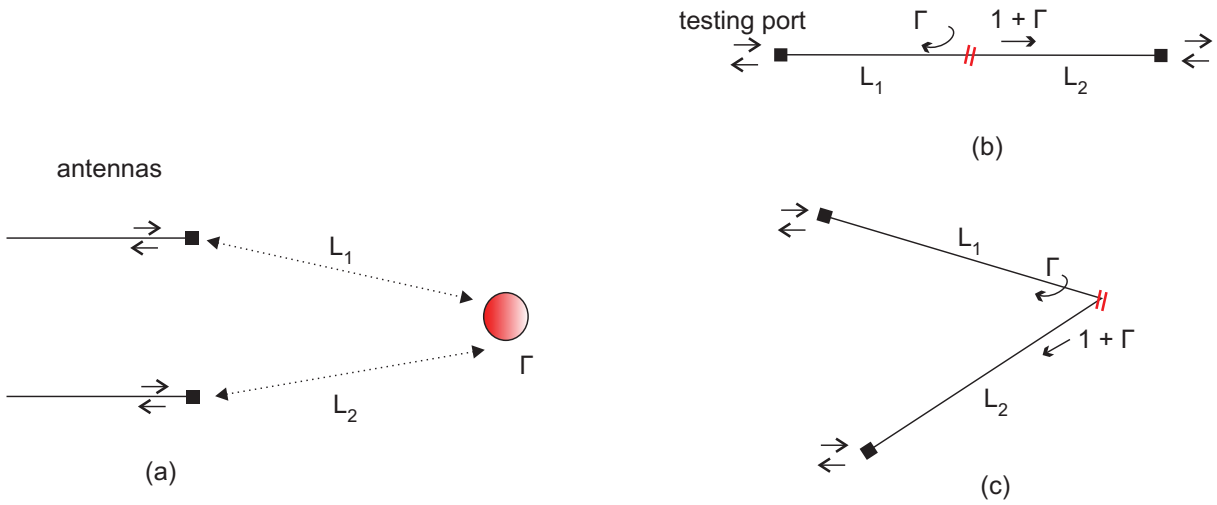

Figure 4.6: Comparison between the three and one dimensional case. A target of reflectivity Γ is present in a homogeneous medium with two transducers (a), and a fault with a reflection coefficient Γ on a simple transmission line (b) with a second representation in (c) facilitating its comparison with (a). The reflectivity and the reflection coefficient are designated with the same symbol Γ for the sake of comparison.

case of guided propagation, where we represent the simple case of a uniform lossless transmission line, terminated at both its extremities with adapted testing ports, emitting and receiving the testing signals. This case is represented again in Fig. 4.6(c) to approach the representation in Fig. 4.6(a) for the sake of comparison.

In the case of free space propagation, if a normalized amplitude wave is emitted from one of the antennas, and if we consider that the target is a point-like scatterer, with the same reflectivity in all directions, then the reflected wave as 'seen' in the vicinity of the target has the same amplitude in all directions; it is equal to the reflectivity coefficient of the scatterer: the scatterer acts as a secondary isotropic source.

In the case of guided propagation, if a testing port emits a normalized amplitude wave, the one that reflects back when reaching the fault has an amplitude equal to the local reflection coefficient at the fault position, Γ, whilst the transmitted one that reaches the other testing port has an amplitude equal to the transmission coefficient at the fault position, $1 + \Gamma$, which is different from the reflection one.

In free space, when the incident wave interacts with the scatterer, the transmitted part continues its propagation beyond the scatterers, as opposed to guided propagation, where the emitted wave reaches the other testing port in our case of Figure 4.6(b). More generally, in guided structures, the wave propagating in the structure will be subject to different interactions with the NUT, but finally will reach one of the testing ports situated at the extremities of this network.

We consider the example of Fig. 4.6(a). Generally, when calculating the transfer matrix of the system, defined according to the injected and received waves at the transducers, we can

obtain information about the scatterer. If we inject a wave which amplitude equals a_1 from the first transducer, supposed to be ideal for simplification purposes. In a homogeneous and isotropic medium, this wave arrives at the scatterer position, and the transfer function between the transducer and the scatterer, denoted as H_1, equals

$$H_1 = a_1 \frac{e^{-jkL_1}}{4\pi L_1} \tag{4.2}$$

where k is the propagation constant of the wave. This wave interacts with the scatterer of reflectivity Γ, and the diffracted wave propagates back to reach the transducers. At the position of the second transducer, the transfer function H_{21} (the input being the injected wave of amplitude a_1 from the first transducer and the output the reflected wave at the second transducer) can be written as

$$H_{21} = a_1 \frac{e^{-jkL_1}}{4\pi L_1} \Gamma \frac{e^{-jkL_2}}{4\pi L_2} \tag{4.3}$$

Measuring the transfer function at the transducers position thus allows to retrieve information about the scatterer. In a general form, transfer matrix K can be written as the product of three matrices [115]:

- a matrix P, describing the propagation from the transducers to the scatterer,
- a scattering matrix S_{fs}, illustrating the contribution of the scatterer in the transfer matrix,
- a matrix describing the backpropagation from the scatterer towards the transducers, which equals the transpose of P due to the reciprocity principle, and will be denoted as ${}^tP$.

$$K = P S_{fs} \, {}^tP \tag{4.4}$$

We are interested in the contribution of the scatterer, so in the following analysis we consider the scattering matrix alone. In this case where a scatterer is present in the medium, this matrix is proportional to

$$S_{fs} = \begin{bmatrix} \Gamma & \Gamma \\ \Gamma & \Gamma \end{bmatrix} \tag{4.5}$$

When no scatterers are present in the medium, this matrix is a zero matrix.

In the case of guided propagation, The scattering matrix in the case of the presence of a fault, denoted as S_{gp}, is proportional to

$$S_{gp} = \begin{bmatrix} \Gamma & (1+\Gamma) \\ (1+\Gamma) & \Gamma \end{bmatrix} \tag{4.6}$$

In the absence of the fault, we still have a non-zero matrix, equal to

$$S_0 = \begin{bmatrix} 0 & 1 \\ 1 & 0 \end{bmatrix} \tag{4.7}$$

This implicates the transmission of the testing signals across the line, so that a testing signal emitted from one testing port reaches the other testing port, as opposed to the case of free space propagation .

We already saw in the second chapter that if we consider the difference system in the case of a soft fault, the latter acts as a secondary source. If we want to apply the same idea here, in order to retrieve the case (4.5) of free space propagation, and given the linearity and time invariance of our system, considering only the fault gives the scattering matrix of the difference system S_d

$$S_d = S_{gp} - S_0 \ = \begin{bmatrix} \Gamma & \Gamma \\ \Gamma & \Gamma \end{bmatrix}. \tag{4.8}$$

We notice how S_d is equal to S_{fs}, apart for eventual proportion terms. In our case of guided propagation, we will use once again the difference system, and its transfer matrix will be simply denoted as K. Note that the rationale for dealing with the difference system in the case of fault location differs from the one in the case of fault detection. In the latter, we applied the difference operation in order to increase the sensitivity to the presence of soft faults, whilst in the case of fault location we needed the scattered part to approach the case of a secondary source, and the constraint of dealing with soft faults is found again; it is necessary in order to be able to apply the Born approximation, and in this case the difference operation gives the desired scattered part.

4.3.3 Application of the DORT to fault location: examples in guided propagation

We begin our study of the DORT method in the domain of guided structures by some examples, in order to derive a heuristic criterion for fault location based on its principles. Next we evaluate the quality of the solutions provided by this method and the parameters influencing its performances through a statistical study aiming to asses the impact of these parameters on the probability of location of an eventual fault. We will see how the DORT method will allow us to synthesize testing signals depending on the nature and position of the fault, as well as the tested NUT, and which are tailored to focus on the position of the fault.

4.3.3.1 Paths designation

The rules we adopted to name the paths in the NUT have been illustrated in the second chapter. Here we briefly remind of the general principles. If we consider the general network structure we considered in our work, illustrated in Fig. 4.7, we first begin by assigning a number to each of the extremities of the network, where a testing port can be plugged. We consider that the first end, i.e. the one numbered (1), is the origin: all the distances will be calculated according to this origin, and consequently all the graphs will be plotted accordingly. When we designate a certain path by the number of the testing port at its ending, we mean the part of the network situated

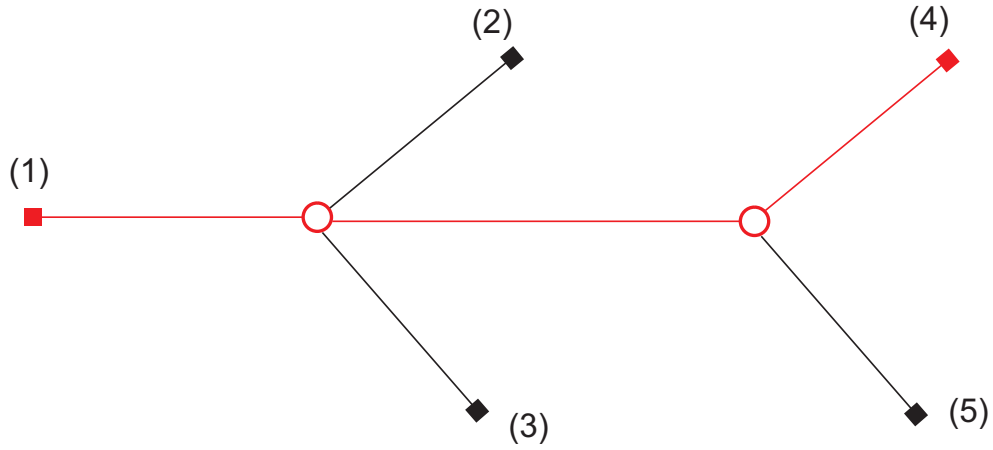

Figure 4.7: The branches nomenclature we adopted to represent specified locations in the NUT.

between this testing port and the origin testing port (1). For example, if we consider Fig. 4.7, the fourth path (marked with a red line) is the one situated between the testing ports (1) and (4). This designation will be necessary when addressing the voltage propagation representation using the ZT diagrams, and also later when deriving the fault location method.

4.3.3.2 Single transmission line

The networks to be studied are represented in Fig. 4.8, where we considered a simple transmission line, then a single and double junction network, with matched testing ports at the end of the three networks. The lengths of the different paths as well as the fault positions in the three NUTs were chosen arbitrarily. These examples are meant to show some examples of fault location using the DORT method, before deriving an heuristic location algorithm for complex structures. We remind that we simulated the networks under Matlab, using the transmission line theory (see Chapter 2). In the three examples, we considered a characteristic impedance equal to $50\ \Omega$, a bandwidth of 2 GHz, a sampling frequency step of 10 MHz, and a propagation velocity that equals 0.8 times the speed of light. We also consider uniform lossless transmission lines, which means that the propagation constant $\gamma = j\beta$. The fault is modeled as a parallel impedance of $400\ \Omega$.

Let us begin by the simple transmission line of Fig. 4.8(a), where the fault is located at 1 m from the first testing port (1) and 1.4 m from the second one (2). Generally, this network can be tested by means of standard reflectometry methods, which can generally determine the location and the value of an eventual fault. The DORT method presents no advantages over standard methods in this scheme, but is going to be applied to the NUT for illustration purposes.

In this case, the TRO T is equal to

$$T = 2\Gamma^2 \begin{bmatrix} 1 & e^{-j\beta(L_1-L_2)} \\ e^{-j\beta(L_2-L_1)} & 1 \end{bmatrix}. \tag{4.9}$$

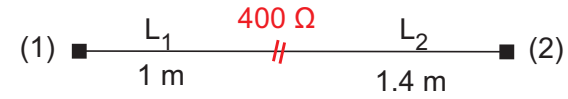

(a)

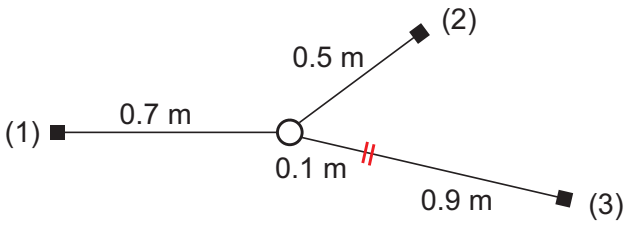

(b)

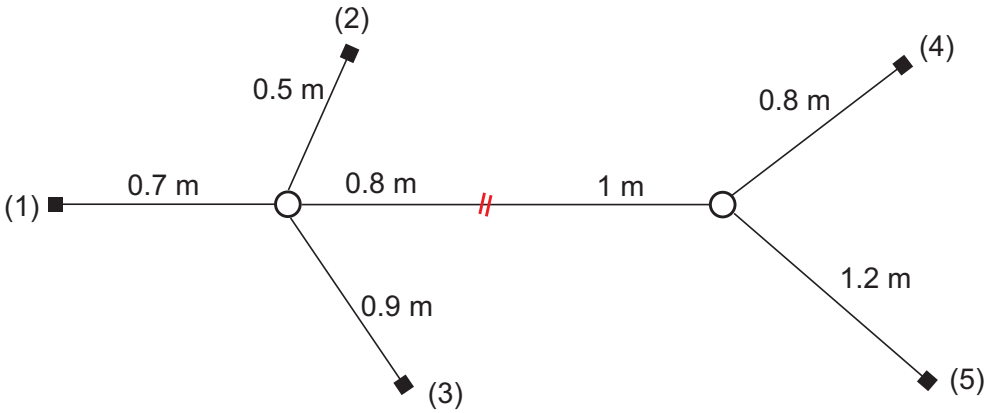

(c)

Figure 4.8: The three networks analyzed when studying the DORT method: a simple transmission line with two testing ports at the extremities (a), a single-junction network (b) and a double-junction network with testing ports at each of the extremities (c).

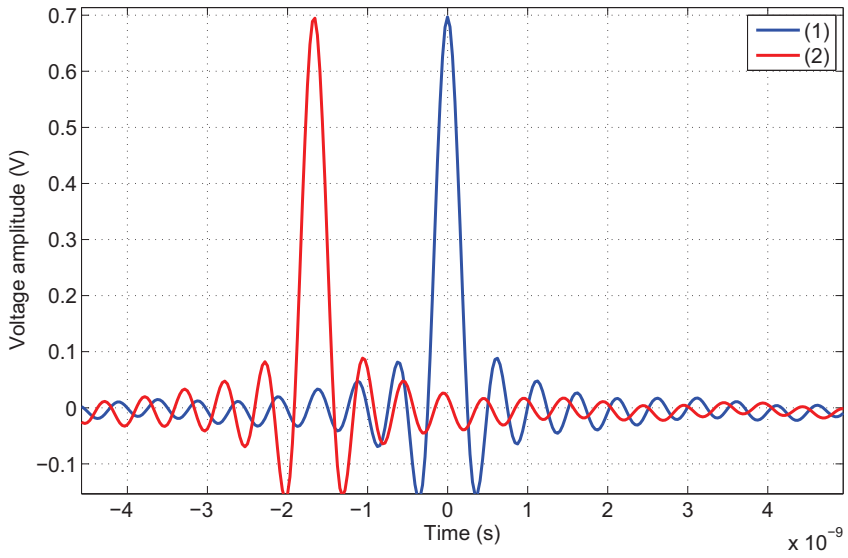

Figure 4.9: The injected signals as applied to the testing ports of the reference model (without the fault), aiming to focus on the target location.

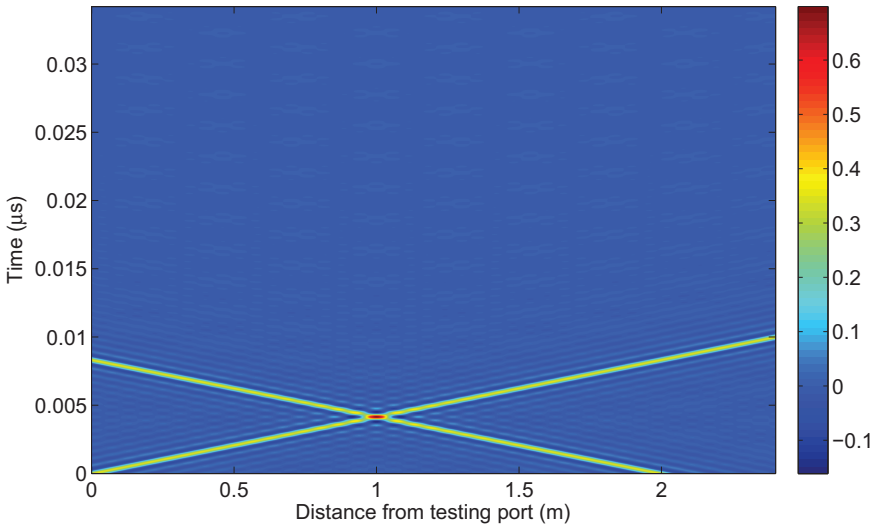

Figure 4.10: The ZT diagram for the network of Fig. 4.8(a), showing the voltage propagation both in space and time, and the focusing on the fault position, at 1 m from the first testing port, chosen to be the origin of the space axis.

The eigenvalues λ_1 and λ_2 of the TRO are obtained by imposing

$$det(T - \lambda I) = 0 \tag{4.10}$$

where I is the identity matrix and det is the determinant of the matrix $T - \lambda I$. These eigenvalues are $\lambda_1 = 4\Gamma^2$ and $\lambda_2 = 0$, they are real and positive because T is hermitian. Notice how the value of λ_1 in this case is proportional to the the square of the fault's reflection coefficient, as in the case in free space propagation in [115]. In this simple case the value of λ_1 can be used to calculate the reflection coefficient from the fault and consequently determine its nature. The simulation of a $400\,\Omega$ parallel load fault gives a non-zero eigenvalue $\lambda_1 = 0.0138$, thus inferring $|\Gamma| = 0.0588$, which is the case for the fault because we have $\Gamma = -0.0588$.

Now let us consider the eigenvector corresponding to the biggest eigenvalue λ_1, and inject its components through the two testing ports, for the given frequency range. The components we injected are represented in Fig. 4.9; The time origin is considered relatively to the injected testing signal from the first source (1), as can be seen on the figure. Notice how these testing signals are time delayed in order to focalize on the fault's position when injected in the reference model we simulated (i.e., the model without the fault), as shown also on the ZT diagram in Fig. 4.10. The signals generated by the DORT include the time delay corresponding for the two signals to interfere constructively at the source location, and focalization can be obtained.

4.3.3.3 Single junction network

The network's structure is represented in Fig. 4.8(b), with three testing ports, at the positions (1), (2) and (3).

A closed-form computation of the eigenvalues of the TRO is no more viable in this example, so we proceed to a numerical calculation. We obtain two null eigenvalues, and the third one represented in Fig. 4.11, in terms of the frequency. The components of the eigenvector corresponding to this eigenvalue are the new testing signals injected through the three testing ports: they are shown in Fig. 4.12. Once again we observe how the signals are time-delayed so as to focus on the fault position at the same instant, as can be seen on the ZT diagram of Fig. 4.13, observed along the third path, where the signals interfere constructively at the fault position. Comparing this ZT diagram to the one of Fig. 4.14, observed along the second path, we notice the elimination of the ambiguity regarding the fault position, observed when using reflectometry techniques: focalization is only observed along the third path, thus suggesting the existence of the fault on the third branch (3).

4.3.3.4 Double junction network

A more complex network is the one represented in Fig. 4.8(c). Here we have two junctions, the first one linking four branches, and the second one three branches. To the best of our knowledge, the location of soft faults embedded in similar networks has never been addressed before. The

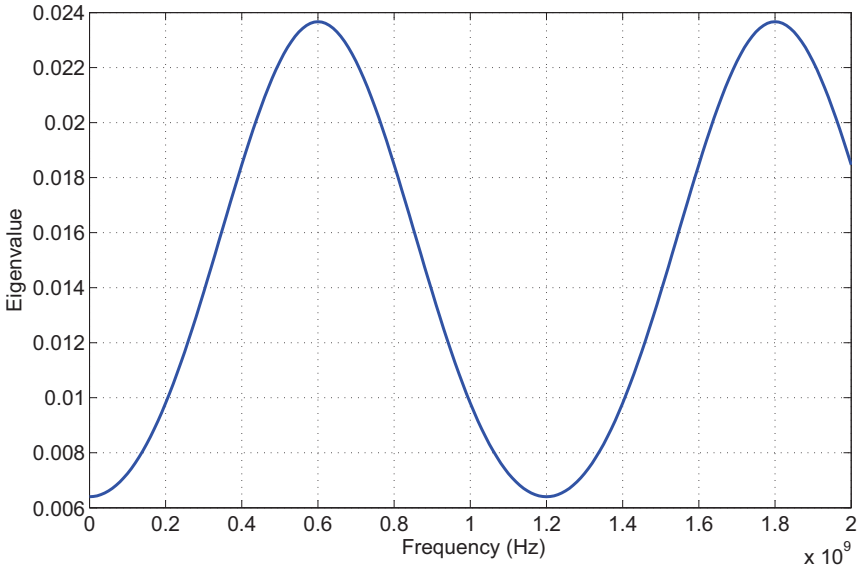

Figure 4.11: The most significant eigenvalue obtained for the TRO of the configuration of Fig. 4.8(b).

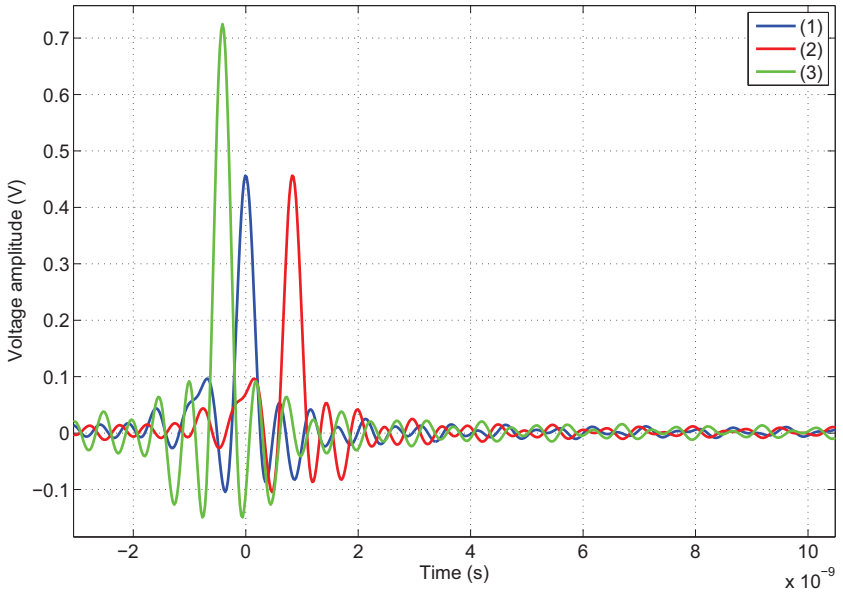

Figure 4.12: The signals injected through the testing ports of Fig. 4.8(b), after being extracted from the eigenvector corresponding to the most significant eigenvalue of the TRO.

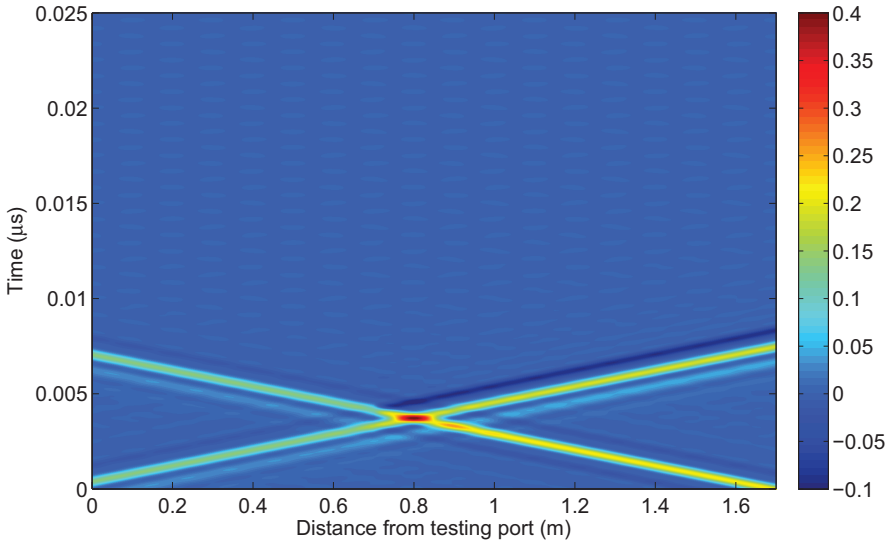

Figure 4.13: The ZT diagram observed along the third path, for the reference model of the configuration of Fig. 4.8(b). We see how the two signals focus on the target position, at a distance of 0.8 m from the testing port (1).

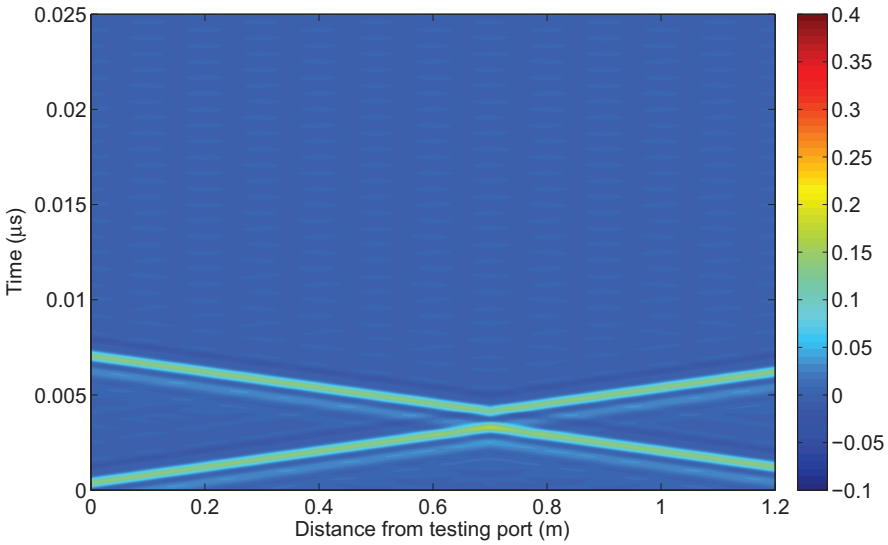

Figure 4.14: The ZT diagram observed along the second path, for the reference model of the configuration of Fig. 4.8(b).

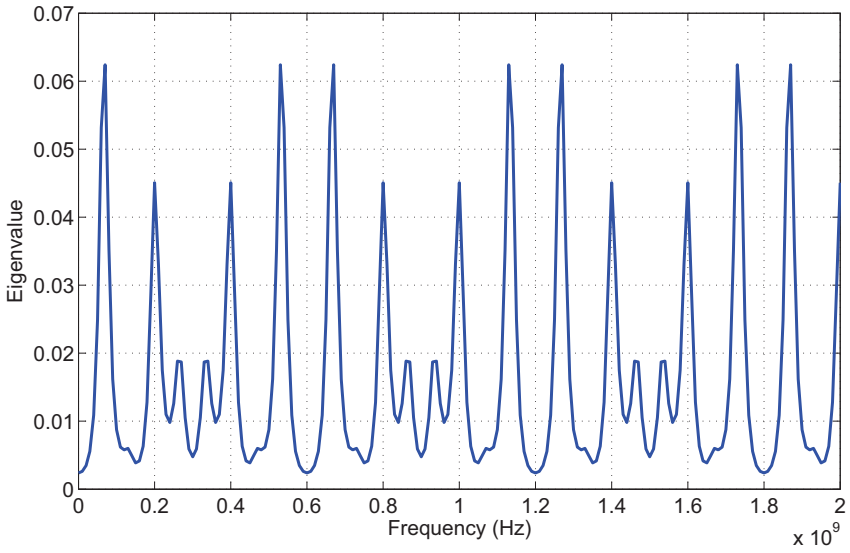

Figure 4.15: The most significant eigenvalue obtained for the TRO of the configuration of Fig. 4.8(c).

case of hard faults situated on one of the branches while all the extremities of the network are terminated with testing ports has been addressed when studying distributed reflectometry [56] but soft faults were not invoked. It is this kind of faults which we are considering in this work, and here we reconsider the same parallel load of the two previous examples, situated between the two junctions, as indicated in Fig. 4.8(c).

We assume having five testing ports, situated at the extremities of the network, as indicated on the same figure. In this case, the calculus of the eigenvalues of the TRO becomes complex, because an analytical model for the network linking its inputs to its outputs is difficult to find. Thus a numerical calculation is done to obtain the eigenvalues, with the most significant one represented in Fig. 4.15. The testing signals are represented in Fig. 4.16; these signals, when applied to the corresponding testing ports, lead to the ZT diagram of Fig. 4.17 along the fourth path. Compared to the previous cases, we notice the increasing complexity in the interpretation of this diagram, where the echoes combine mainly at the fault position, and also in other positions given the guided nature of the propagation medium, whence the need to find a suitable criterion for fault location able to clearly point the fault position.

4.4 Fault location criterion using the DORT method

Based on the examples discussed in the last section, we saw the necessity of finding an adequate criterion to describe whether or not we locate a fault in a complex network, based on the DORT method. We opted for a heuristic location method that we derived based on examining different examples of complex networks, taking into account the DORT properties.

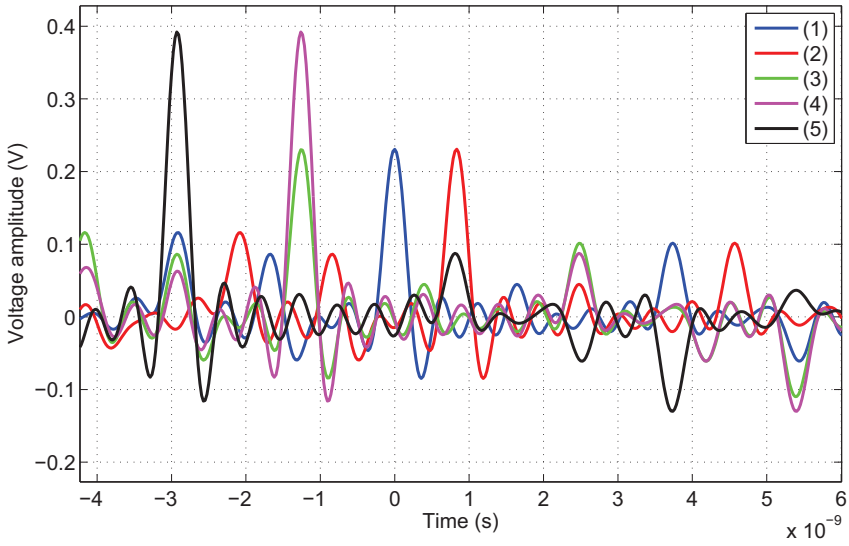

Figure 4.16: The signals injected through the testing ports of Fig. 4.8(c), after being extracted from the eigenvector corresponding to the most significant eigenvalue of the TRO.

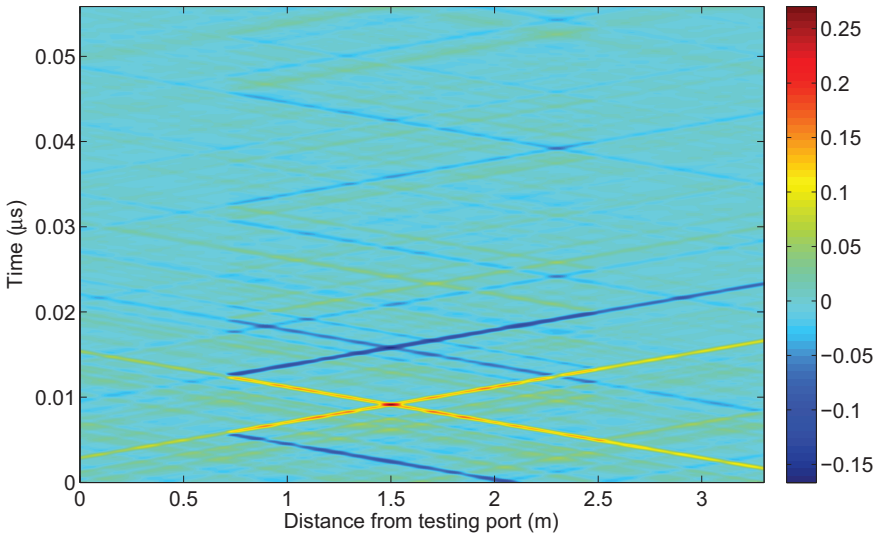

Figure 4.17: The ZT diagram observed along the fourth path, for the reference model of the configuration of Fig. 4.8(c), where we have 5 testing ports at each of the extremities of the NUT.

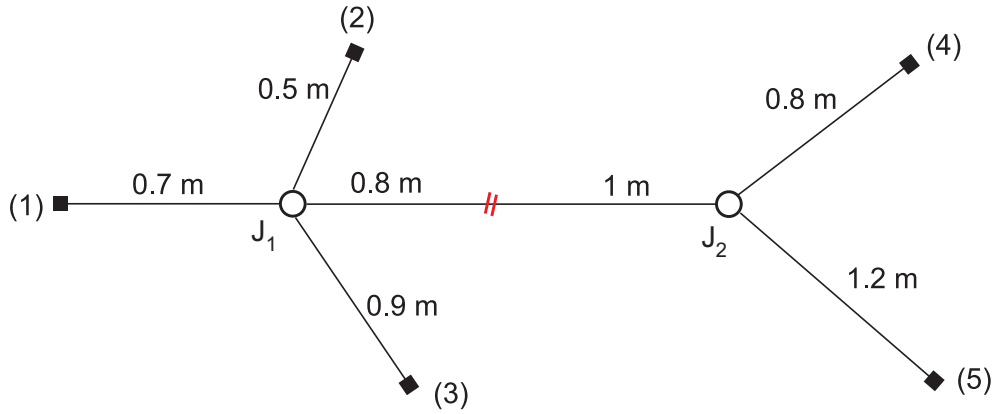

Figure 4.18: A double-junction network with testing ports at each of the extremities, representing the network we used to illustrate the derivation of the fault location method.

4.4.1 The local maximum

The network structure we chose to illustrate in order to study our location method is the one earlier considered, represented in Fig. 4.18. This structure is composed of two junctions, and five extremities. In section 4.3.3.4, we saw the limitation of the ZT diagram (see Fig. 4.17) when trying to establish a visual criterion to locate an eventual fault, based on the DORT property that aims at synthesizing testing signals focalizing on the fault position. This limitation is normal since we are dealing with guided structures, where the different echoes will inevitably interfere at different positions of the NUT. Therefore, a more precise criterion must be found; it will be based on the ability of the DORT method to focus the biggest part of the energy on the fault position. This criterion is necessary to find in order to provide an automatic fault location method that is going to be needed when addressing the statistical study later.

In the ZT diagram earlier shown in Fig. 4.17, we see how the different echoes combine at different positions that cannot be predicted in the first place. However, these signals are built using the DORT method, and consequently not all their interactions are random: if we examine the fault position, at 1.5 m from the testing port S_1, we notice a major part of the echoes combining constructively at this position, at different time instants; this is no coincidence, since these signals were originally bound to focus on the position of the fault. However, the guided propagation imposes that these signals also interact with each other, that is why we obtain other constructive interferences at different points in the network.

As previously mentioned, the DORT method enables us to synthesize signals focusing at the target position, thus leading to a higher energy observed at this position. To benefit from this property, we propose to observe a new ZT diagram, which traces the instantaneous power rather than the instantaneous amplitude of the propagating wave. This diagram is called the ZT power diagram, and an example is illustrated in Fig. 4.19, for the NUT of Fig. 4.18, with 5 testing ports, which ZT amplitudes diagram have been previously illustrated in Fig. 4.17.

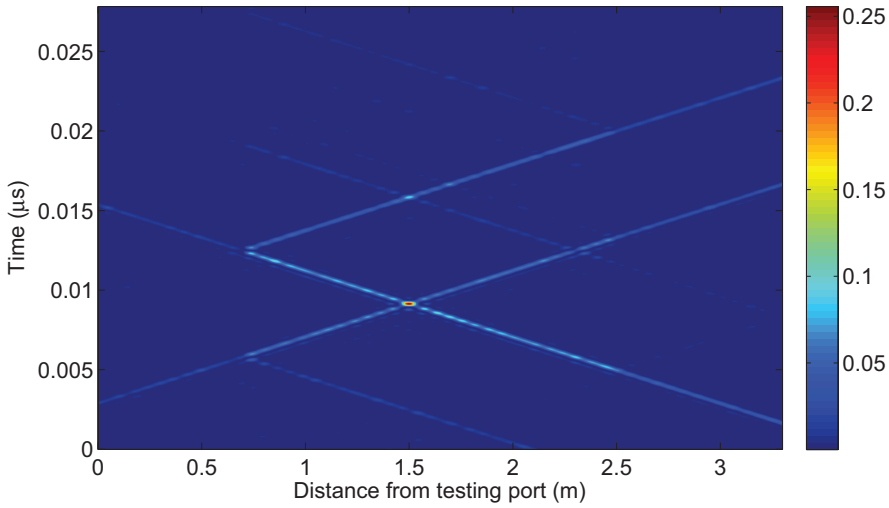

Figure 4.19: The ZT power summation observed along the branch between the testing ports (1) and (4), for the reference model of the configuration of Fig. 4.8(c).

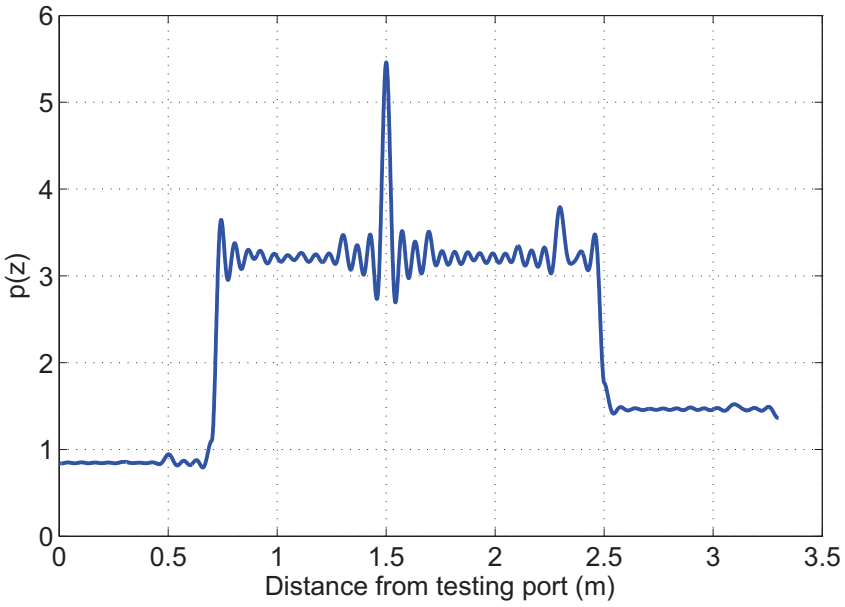

Figure 4.20: The diagram showing the power summation along the fourth branch of the network of Fig. 4.8(c).

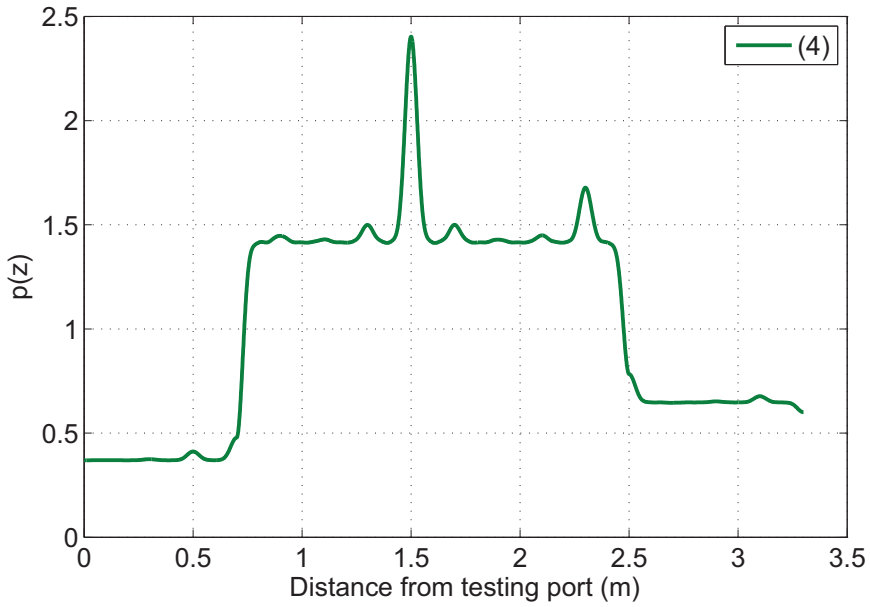

Figure 4.21: The power summation diagram along the fourth path of the NUT represented in Fig. 4.8(c), with five testing ports, obtained after filtering the eigenvectors of the TRO with a gaussian window which bandwidth is 840 MHz at -3 dB.

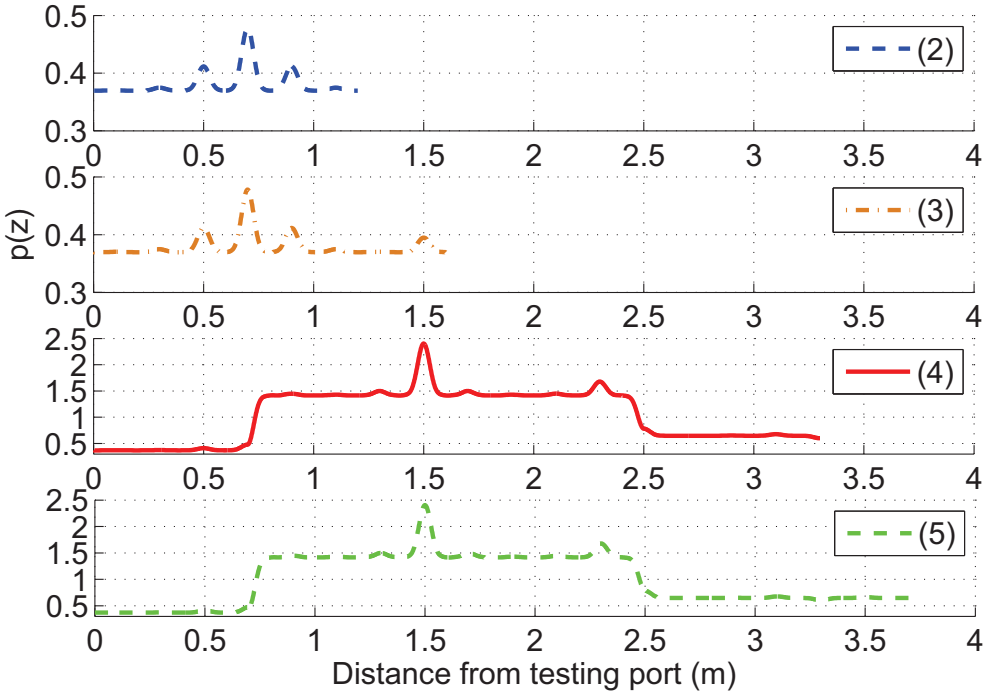

Figure 4.22: The diagram showing the power summation along the four paths (separately) of the network of Fig. 4.8(c).

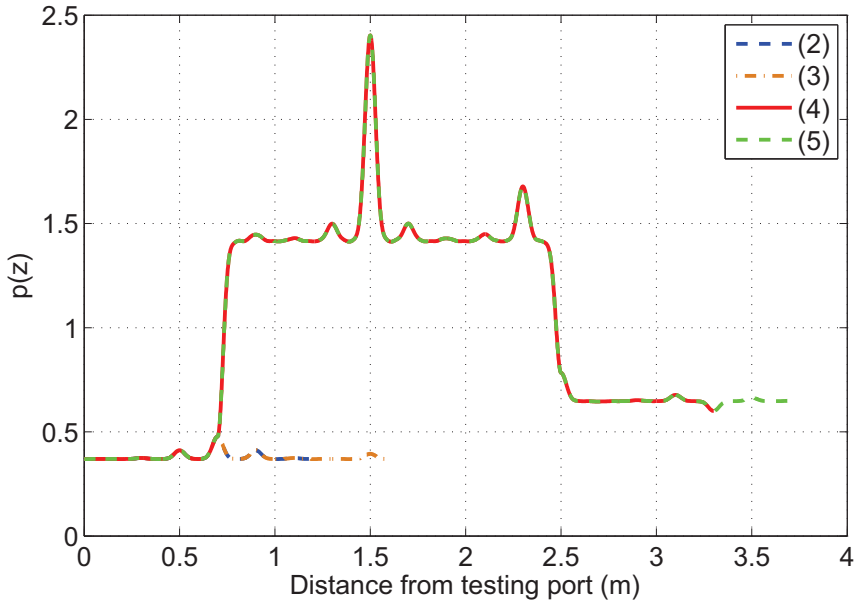

Figure 4.23: The diagram showing the power summation along the four paths of the network of Fig. 4.8(c).

This diagram results from squaring the amplitudes of the propagating wave. At the fault position, i.e., at 1.5 m from the origin, in the original ZT amplitudes diagram, the echoes combining at this position may have either positive or negative amplitudes. When we observe the ZT power diagram, and in order to benefit from all the contributions, now of the same sign, we propose to sum these contributions along the time axis; in other words we sum the instantaneous powers at each spatial position in time. The curve we obtain is the power summation diagram, represented in Fig. 4.20, along the fourth path.

In a formal way, let $v(z,t)$ denote the value of the voltage wave at the spatial position z, at the time instant t. The corresponding point in the ZT power diagram, at the position z and the time instant t has a value that equals $v^2(z,t)$. Consequently, in the power summation diagram, at each spatial position z, the value pz of the power sum is equal to

$$p(z) = \int_t v^2(z,t)dt \tag{4.11}$$

This operation allows taking into account all the contributions of the different echoes constructively interfering at the fault position. Observing the power summation diagram points to the fact of having a dominant peak at the fault position. Also, we notice an almost constant level of power sum on each of the three branches: the first one between the testing port (1) and the first junction J_1, the second one between J_1 and J_2, and the third one between J_2 and the testing port (4). Note that if we needed to attenuate the effect of high frequency components, a filter can be applied to the eigenvector components before injecting them into the reference network. This filtering operation allows to attenuate the oscillations around the dominant peaks,

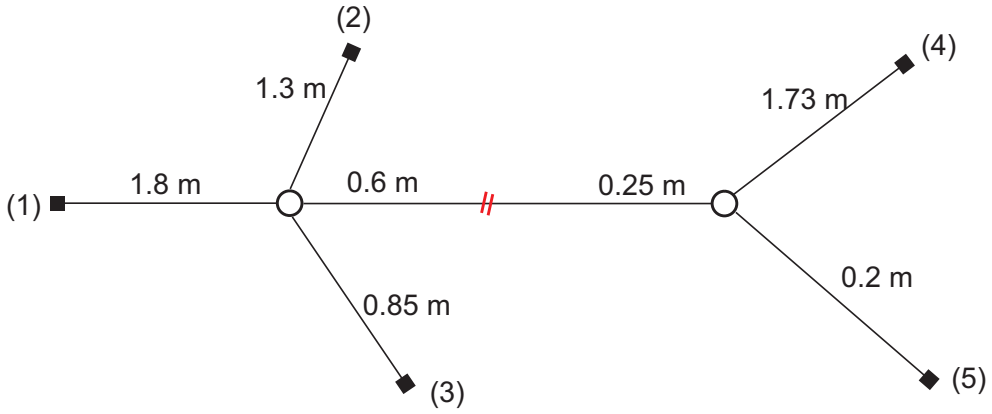

Figure 4.24: A double-junction network with testing ports at the extremities (1) and (4).

and is thus necessary when we calculate the mean values of the three power sum levels later. We applied a gaussian window to the eigenvectors, which bandwidth is 840 MHz at -3 dB, so as to result in the new power summation diagram of Fig. 4.21 along the fourth path. Here, the three levels form a kind of plateau, with the higher level reached on the fault's branch between J_1 and J_2. These plateaus are formed by the traces of the propagating pulses in the network; an illustrating example will be presented in the next section.

In order to examine the other positions in the NUT, we plotted the power summation diagrams at all the spatial positions in the network on Fig. 4.22, for the four paths separately, then superimposed on the same diagram in Fig. 4.23. The dominant peak in this case is still at the fault position. We can directly point the fault position in this case if we adopted the global maximum as a criterion.

In the second case where we considered the NUT structure illustrated in Fig. 4.24, with two testing ports (1) and (4), the other extremities being matched, the power summation diagram we obtain along the fourth path is represented in Fig. 4.25. If we consider the absolute values of the peaks, the dominant value will be that of the peak situated at 3 m from the first testing port, not corresponding to the fault which is situated at 2.4 m from the testing port (1). But if we consider the amplitude of each peak relatively to the local plateau, the fault's peak will be the dominant one and we will be able to point the fault position directly. This example shows the necessity of considering the relative amplitudes of the peaks when deriving a fault location criterion, instead of considering the absolute amplitudes, whence the need to calculate some kind of contrast, to be able to formalize the location process accordingly. The following section highlights the subject.

4.4.2 The contrast

Let us consider a simple example of two propagating waves, interfering constructively at a certain position x_0, considered to be the fault position, as shown in Fig. 4.26. We suppose that

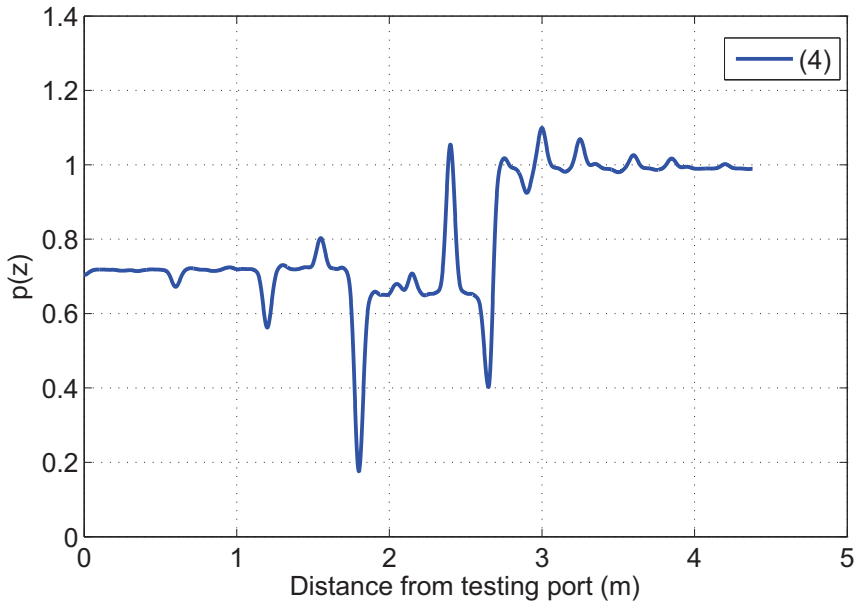

Figure 4.25: The power summation diagram along the fourth path of the NUT represented in Fig. 4.24, with two testing ports (1) and (4), obtained after filtering the eigenvectors of the TRO with a gaussian window which bandwidth is 840 MHz at -3 dB. The fault is situated at 2.4 m from the testing port (1).

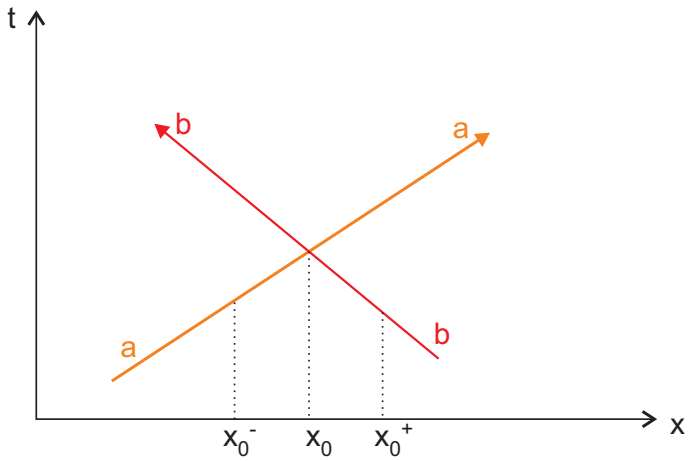

Figure 4.26: Example of two propagating waves of amplitudes a and b, interfering at the position x_0.

the amplitudes of these waves in the vicinity of x_0 are a and b. At x_0, the amplitude of the wave equals $(a+b)$. At a position x_0^- inferior to x_0, if we want to sum the traces of the amplitudes of the propagating waves in time, we find a value of $(a+b)$. In the same way, at a position x_0^+ superior to x_0, the same value $(a+b)$ is found. This value is equal to the amplitude of the peak at x_0, and consequently no contrast appears between the peak at x_0 and the surrounding plateau, if we consider the summation of the amplitudes of the propagating waves in time.

Let us now consider the summation of the instantaneous power in time, as illustrated in (4.11). At x_0^- and x_0^+ this sum is equal to (a^2+b^2), whilst at the position x_0, it is equal to $(a+b)^2$. If we consider for example a case where $a=b=1$, the sum at x_0^- and x_0^+ will be equal to 2, and at x_0 it will be equal to 4, suggesting a local contrast of 2. This example suggests the advantage of considering the instantaneous powers instead of the amplitudes when calculating a contrast. It also points an important idea: in order to be able to locate a fault, we have to obtain focalization at its position, which means we must have pulses interfering constructively at the fault position. This cannot be insured unless we have at least two testing ports, situated at both sides of the fault (to the right and left of the fault), so as to generate pulses that can propagate from both sides to reach the fault position and interfere constructively at its position; focalization can be thus obtained and we will be able to locate the fault based on the increase in the local contrast at the corresponding position. In the opposite case where one or several testing ports are disposed from one side of the fault, focalization cannot be obtained and we will not be able to locate the fault, as can be seen if we consider only one propagating wave in the previous example. In a formal way, if z_p denotes the spatial position of a certain peak, then the contrast at this position, referred to as $c(z_p)$, is calculated according to the following formula

$$c(z_p) = \frac{a(z_p)}{pl(z_p)} \tag{4.12}$$

where $a(z_p)$ represents the amplitude of the peak and $pl(z_p)$ the value of the plateau at the corresponding position.

In the general case, the power summation diagram presents several dominant peaks and plateaus. To define a local contrast for each peak, we need to define the values of the corresponding plateaus.

4.4.2.1 Definition of the plateau

We already saw in Section 4.4.1 the existence of several plateaus when plotting the power summation diagrams. Whence the need to calculate the mean value of each plateau to be able to calculate the contrast in a following step. The filtering operation we did in the same section aimed to attenuate the effects of high frequency components, thus decreasing the amplitudes of the oscillations observed in the diagrams. However, we still notice that in order to calculate a mean value for the local plateau, we have to define the spatial points that contribute to the calculus of a certain plateau, and the points that do not contribute to this plateau, such is the

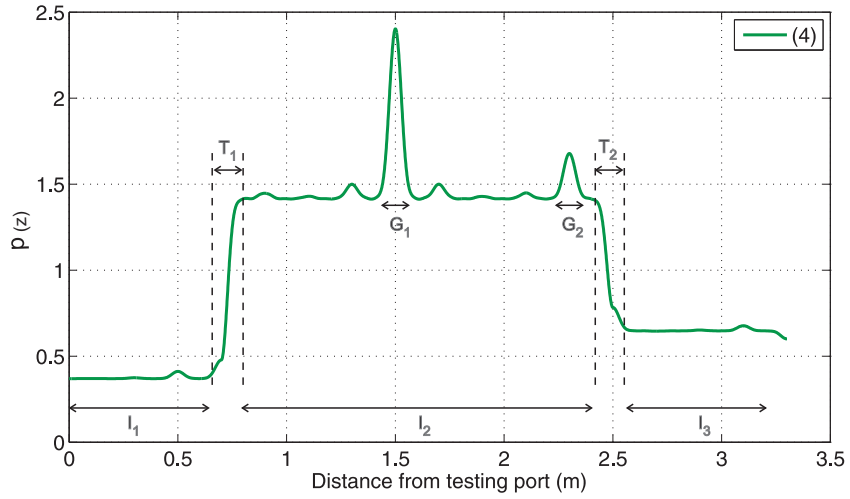

Figure 4.27: The power summation diagram along the fourth path of the NUT represented in Fig. 4.21, where the different notations used for the contrast calculation appear.

case for the peaks for example. This consists in a two-step procedure:

- Definition of the intervals I_i,

as represented on Fig. 4.27, where $i = 1, 2$ or 3. Each one of these intervals represent a set of points (spatial positions in the NUT) that are situated between two discontinuities. For example the set contained in I_1 is situated between the testing port (1) and the first junction J_1, I_2 contains points between J_1 and J_2, and so on. The first step to determine the contrast is to limit these intervals, which means excluding the points where we observe level transitions, i.e., in the vicinity of the discontinuities, as observed at the junctions positions, with the intervals denoted as T_1 and T_2.

- Definition of the intervals G_i.

These intervals are contained in the intervals I_i; because level transitions not only occur at the discontinuities positions, but also at different positions where echoes interfere. Consequently the points in the vicinity of these positions should not be accounted for when calculating the contrast. As a result, the points contained in the intervals G_i will be also excluded from the contrast calculation. To conclude, points having the same value of the plateau will belong to one of the intervals I_i but not to any of the intervals G_i contained in I_i. The plateau's value of these points will be the mean of their power sum values. Now we proceed by presenting the method we adopted to practically define these intervals.

4.4.2.2 Calculus of the delimiting intervals

In Section 4.4.1, we mentioned that the testing signals, before being injected into the NUT, are filtered in order to reduce the secondary peaks, thus facilitating the definition of the mean value

of the plateau. We chose a gaussian window and defined it in the frequency domain following the equation

$$H(f) = \frac{1}{\sigma\sqrt{2\pi}} e^{-f^2/(2\sigma^2)}, \tag{4.13}$$

where the constant σ controls the width of the gaussian 'bell'. To practically define the intervals G_i, we need to find a certain threshold, i.e., a fraction of the maximal amplitude of the gaussian curve which we chose next to be $1/10$. This choice was based on the fact that, practically, we can assume that the amplitudes which are inferior to one tenth of the maximal amplitude can be considered as negligible compared to this maximal value and thus the corresponding points can be considered not to belong to any interval G_i and are taken into account when calculating the mean values of the corresponding plateaus. On the opposite, points which amplitudes are not weaker than one tenth of the maximal value will be considered to belong to one of the intervals G_i, and consequently will not be accounted for when calculating the local plateau value.

Let us denote by Δt the time interval where the amplitude of the temporal gaussian window decreases from its maximal value to one tenth of this value, and by Δf the frequency interval where the same attenuation affects the frequency gaussian window (the Fourier transform of the temporal window), then a simple relation links the frequency support Δf to Δt [124], as follows:

$$\Delta t \Delta f = \frac{\ln(10)}{\pi} \tag{4.14}$$

where we have

$$\Delta f = \sigma\sqrt{2\ln(10)} \tag{4.15}$$

We remind that $\ln$ is the natural logarithm operator.

To conclude, by calculating Δt based on (4.14) and (4.15), we can calculate the temporal width of the intervals G_i as being equal to $2\Delta t$. The same ideas apply when calculating the limits of the intervals I_i; here we excluded the points situated in the vicinity of the discontinuities, within a distance of $\Delta t/2$ from the discontinuity's position. Once again the considered distance is based on our observations based the NUT structure we considered in our simulations, and given that we needed a criterion that can be implemented when studying this method in a statistical context in Section 4.5.

4.4.2.3 Calculus of the contrast

Having defined each of the delimiting intervals I_i and G_i, and calculated the plateau related to each one of them, we now proceed to the calculation of the contrast of the local peaks found in the power sum curve. Thus, we used the function *findpeaks* available in Matlab. This function compares the power sum value of the current point to that of the two neighboring points, and if this value is the largest one among the three values then the corresponding point is a local maximum.

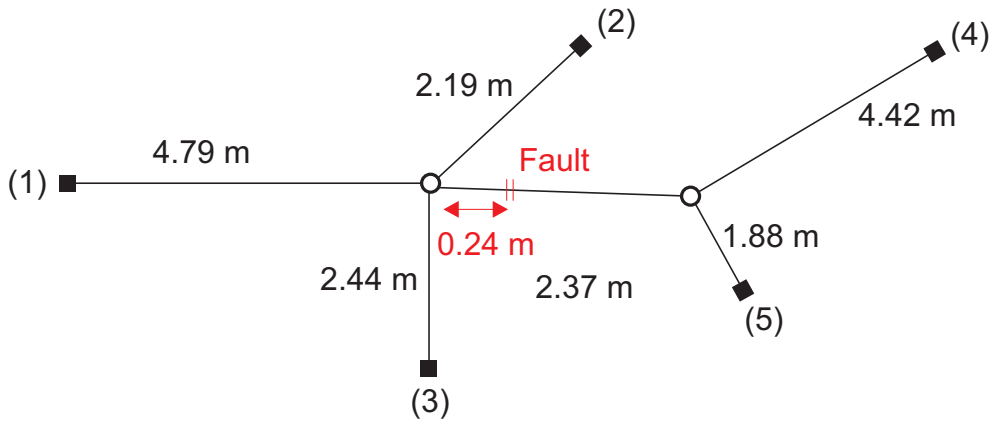

Figure 4.28: Example of a network where the soft fault (a parallel load which value is 400 Ω) is embedded in the system. This example is used to illustrate the calculus of the contrast in Fig. 4.30.

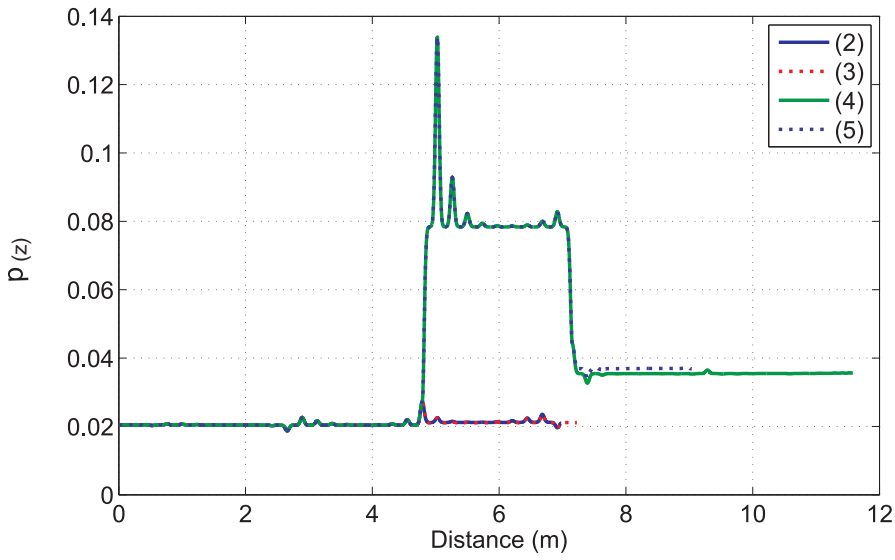

Figure 4.29: The power summation diagram along the four branches of the network illustrated in Fig. 4.28.

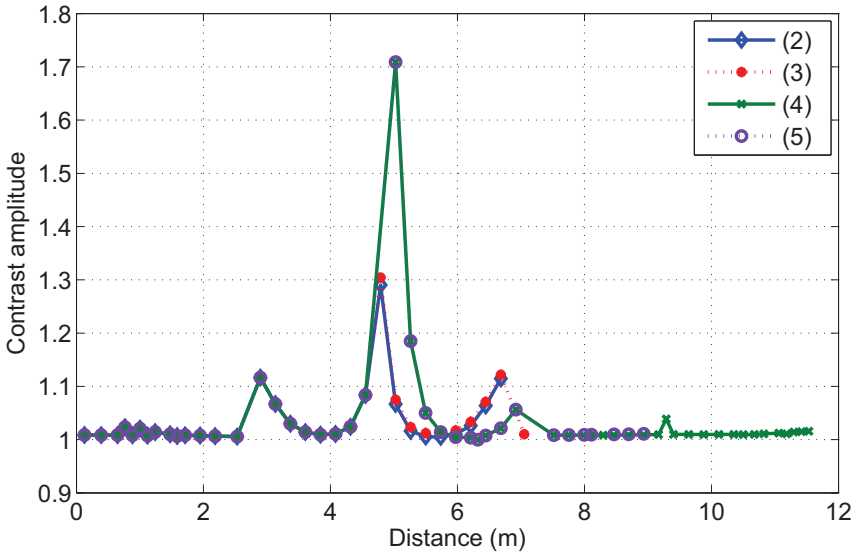

Figure 4.30: The contrast calculated along the four branches of the network of Fig. 4.28.

When the step of determining the local peaks is finished, the contrast of these peaks is found by calculating the ratio of the amplitude of the peak to that of the corresponding plateau previously calculated.

For illustration purposes, we considered the example of Fig. 4.28, and the corresponding power summation diagram for all the branches, represented in Fig. 4.29. The calculus of the contrast among the four paths leads to the diagram represented in Fig. 4.30.

The observation of the results points out an important fact: we are able to directly point the soft fault location. It is situated on the fourth (or fifth) path, at a distance of 5.03 m from the testing port (1), corresponding to the actual position of the fault.

4.4.3 Influence of the number of testing ports on the DORT performance

In the previous example, we were able to directly point the position of the fault in the NUT, using five testing ports. In Section 4.4.2, we pointed out the necessity of having testing ports situated from both sides of the fault in order to obtain focalization. The aim of this section is to investigate this idea through simulations, before proceeding to a more detailed study.

We reconsider the NUT shown in Fig. 4.24, which we represented in Fig. 4.31 for illustration purposes. If we have one testing port at the position (1), the other ends being matched, then the power summation diagram we obtain is illustrated in Fig. 4.32. We observe three plateaus, corresponding to the traces of the propagating waves in the NUT, and we clearly notice the absence of focalization. In the same way, if two testing ports were present from one side of the fault, at the positions (1) and (2) for example, we obtain the diagram of Fig. 4.33 not showing any focalization. But if the two testing ports were present at the positions (1) and (5), the

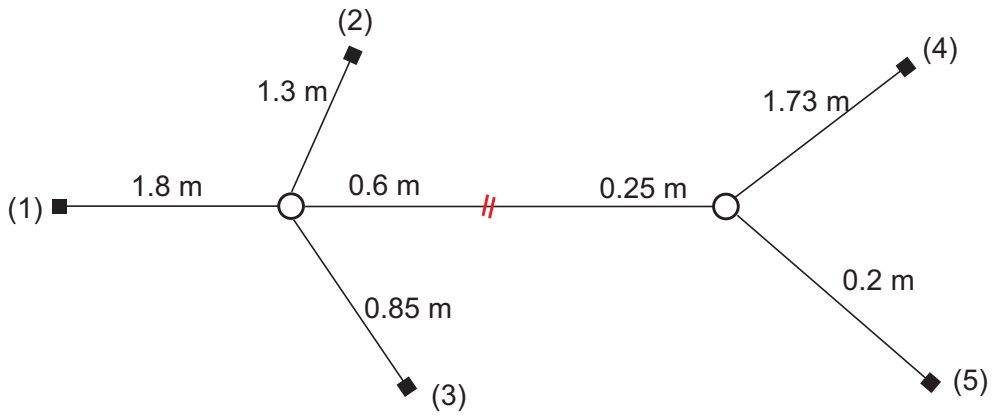

Figure 4.31: A double-junction network with five extremities where testing ports can be connected, the other extremities being matched.

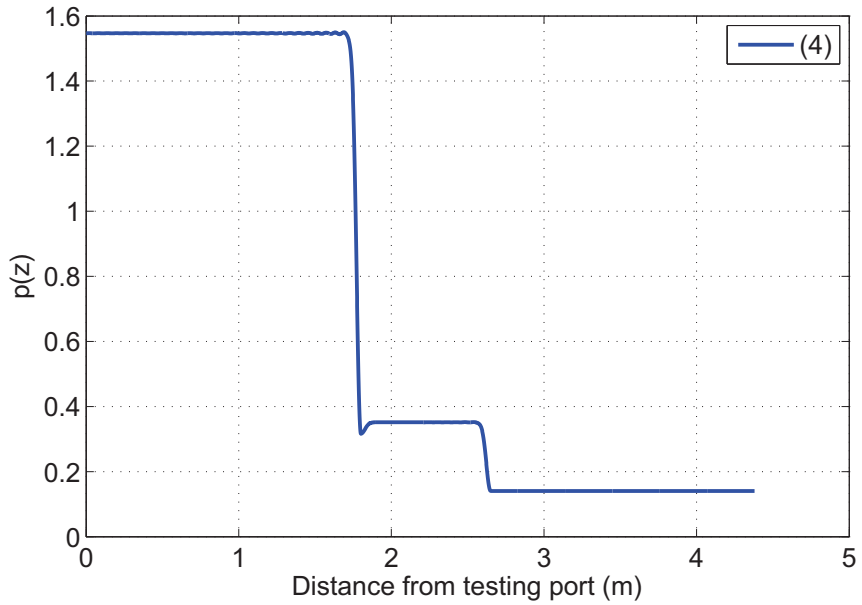

Figure 4.32: The power summation diagram along the fourth path of the NUT represented in Fig. 4.31, with one testing port at (1) and a fault of $400\ \Omega$ at 2.4 m from the testing port (1).

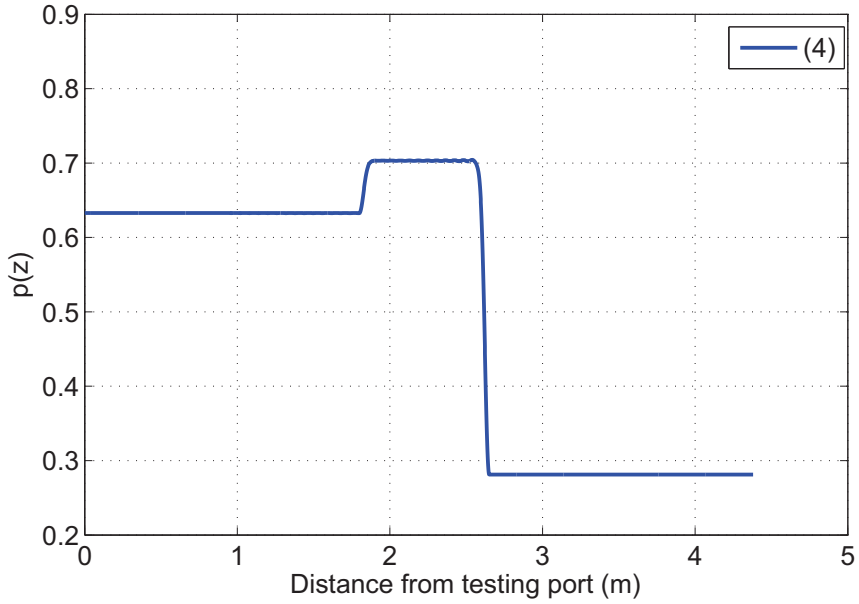

Figure 4.33: The power summation diagram along the fourth path of the NUT represented in Fig. 4.31, with two testing ports at (1) and (2) and a fault of 400 Ω at 2.4 m from the testing port (1).

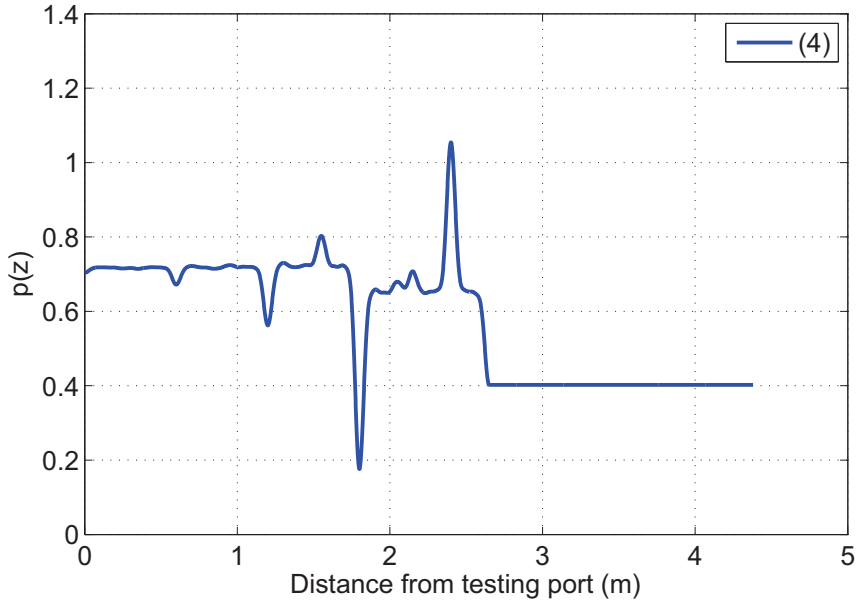

Figure 4.34: The power summation diagram along the fourth path of the NUT represented in Fig. 4.31, with two testing ports at (1) and (5) and a fault of 400 Ω at 2.4 m from the testing port (1).

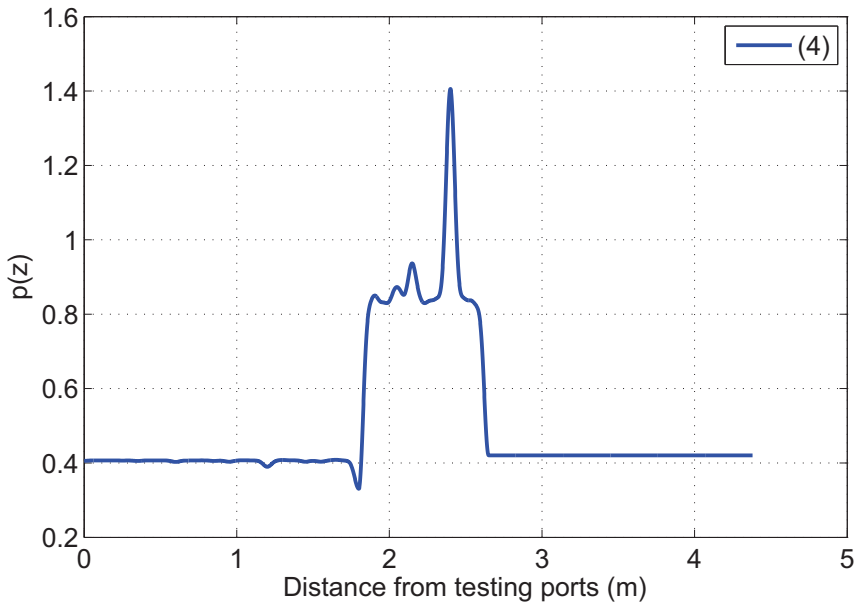

Figure 4.35: The power summation diagram along the fourth path of the NUT represented in Fig. 4.31, with three testing ports at (1), (2) and (5) and a fault of 400 Ω at 2.4 m from the testing port (1).

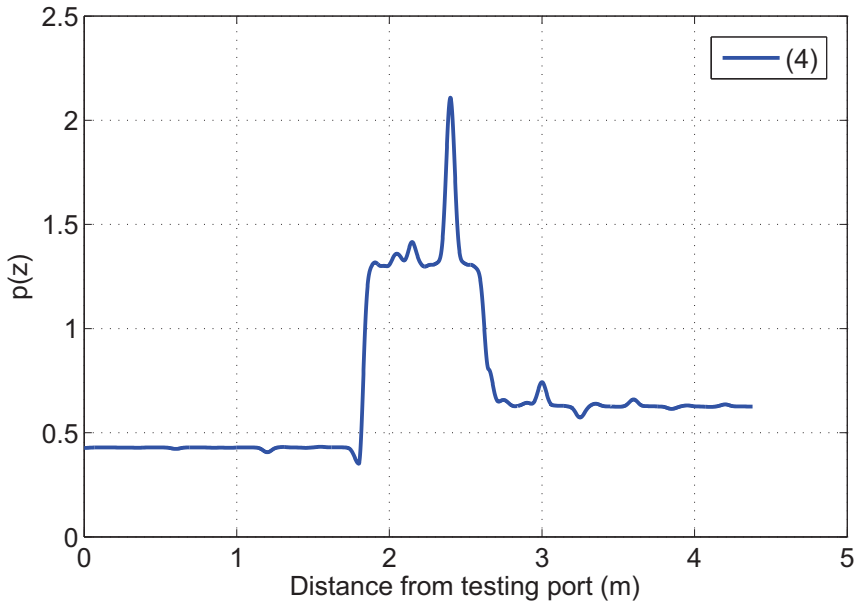

Figure 4.36: The power summation diagram along the fourth path of the NUT represented in Fig. 4.31, with four testing ports at (1), (2), (4) and (5) and a fault of 400 Ω at 2.4 m from the testing port (1).

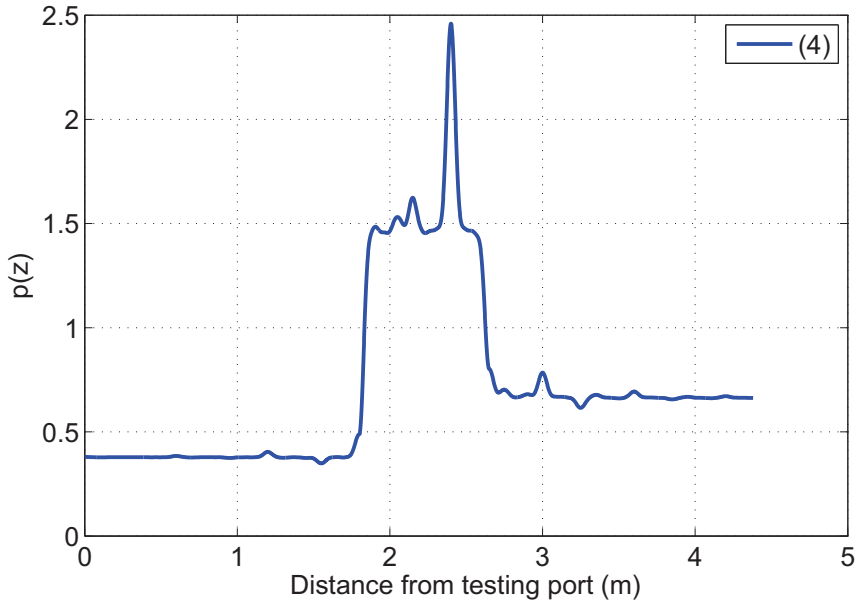

Figure 4.37: The power summation diagram along the fourth path of the NUT represented in Fig. 4.31, with five testing ports and a fault of $400\ \Omega$ at 2.4 m from the testing port (1).

obtained diagram is the one illustrated in Fig. 4.34, where focalization at the fault position is obtained and the fault can be thus localized. Raising the number of testing ports to three, situated at the positions (1), (2) and (5) gives the diagram of Fig. 4.35, where the contrast at the fault position is almost the same than the one in the previous case (≈ 1.75). If we put four testing ports at the positions (1), (2), (4) and (5), we observe the diagram of Fig. 4.36, and with a total number of five testing ports we obtain the diagram of Fig. 4.37. In the two last cases focalization at the fault position is also obtained and the fault is once again directly located.

The previous examples show that the performance of the DORT method is influenced by the number of testing ports and their positions; this factor is one many other factors that might influence the method's performance, whence the necessity to analyze these parameters and their possible effects on the DORT performance through a statistical study which is going to be presented next.

4.5 Statistical study: database definition

In order to conduct a statistical study, a database containing a large number of NUTs is necessary. The way such a database is defined is thus essential, after having predefined the parameters of interest that might influence the method's performance. These parameters serve to define the network structures that are going to be generated and studied, in order to derive trends and rules allowing to characterize our new fault location method, which we will refer to as the differential

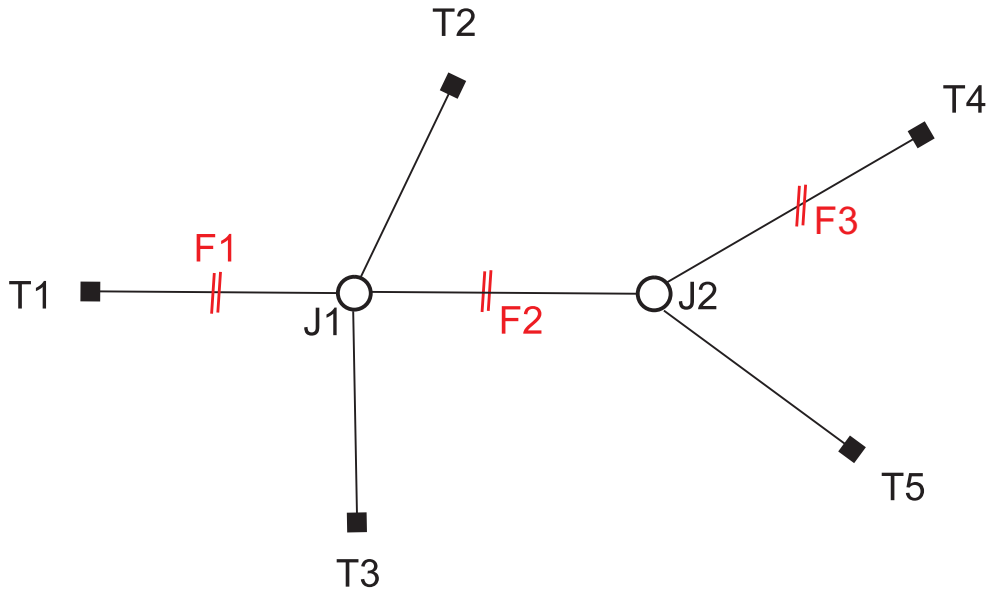

Figure 4.38: The network structure to be studied in the statistical analysis part.

DORT.

4.5.1 Studied model and influencing parameters

The network structure we chose is the one we earlier considered in our different examples, represented in Fig. 4.38. It is a double junction network, where the two junctions are denoted as J_1 and J_2. A total of five testing ports can be inserted on the extremities of this network, at the positions referred to as T_i, having $i = 1, 2, ..., 5$. Three fault positions were considered, that are indicated as F_i ($i = 1, 2, 3$). The five extremities T_i were considered matched to the network, whether testing ports existed or not at these positions.

The reason to choose this structure is that, on one hand it is considered to be complex compared to those usually studied in this domain (single cables in most cases) especially if the fault is soft, which is our case. On the other hand, this structure presents a good compromise concerning the limitations of the code we wrote in Matlab, and the processing time to generate the database and analyze the results thereafter. In our present study we consider the case of one soft fault.

In a first step, we define the set of parameters which are going to be addressed in our study. Of course, this choice does not cover all the influencing parameters, but was done in terms of the time and code limitations, and based on a few examples we considered before proceeding with the study, aiming to asses the different elements possible influence on the location of an eventual fault.

In the present analysis, we considered the following parameters

The number of testing ports One of the important parameters to study is the number of testing ports used in the differential DORT, as we already saw when considering several examples in the previous section, where a change in the number of testing ports allowed or not to locate the soft fault. This intuitively implies that the fault position with respect to these testing ports should also be taken into account. In the configuration we will be studying, the number of testing ports varies from 1 to 5, and several fault positions will be considered, as already indicated. However, based on the DORT properties and the preliminary analysis done in Section 4.4.3, one can expect to have a higher location probability when testing ports exist from both sides of the fault, and a low location probability in the opposite cases. This is due to the fact that the DORT aims at synthesizing signals bound to focus on the fault position, and thus signals from both sides of the fault are needed in order to obtain focalization at the fault position. The validity of these intuitive ideas will be assessed through the statistical analysis and the results we obtain.

The fault position The fault position is also a factor that is expected to influence the differential DORT performance. Apart from the fault position relatively to the testing ports (as for example if surrounded by testing ports or not), a factor that might have an impact on the method's performance is its distance from the testing port: for F_1 and F_3, we expressed this parameter in terms of the distance of the fault to the nearest testing port, relatively to the distance between this testing port and the nearest junction (the ratio is expressed as a percentage). For F_2, this parameter is the distance between J_1 and F_2, compared to the distance between J_1 and J_2. For example, if F_1 is situated at 50 percent from T_1, that means it is in the middle of T_1 and J_1, and so on.

However, this distance parameter is not expected to influence the probability of localization, based on the fact that the DORT yields signals that focus on the fault position. In fact, propagation delays in terms of distances are directly compensated by the TRO definition.

Several other parameters exist, such as the nature of the fault, the threshold we use in the location algorithm, the bandwidth, the noise impact, etc. The nature of the fault will be considered when studying experimentally the differential DORT. The other parameters were not considered in this study.

Concerning the nature of the fault, we already saw in the experimental results in the previous chapter that a soft fault has a reflection coefficient that depends on the frequency, suggesting its dispersive nature. However, the statistical analysis in this chapter was conducted before the experimental results of the previous chapter, that is why we considered a resistive parallel load in the simulations, and we did not consider dispersive faults. Nevertheless, real dispersive faults will be studied in the experimental results section in the present chapter. For the statistical study we consider the fault as a parallel resistive load which value is $400\ \Omega$. Note however that the resistive and dispersive cases result in similar performances, thus suggesting the validity of our simulations.

4.5.2 Database generation

In the double junction configuration we adopted in Fig. 4.38, we considered three fault positions, denoted as F_1, F_2 and F_3. For each position, we generated a set of NUTs, where the lengths were randomly chosen, and then the fault was introduced on a certain distance of the testing port (or the junction J_1 in the case of F_3) based on a set of predefined ratios representing the fault's distance to the testing port, invoked in the previous section. For each of these configurations, we also considered the cases of having 1, 2, 3, 4 and 5 testing ports, and all their possible positions in the network (further discussion about this subject will be next addressed). We generated a total set of 3720 files.

After this first step of generating the database, we proceeded to analyzing the results. Thus we wrote several functions aiming to extract and analyze the desired information, based on the location criterion we earlier developed. The first step is to determine the contrast for all the peaks in the NUT, based on the ideas discussed in Section 4.4, and then we choose the maximum contrast. If its spatial position corresponds to the fault's one, we consider that the fault is located. If this is not the case, the fault is not correctly located.

4.6 Statistical study: results analysis

Before proceeding with the results analysis, we draw the reader's attention to the fact that, given the limitations in the number and configurations of the generated NUTs, we will not be observing the values of the location probabilities, but rather the rates of the number of successes (i.e., when we locate the fault for a given NUT) to the total number of analyzed NUTs. This rate will be referred to as p_{SR}, with SR being the acronym of Success Rate. Consequently, in order to have an idea of the value of the location probability, we proceeded to an estimation of the latter based on the Maximum Likelihood Estimation (MLE) [125], and the estimated value of this probability is going to be referred to as p_{MLE}. The following section highlights the subject.

4.6.1 Estimator of the fault location probability

Let x_i denote the random variable corresponding to the result of one test, with a probability p of having a success, i.e., locating the fault. Our goal is to determine this probability.

The variable x_i follows a Bernoulli distribution, with a success probability p, and a failure probability (no location) of $q = 1 - p$. Consequently, the sum X of the variables x_i follows a binomial distribution, $X \sim B(n, p)$, where n is the total number of experiments, i.e., the number of analyzed files.

The probability mass function of the variable X can thus be written as

$$f(k; n, p) = Pr(X = k) = C_n^k p^k (1 - p)^{(n-k)} \tag{4.16}$$

where Pr stands for probability, and C_n^k is known as the binomial coefficient,

$$C_n^k = \frac{n!}{k!(n-k)!} \tag{4.17}$$

The formula (4.16) can be understood as follows: we want to have k successes among n trials. These successes can occur anywhere among the n trials, so we consider all the different possible ways of distributing the k successes among the sequence of n trials, equal to C_n^k.

Looking back at this same formula, the parameter p is unknown. To estimate it, we chose the Maximum Likelihood Estimator (MLE), given that it is a powerful estimator that allows us to obtain a better estimation of the probability value than the frequency of occurrence does, given the relatively low number of analyzed NUTs.

To calculate the estimated location probabilities in each of the analyzed situations, we used two functions in matlab, *binornd* and *binofit*; the first function is used to generate a binomial distribution, with n trials and the success rate p_{SR} found in the statistical results. Then *binofit* is used to estimate p_{MLE} and the 95% confidence interval (denoted later as $95\%ci$) of p_{MLE}. Note that the function *binofit* uses the Clopper-Pearson [126] method to calculate the confidence interval.

One important thing to note is that the number of analyzed files changes from one case to another. For example, given that we considered 3 different positions of the fault, F_1, F_2 and F_3, the number of generated files for each of them is 1240 files. This number is further reduced if we consider a certain fault and a certain distance percentage of the 5 considered values (see Section 4.6.2); it will be 248 files. Another reduction occurs when we consider all the possible configurations (see Section 4.6.3) of the sources. That is why the number of analyzed files will be indicated in each of the studied cases.

4.6.2 Influence of the relative position of the fault

We start by studying the influence of the fault position on the location probability. As already invoked, the fault position was expressed as a distance percentage, relatively to the nearest testing port (for F_1 and F_3) or to a neighboring discontinuity (for F_2). For each value of the distance percentage we considered the cases of 1, 2, 3, 4 and 5 testing ports, with all their possible configurations. By configuration we mean their position in the NUT: for example one testing port can be placed at T_1 or T_2 or T_3 or T_4 or T_5, whilst two testing ports can be for example placed at T_1 and T_2, or T_3 and T_4, and so on. Each possible configuration was taken into account within the total number of testing ports in this section, and the total number of analyzed files for a particular fault and a particular distance percentage is indicated in Table 4.1. In the next section we detail the influence of each possible configuration on the location probability.

The results of p_{SR} are shown in three tables, each one corresponding to one fault position. Table 4.2 corresponds to the fault F_1, where the distance percentages vary from 10 to 70, and

number of testing ports	1	2	3	4	5
number of files	40	80	80	40	8

Table 4.1: Number of analyzed configurations (or files) for each particular fault, at a particular distance percentage, in terms of the number of test ports illustrated in the cells of the first row. The number of files is indicated in the cells of the second row.

Number of	Relative distance percentages				
testing ports	10%	20%	40%	50%	70%
1	0	0	0	0	0
2	0.25	0.25	0.25	0.25	0.25
3	0.55	0.55	0.55	0.55	0.55
4	0.8	0.8	0.8	0.8	0.8
5	1	1	1	1	1

Table 4.2: Success rates for the localization of fault F_1 as represented on Fig. 4.38, in terms of the distance percentage of the extremity T_1 and the number of testing ports.

the number of testing ports changes horizontally from 1 to 5. In the same way, Table 4.3 corresponds to the fault F_2 and Table 4.4 to the fault F_3.

Observing the values of the obtained success rates for the three faults, we clearly notice that they do not depend on the percentage of the fault's distance from the corresponding extremity, which validates our expectations. We also see that the faults F_1 and F_3 are equivalent in terms of probabilities; indeed, the two faults have equivalent positions when it comes to testing ports: they are both 'seen' by a single testing port from one side, and by the others from the other side. Consequently, we will later reduce the number of studied faults to two, F_1 and F_2.

Let us now estimate the probabilities p_{MLE} taking into account the previous observations. Thus we consider the two faults F_1 and F_2, and one set of success rates corresponding to a

Number of	Relative distance percentages				
testing ports	10%	20%	40%	50%	70%
1	0	0	0	0	0
2	0.5	0.5	0.5	0.5	0.5
3	0.9	0.9	0.9	0.9	0.9
4	1	1	1	1	1
5	1	1	1	1	1

Table 4.3: Success rates for the localization of fault F_2 as represented on Fig. 4.38, in terms of the distance percentage of the extremity T_2 and the number of testing ports.

Number of testing ports	Relative distance percentages				
	10%	20%	40%	50%	70%
1	0	0	0	0	0
2	0.25	0.25	0.25	0.25	0.25
3	0.55	0.55	0.55	0.55	0.55
4	0.8	0.8	0.8	0.8	0.8
5	1	1	1	1	1

Table 4.4: Success rates for the localization of fault F_3 as represented on Fig. 4.38, in terms of the distance percentage of the junction J_1 and the number of testing ports.

Number of testing ports	p_{SR}	p_{MLE}	95% ci
1	0	0	[0; 0.0881]
2	0.25	0.3125	[0.2135; 0.4259]
3	0.55	0.5875	[0.4718; 0.6965]
4	0.8	0.75	[0.588; 0.8731]
5	1	1	[0.6306; 1]

Table 4.5: Estimated location probabilities p_{MLE} and the 95% confidence interval (ci) of this probability, for fault F_1 (equivalently F_3) as represented on Fig. 4.38. The number of testing ports is indicated in the first left column.

certain relative distance percentage (given that there is the same set of success rates for all the percentages). The case of fault F_1 is shown in Table 4.5, whilst the one corresponding to the second fault F_2 is shown in Table 4.6. In the two cases, one testing port leads to a null location probability, whilst adding more testing ports increase this probability so as to reach 1 when using five testing ports. In the case of the fault F_1, situated in front of the testing port T_1, i.e., not masked from this port by any junction or discontinuity, the differential DORT method is not able to locate the fault whilst standard TDR is able to, and consequently the DORT does not present any advantage over TDR in this particular case. The case of one testing port not leading to fault location in the case of the differential DORT was predicted when we considered the preliminary study in Section 4.4.3, where it was revealed that the DORT synthesizes signals that focalize on the fault position, requiring the existence of testing ports from both sides of the fault. Thus a more detailed analysis taking into account the configuration of the testing port relatively to the fault is going to be presented in the following section, aiming to generalize these ideas.

The case of five testing ports leads to an estimated location probability of 1 in the case of F_1, with a 95% confidence interval of plausible values for the probability ranging from 0.6306 to 1. This refers to the fact that, if a sample of analyzed files is taken repeatedly from the

Number of testing ports	p_{SR}	p_{MLE}	95% ci
1	0	0	[0; 0.0881]
2	0.5	0.525	[0.4102; 0.6379]
3	0.9	0.9	[0.828; 0.9641]
4	1	1	[0.9119; 1]
5	1	1	[0.6306; 1]

Table 4.6: Estimated location probabilities p_{MLE} and the 95% confidence interval (ci) of this probability, for fault F_2 as represented on Fig. 4.38. The number of testing ports is indicated in the first left column.

same analyzed population (all the analyzed files), and a confidence interval calculated for each sample, then 95% of the intervals will include the unknown parameter p_{MLE}. In this case the width of the interval is 0.3694, whilst for one testing port it is 0.0881, suggesting that in the first case of five testing ports, more files should be analyzed if we want to reduce the interval width, which will eventually increase the precision on calculated probability value p_{MLE}.

In the case of F_2, for the same number of testing ports, we notice a bigger value of p_{MLE} compared to the case of F_1. This will be explained based on the testing ports configuration that is going to be addressed in the next section. In this case, an estimated probability of 1 is reached with four and five testing ports, which points the advantage of the DORT method in such cases where we are able to directly locate the fault without any need for iterations.

Based on the conclusion of the apparent invariance of the location probability with the fault's distance percentage, we will limit the remaining analysis to a single relative distance, considered to be 40.

4.6.3 Influence of the sources configuration and number

As observed in Section 4.4.3, the position of the testing ports regarding the fault's one influences the ability of the differential DORT to localize the fault. The aim of this section is to investigate this issue through a more extended study including several configurations of the testing ports.

One testing port can be placed on one of the five positions T_i ($i = 1, ..., 5$), meaning C_5^1 different possibilities, where C_5^1 is the number of possible combinations, when picking out one position in five potential choices. In the same way, two testing ports can be chosen according to C_5^2 different combinations, and so on.

The total number of possible configurations of the testing ports is thus:

$$C_5^1 + C_5^2 + C_5^3 + C_5^4 + C_5^5 = 31 \tag{4.18}$$

We remind that

$$C_n^p = \frac{n!}{p!(n-p)!}. \tag{4.19}$$

	Number of testing ports				
Fault	1	2	3	4	5
$F1$	0	0.3125	0.5875	0.75	1
$F2$	0	0.525	0.9	1	1

Table 4.7: Estimated location probabilities of the faults as represented on Fig. 4.38, in terms of the number of sources.

Based on all the possible configurations, we calculated the success rates when trying to locate the fault for the two positions F_1 and F_2 and for each configuration; the results confirmed the preliminary results obtained in Section 4.4.3: for all the configurations where the testing ports were all situated from one side of the fault, we obtained a null success rate, and this result applies for both F_1 and F_2. The testing signals synthesized using the differential DORT are bound to focus on the fault position, and this focalization is hard to obtain if there are not testing ports from both sides of the fault.

Taking into account these results, we now turn our attention to the location probabilities when testing ports are arranged from both sides of the fault. We already mentioned that we consider one distance percentage, so we put the corresponding estimated probabilities values for F_1 and F_2, taken from Tables 4.5 and 4.6 in the same Table 4.7, for illustration purposes.

4.6.3.1 Conditional location probabilities

Let $P_{l|n,2s}$ denote the conditional location probability when having n testing ports arranged on both sides of the fault, and $P_{l|n,1s}$ the conditional location probability when having the n testing ports arranged from one side of the fault. The global location probability when having n testing ports, $P_{l,n}$, can be written as

$$P_{l,n} = P_{l|n,1s}P_{n,1s} + P_{l|n,2s}P_{n,2s} \tag{4.20}$$

where $P_{n,1s}$ and $P_{n,2s}$ are the probabilities of having the n testing ports at one side from the fault and at both sides respectively.

Based on the analysis we did in the previous section, we have verified that the location probability when having the testing ports from one side of the fault $P_{l/n,1s}$ is equal to zero, and consequently (4.20) can be written as

$$P_{l,n} = P_{l|n,2s}P_{n,2s}, \tag{4.21}$$

so as to have

$$P_{l|n,2s} = \frac{P_{l,n}}{P_{n,2s}} \tag{4.22}$$

It is this probability which we will be calculating next for the two faults, for a varying number of testing ports.

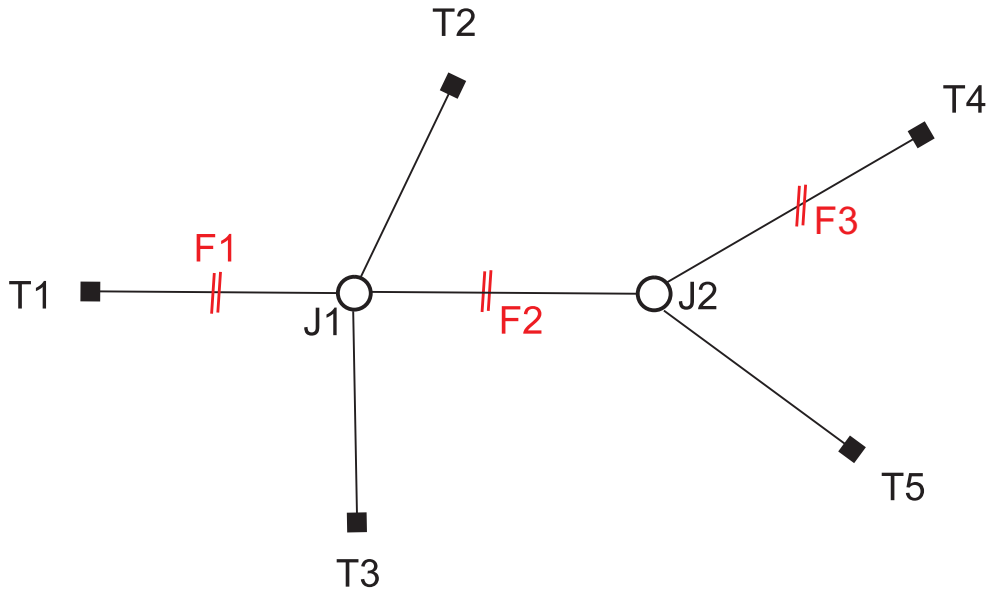

Figure 4.39: the studied network structure.

n	2	3	4
$P^{F1}_{n,2s}$	4/10	6/10	4/5
$P^{F1}_{l/n,2s}$	0.7813	0.9792	0.9375

Table 4.8: Conditional estimated location probabilities of the faults $F1$ as represented on Fig. 4.38, in terms of the number of sources, for a percentage of 40.

Let us begin by considering the first fault $F1$, represented in Fig. 4.39. In the case of one testing port ($n = 1$), the probability of locating an eventual fault is zero. If we consider two testing ports, we will have $C^2_5 = 10$ possible configurations. Among these ten configurations, the number of configurations where the testing ports are on both sides of $F1$ is four (one source at position (1) and the other at any position of the four remaining ones). Consequently, given that the global location probability calculated using the simulation results is 0.3125 (see Table 4.7), the conditional location probability is

$$P^{F1}_{l|2,2s} = \frac{P_{l,2}}{P_{2,2s}} = \frac{0.3125}{4/10} = 0.7813 \tag{4.23}$$

We resume the calculated probabilities for $F1$ in Table 4.8, where the first line contains the number of testing ports; we excluded $n = 1$ and $n = 5$ because the probabilities are respectively 0 and 1 for the two cases.

We notice how, for both cases of fault positions, when the number of testing ports on both sides of the fault increases, the location probability increases until it reaches the value 1 for five testing ports and for both cases F_1 and F_2. In this case using the differential DORT would allow us to directly locate the fault, without any need for iterations. For the case of F_2 where the fault

n	2	3	4
$P^{F2}_{n,2s}$	6/10	9/10	5/5
$P^{F2}_{l/n,2s}$	0.8750	1	1

Table 4.9: Conditional Location probability of the faults $F2$ as represented on Fig. 4.38, in terms of the number of sources, for a percentage of 40.

is embedded in the system, using three or more testing ports leads to a location probability that equals 1, illustrating once more the advantage of the method in this case where the fault is not directly 'seen' by the testing ports, but rather masked by junctions.

4.7 Experimental study

The statistical study we conducted in this chapter dealt with resistive faults, i.e., with reflection coefficients not depending on the frequency. In order to examine the differential DORT performance in real soft faults cases, we propose to conduct an experimental study to asses the accuracy of the location method in practical situations.

4.7.1 Experimental setup

The experimental measurements were conducted using the same material and procedure as in the previous chapter. However, we remind of these elements for the sake of clarity.

The VNA we used is a Rohde & Schwarz ZVB network analyzer, with a frequency range from 300 kHz to 8 GHz, and four testing ports. The intermediate-frequency filter bandwidth was set to 100 kHz, and the input power to a 0 dBm harmonic excitation signal. The cables we used are coaxial cables, with a $50\ \Omega$ characteristic impedance, and a velocity of propagation that equals 0.8 times the speed of light. One of the faults we studied in the previous chapter, obtained by crushing the 30-cm semi-rigid coaxial cable over a distance of 1 cm, was the one we considered in our experimentations in this chapter, as shown in Fig. 4.40(a) and (b). The need for a baseline measurement was satisfied by considering an unaltered sample as the reference one; the two sections are shown in Fig. 4.40(c); they share the same dimensions and features.

The studied configurations are shown in Fig. 4.41(a) and (b). We chose these configurations to prove experimentally the capacity of the DORT to locate soft faults in complex configurations where standard methods are insufficient. The need for a numerical model in order to inject the synthesized signals resulting from the TRO decomposition was satisfied by using the model we earlier developed for the statistical study. We also note that the VNA we used for our experiments had three operating testing ports (the fourth one being damaged) which constrained us to limit the number of testing ports that can be used simultaneously to three. However, if one wishes to increase the number of testing ports, one could have conducted several measurements,

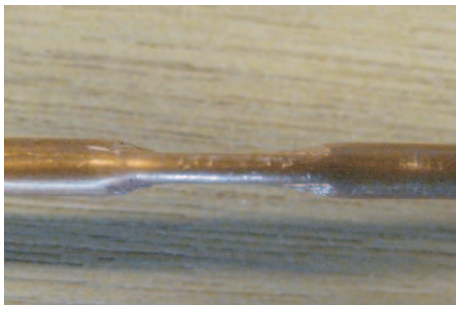

(a)

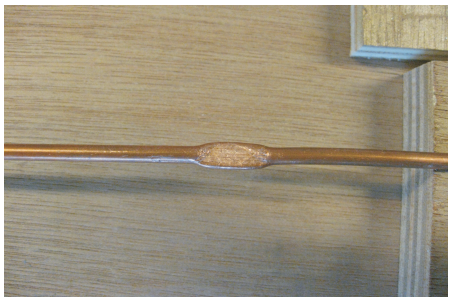

(b)

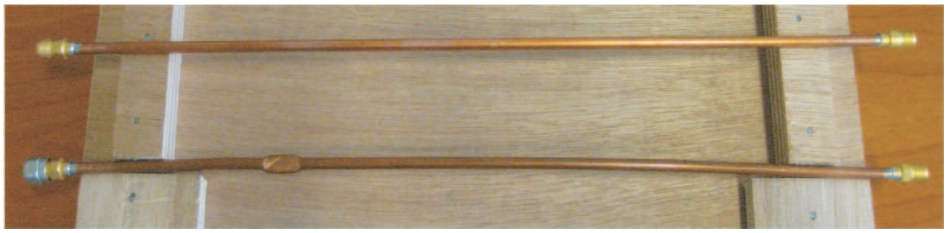

(c)

Figure 4.40: The soft fault considered in the experimental validations, as obtained by crushing a 1-cm long portion of a semi-rigid cable. The three pictures present: (a) a side view of the fault, with the cable reduced to a 2 mm thickness; (b) a front view of the fault; (c) the two samples used for the measurements, i.e., the reference semi-rigid cable without fault and the one presenting the fault. They share the same dimensions and features.

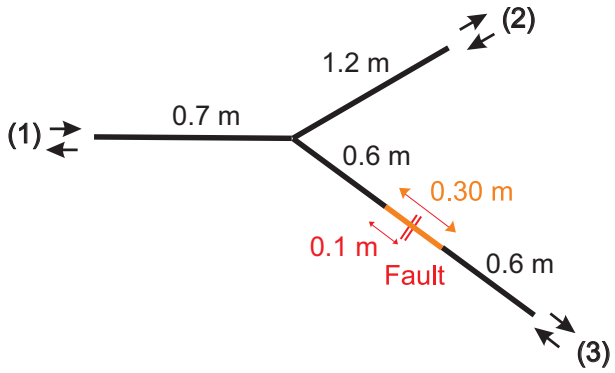

(a)

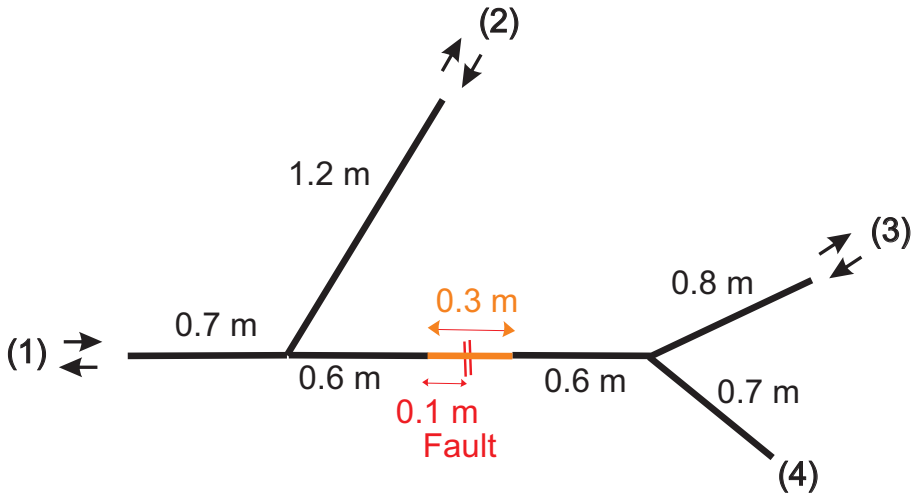

(b)

Figure 4.41: Layouts of the two NUTs considered for the experimental validation: (a) a single-Y structure; (b) a double-Y structure. Each branch of the NUTs consisted of a flexible coaxial cable with a 50 Ω characteristic impedance, while the red portions represent the samples containing the fault, as shown in Fig. 4.40. Three testing ports were considered in (a) and (b). The extremity (4) in (b) was left either matched to the network or open circuited depending on the studied case. The junctions were implemented by means of BNC T-junctions. The length of each branch is shown in the figures. The double-arrow symbols stands for the ports connected to the VNA (the testing ports).

where different network extremities are connected each time to the network, in order to measure the scattering matrix K. However, due to the fact that we are considering a linear time-invariant system, we tried to minimize as much as possible the cables movement, in order to capture the fault's weak signature, not introducing any perturbation that could be seen as a secondary source in the difference system, thus affecting the fault location. So we limited the number of testing ports to 3.

The network of Fig. 4.41(a) is a single-junction network, with three testing ports placed at the three extremities of the network, whilst the network of Fig. 4.41(b) is a double junction network, with the three testing ports placed on the three extremities labeled (1), (2) and (3). The fourth extremity labeled (4) was left either open-circuited or matched to the network; these two cases aimed to investigate a possible effect of the mismatch of this discontinuity on the location process.

The implementation of the networks of Fig. 4.41 is shown in Fig. 4.42. We considered a total bandwidth of 2 GHz, a frequency sampling step of 2 MHz, and the gaussian window that was applied to the eigenvector's components before injecting them into the numerical model had a bandwidth of 834 MHz at -3 dB.

A first step in the measurement procedure is the calibration of the VNA. Thus we connected three identical 50-cm cables to the three operating testing ports, and calibrated the VNA according to these cables, using the calibration kit provided by the manufacturer. The three cables can be seen on Fig. 4.42, connected to the analyzer.

After the calibration step, we considered each of the studied networks and measured the transfer matrix of the difference system in each case. For each studied NUT the measurement consisted in a two-step procedure:

- measurement of K of the reference system (without the fault),

to this end we considered the network with the unaltered 30-cm semi-rigid section, and measured the transfer matrix of the system, for a frequency range from 300 kHz to 2 GHz. In order to minimize as much as possible the cable movements for the two measurements, we attached them to the table.

- Measurement of the transfer matrix of the faulty system,

After measuring the transfer matrix of the reference system, we replaced the unaltered sample with the faulty one, to measure the new transfer matrix. A particular attention was paid to the connection and disconnection of the semi-rigid cables, to minimize the effect of the connectors when considering the difference system, i.e., to avoid having residual responses that can mask the fault's signature.

Having measured the two transfer matrices of the considered NUT, the following post processing was done using Matlab: we first applied an averaging operation to have both matrices symmetrical, as indicated in Section 4.3.2.2. Then we calculated the TRO of the transfer matrix

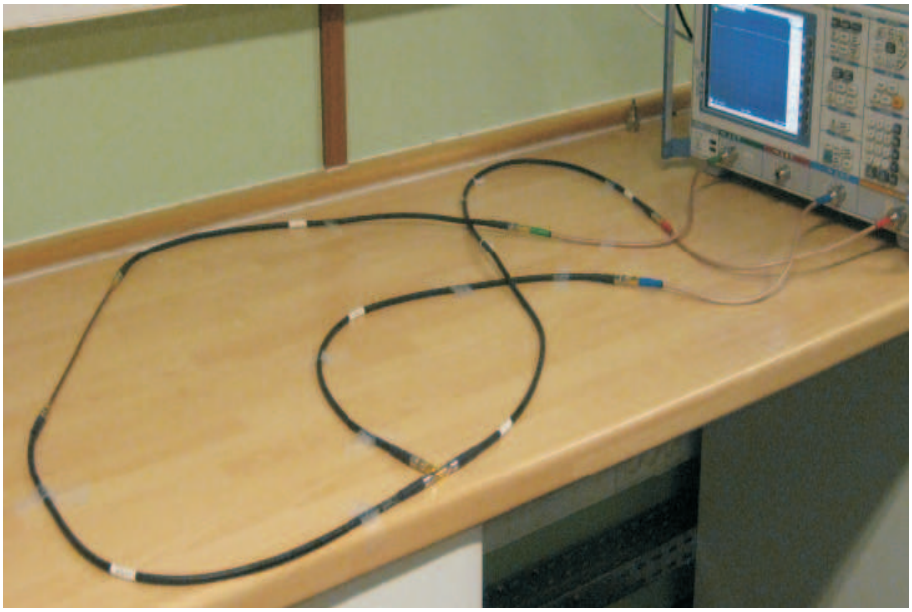

(a)

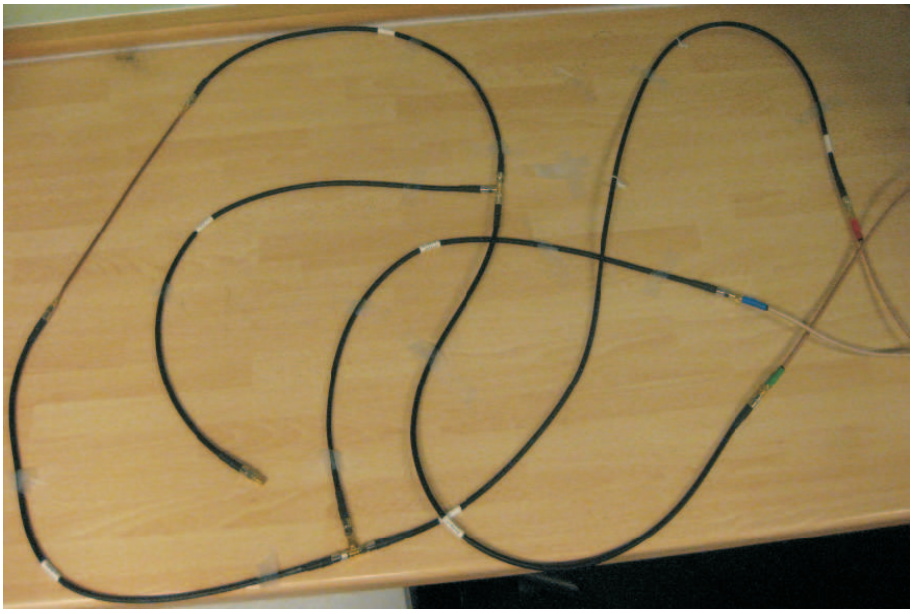

(b)

Figure 4.42: Implementations of the NUTs described in Fig. 4.41, as connected to a vector network analyzer for experimental work. The 30-cm long semi-rigid cable implementing the fault sample is clearly visible.

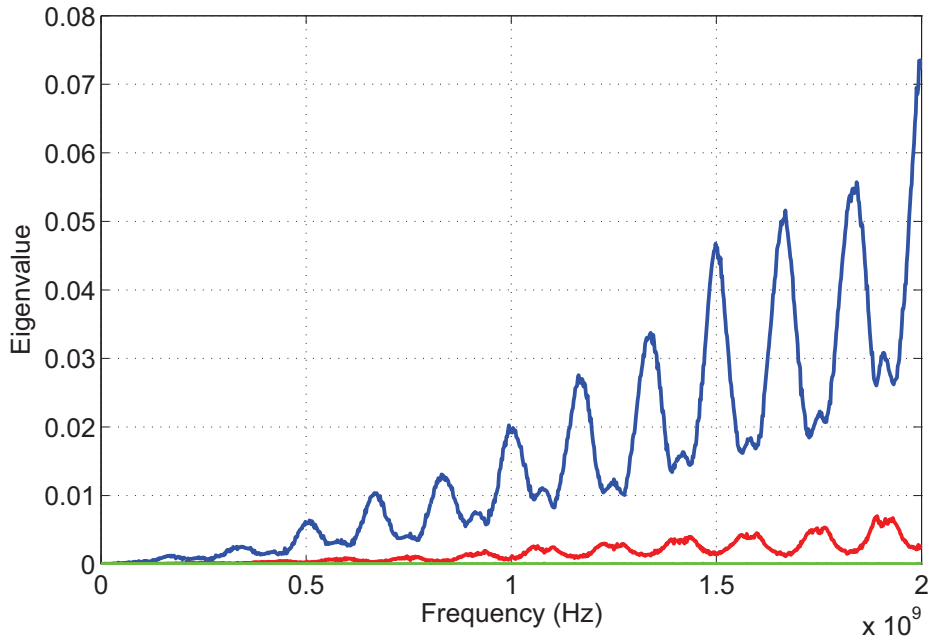

Figure 4.43: The eigenvalues of the TRO, calculated for the difference system of the NUT of Fig. 4.41(a), with three testing ports and fault characterized in Fig. 4.40.

of the difference system, and derived the corresponding eigenvalues and eigenvectors. The following step was to consider the eigenvector corresponding to the most significant eigenvalue, and inject its components into the numerical model of the studied NUT. This was done using the code we developed in Matlab, and the ZT and power summation diagrams were derived to allow fault location using the differential DORT. The results for the considered NUTs are shown in the following sections.

4.7.2 Single-junction network

The studied network is illustrated in Fig. 4.41(a). The obtained eigenvalues are shown in Fig. 4.43, where we notice the presence of a dominant one. The components of the most significant eigenvalue, that are to be injected in the numerical model, are shown in Fig. 4.44, where we clearly see that the time delay between the different peaks allows to obtain signals focalizing on the fault position, as can be seen on the ZT diagram of Fig. 4.45, observed along the third path. The corresponding power summation diagram is represented in Fig. 4.46, where we notice a maxima at the fault position. This points the fact that, using the differential DORT, we are able to directly locate the fault in this network, without any ambiguity on its position.

A second non-zero eigenvalue appears in the experimental measurements, due to the presence of other secondary sources, such as imperfect connections or cables moving during the measurement process, that might cause a residual signature to appear when considering the dif-

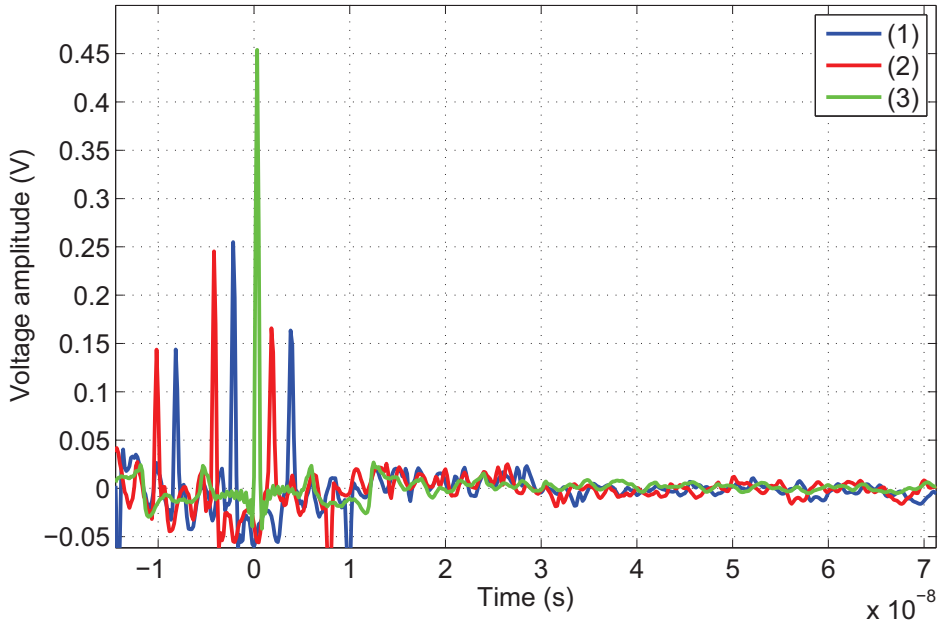

Figure 4.44: The components of the eigenvector corresponding to the most significant eigenvalue of the TRO, calculated for the difference system of the NUT of Fig. 4.41(a), with three testing ports and fault characterized in Fig. 4.40.

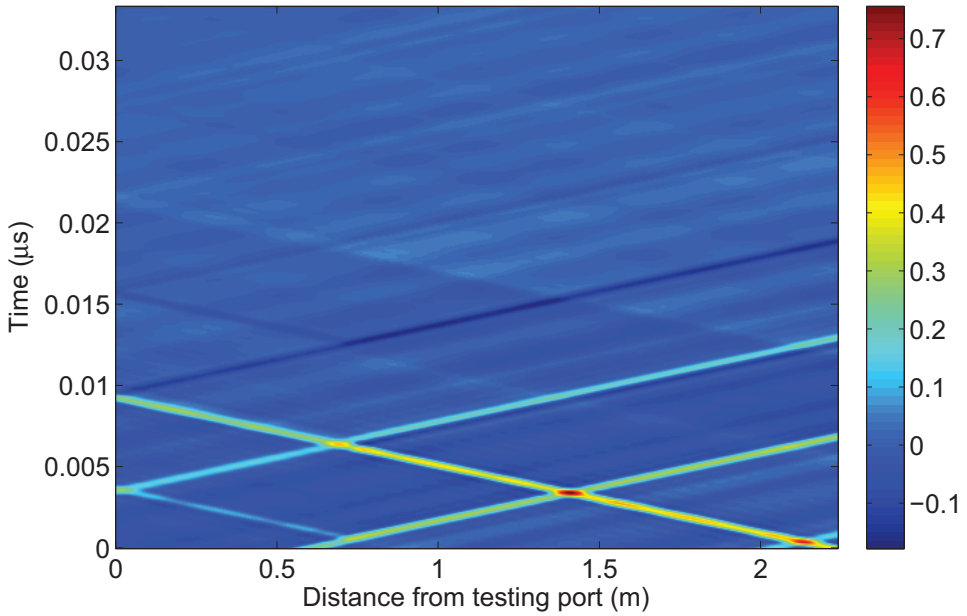

Figure 4.45: The ZT diagram corresponding to the NUT of Fig. 4.41(a), observed along the third path and showing the injected signals focalizing on the fault position, situated at 1.4 m from the testing port (1).

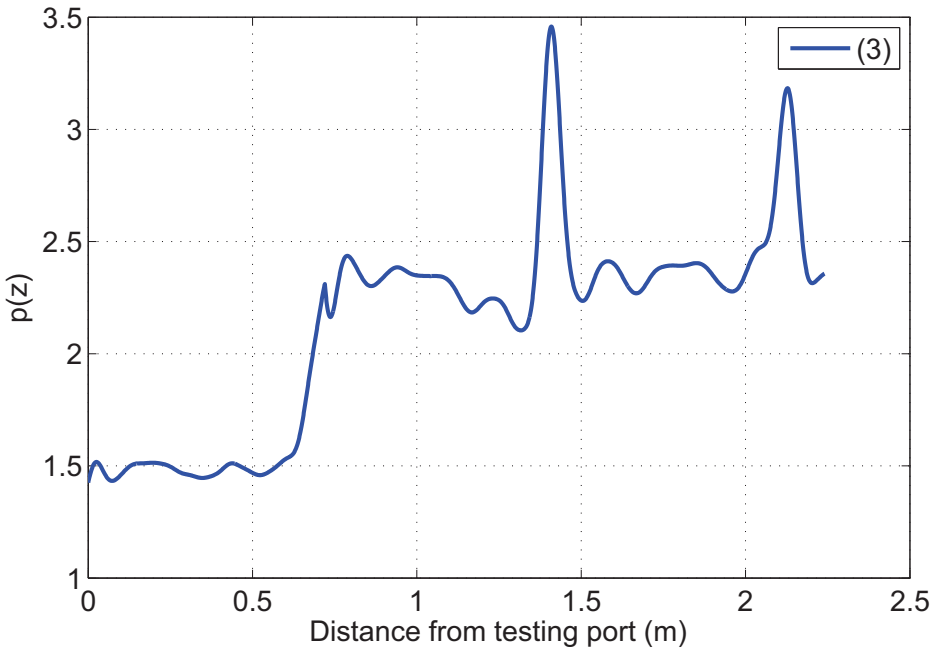

Figure 4.46: The power summation diagram corresponding to the ZT diagram of Fig. 4.45, observed along the third path in the NUT Fig. 4.41(a), corresponding to the most significant eigenvalue. We notice a maxima at the fault position, i.e., at 1.4 m from the testing port (1).

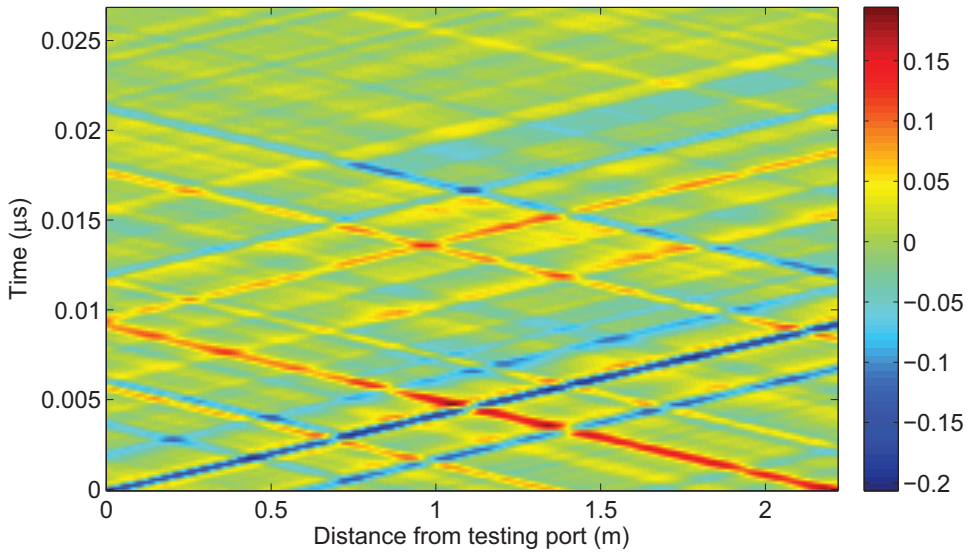

Figure 4.47: The ZT diagram corresponding to the NUT of Fig. 4.41(a), observed along the third path and corresponding to the second most significant eigenvalue.

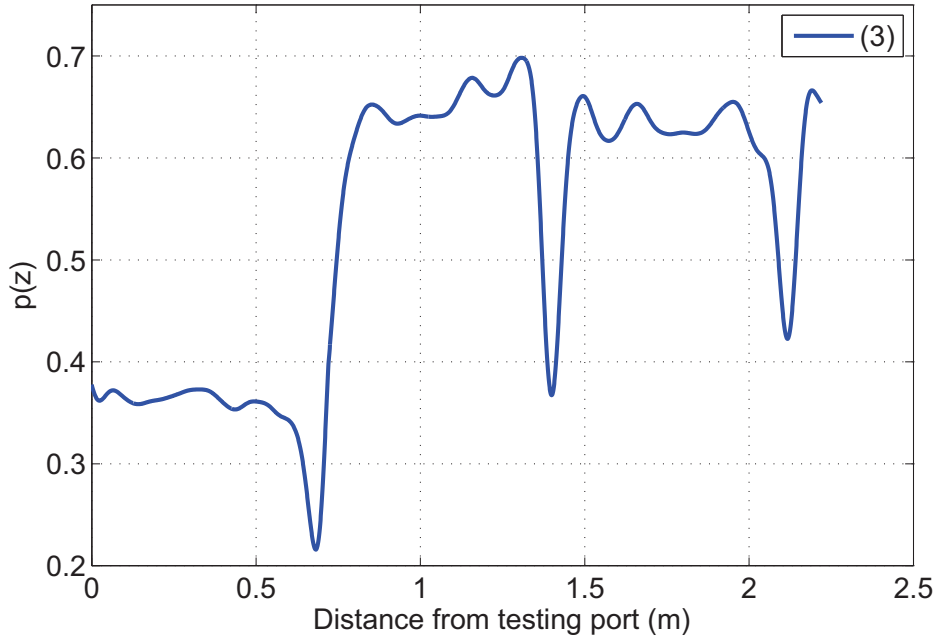

Figure 4.48: The power summation diagram corresponding to the ZT diagram of Fig. 4.47, observed along the third path in the NUT Fig. 4.41(a), corresponding to eigenvector of the second most significant eigenvalue.

ference system response. The ZT diagram corresponding to this second most significant eigenvalue is represented in Fig. 4.47 where we notice destructive interferences at different positions in the NUT, among which the fault position. The corresponding power summation diagram is shown in Fig. 4.48.

4.7.3 Double junction network

Let us now consider a more complex case, where we have a double-junction network, illustrated in Fig. 4.41(b) and its implementation in Fig. 4.42(b). When we conducted the statistical study, the simulated NUTs we considered contained a variable number of testing ports, which was in several cases lower than the number of extremities in the network. In all these cases, we considered the extremities without testing ports adapted to the network. Thus it seemed interesting here to observe the effect of a mismatch of the extremity (the fourth one in the NUT of Fig. 4.41(b)) on the location process, although we do not expect that the performance of the method concerning the location of the fault be affected. Nevertheless, we considered two cases of the configuration of Fig. 4.41(b): the first one with the extremity (4) being matched to the network, the second one with the same extremity being open-circuited.

Let us first consider the case where the fourth extremity is matched to the network. The eigenvalues of the TRO in this case are shown in Fig. 4.49, where we also notice a dominant

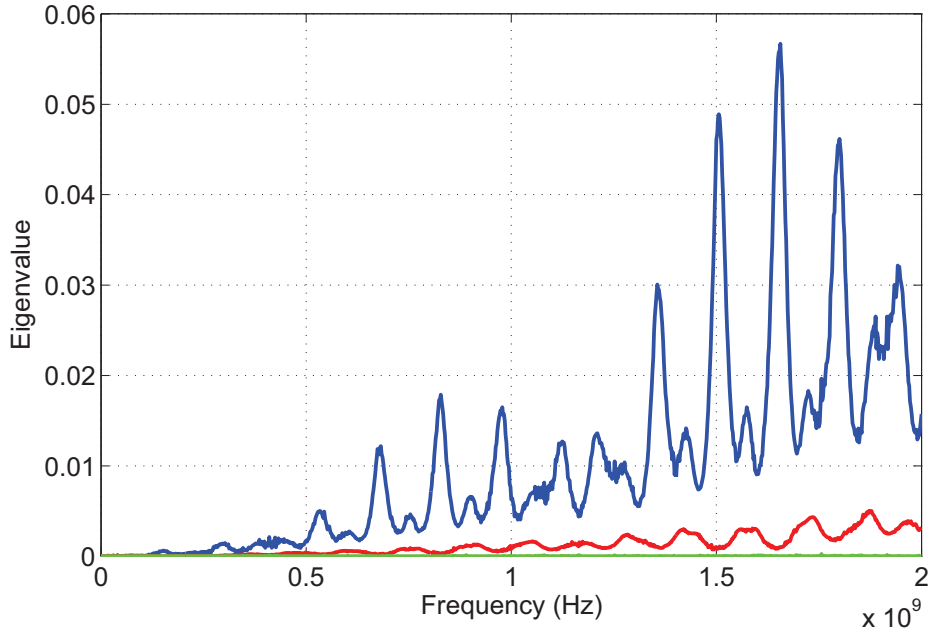

Figure 4.49: The eigenvalues of the TRO, calculated for the difference system of the NUT of Fig. 4.41(b), with three testing ports, a matched end (4), and fault characterized in Fig. 4.40.

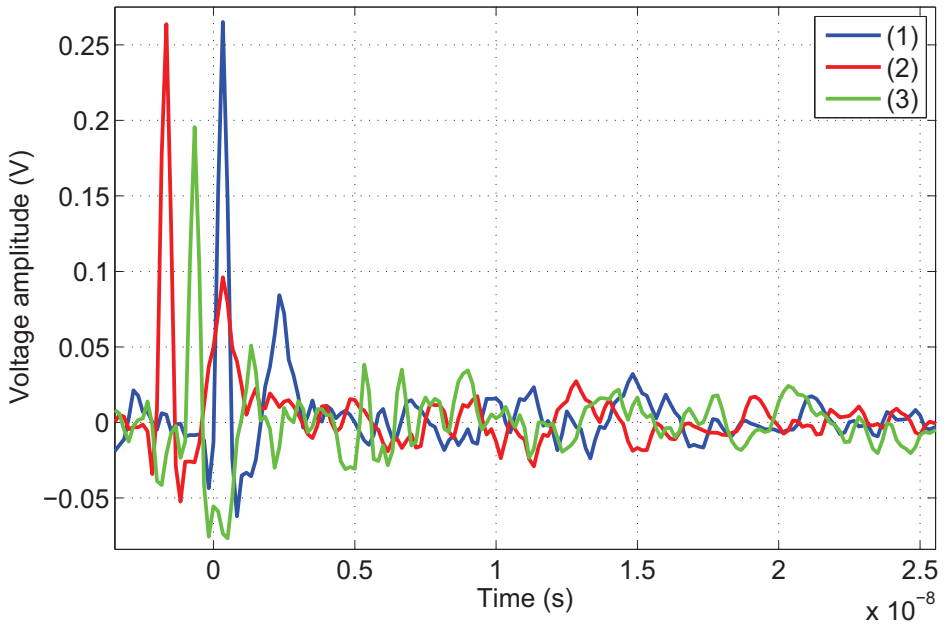

Figure 4.50: The components of the eigenvector corresponding to the most significant eigenvalue of the TRO, calculated for the difference system of the NUT of Fig. 4.41(b), with three testing ports, a matched end (4), and a fault characterized in Fig. 4.40.

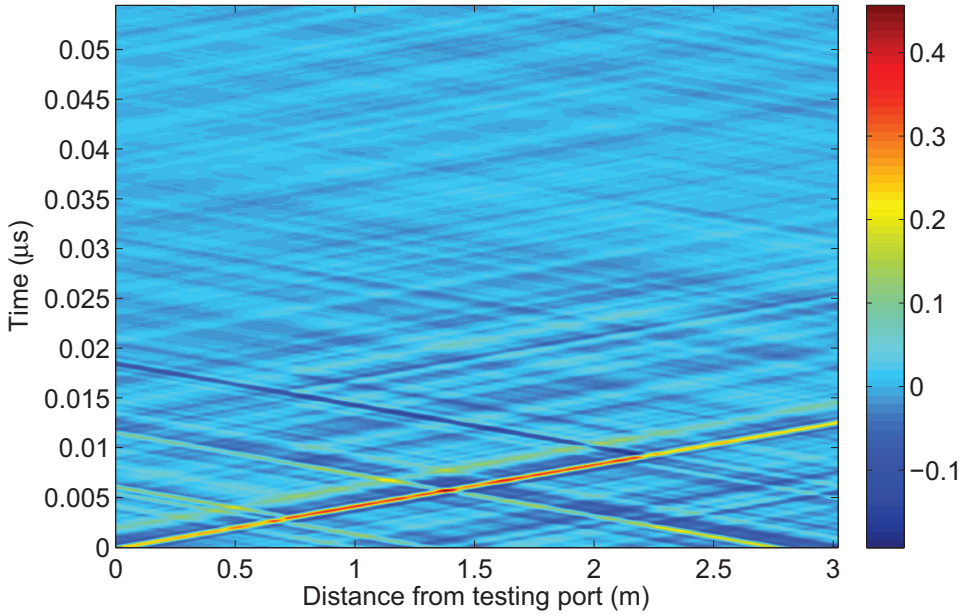

Figure 4.51: The ZT diagram corresponding to the NUT of Fig. 4.41(b), with three testing ports and a matched end (4). It is observed along the third path and showing the injected signals focalizing on the fault position, situated at 1.4 m from the testing port (1).

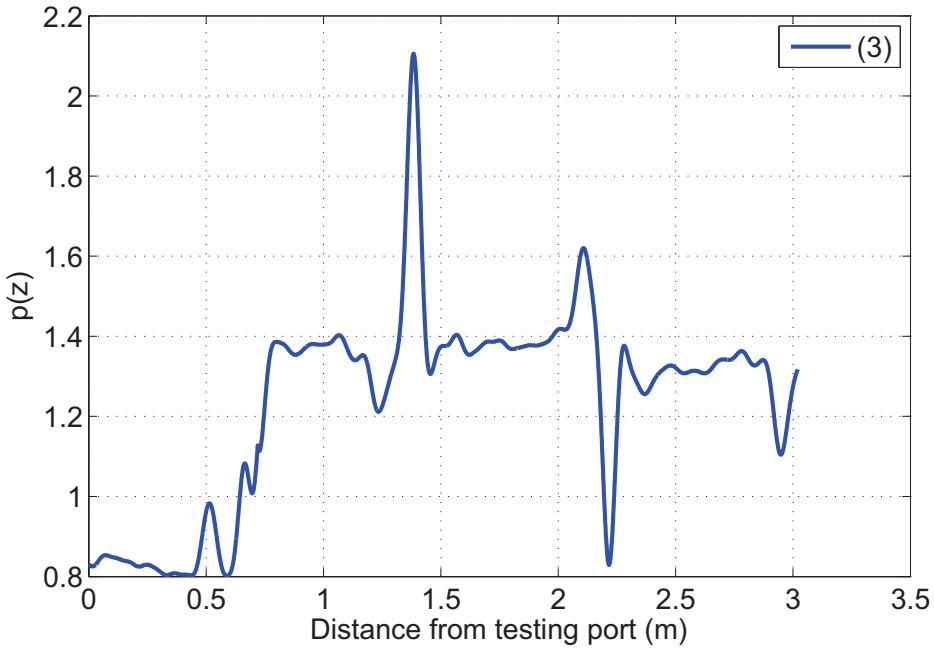

Figure 4.52: The power summation diagram corresponding to the ZT diagram of Fig. 4.51, observed along the third path in the NUT Fig. 4.41(b). We notice a maxima at the fault position, i.e., at 1.4 m from the testing port (1).

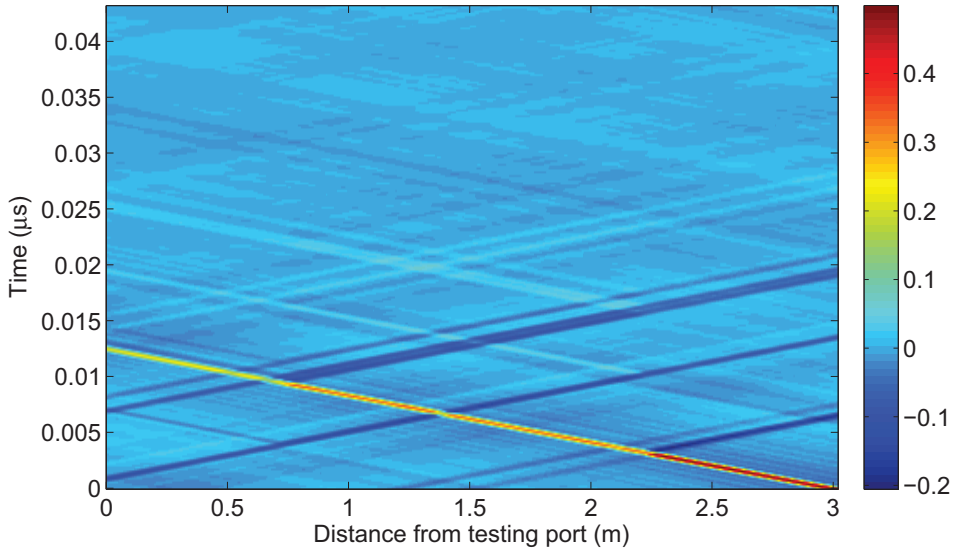

Figure 4.53: The ZT diagram corresponding to the NUT of Fig. 4.41(b), with three testing ports and a matched end (4). It is observed along the third path and corresponds to the second most significant eigenvalue.

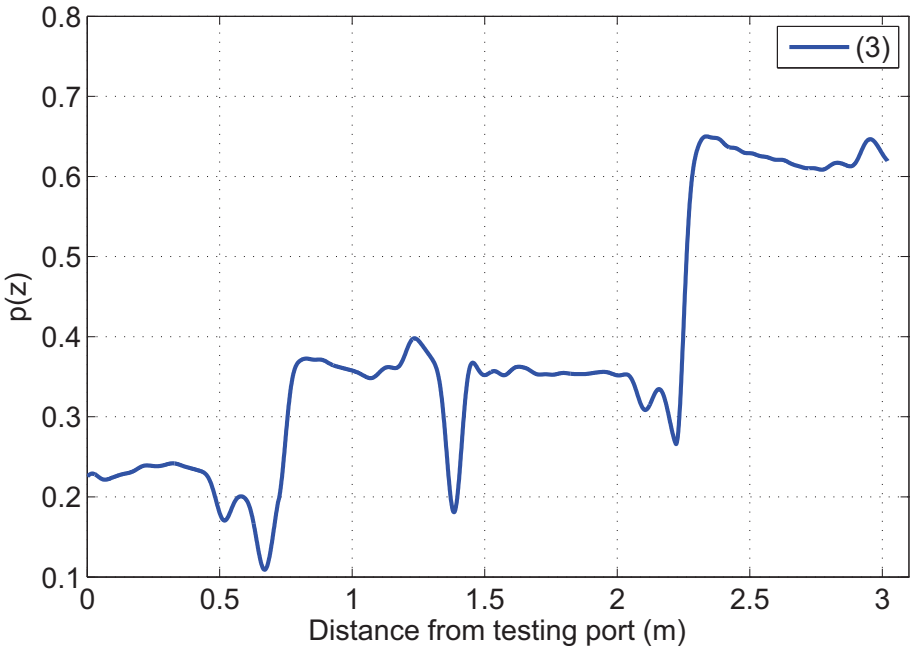

Figure 4.54: The power summation diagram corresponding to the ZT diagram of Fig. 4.53, observed along the third path in the NUT Fig. 4.41(b) and corresponding to the second most significant eigenvalue.

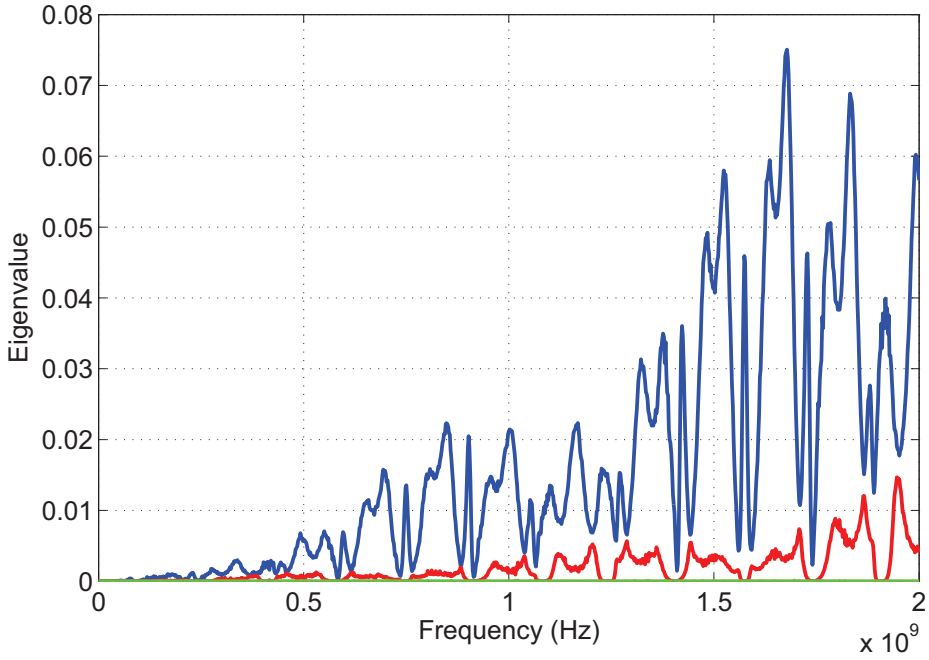

Figure 4.55: The eigenvalues of the TRO, calculated for the difference system of the NUT of Fig. 4.41(b), with three testing ports, an open-circuited end (4), and fault characterized in Fig. 4.40.

eigenvalue. The testing signals corresponding to this most significant eigenvalue are represented in Fig. 4.50. These signals propagate into the NUT model, and the ZT diagram observed along the third path is shown in Fig. 4.51. Here, the echoes contained in the testing signals complicates the location process based on this diagram. The power summation diagram represented in Fig. 4.52 points the fact of having a dominant peak at the fault position, and once again we are able to directly locate the fault using the differential DORT method.

The ZT diagram corresponding to the propagation of the components of the eigenvector corresponding to the second most significant eigenvalue is shown in Fig. 4.53, and the power summation diagram in Fig. 4.54. As we already observed for the case of the single-Y network, we notice destructive interferences at different positions, among which the fault's one.

The last case to be studied is when having the extremity (4) open-circuited. The eigenvalues observed in Fig. 4.55 show a dominant one, and the corresponding testing signals are illustrated in Fig. 4.56. When propagating these signals into the reference network model we have, We obtain a ZT diagram illustrated in Fig. 4.57; here also several echoes focalize on the fault position, at 1.4 m from the testing port. The power summation diagram shown in Fig. 4.58 shows once more a dominant peak at the fault position, suggesting a direct location of the latter. Comparing this case to the one with the fourth extremity matched, we notice that fault location was not affected. The ZT and power summation diagrams corresponding to the second most

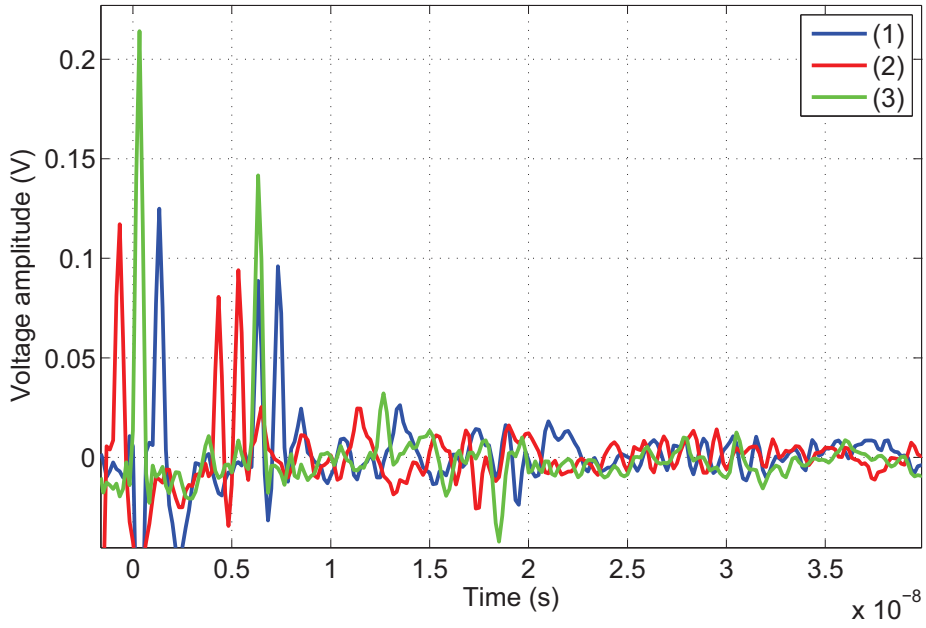

Figure 4.56: The components of the eigenvector corresponding to the most significant eigenvalue of the TRO, calculated for the difference system of the NUT of Fig. 4.41(b), with three testing ports, an open-circuited end (4), and a fault characterized in Fig. 4.40.

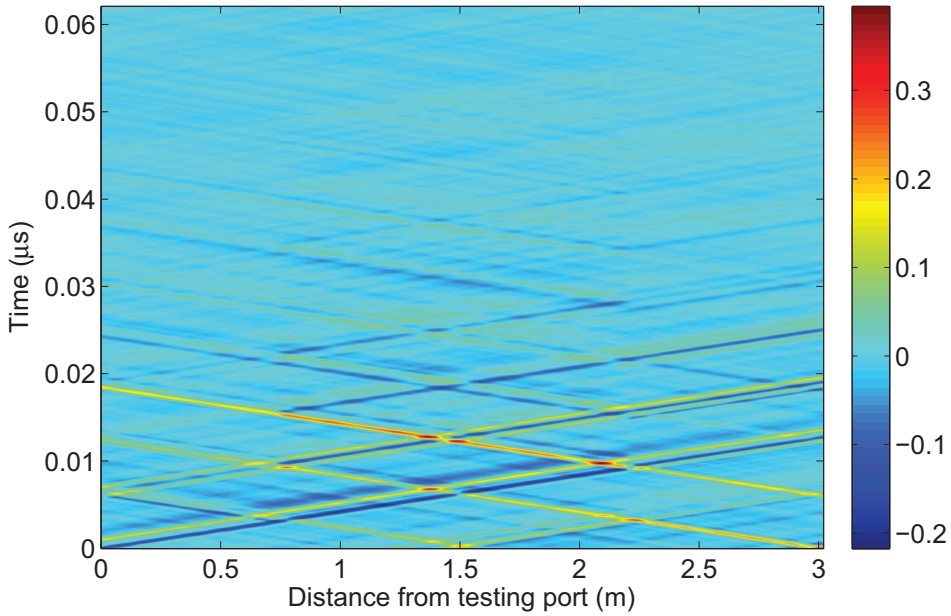

Figure 4.57: The ZT diagram corresponding to the NUT of Fig. 4.41(b), with three testing ports and an open-circuited end (4). It is observed along the third path and showing the injected signals focalizing on the fault position, situated at 1.4 m from the testing port (1).

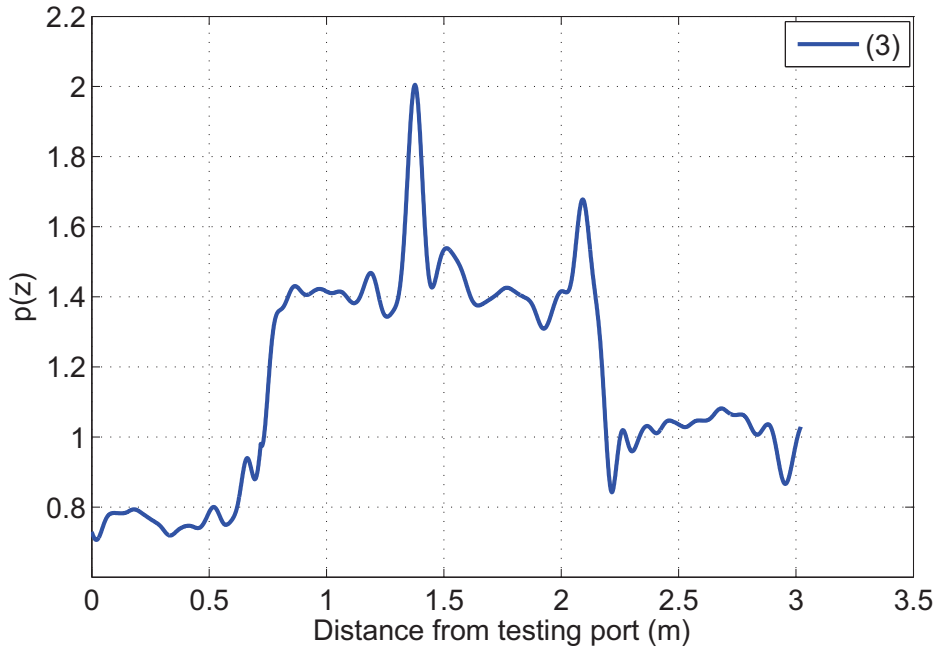

Figure 4.58: The power summation diagram corresponding to the ZT diagram of Fig. 4.57, observed along the third path in the NUT Fig. 4.41(b). We notice a maxima at the fault position, i.e., at 1.4 m from the testing port (1).

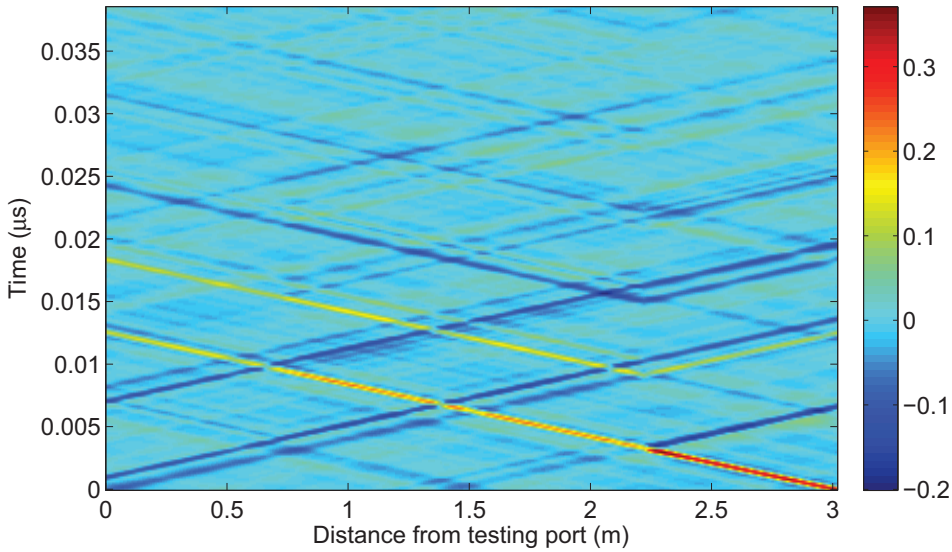

Figure 4.59: The ZT diagram corresponding to the NUT of Fig. 4.41(b), with three testing ports and an open-circuited end (4). It is observed along the third path, and corresponds to the second most significant eigenvalue.

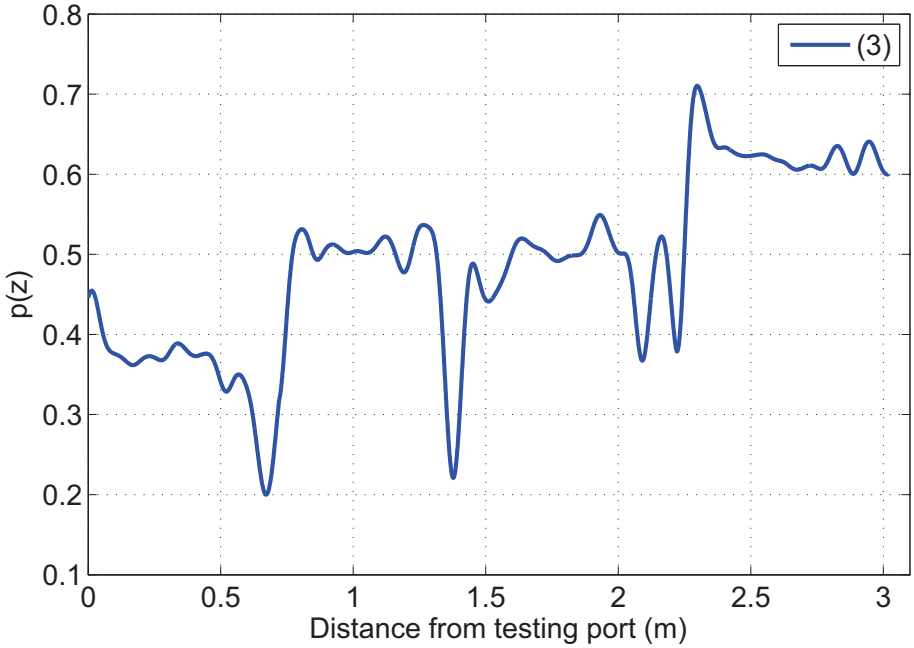

Figure 4.60: The power summation diagram corresponding to the ZT diagram of Fig. 4.59, observed along the third path in the NUT Fig. 4.41(b) and corresponding to the second most significant eigenvalue.

significant eigenvalue are shown in Figs. 4.59 and 4.60 respectively.

4.7.4 Conclusion

In the experimental study we conducted, we saw that the differential DORT is a promising method for locating soft faults in complex networks. Without any need for iterative algorithms, we were able to locate a soft fault in a single and double-junction configurations, proving once again the capacity of the method to synthesize testing signals that are bound to focus on the fault position.

However, we saw that in order to be able to apply the DORT, a model of the NUT is necessary, i.e., *a priori* information on the network configuration must be available. Thus the sensitivity of the method to tolerances on the available information must be assessed in future studies, also its practical implementation, for example in a system when the wire lengths are big enough so as not to allow to the extremities to be connected to the same measuring device (when measuring K). In such cases, the GPS might be used for signals synchronization, but however the advantage of the DORT itself in such systems should be evaluated in order to determine if it is beneficial over the other methods or not, and consequently if it is worth to practically implement it. To sum up, an extended study of the DORT is necessary, after the preliminary study we did in this chapter, in order to fully characterize the method and assess the situations

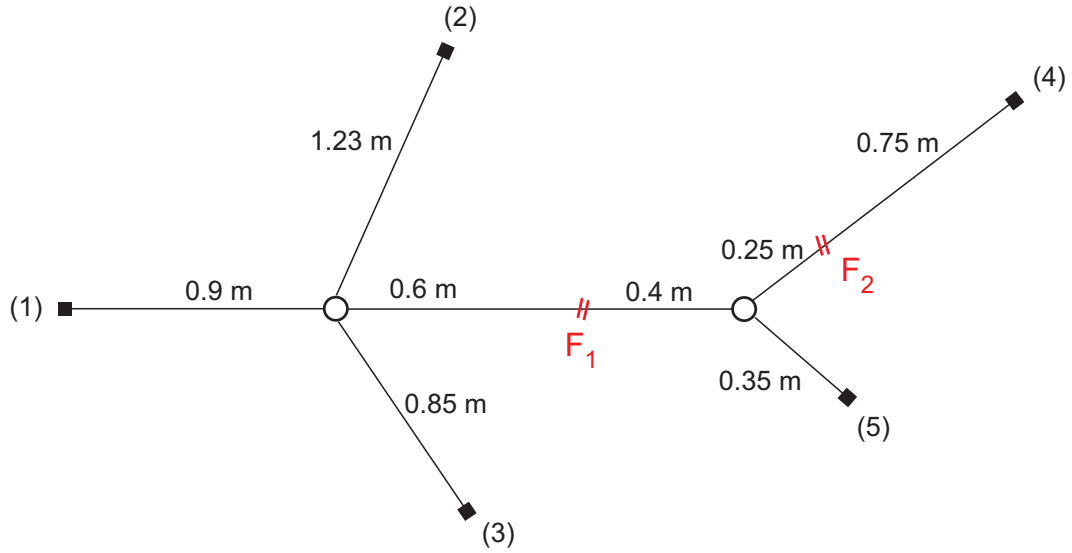

Figure 4.61: The network structure we used to test the ability of the differential DORT in locating multiple faults. Five testing ports are used, and the lengths of the lines are chosen arbitrarily. The faults F_1 and F_2 are capacitive parallel loads, with respective values of 12 nF and 1.8 nF.

where it presents advantages over the existing methods.

4.8 Multiple fault location using the differential DORT method

Till now we considered the case of locating one fault using the differential DORT, and conducted all the statistical and experimental studies accordingly. However, an interesting case to be investigated is the possibility of locating multiple faults using the DORT method. This is motivated by the DORT properties, encountered in acoustics, that synthesizes signals focusing on one of several scatterers, depending on the chosen eigenvector which components are to be emitted.

In this section we investigate the ability of the DORT in locating multiple faults, using the simulation model we have, and considering capacitive faults whose responses depend on the frequency; this is motivated by the results of the experimental study in the previous chapter, that dealt with real soft faults.

4.8.1 Location of two faults using the differential DORT

We consider the case of the network illustrated in Fig. 4.61, with five testing ports, and two faults, F_1 and F_2, modeled as parallel capacitive loads, with respective values of 12 nF and 1.8 nF, chosen arbitrarily.

In this case, expansion of the TRO leads to two most significant eigenvalues, represented in

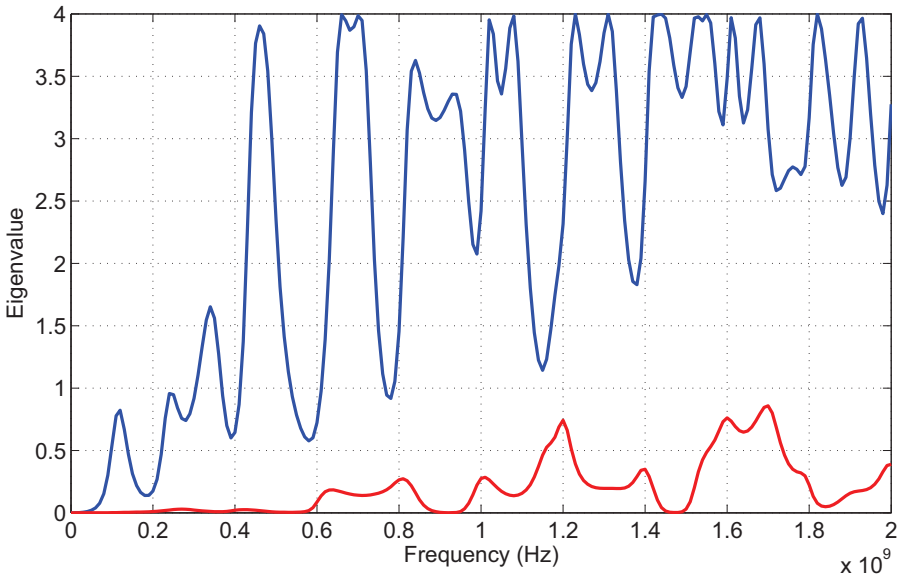

Figure 4.62: The eigenvalues of the TRO, calculated for the difference system of the NUT of Fig. 4.61, with five testing ports, and two faults F_1 and F_2.

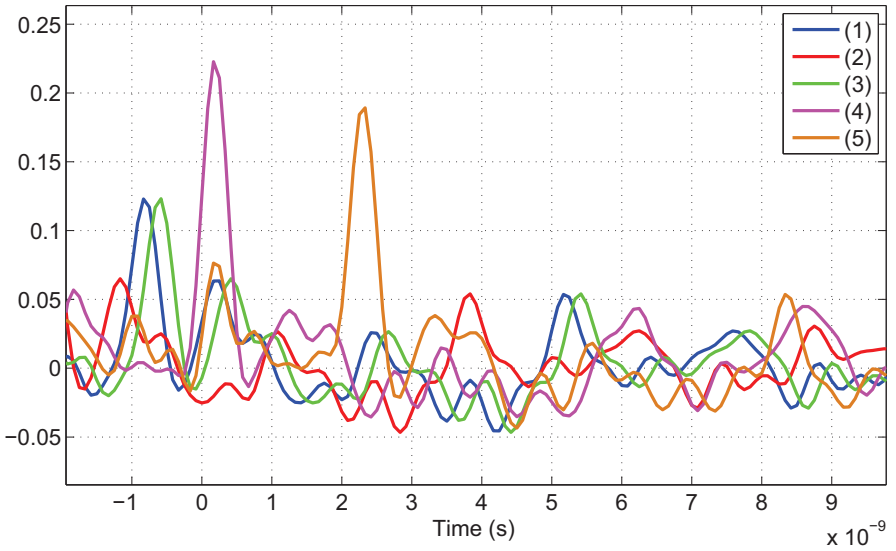

Figure 4.63: The components of the eigenvector corresponding to the most significant eigenvalue of the TRO, calculated for the difference system of the NUT of Fig. 4.61, where the eigenvalues are represented in Fig. 4.62.

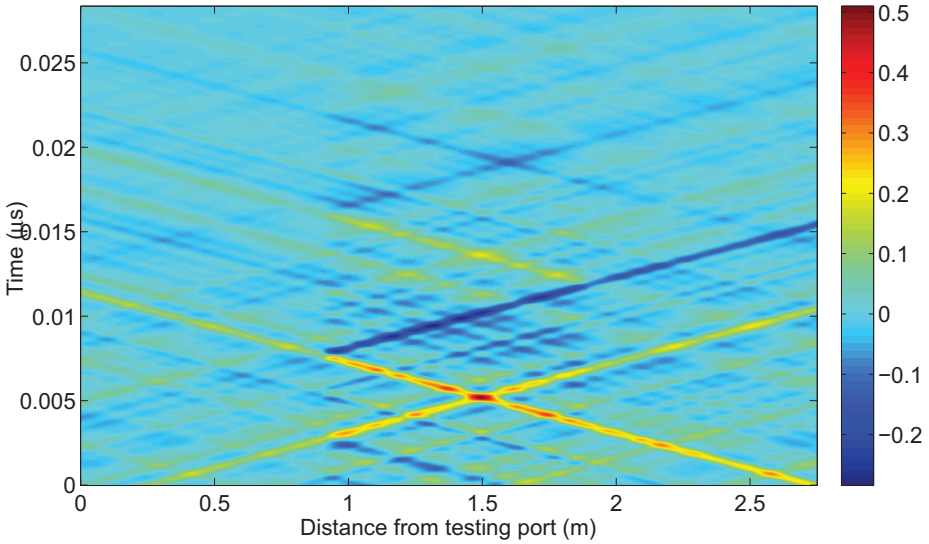

Figure 4.64: The ZT diagram corresponding to the NUT of Fig. 4.61, when propagating the testing signals represented in Fig. 4.63, observed along the fourth path. We see the signals focalizing on the position of the first fault F_1, situated at 1.5 m from the testing port (1).

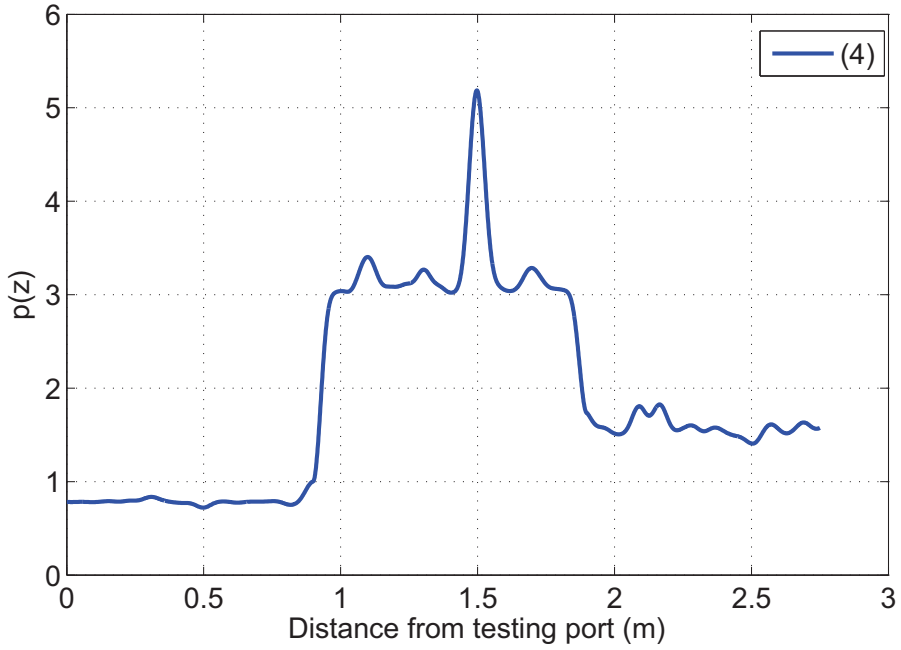

Figure 4.65: The power summation diagram corresponding to the ZT diagram of Fig. 4.64, observed along the fourth path in the NUT of Fig. 4.61. We notice a maxima at the fault F_1 position, i.e., at 1.5 m from the testing port (1).

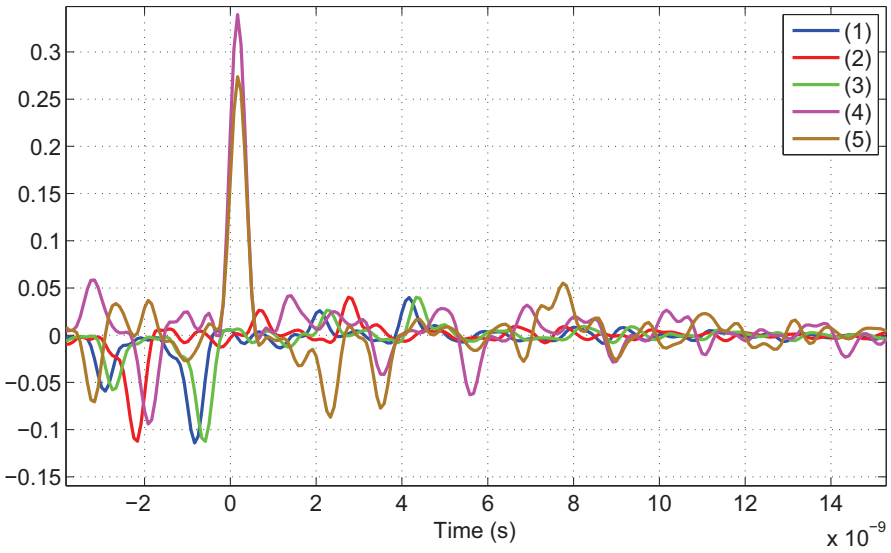

Figure 4.66: The components of the eigenvector corresponding to the second most significant eigenvalue of the TRO, calculated for the difference system of the NUT of Fig. 4.61, where the eigenvalues are represented in Fig. 4.62.

Fig. 4.62, the three left being identically null. The propagation of the testing signal corresponding to the most significant eigenvalue, represented in Fig. 4.63, in the network reference model (without faults) leads to the ZT diagram along the fourth path observed in Fig. 4.64, and the corresponding power summation diagram of Fig. 4.65. We clearly notice that the signals are bound to focus on the position of the first fault F_1, situated at a distance of 1.5 m from the first testing port (1), as if the second fault (situated at the distance of 2.15 m from (1)) did not exist.

Conversely, when propagating the testing signals corresponding to the second most significant eigenvalue (shown in Fig. 4.66), the ZT diagram we obtain along the fourth path is represented in Fig. 4.67, we notice the focalization on the position of the second fault position F_2, situated at a distance of 2.15 m, whilst a destructive interference is observed at the position of F_1. The power summation diagram once more points directly the position of the second fault F_2; it is illustrated in Fig. 4.68.

This example shows an important benefit of the differential DORT method: it is able to locate multiple soft faults in complex networks. This simulation investigated the possibility of using the differential DORT for multiple fault location, and proved our method to be a promising method, that needs to be further studied and characterized.

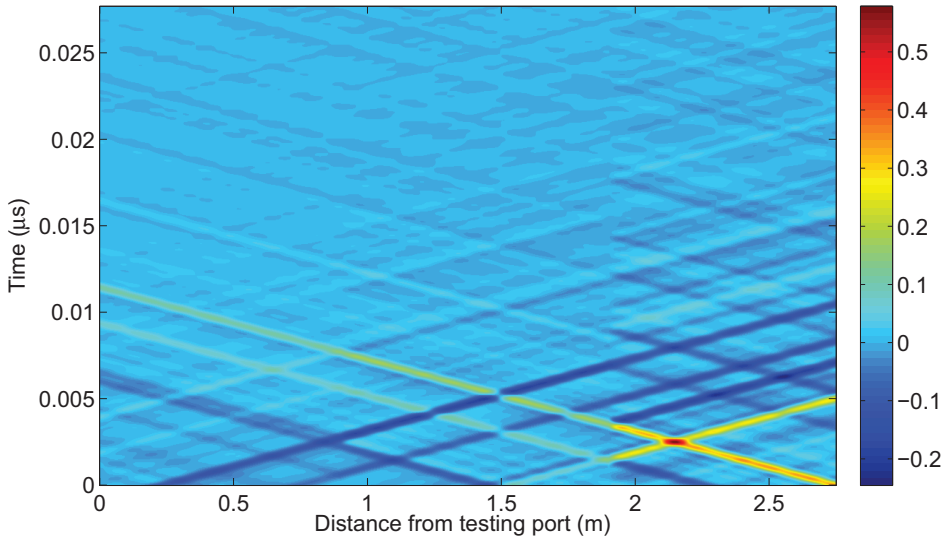

Figure 4.67: The ZT diagram corresponding to the NUT of Fig. 4.61, when propagating the testing signals represented in Fig. 4.66, observed along the fourth path. We see the signals focalizing on the position of the first fault F_2, situated at 2.15 m from the testing port (1).

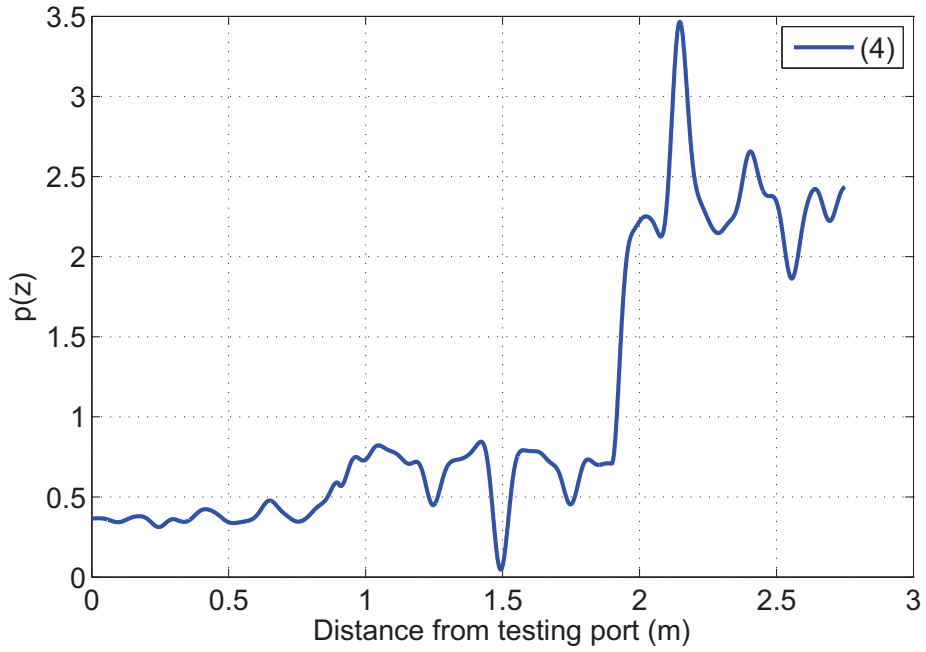

Figure 4.68: The power summation diagram corresponding to the ZT diagram of Fig. 4.67, observed along the fourth path in the NUT of Fig. 4.61. We notice a maxima at the fault F_2 position, i.e., at 2.15 m from the testing port (1).

4.9 Conclusion

A new method of soft fault location in complex networks was presented in this chapter. Based on the DORT properties, we derived an heuristic method which we called the differential DORT, able to synthesize signals that focus directly on the fault position, without any need for iterative algorithms. A part of the elements influencing the performance of the method were investigated through a statistical study, where it was revealed that the number and positions of the testing ports played an important role in determining the method's ability to locate a certain fault; it is necessary to have testing ports from both sides of the fault for a possible location of the fault. The statistical study was followed by an experimental study, aiming to asses the method's performance in practical cases, where faults are dispersive and the NUTs elements are imperfect. This study showed once more the important advantage of our method over standard iterative methods, because it was able to directly point the position of the fault, without the need for iterations. The last section of the chapter showed a simulated case where two faults were considered, and here also, the DORT was able to locate directly each one of them by propagating the corresponding signals according to the corresponding eigenvalue.

Given that the study we conducted in this chapter is a feasibility study of the method, a more extended analysis of the DORT should be conducted; starting with a wider database, including more network configurations, and real soft faults model, as well as the extension of the influencing parameters to include the bandwidth, losses, noise, model perturbations, etc. A comparison of the DORT with other methods in given scenarios is also useful to asses the configurations where our method presents advantages over these methods. The practical implementation of the method should be further investigated, depending on the configuration of the NUT. For example, if we consider networks that are extended over wide distances, their extremities cannot be connected to one VNA in order for the K matrix to be measured. In such scenarios, several measuring devices must be used, and thus the synchronization of these devices in order to obtain a time origin for the injected and received signals is necessary (which can be done by means of the GPS network for example). This shows that the practical implementation of the method for a given network needs to be investigated.

An important aspect we addressed in the end of this chapter is multiple-fault location using the DORT. In this domain it is shown that the DORT is a promising technique that needs to be further studied. Also an extended study of this method to the case of multi-conductor transmission lines is interesting given that cables are most often packed together into bundles. To sum up, an extended study of the DORT in the domain of fault location is necessary to analyze the performance of the method and asses the conditions where it could provide advantages over the existing fault location methods.

Conclusion

In this thesis, we discussed fault detection and location in wire networks. Motivated by the existing need when dealing with soft faults and complex network configurations, as current techniques start to fail, we proposed new approaches in this domain, based on the properties of time reversal.

In the domain of fault detection, the idea was that, instead of having a predefined testing signal, as for the case of standard reflectometry techniques, we synthesize a signal adapted to the network; this new testing signal, which we named the Matched Pulse (MP), depends on the configuration of the network, and is designed so as to result in a maximal SNR at the fault position. The MP was derived based on the properties of time reversal, or, equivalently, the matched filter principle encountered in telecommunications. To asses the situations where the new approach presents major advantages, a comparison of the MP and standard TDR methods was held in a formal way, by means of a mathematical analysis aiming to quantify these advantages through the calculus of a detection gain, and the detection probabilities. This was followed by simulation and experimental validation of the method; the results show that the MP is more beneficial whenever the system's response is more complex, i.e., the signal to be analyzed contains longer sequences of echoes. This positive effect of the complexity of the system's response on the gain offered by the MP is opposed to common understanding, because the standard reflectometry techniques become insufficient as soon as the network's response becomes more complex, i.e., richer in echoes. The MP approach is a complementary technique with major advantages in complex configurations where standard techniques are no more reliable; it ensures a higher sensitivity to the presence of soft faults.

In the second part of our work, we turned our attention to dealing with fault location, especially when it comes to localize soft faults in complex networks. Based on the DORT method, we conducted a feasibility study aiming to asses the contribution of the method in the domain of wire fault location. We derived a heuristic location criterion, based on the DORT ability to synthesize testing signals adapted to the network so as to directly focalize signals on the fault location, thus ensuring a direct estimation of the fault position without the need for iterations. The elements influencing the performance of the new wire fault location method were investigated through a statistical study, where it was revealed that the number and positions of the testing ports played an important role in determining the method's ability to locate a fault; it is necessary to have testing ports from both sides of the fault in order to obtain direct focalization

on the fault position. This study also showed that increasing the number of testing ports on the extremities of the NUT increased the location probability of a fault; in such cases we are able to locate the soft fault without the need for iterations. The statistical study was followed by an experimental study, aiming to asses the method's performance in practical cases, where faults are dispersive and the NUT elements are imperfect. This study showed once more that the differential DORT was able to directly point the position of the fault, without any iteration.

Perspectives

The ideas and methods we developed in this thesis, relating the use of time-reversal properties to detect and locate wire faults, are promising methods that need to be further studied and investigated. Some of the important points to be analyzed are the following:

- when addressing fault location using the DORT method, we pointed out that it was a feasibility study aiming to assess the different possibilities offered by this method in the domain of wire fault location. That is why a more extended study of the observed aspects and results should be addressed. When calculating the TRO, we saw theoretically that the number of non-zero eigenvalues corresponds to the number of faults; this could be a starting point to study multiple fault detection using the DORT because the existence of non-zero eigenvalues points automatically the existence of one or several faults depending on the number of these eigenvalues. However we should not forget that according to our study of the DORT, it appeared that this method does not work in the case of a single testing port, so if we want to address multiple-fault detection in the context of having a single testing port, the MP approach should be addressed instead of the DORT in this case.

- The robustness of the methods (MP and DORT) with respect to tolerances on the experimental measurements (i.e., perturbations of the system that should have been time-invariant during the measurement process) as well as the *a priori* information available on the system's configuration is an important issue that should be investigated.

- The impact of different types of noise on the performance of the DORT method needs to be studied, and its impact on the distribution of the eigenvalues of the TRO evaluated. However, given that the DORT method is a sub-space method, it can be expected to be capable of ensuring an effective filtering, as long as the noise is orthogonal to the signals of interest. In the same context of the noise influence, when using the MP we considered an additive white gaussian noise when calculating the SNR; however, depending on the system and its environment, several other types of noise exist, such as impulsive noise in vehicular networks [127]. So if applying the method to such systems, it will be useful to evaluate the SNR accordingly.

- In the statistical study conducted when studying the DORT, we opted for a given network topology, with a limited number of studied parameters and generated network configurations. Thus in order to fully characterize the method, to consider a wider range of topologies and generated configurations, whilst studying the influence of different parameters such as the bandwidth, the noise, the losses in the NUT, etc., and considering realistic soft faults models, other than the resistive loads we considered. The comparison of the method to distributive reflectometry and iterative methods is also important to show the scenarios where it would provide advantages over these methods.

- The experimental study also conducted in the fourth chapter showed an example of a practical implementation of the DORT where the lengths of the cables in the NUT do not exceed a few meters, and consequently it was possible to connect the ends of the NUTs to the same VNA, thus facilitating the measurement of the transfer matrix of the system. However in systems where the NUT stretches over wider distances, it would not be possible to connect its extremities to the same measuring device. In such cases several measuring devices are used, and consequently a solution to synchronize the injected and received signals from these devices must be found (such as using the GPS network for example). This means that the practical implementation of the method should be taken into account and studied depending on the configuration of the studied system.

- The last point that was invoked in the fourth chapter is multiple fault location using the DORT; indeed this is a promising idea showing that the DORT is able to isolate and locate multiple soft faults, without any need for iterations. This issue should be further studied and investigated, along with experimental results addressing different types of soft faults.

- An extended study of the MP and DORT methods in the case of multi-transmission lines is interesting to study, since a wide range of cables consist of multi-conductors lines that are packed together into bundles. When considering MTLs, several parameters such as the coupling between the conductors should be taken into account, and also the way to adapt and implement the methods should be investigated.

DORT	Décomposition de l'Opérateur de Retournement Temporel
FP	False Positive
MP	Matched Pulse
MTL	Multi-conductor Transmission Line
NUT	Network Under Test
ROC	Receiver Operating Characteristic
SNR	Signal-to-Noise Ratio
ST	Standard reflectometry Techniques
TDR	Time-Domain Reflectometry
TP	True Positive
TR	Time Reversal
TRO	Time Reversal Operator
VNA	Vector Network Analyzer
ZT	space-time diagram

List of Tables

List of Figures

Publications

Journal papers

Layane Abboud, Andrea Cozza and Lionel Pichon, *A Matched-Pulse Approach for Soft-Fault Detection in Complex Wire Networks*. IEEE Transactions on Instrumentation and Measurement (TIM) (accepted).

International conferences

Layane Abboud, Andrea Cozza and Lionel Pichon, *A Distributed Non-Iterative Approach for Soft-Fault Location in Complex Wire Networks*. 15th International Symposium on Applied Electromagnetics and Mechanics (ISEM 2011), Napoli, Italy

Layane Abboud, Andrea Cozza and Lionel Pichon, *Performance Analysis of the Matched-Pulse-Based Fault Detection*. Proceedings of the First International Conference on Complex Systems Design and Management (CSDM 2010) (2010) 161-172

Layane Abboud, Andrea Cozza and Lionel Pichon, *Impact of network topology on the matched-pulse-based fault detection*. Progress in Electromagnetic Research Symposium (PIERS'10), Chine (2010)

Layane Abboud, Andrea Cozza and Lionel Pichon, *Utilization of matched pulses to improve fault detection in wire networks*. Proceedings of International Conference on ITS Telecommunications (ITST), France (2009)

Florian Monsef, Andrea Cozza and **Layane Abboud**, *Effectiveness of Time-Reversal technique for UWB wireless communications in standard indoor environments*. 20th International Conference on Applied Electromagnetics and Communications, Croatia (2010).

Bibliography

[1] Cynthia Furse and Randy Haupt. Down to the wire. *IEEE Spectrum*, 38(2):34–39, 2001.

[2] `www.nrc.gov/reading-rm/doc-collections/nuregs/staff/.../appa-i.pdf`.

[3] Joseph F. McPartland Brian J. McPartland and Frederic Hartwell. *National Electrical Code 2008 Handbook*. McGraw-Hill, 26th edition, 2008.

[4] E. Lakervi and E. J. Holmes. *Electricity distribution network design*. 21. Peter Peregrinus Ltd., on behalf of the Institution of Electrical Engineers (IEE), London, UK, 2nd edition, 2003.

[5] R.K.R. Yarlagadda. *Analog and Digital Signals and Systems*. Springer, 2009.

[6] S. Y. King and N. A. Halfter. *Underground power cables*. Longman, 1982.

[7] `www.nexans.fr`.

[8] L. Rochester. *Coaxial cables: application data*. Boston Technical Publishers, 1969.

[9] `http://www.cirris.com/testing/twisted_pair/twist.html`.

[10] M. T. Traskos R. L. Williams W. G. Linzey, E. B. Wiesenfeld and T. A. Mazzuchi. A risk assessment of a wire potential in the aircraft industry. In *the Eighth Aging Aircraft Conference*, February 2005.

[11] General Cable. *coaxial cable*. `http://www.generalcable.com`.

[12] H. Ward Silver and Mark J. Wilson. *The ARRL Handbook for Radio Communications*. The American Radio Relay League, 87th edition, 2010.

[13] Martin J. Van Der Burgt. *Coaxial cables and applications*. Belden, 2011.

[14] Feasibility and technical aspects of partial undergrounding of extra high voltage power transmission lines. Technical report, ENTSOE and Europacable, December 2010.

[15] ABB submarine cables. `http://www.abb.fr/product/us/9AAC30200079.aspx`.

[16] Wiring integrity research (WIRe) pilot study. Technical report, NASA, August 2000.

[17] Dogan Timucin Kevin wheeler, Xander Twombly and Jules Friederich. Model-based diagnostics for wire health management. Aging Aircraft - EWIS, 2008.

[18] `http://www.usfa.fema.gov/citizens/home_fire_prev/electrical.shtm`.

[19] `http://www.cdc.gov/injury/index.html`.

[20] Cynthia Furse Paul K. Kuhn and Paul Smith. Locating hidden hazards in electrical wiring. In *Aged Electrical Systems Research Application Symposium*, October 2006.

[21] Benoit Calmet. *Protection des réseaux de transport et de répartition : présentation*. Centre national d'expertise réseaux de RTE, techniques de l'ingénieur edition.

[22] Wire System Safety Interagency Working Group Committee on Technology. Review of federal programs for wire system safety, final report. Technical report, National Science and Technology Council, November 2000. `http://www.ostp.gov/html/wire_rpt.pdf`.

[23] L.A. Griffiths, R. Parakh, C. Furse, and B. Baker. The Invisible Fray: A Critical Analysis of the Use of Reflectometry for Fray Location. *IEEE Sensors Journal*, 6(3):697–706, June 2006.

[24] Mehdi Safavi Cynthia Furse, Paul Smith and Chet Lo. Feasibility of spread spectrum sensors for location of arcs on live wires. *IEEE Sensors Journal*, 5(6), December 2005.

[25] Devendra Tolani Eric van Doorn and Benjamin Lonske. Detection and localization of chafes in Electrical Wiring Interconnection Systems (EWIS). In *Aging Aircraft*, April 2008.

[26] H. J. Hall and al. In the matter of the investigation of the accident involving trans world airlines, inc. flight 800.

[27] Cynthia Furse. Finding fault: Locating hidden hazards on aircraft wiring. College of Engineering, University of Utah, February 2004.

[28] G. Parker. Electrical cable fault locating. Technical report, Radiodetection Canada, 2001.

[29] Michel Pays. Localisation de Défauts dans les Réseaux de Cables d'énergie. Technical report, Techniques de l'ingénieur.

[30] James W. Nilson and Susan A. Riedel. *Electric circuits*. Prentice Hall, 8th edition, 2008.

[31] Chester Laurens Dawes. *Course in electrical engineering*. McGraw-Hill Interamericana, 1955.

[32] Nirmal Nath. Capacitance and inductance sensors for location of faults in wires. Master's thesis, University of Utah, 2004.

[33] N. Nunalee T. Bai T. Mason K. Shull, L. C. Brinson and S. Carr. Aging characterization of polymeric insulation in aircraft wiring via impedance spectroscopy. In *5th Joint NASA / FAA / DoD Conference on Aging Aircraft*, September 2001.

[34] D. Rogovin. Impedance monitoring for health management of electrical insulation, April 2000.

[35] P. Somlo and D. Hollway. Microwave locating reflectometer. *Electronics Letters*, 5:468–469, 1969.

[36] Carine Neus Patrick Boets and Leo Van Biesen. Channel capacity estimation of digital subscriber line: a frequency domain approach. In *Proceedings of the IEEE International conference on Communications*, 2007.

[37] C. Dowding and K. O'Connor. Geotechnical applications of time domain reflectometry. Technical report, Northwestern University, Department of civil engineering, 2000.

[38] K. Noborio. Measurement of soil water content and electrical conductivity by time domain reflectometry, a review. *Computer and Electronics in Agriculture*, 31:213–237, 2001.

[39] R. Hunsperger M. Chajes, W. Liu and E. Kunz. An overview of corrosion damage detection in steel bridge strands using TDR. In *Proceedings of the 2nd international Symposium on TDR for innovative applications*, 2001.

[40] J. Hanson. Testing methods for detection of insulation damage in aerospace wiring harness. In *5th joint FAA / NASA / DoD Conference on Aging Aircraft*, September 2001.

[41] J.P. Steiner, W.L.R. Weeks, Electric Power Research Institute, and Purdue University. *Time-domain reflectometry for monitoring cable changes: feasibility study*. EPRI (Series). The Institute, 1990.

[42] Cynthia Furse, You Chung Chung, Rakesh Dangol, Marc Nielsen Glen Mabey, and Raymond Woodward. Frequency-Domain Reflectometery for on-Board Testing of Aging Aircraft Wiring. *IEEE Transactions on Electromagnetic Compatibility*, 45(2):306–315, May 2003.

[43] Paul Smith. *Spread Spectrum Time Domain Reflectometry*. PhD thesis, Utah State University, 2003.

[44] Paul Smith, Cynthia Furse, and Jacob Gunther. Analysis of Spread Spectrum Time Domain Reflectometry for Wire Fault Location. *IEEE Sensors Journal*, 5(6):1469–1478, December 2005.

[45] Cynthia Furse, Paul Smith, Chet Lo, You Chung Chung, Praveen Pendayala, and Kedarnath Nagoti. Spread spectrum sensors for critical fault location on live wire networks. *Structural Control and Health Monitoring*, 12(3-4):257–267, 2005.

[46] Cynthia Furse and Nilesh Kamdar. An inexpensive distance measuring system for navigation of robotic vehicles. *Microwave and Optical Technology Letters*, 33(2):84–87, 2002.

[47] You Chung Chung, C. Furse, and J. Pruitt. Application of phase detection frequency domain reflectometry for locating faults in an f-18 flight control harness. *IEEE Transactions on Electromagnetic Compatibility*, 47(2):327 – 334, may 2005.

[48] P. J. Medelius et al. Non-intrusive impedance-based cable tester, 1999.

[49] Chet Lo and C. Furse. Noise-Domain Reflectometry for Locating Wiring Faults. *IEEE Transactions on Electromagnetic Compatibility*, 47(1):97–104, February 2005.

[50] Clayton R. Paul. *Analysis of Multiconductor Transmission Lines*. Wiley-Interscience, 1994.

[51] C. Buccella, M. Feliziani, and G. Manzi. Detection and Localization of Defects in Shielded Cables by Time-Domain Measurements with UWB Pulse Injection and Clean Algorithm Postprocessing. *IEEE Transactions on Electromagnetic Compatibility*, 46(4):597 – 605, November 2004.

[52] P. Tsai, Chet Lo, You Chung Chung, and C. Furse. Mixed-Signal Reflectometer for Location of Faults on Aging Wiring. *IEEE Sensors Journal*, 5(6):1479–1482, December 2005.

[53] Y.-J. Shin, E.J. Powers, T.-S. Choe, Chan-Young Hong, Eun-Seok Song, Jong-Gwan Yook, and Jin Bae Park. Application of Time-Frequency Domain Reflectometry for Detection and Localization of a Fault on a Coaxial Cable. *IEEE Transactions on Instrumentation and Measurement*, 54(6):2493 – 2500, December 2005.

[54] S. Naik, C.M. Furse, and B. Farhang-Boroujeny. Multicarrier reflectometry. *IEEE Sensors Journal*, 6(3):812 –818, June 2006.

[55] Eunseok Song, Yong-June Shin, P.E. Stone, Jingjiang Wang, Tok-Son Choe, Jong-Gwan Yook, and Jin Bae Park. Detection and location of multiple wiring faults via time frequency-domain reflectometry. *IEEE Transactions on Electromagnetic Compatibility*, 51(1):131 –138, feb. 2009.

[56] Nicolas Ravot. *Analyse et Diagnostic de Réseaux Filaires Complexes par Réflectométrie*. PhD thesis, Université Paris-Sud 11, 2007.

[57] R.E. Scott. *Frequency-domain analysis*. Addison-Wesley Series in the engineering sciences. Addison-Wesley, 1960.

[58] Kiyoshi Morita. *Applied Fourier Transform*. Ohmsha Ltd. Japan, 1995.

[59] Paul G. Huray. *Maxwell's Equations*. Wiley, 2010.

[60] K. Kurokawa. Power waves and the scattering matrix. *IEEE Transactions on Microwave Theory and Techniques*, 13(2):194 – 202, mar 1965.

[61] B.C. Wadell. *Transmission line design handbook*. Artech house antennas and propagation library. Artech House, 1991.

[62] J.D. Irwin and R.M. Nelms. *Basic Engineering Circuit Analysis*. John Wiley & Sons, 2010.

[63] Berkeley. Electronics Research Laboratory University of California, L.W. Nagel, and D.O. Pederson. *SPICE (simulation program with integrated circuit emphasis)*. Memorandum (University of California, Berkeley, Electronics Research Laboratory). Electronics Research Laboratory, College of Engineering, University of California, 1973.

[64] *CST Microwave Studio*, 2003.

[65] Paul Madden DeRusso. *State variables for engineers*. Wiley-Interscience publication. Wiley, 1998.

[66] Craig F. Bohren and D.R. Huffman. *Absorption and scattering of light by small particles*. Wiley science paperback series. Wiley, 1983.

[67] Société française de physique. *Journal de physique: Proceedings*. Number vol. 11. EDP Sciences, 2001.

[68] G. Cerri, R. De Leo, L. Della Nebbia, S. Pennesi, V.M. Primiani, and P. Russo. Fault locatio o shielded cables: Electromagnetic modelling and improved measurement data processing. In *IEE Proceedings on Science, Measurement and Technology*, volume 152, pages 217–226. IET, 2005.

[69] Mathias Fink. Time Reversal of Ultrasonic Fields - Part 1: Basic Principles. *IEEE Transactions on Ultrasonics, Ferroelectrics, and Frequency Control*, 39(5):555–566, September 1992.

[70] F. Wu, J.-L. Thomas, and M. Fink. Time reversal of ultrasonic fields Il: Experimental results. *IEEE Transactions on Ultrasonics, Ferroelectrics and Frequency Control*, 39(5):567 –578, sep 1992.

[71] D. Cassereau and M. Fink. Time-reversal of ultrasonic fields III: Theory of the closed time-reversal cavity. *IEEE Transactions on Ultrasonics, Ferroelectrics and Frequency Control*, 39(5):579 –592, sep 1992.

[72] D. M. Pepper. Nonlinear optical phase conjugation. *Optical Engineering*, 21:156–183, April 1982.

[73] R. W. Byren and D. Filgas. Phase conjugate relay mirror apparatus for high energy laser system and method, 2005.

[74] M. Skolnik and D. King. Self-phasing array antennas. *IEEE Transactions on Antennas and Propagation*, 12(2):142 – 149, mar 1964.

[75] B. Sichelstiel, W. Waters, and T. Wild. Self-focusing array research model. *IEEE Transactions on Antennas and Propagation*, 12(2):150 – 154, mar 1964.

[76] Yian Chang, H.R. Fetterman, I.L. Newberg, and S.K. Panaretos. Microwave phase conjugation using antenna arrays. *IEEE Transactions on Microwave Theory and Techniques*, 46(11):1910 –1919, nov 1998.

[77] R.Y. Miyamoto and T. Itoh. Retrodirective arrays for wireless communications. *IEEE Microwave Magazine*, 3(1):71 –79, mar 2002.

[78] M. Fink. Time reversal mirrors. *Journal of Physics D: Applied Physics*, 26(9), 1993.

[79] Arnaud Derode Claire Prada Philippe Roux Mickael Tanter Jean-Louis Thomas Mathias Fink, Didier Cassereau and François Wu. Time reversed acoustics. *Reports on Progress in Physics*, 63(12), 2000.

[80] Jean-Louis Thomas, François Wu, and Mathias Fink. Time reversal focusing applied to lithotripsy. *Ultrasonic Imaging*, 18(2):106 – 121, 1996.

[81] Gabriel Montaldo, Philippe Roux, Arnaud Derode, Carlos Negreira, and Mathias Fink. Ultrasound shock wave generator with one-bit time reversal in a dispersive medium, application to lithotripsy. 80(5):897–899, 2002.

[82] P. Kosmas and C.M. Rappaport. Time reversal with the fdtd method for microwave breast cancer detection. *IEEE Transactions on Microwave Theory and Techniques*, 53(7):2317 – 2323, july 2005.

[83] Luzhou XU. Jian LI., Guo Bin. Time-reversal-based microwave hyperthermia treatment of cancer, November 2006.

[84] Q. Liu C. Larmat, J. Tromp and J.-P. Montagner. Time reversal location of glacial earthquakes. *Journal of geophysical research*, 113, 2008.

[85] P Vincent M Saillard and G Micolau. Reconstruction of buried objects surrounded by small inhomogeneities. *Inverse Problems*, 16(5), 2000.

[86] Tobias Leutenegger and Jürg Dual. Non-destructive testing of tubes using a time reverse numerical simulation (trns) method. *Ultrasonics*, 41(10):811 – 822, 2004.

[87] Tobias Leutenegger and Jürg Dual. Detection of defects in cylindrical structures using a time reverse method and a finite-difference approach. *Ultrasonics*, 40(1-8):721 – 725, 2002.

[88] N. Chakroun, M.A. Fink, and F. Wu. Time reversal processing in ultrasonic nondestructive testing. *IEEE Transactions on Ultrasonics, Ferroelectrics and Frequency Control*, 42(6):1087 –1098, nov. 1995.

[89] G.F. Edelmann, T. Akal, W.S. Hodgkiss, Seongil Kim, W.A. Kuperman, and Hee Chun Song. An initial demonstration of underwater acoustic communication using time reversal. *IEEE Journal of Oceanic Engineering*, 27(3):602 – 609, jul 2002.

[90] G.F. Edelmann, H.C. Song, S. Kim, W.S. Hodgkiss, W.A. Kuperman, and T. Akal. Underwater acoustic communications using time reversal. *IEEE Journal of Oceanic Engineering*, 30(4):852 –864, oct. 2005.

[91] W. J. Higley, Philippe Roux, W. A. Kuperman, W. S. Hodgkiss, H. C. Song, T. Akal, and Mark Stevenson. Synthetic aperture time-reversal communications in shallow water: Experimental demonstration at sea. *The Journal of the Acoustical Society of America*, 118(4):2365–2372, 2005.

[92] Yi Jiang, D.D. Stancil, and Jian-Gang Zhu. Antenna Array Detection in Highly Cluttered Environment Using Time Reversal Method. In *Microwave Symposium, 2007. IEEE/MTT-S International*, pages 1731–1734, Honolulu, June 2007.

[93] J. M. F. Moura and Y. Jin. Detection by Time Reversal: Single Antenna. *IEEE Transactions on Signal Processing*, 55(1):187 –201, January 2007.

[94] F.P. Miller, A.F. Vandome, and J. McBrewster. *Matched Filter*. VDM Publishing House Ltd., 2010.

[95] D.G. Zill, W.S. Wright, and M.R. Cullen. *Advanced Engineering Mathematics*. Jones and Bartlett Publishers, 2009.

[96] J.R. Barry, E.A. Lee, and D.G. Messerschmitt. *Digital communication*. Kluwer Academic Publishers, 2004.

[97] Peter Kahn. *Mathematical Methods for Scientists and Engineers: Linear and Nonlinear Systems.* New York : J. Wiley, 1990.

[98] D.W. Ricker. *Echo signal processing*, volume 725. Springer Netherlands, 2003.

[99] R.L. Burden and J.D. Faires. *Numerical Analysis*. Cengage Learning, 2010.

[100] F. Gorunescu. *Data Mining: Concepts, Models and Techniques*. Intelligent Systems Reference Library. Springer, 2011.

[101] A. Lelong, L. Sommervogel, N. Ravot, and M.O. Carrion. Distributed reflectometry method for wire fault location using selective average. *IEEE Sensors Journal*, 10(2):300 –310, feb. 2010.

[102] E. Nishiyama and K. Kuwanami. Fault detection for power transmission line by use of m-sequence correlation. In *Transmission and Distribution Conference and Exhibition 2002: Asia Pacific. IEEE/PES*, volume 1, pages 465 – 469 vol.1, oct. 2002.

[103] A.B. Bakushinskii and M.Y. Kokurin. *Iterative methods for approximate solution of inverse problems*. The IMA volumes in mathematics and its applications. Springer, 2004.

[104] Filippo Visco Comandini. *Quelques problèmes de scattering inverse sur les réseaux : application à la détection des fautes électriques sur les réseaux de transmission.* PhD thesis, Université de Versailles ST-Quentin en Yvelines, 2011.

[105] Mostafa Smail. *Développement d'une méthodologie dédiée à la réflectométrie en vue du diagnostic filaire*. PhD thesis, Université Paris Sud 11, 2010.

[106] Yahya Rahmat-Samii and E. Michielssen. *Electromagnetic optimization by genetic algorithms*. Wiley series in microwave and optical engineering. J. Wiley, 1999.

[107] P.J.M. Laarhoven and E.H.L. Aarts. *Simulated annealing: theory and applications*. Mathematics and its applications. D. Reidel, 1987.

[108] M. Hanke. *Conjugate gradient type methods for ill-posed problems*. Pitman research notes in mathematics series. Longman Scientific & Technical, 1995.

[109] P. Kosmas and C.M. Rappaport. A matched-filter fdtd-based time reversal approach for microwave breast cancer detection. *IEEE Transactions on Antennas and Propagation*, 54(4):1257 – 1264, april 2006.

[110] Yi Jiang, Jian-Gang Zhu, D.D. Stancil, and M.J. Chabalko. Polarization sensitive time reversal sar imaging in an environment filled with trees. In *Antennas and Propagation Society International Symposium, 2007 IEEE*, pages 4000 –4003, june 2007.

[111] Yi Jiang, Jian-Gang Zhu, and D.D. Stancil. Synthetic aperture radar ghost image cancellation using broadband time reversal averaging techniques. In *Microwave Symposium, 2007. IEEE/MTT-S International*, pages 1479 –1482, june 2007.

[112] G. Micolau, M. Saillard, and P. Borderies. Dort method as applied to ultrawideband signals for detection of buried objects. *IEEE Transactions on Geoscience and Remote Sensing*, 41(8):1813 – 1820, aug. 2003.

[113] Gilles Micolau and Marc Saillard. D.O.R.T. method as applied to electromagnetic sensing of buried objects. *Radio Science*, 38:1038, 2003.

[114] H. Tortel, G. Micolau, and M. Saillard. Decomposition of the time reversal operator for electromagnetic scattering. *Journal of Electromagnetic waves and applications*, 13:687–719, 1999.

[115] Claire Prada and Mathias Fink. Eigenmodes of the time reversal operator: a solution to selective focusing in multiple-target media. *Wave Motion*, 20:151–163, 1994.

[116] Claire Prada, Jean-Louis Thomas, and Mathias Fink. The iterative time reversal process: Analysis of the convergence. *The Journal of the Acoustical Society of America*, 97(1):62–71, 1995.

[117] Claire Prada, Sébastien Manneville, Dimitri Spoliansky, and Mathias Fink. Decomposition of the time reversal operator: Detection and selective focusing on two scatterers. *Journal of the Acoustical Society of America*, 99(4):2067–2076, 1996.

[118] Nicolas Mordant, Claire Prada, and Mathias Fink. Highly resolved detection and selective focusing in a waveguide using the d.o.r.t. method. *Journal of the Acoustical Society of America*, 105(5):2634, 1999.

[119] E. Kerbrat, C. Prada, D. Cassereau, and M. Fink. Ultrasonic nondestructive testing of scattering media using the decomposition of the time-reversal operator. *IEEE Transactions on Ultrasonics, Ferroelectrics and Frequency Control*, 49(8):1103 –1113, aug. 2002.

[120] Claire Prada and Jean-Louis Thomas. Experimental subwavelength localization of scatterers by decomposition of the time reversal operator interpreted as a covariance matrix. *The Journal of the Acoustical Society of America*, 114(1):235–243, 2003.

[121] Gabriel Montaldo, Mickael Tanter, and Mathias Fink. Real time inverse filter focusing through iterative time reversal. *The Journal of the Acoustical Society of America*, 115(2):768–775, 2004.

[122] Gabriel Montaldo, Mickael Tanter, and Mathias Fink. Revisiting iterative time reversal processing: Application to detection of multiple targets. *The Journal of the Acoustical Society of America*, 115(2):776–784, 2004.

[123] Mehmet Emre Yavuz and Fernando Texeira. *Time Reversal Based Signal Processing Techniques*. VDM Verlag Dr. Muller, 2009.

[124] E. Roubine. *Introduction à la théorie de la communication*. Masson, 1979.

[125] R.B. Millar. *Maximum Likelihood Estimation and Inference: With Examples in R, SAS and ADMB*. Statistics in Practice. John Wiley & Sons, 2011.

[126] W.E. Deming. *Some theory of sampling*. Dover Books on Advanced Mathematics. Dover Publications, 1966.

[127] F. Rouissi, V. Degardin, M. Lienard, and P. Degauque. Low amplitude impulsive noise in vehicular power line network. In *Intelligent Transport Systems Telecommunications,(ITST),2009 9th International Conference on*, pages 538 –542, oct. 2009.

Chapitre I

Résumé

I.1 Introduction

Depuis l'apparition des systèmes électriques, l'utilisation des câbles électriques est devenue primordiale. Ces derniers sont largement utilisés dans la majorité des systèmes modernes, véhiculant énergie et information entre différentes parties d'un système. Nous pouvons citer plusieurs exemples, tels les systèmes de transport, les centrales nucléaires, la machinerie industrielle, les réseaux de transport d'électricité, etc. Les types de câbles peuvent varier en fonction de la nature des signaux transmis et de l'environnement dans lequel le câble est placé ; Les signaux transmis peuvent être analogiques ou numériques, les câbles peuvent être placés dans l'air comme pour les réseaux de transport d'électricité, aussi enfouis dans le sol comme pour les lignes de métro. Un autre exemple est celui des réseaux informatiques, qui peuvent utiliser deux types différents de câbles : le câble coaxial ou la paire torsadée.

Avec cette utilisation croissante de câbles électriques, leur longueur dans certains systèmes a également augmenté au cours des dernières années. Avions et bateaux sont des exemples où la longueur cumulée des câbles pourrait atteindre plusieurs centaines de kilomètres ; tel est le cas d'un Airbus A380 (500 km) ou du bateau 'Queen Mary 2' (2500 km).

Un 'fil sain est l'élément le plus simple et le plus important dans un système électrique'. Plusieurs causes sont à l'origine d'anomalies pouvant affecter les performances d'un câble, perturbant ainsi le transfert d'information fiable entre différents parties du système. Selon les domaines d'application, la conséquence d'une telle dégradation de performance peut avoir des conséquences catastrophiques : les défauts de câblage ont été impliqués dans un certain nombre

d'accidents avioniques sévères, y compris ceux de Swissair-111, TWA-800, et UAL-811 vol. Selon le capitaine Jim Shaw, dirigeant du projet incendie en vol mené par l'association des pilotes Américains 'Air Line Pilots Association' (ALPA), il y a en moyenne trois incendies journaliers dans les avions de transport aux Etats-Unis et au Canada seulement, et la grande majorité sont d'origine électriques. le câblage électrique défectueux et mal installé est l'un des principales causes des incendies dans les maisons et les bâtiments commerciaux : en 2005, presque 400000 incendies se sont produits aux États-Unis conduisant à plus de 3000 morts et près de 14000 blessés ; parmi ces incendies environ 65000 étaient liés à un câblage électrique. Les données montrent aussi que ce genre d'incendie provoque aussi des pertes matérielles estimées à 703 million de dollars environ.

Les questions de sécurité liées au câblage électrique défectueux, ainsi que le cout de maintenance élevé, ont encouragé le financement gouvernemental et industriel des études visant à trouver des méthodes efficaces de détection et de localisation des défauts filaires. En général, ces derniers sont classés en deux catégories :

- Les défauts francs : circuits ouverts et courts circuits.
- Les défauts non-francs : tout autre type de défauts, tels qu'isolants endommagés, fissures, etc.

En se basant sur le coefficient de réflexion, un défaut franc résulte en une réflexion totale, soit un coefficient égal à $+1$ pour le circuit ouvert et -1 pour le court-circuit, tandis qu'un défaut non franc a un coefficient de réflexion dont l'amplitude est inférieure à 1. Figures I.3, I.1 et I.2 montrent des statistiques menées par la marine américaine (Navy), les garde-côtes (coastguard) et l'administration fédérale de l'aviation (Federal Aviation Administration (FAA)), montrant les différents types de défauts rencontrés dans les équipements des trois administrations. Les trois diagrammes montrent différents types de défauts non-francs, avec un taux d'occurrence non négligeable par rapport à celui des défauts francs. Et puisque les défauts non-francs peuvent évoluer vers des défauts francs, ils présentent un risque non négligeable par rapport à la sécurité et la fiabilité du système, d'où la nécessité de trouver des méthodes pouvant détecter et localiser ce type de défauts.

Les défauts apparaissent pour plusieurs raisons, pouvant être internes ou externes au câble.

- Les causes internes, comme par exemple :
  - Un défaut de fabrication qui n'a pas été détecté lors des tests d'usine.

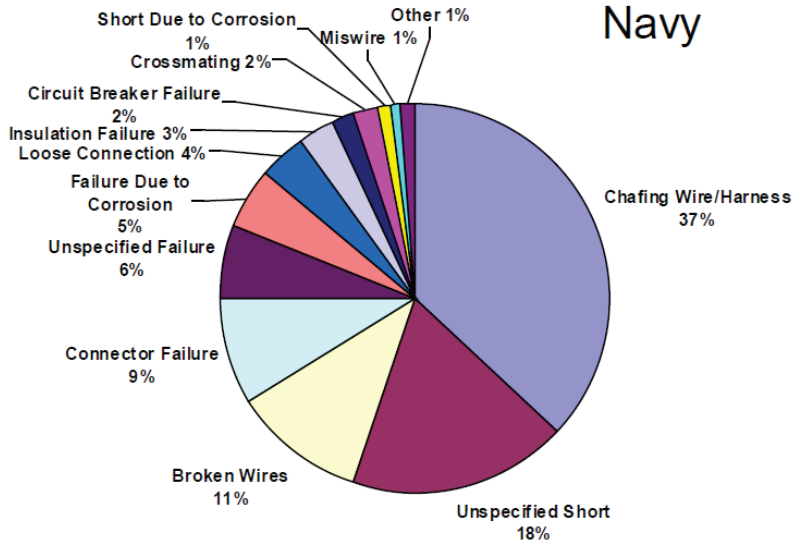

FIGURE I.1 : Les types de défauts rencontrés dans les équipements de la marine Américaine.

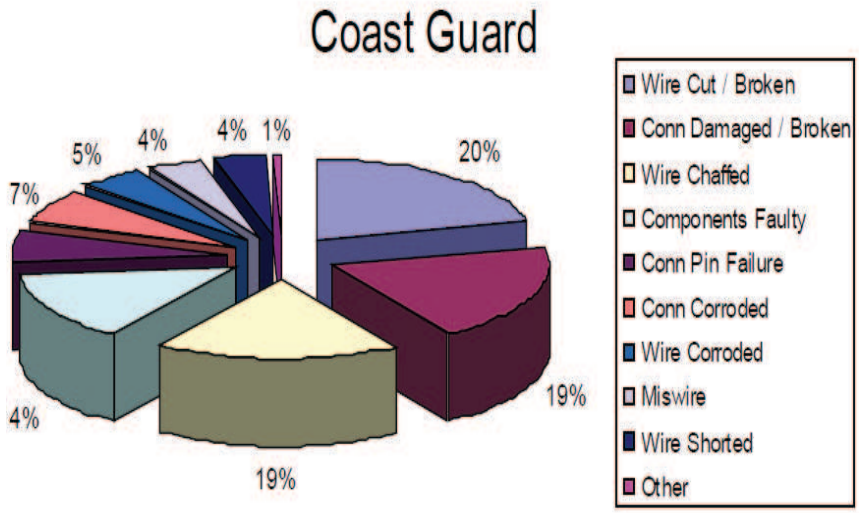

FIGURE I.2 : Les types de défauts rencontrés dans les équipements des garde-cotes Américains.

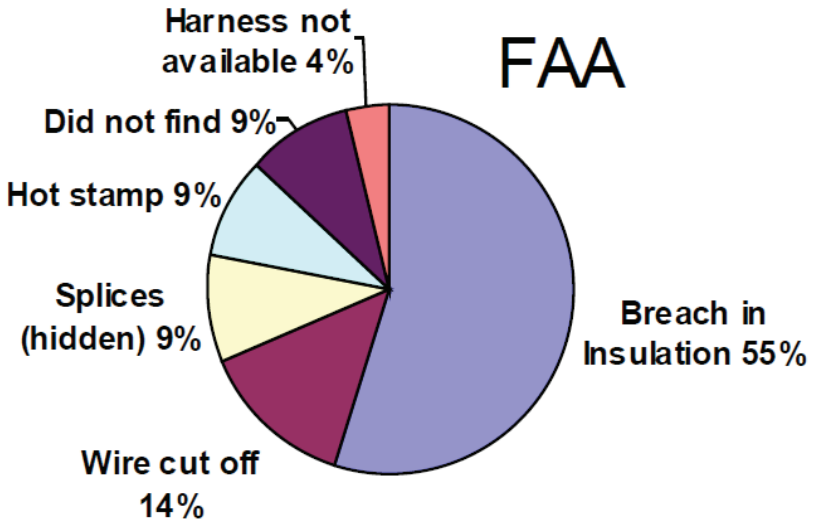

FIGURE I.3 : Les types de défauts rencontrés dans les équipements de l'agence fédérale de l'aviation Américaine.

  - Un échauffement local important.
  - le vieillissement du diélectrique.
- les causes externes :
  - Les agressions mécaniques extérieures.
  - Les défauts d'assemblage, tels que l'intervention humaine dans le processus de maintenance.
  - La corrosion, l'oxydation, les effets environnementaux (température, humidité, etc.).

I.2 Méthodes de réflectométrie

Dans la section précédente, nous avons inspecté les différents types de défauts pouvant exister dans les câbles électriques, et leur raisons d'apparition. Par conséquent, plusieurs méthodes ont émergé pour détecter la présence des défauts dans les câbles, dont la majorité a porté sur les défauts francs, car ils sont généralement à l'origine des incidents les plus conséquents qui se produisent, tels que les incendies, et sont également plus faciles à détecter et à localiser. Toutefois, l'importance des défauts non-francs ne devrait pas être sous-estimée, parce que un défaut non-francs peut se développer en un défaut franc et peut également provoquer l'appari-

tion d'un arc électrique tandis que le câble est en cours d'utilisation, menaçant ainsi la sécurité du système.

Parmi les méthodes les plus connues pour inspecter la présence de défauts dans les câbles, Les méthodes de réflectométrie sont les méthodes les plus couramment utilisés. Depuis le milieu du XXe siècle, la réflectométrie a été utilisé pour détecter et localiser des défauts dans les câbles électriques, ainsi que dans les réseaux de télécommunication ; à ne pas oublier aussi d'autres applications, telles que la géotechnique, l'hydrologie et la construction.

Il existe plusieurs méthodes de réflectométrie, divisées en deux grandes catégories, en fonction du domaine d'analyse : réflectométrie dans le domaine temporel (Time Domain Reflectometry ou TDR) et dans le domaine fréquentiel (Frequency Domain REflectometry ou FDR). Le principe général de ces méthodes est cependant le même : elles reposent sur la propagation d'une onde électromagnétique dans le réseau à tester, et l'analyse de l'onde réfléchie (causée par la présence de discontinuités d'impédance, des jonctions, etc. dans le réseau) pour essayer de détecter et de localiser un défaut éventuel.

Les méthodes de réflectométrie diffèrent dans la forme de l'onde injectée, ou dans les techniques de post-traitement utilisées pour extraire des informations de l'onde réfléchie. Par exemple, dans la famille des méthodes TDR, la TDR standard injecte un échelon ou une impulsion dans le réseau sous test, puis s'appuie sur l'analyse de l'onde réfléchie dans le domaine temporel afin d'en extraire la signature du défaut, tandis que la TDR séquentielle (Sequence TDR ou STDR) et la TDR à étalement de spectre (Spread Spectrum TDR ou SSTDR) injectent une séquence numérique (pseudo-bruit), et lorsque l'onde réfléchie est reçue, une opération de corrélation de cette onde avec l'onde initialement injectée est effectuée pour essayer de déterminer la position d'un défaut éventuel.

Dans le domaine fréquentiel, nous distinguons trois méthodes principales, en fonction du paramètre qui doit être mesurée afin de pouvoir localiser le défaut : l'onde continue modulée en fréquence (Frequency modulated continous wave), qui est basée sur la mesure de la fréquence, la détection de phase basée sur la mesure de phase, et la réflectométrie d'ondes stationnaire basée sur la mesure de l'amplitude de l'onde stationnaire (superposition des ondes incidentes et réfléchies). Il existe aussi un troisième type de méthodes qui a été récemment mis au point, appelé la réflectométrie dans le domaine du bruit. Il utilise également l'analyse basée sur la corrélation pour essayer de déterminer la position d'un défaut éventuel, mais diffère des techniques

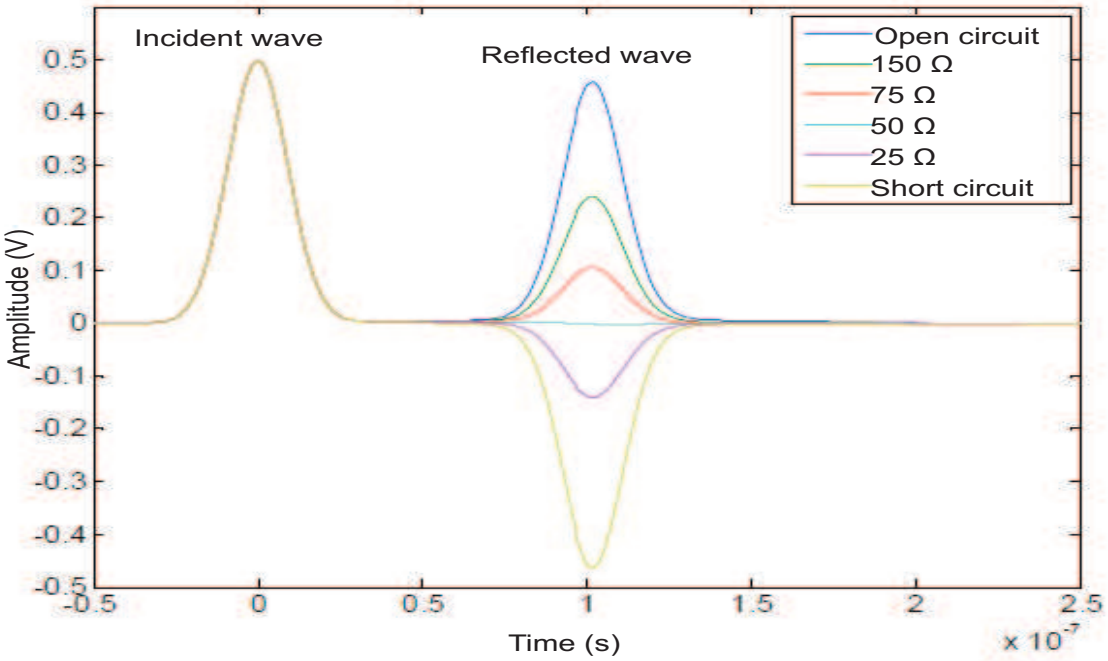

FIGURE I.4 : Example de la TDR standard appliquée à un cable coaxial $50\ \Omega$, pour différentes valeurs de la charge à l'extrémité. Source : N. Ravot, *Analyse et Diagnostic de Réseaux Filaires Complexes par Réflectométrie.* Thèse de l'Université Paris-Sud 11, 2007.

d'étalement de spectre dans le fait qu'elle utilise les signaux déjà présents sur le câble, et ainsi exige que le câble testé soit en utilisation.

Pour mieux illustrer le principe de base de ces méthodes, nous avons choisi l'exemple simple d'un câble coaxial d'impédance caractéristique $50\ \Omega$, où l'on dispose d'un port de test servant à émettre le signal de test et recevoir le signal réfléchi. Nous considérons la TDR standard, la méthode que nous avons choisie dans notre étude en vue de comparer ses performances à la nouvelle méthode que nous avons développée.

Dans la propagation guidée, une onde se déplace le long du câble jusqu'à ce qu'elle rencontre une discontinuité d'impédance : alors une partie de cette onde est réfléchie, tandis qu'une autre partie est transmise à travers la discontinuité. Par conséquent, l'onde réfléchie contient des informations sur la nature du défaut, et le temps (en TDR standard) nécessaire pour que l'écho lié au défaut (dans l'onde réfléchie) atteigne la position du port de test fournit des informations sur la position du défaut.

Dans l'exemple que nous avons considéré, plusieurs charges résistives ont été relié à l'extrémité du câble, et les ondes réfléchies par rapport à celle injectée ont été montrés sur la Fig. I.4.

Nous remarquons clairement les réflexions importantes dans le cas de défauts francs, et les réflexions faibles dans le cas de défauts non-francs. Par conséquent, un défaut non-franc est généralement moins facile à détecter qu'un défaut franc, car il en résulte une réflexion moins importante, et aussi parce que les techniques de détection habituelles reposent sur la détection de pic pour évaluer la présence d'un défaut éventuel. En outre, la détection devient plus compliquée dans les réseaux complexes, où plusieurs réflexions résultant de la présence de discontinuités dans le réseau sous test (jonctions, variations d'impédance, etc.) peuvent masquer la réflexion provenant d'un défaut éventuel, surtout si ce défaut est non-franc, et séparé du port de test par une ou plusieurs discontinuités.

En règle générale, les méthodes de réflectométrie fonctionnent bien dans les cas simples comme pour les lignes simples de transmission, mais sont insuffisantes dès que la structure du réseau devient de plus en plus complexe, et que les défauts devient de plus en plus 'non-francs', de sorte que l'amplitude de l'onde réfléchie causés par ces défauts devient comparable au niveau de bruit.

Dans notre étude, nous adressons les défauts non-francs dans les réseaux filaires à structure complexe. Dans un premier temps, nous étudions la détection des défauts, et introduisons l'idée de l'impulsion adaptée (Matched Pulse ou MP), et dans un deuxième temps nous discutons la localisation des défauts en dérivant une nouvelle méthode basée sur les propriétés de la méthode DORT (décomposition de l'opérateur de retournement temporel).

I.3 Détection des défauts

I.3.1 Introduction

Les techniques de réflectométrie standard essayent de détecter la présence d'un défaut éventuel par injection d'un signal de test prédéfini dans le réseau, et par analyse du signal réfléchi, recherchant la signature du défaut. Cependant, les signaux de test utilisés en réflectométrie sont les mêmes pour tous les réseaux, et donc ne peuvent garantir une performance optimale dans tous les cas, surtout quand le défaut est non-franc et lorsqu'il s'agit d'un réseau complexe. Dans ces conditions, les techniques de réflectométrie deviennent insuffisantes. Or, le problème de la détection des défauts dans des réseaux complexes peut être assimilé à celui de la détection de cibles dans un environnement complexe, rencontré dans le domaine des radars.

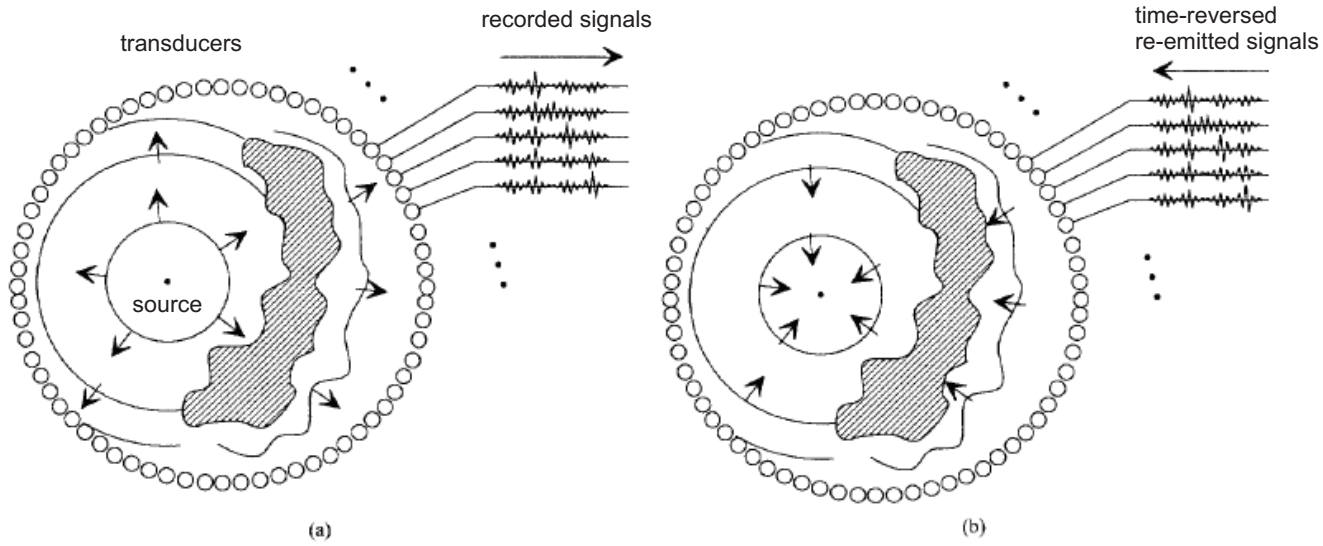

FIGURE I.5 : Example d'une cavité de retournement temporel en acoustique. Dans une première étape, une source émet des ondes acoustiques qui sont enregistrées par un ensemble de transducteurs (a), et dans une deuxième étape les signaux enregistrés sont inversés dans le temps et ré-émis dans le milieu (b) ; ils se focalisent à la position de la source initiale.

Pour résoudre ce problème, l'idée était d'adapter le signal de test au milieu de propagation, de manière à entraîner une performance optimale ; ceci s'effectue par l'utilisation du retournement temporel (Time Reversal ou TR), technique introduite dans les années 1990, qui transforme le multi-trajet, traditionnellement nuisible à la performance, en un facteur qui renforce les performances et augmente le SNR.

I.3.2 Retournement temporel

Le retournement temporel a été introduit pour la première fois dans le domaine des ondes acoustiques par Fink et al. Cette technique a montré ses avantages lorsqu'il s'agit d'environnements complexes, car elle permet de transformer le multi-trajet en un élément qui améliore les performances des méthodes de détection dans de tels environnements.

Le retournement temporel implique la retransmission physique ou synthétique de signaux acquis par un ensemble d'émetteurs-récepteurs, en les retournant dans le temps, ce qui ressemble à jouer une cassette en arrière. Les signaux retransmis se propagent en retraçant le même trajet initial, et l'on obtient une focalisation à la position de la source initiale.

Un exemple de l'acoustique physique pour illustrer le principe du retournement temporel est illustré par la Fig. I.5. Nous considérons une source émettant des ondes acoustiques dans un milieu inhomogène, et un ensemble de transducteurs piézo-électriques qui servent à émettre et recevoir les ondes.

Dans une première étape illustrée à la Fig. I.5(a), la source émet des ondes qui se propagent dans le milieu ; ces ondes subissent des déformations à cause des discontinuités et des hétérogénéités dans le milieu de propagation. Lorsque les ondes réfléchies atteignent les transducteurs, ceux-ci enregistrent les signaux détectés. Cette première étape est l'étape d'enregistrement.

Dans une deuxième étape (Fig. I.5(b)) la source est éteinte. Les signaux enregistrés dans la première phase sont inversés dans le temps ; ensuite chaque transducteur émet le signal correspondant en synchronie avec les autres transducteurs. Les ondes émises retracent le passage d'origine à travers le milieu, et focalisent à la position initiale de la source. A noter que les ondes ré-émises contiennent des informations sur le milieu de propagation, et dépendent de celui-ci ; ils sont adaptés à ce milieu. On a démontré que le retournement temporel est optimal dans le sens où il permet de focaliser une plus grande quantité d'énergie sur la position de la source initiale, en particulier dans des environnements complexes où les méthodes classiques subissent une dégradation de leur performance.

La propriété de focalisation nous sera d'une grande importance lorsqu'on abordera la localisation des défauts. Dans la partie où nous aborderons la détection, nous serons intéressés à maximiser le SNR à la position du défaut, donc à obtenir une plus grande quantité d'énergie en cette position ; dans ce contexte, le retournement temporel est optimal car son principe est équivalent au principe du filtre adapté, rencontré dans les télécommunications.

Avant de continuer notre étude, et étant donné que les défauts non-francs sont difficiles à détecter, nous adopterons la définition du système différence ; c'est-à-dire que le signal réfléchi du système avec défaut est soustrait de celui du système sans défaut, en faisant comme hypothèse que notre système (le réseau sous test) est linéaire et invariant dans le temps, sauf pour l'apparition du défaut. Le nouveau système est alors appelé le système différence.

I.3.3 Impulsion adaptée (Matched Pulse ou MP)

Dans l'exemple précédent, nous avons vu que le signal de test adapté est obtenu après une première étape consistant à injecter un signal prédéfini dans le milieu, et ensuite l'enregistre-

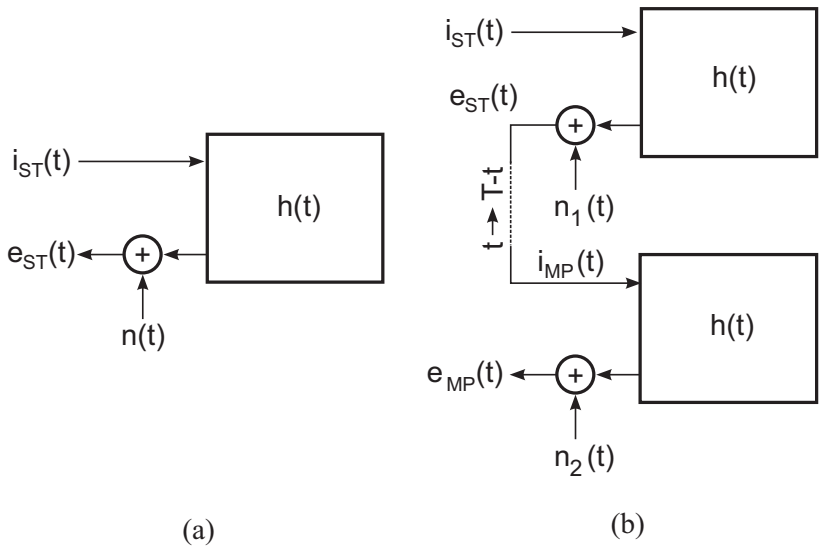

FIGURE I.6 : Schémas-blocs pour : (a) TDR standard et (b) Méthode MP. La réponse impulsionnelle du réseau sous test est notée $h(t)$, et les signaux $n_i(t)$ sont des sources de bruit équivalentes à la sortie du système. La durée T est celle du test standard TDR.

ment du signal réfléchi : le nouveau signal de test est la version retournée dans le temps de celui-ci.

Dans notre cas de détection de défauts dans les réseaux filaires, les mêmes idées s'appliquent. Dans cette section, nous expliquons la procédure d'obtention de ce signal test que nous avons appelé impulsion adaptée (MP), et le comparons au cas des techniques de réflectométrie Standard, notées avec l'acronyme ST.

Fig.I.6(a) représente le test d'un réseau avec une technique TDR standard : le signal injecté dans le domaine temporel est noté en tant $i_{ST}(t)$. Le signal réfléchi (echo TDR standard), est noté avec $e_{ST}(t)$. C'est le signal qui, dans n'importe quelle méthode TDR et après avoir subi un post-traitement adéquat, permet de détecter et localiser un défaut éventuel. $h(t)$ désigne la réponse impulsionnelle du système différence. Le cas de la MP est illustré à la Fig. I.6(b). Ici, $e_{ST}(t)$ n'est plus le point final du test, mais il marque une étape intermédiaire. En fait, nous définissons notre signal de test, ou MP, comme la version inversée dans le temps de l'écho TDR standard. Le signal de test MP, noté $i_{MP}(t)$, est le signal de test effectif, et par conséquent il est injecté dans le réseau de test afin d'obtenir l'écho MP, noté $e_{MP}(t)$. Cette procédure ne nécessite aucune hypothèse sur la nature du signal TDR injecté $i_{ST}(t)$; ça pourrai donc être n'importe quel signal de test développé dans le contexte des méthodes TDR. La MP est aussi

une méthode TDR, mais avec une nouvelle définition du signal de test. Dans ce qui suit nous prouvons que l'utilisation de la MP résulte en l'amélioration de performance, comparée aux méthodes usuelles de TDR.

I.3.4 Etude mathématique

Après l'introduction de l'approche MP, et afin de quantifier ses avantages et analyser les situations où elle présente des avantages majeurs par rapport aux méthodes existantes, nous proposons de la comparer aux techniques de réflectométrie standard, car celles-ci représentent les méthodes les plus couramment utilisés aujourd'hui. La comparaison sera effectuée d'une manière formelle, à partir d'une analyse mathématique visant à calculer un gain de détection. Mais tout d'abord, nous avons besoin d'introduire un modèle de propagation.

I.3.4.1 Modélisation de la réponse impulsionnelle du système différence

La réponse impulsionnelle est modélisée comme une superposition d'échos retardés dans le temps, avec des amplitudes variées dépendant de la séquence d'interactions entre le signal de test et les discontinuités présentes dans le réseau sous test. Aucune hypothèse n'est faite sur la nature du défaut, mais pour les défauts non-francs considérés dans notre travail, l'énergie qu'ils réfléchissent est une fraction de celle incidente, nécessitant

$$\Gamma^2_{F,\mathrm{rms}} = \frac{1}{B_T}\int |\Gamma_F(\omega)|^2 \mathrm{d}\omega \ll 1. \tag{I.1}$$

B_T étant la région du spectre de Fourier occupée par le signal d'excitation. La racine carrée de la valeur moyenne (rms) $\Gamma_{F,\mathrm{rms}}$ de la réflectivité du défaut doit être suffisamment faible pour considérer le défaut comme étant non-franc. Par conséquent, la réponse impulsionnelle du réseau sous test pourra être modélisée comme suit

$$h(t) = \Gamma_F(t) * \sum_{i=1}^{N} \alpha_i \delta(t - t_i), \tag{I.2}$$

Avec $\delta(t)$ l'impulsion de Dirac, et l'étoile $*$ indiquant l'opération de convolution. Dans le reste de l'analyse, les sommes seront caractérisées par l'indice de sommation, sans détails supplémentaires

I.3.4.2 Gain de détection

La détection d'un défaut non-franc est généralement basée sur l'identification du plus fort signal réfléchi par le réseau sous test, après avoir soustrait l'écho de référence. En termes simples, le signal de sortie est analysé à la recherche d'une contribution qui soit plus élevée qu'seuil de référence convenablement fixé à l'avance. Ce seuil est généralement défini comme un compromis entre la capacité de détecter la présence d'un écho (et donc un défaut éventuel) et la nécessité de prévoir une immunité robuste contre le bruit. Indépendamment du type du signal de test, l'utilisation d'une approche de seuil de détection implique que la quantité qui nous intéresse est la puissance maximale instantanée de l'écho. Elle est défini, dans le cas d'un signal d'essai standard comme

$$\mathcal{P}_{\mathrm{ST}}^{\mathrm{out}} = \max_{t} |e_{\mathrm{ST}}(t)|^2 \tag{I.3}$$

où $e_{\mathrm{ST}}(t)$ est l'écho généré par l'application d'un signal de test $i_{\mathrm{ST}}(t)$.

Dans les configurations de réseaux simples, on peut s'attendre à que ce maximum coïncide avec le premier écho généré par l'interaction avec le défaut, ce qui permet de déterminer la position de ce dernier. En fait, comme il sera montré dans les résultats expérimentaux, cette hypothèse ne tiendra plus dans les réseaux complexes. Les schémas de détection basés sur la détection du pic ne peuvent pas assurer une localisation précise du défaut dans de telles circonstances.

L'efficacité des méthodes TDR peut donc être mesurée en observant le rapport $\mathcal{P}^{\mathrm{out}}/\mathcal{E}^{\mathrm{in}}$, où $\mathcal{E}^{\mathrm{in}}$ est l'énergie du signal de test appliqué au réseau à tester.

Par conséquent, l'amélioration apportée par l'approche MP comparée aux méthodes TDR standard peut être évaluée d'après la définition suivante du gain de détection

$$G = \frac{\mathcal{P}_{\mathrm{MP}}^{\mathrm{out}}/\mathcal{E}_{\mathrm{MP}}^{\mathrm{in}}}{\mathcal{P}_{\mathrm{ST}}^{\mathrm{out}}/\mathcal{E}_{\mathrm{ST}}^{\mathrm{in}}}, \tag{I.4}$$

où les quantités indexés par MP sont définis comme ceux par ST, mais compte tenu des signaux générés par l'application du signal de test MP $i_{\mathrm{MP}}(t)$.

I.3.4.2.1 Calcul des énergies d'entrée

Pour calculer le gain, on considère le signal de sortie $e_{\mathrm{ST}}(t)$, obtenu dans le cas de la TDR standard

$$e_{\mathrm{ST}}(t) = i_{\mathrm{ST}}(t) * h(t) = \sum_{i} \alpha_i e_{\mathrm{ST}}^{o}(t - t_i), \tag{I.5}$$

avec

$$e^o_{\mathrm{ST}}(t) = i_{\mathrm{ST}}(t) * \Gamma_F(t), \tag{I.6}$$

, La réponse élémentaire de chaque écho trouvé dans $e_{\mathrm{ST}}(t)$. Les énergies d'entrée en (I.4) sont données par

$$\mathcal{E}^{\mathrm{in}}_{\mathrm{ST}} = \int |i_{\mathrm{ST}}(t)|^2 \mathrm{d}t, \tag{I.7}$$

Et pour la méthode MP

$$\mathcal{E}^{\mathrm{in}}_{\mathrm{MP}} = \int |i_{\mathrm{MP}}(t)|^2 \mathrm{d}t = \int |e_{\mathrm{ST}}(T-t)|^2 \mathrm{d}t, \tag{I.8}$$

T étant la durée de la première étape où $i_{\mathrm{ST}}(t)$ est appliqué au réseau sous test. Pour simplifier l'analyse, nous négligerons ce terme, comme il n'aura pas d'influence sur ce qui suit.

En insérant (I.5) dans (I.8), on obtient

$$\mathcal{E}^{\mathrm{in}}_{\mathrm{MP}} = \mathcal{E}_o \left[\sum_i \alpha_i^2 + \sum_{i \neq j} \alpha_i \alpha_j \phi_o(t_i - t_j) \right], \tag{I.9}$$

Ayant introduit l'énergie $\mathcal{E}_o$ de l'écho $e^o_{\mathrm{ST}}(t)$, et sa fonction d'autocorrélation normalisée $\phi_o(t)$,

$$\phi_o(t_i - t_j) = \frac{\int e^o_{\mathrm{ST}}(t - t_i) e^o_{\mathrm{ST}}(t - t_j) dt}{\mathcal{E}_o} \tag{I.10}$$

L'équation (I.9) est composée de deux termes : le premier est la somme des énergies des échos, comme s'ils n'étaient pas superposés, et le deuxième représente la somme des énergies mutuelles de chaque couple d'échos. En comparant ces deux termes, nous remarquons que le premier terme est une somme cohérente, plus précisément une série à terme positifs, tandis que le deuxième contient des produits $\alpha_i \alpha_j$, et est donc incohérente. Etant donné que dans les réseaux complexes, la plupart des échos sont générés par des discontinuités ayant un coefficient de réflexion négatif, on pourra alors appliquer l'approximation suivante

$$\sum_{i \neq j} \alpha_i \alpha_j \phi_o(t_i - t_j) \ll \sum_i \alpha_i^2. \tag{I.11}$$

I.3.4.2.2 Calcul des puissances instantanées

Avant de pouvoir calculer le gain de détection, il nous reste à calculer les puissances instantanées à la position du défaut pout les deux cas. On considère le signal de sortie dans le cas

MP

$$\begin{aligned} e_{\mathrm{MP}}(t) &= i_{\mathrm{ST}}(-t) * h(-t) * h(t) \\ &= \mathcal{E}_{\Gamma_F} i_{\mathrm{ST}}(-t) * \phi_{\Gamma_F}(t) * \sum_k \beta_k \delta(t - t'_k) \\ &= \mathcal{E}_{\Gamma_F} e^o_{\mathrm{MP}}(t) * \sum_k \beta_k \delta(t - t'_k), \end{aligned} \tag{I.12}$$

avec $\phi_{\Gamma_F}(t)$ la fonction d'autocorrélation normalisée de $\Gamma_F(t)$

$$\phi_{\Gamma_F}(t) = \frac{\Gamma_F(-t) * \Gamma_F(t)}{\mathcal{E}_{\Gamma_F}} \tag{I.13}$$

Et $e^o_{\mathrm{MP}} = i_{\mathrm{ST}}(-t) * \phi_{\Gamma_F}(t)$ est la réponse élémentaire du défaut dans le cas MP. Le terme $\mathcal{E}_{\Gamma_F}$ est l'énergie de la fonction $\Gamma_F(t)$. Aussi la série $\{\beta_k\}$ est définie

$$\beta_k = \begin{cases} \sum_i \alpha_i^2 & k = 0 \\ \alpha_i \alpha_j & k \neq 0 \end{cases} \tag{I.14}$$

Avec

$$t'_k = t_j - t_i \tag{I.15}$$

Les puissances instantanées sont alors trouvées en appliquant (I.3)

$$\mathcal{P}^{\mathrm{out}}_{\mathrm{ST}} \simeq \alpha^2_{\max} \max_t |e^o_{\mathrm{ST}}(t)|^2 \tag{I.16}$$

Avec $\alpha_{\max} = \max_i \alpha_i$, tandis que dans le cas MP

$$\mathcal{P}^{\mathrm{out}}_{\mathrm{MP}} = \max_t |e_{\mathrm{MP}}(t)|^2 \simeq \mathcal{E}^2_{\Gamma_F} \beta_0^2 \max_t |e^o_{\mathrm{MP}}(t)|^2. \tag{I.17}$$

I.3.4.2.3 Calcul du gain de détection

En utilisant (I.7), (I.9), (I.16) et (I.17), (I.4) on obtient

$$G = G' G'' \tag{I.18}$$

avec

$$G' = \sum_i \alpha_i^2 / \alpha^2_{\max} \tag{I.19a}$$

$$G'' = \frac{\mathcal{E}^2_{\Gamma_F} \mathcal{E}^{\mathrm{in}}_{\mathrm{ST}}}{\mathcal{E}_o} \frac{\max_t |e^o_{\mathrm{MP}}(t)|^2}{\max_t |e^o_{\mathrm{ST}}(t)|^2} \tag{I.19b}$$

Les deux termes de gains sont liés à des caractéristiques spécifiques du réseau : G' est directement lié à la complexité du réseau, spécialement sa topologie, indépendamment de la nature du défaut, tandis que G'' dépend de la réponse du défaut et la nature du signal d'excitation. Les résultats expérimentaux illustreront mieux les résultats obtenus.

I.3.4.3 Gain en SNR et probabilités de détection

De la même manière, on calcule le gain en SNR des deux méthodes MP et TDR standard. Si S_{MP} et S_{ST} repésentent les SNR dans le cas MP et TDR respectivement, on obtient un gain en SNR

$$R = \frac{S_{\mathrm{MP}}/\mathcal{E}^{\mathrm{in}}_{\mathrm{MP}}}{S_{\mathrm{ST}}/\mathcal{E}^{\mathrm{in}}_{\mathrm{ST}}} = \frac{G}{1+\Gamma^2_{F,\mathrm{rms}}\sum_i \alpha_i^2}. \tag{I.20}$$

Pour calculer les probabilités de détection, nous notons par TP (True Positive) la probabilité conditionnelle de détection d'un défaut, sachant qu'il existe, et par FP (False Positive) la probabilité conditionnelle de détection d'un défaut sachant que celui-ci n'existe pas. Le calcul des deux probabilités donne

$$P^{\mathrm{TP}} = \frac{1}{2}\mathrm{erfc}\left((\rho-1)\sqrt{S/2}\right), \tag{I.21}$$

et

$$P^{\mathrm{FP}} = \frac{1}{2}\mathrm{erfc}\left(\rho\sqrt{S/2}\right). \tag{I.22}$$

Avec ρ désignant la fraction de l'écho considéré pour la détection (par exemple 80% du pic maximal) et S le SNR dans le cas spécifique considéré, MP soit-il ou TDR.

I.3.5 Résultats expérimentaux

Nous exposons dans cette section quelques résultats expérimentaux obtenus. Les réponses impulsionnelles des différentes configurations de réseaux ont été mesurées en utilisant un analyseur de réseau vectoriel connecté aux ports de test. La bande de fréquence de cet analyseur, un Rohde & Schwarz ZVB-8, est de 300 KHz à 8 GHz. En utilisant l'analyseur on a accès au spectre de Fourier de la réponse impulsionnelle, donc les résultats obtenus ont été traités par la suite en appliquant une transformée de Fourier inverse. En s'appuyant sue ces données, les quantités introduites dans l'analyse mathématique peuvent être obtenues par des techniques de post-traitement ; en particulier, la réponse du système à n'importe quel signal de test peut être

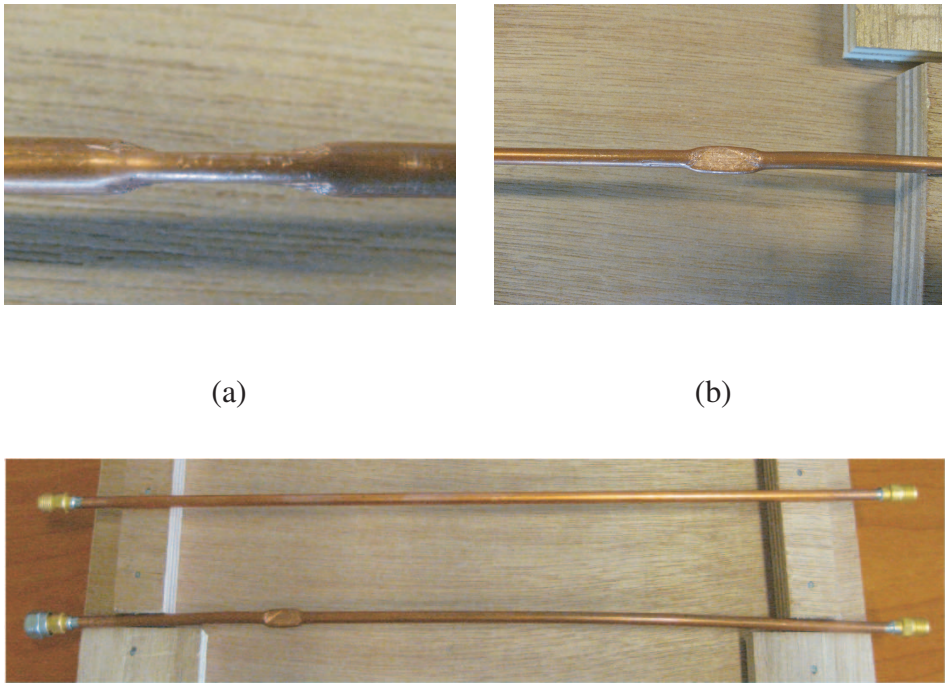

(a) (b)

(c)

FIGURE I.7 : Le défaut non-franc considéré dans les expérimentations, obtenu en écrasant, sur une distance de 1 cm, une portion d'un cable semi-rigide. Les trois images représentent : (a) une vue de profil du défaut, avec le cable écrasé jusqu'à une épaisseur de 2 mm ; (b) une vue de face du défaut ; (c) les deux échantillons utilisés dans les mesures c'est à dire la section référence et celle présentant le défaut.

obtenue par convolution du signal de test désiré avec la réponse impulsionnelle mesurée du système.

Les défauts ont été créés en utilisant une section de câble semi-rigide, de 30 cm de longueur, terminée avec deux connecteurs SMA. La réponse impulsionnelle du système référence est obtenue avec une section non altérée, alors que celle du système défectueux avec une section défectueuse. Le défaut non-franc qu'on a considéré pour notre étude est un défaut d'écrasement, illustré par la Fig. I.7. Les câbles utilisés sont des câbles coaxiaux d'impédance caractéristique 50 $Omega$.

Nous considérons les deux configurations de réseaux représentées dans la Fig. I.8 : un réseau en Y et un réseau en 2Y. Quatre cas ont été analysés, pour des extrémités adaptés et en circuit ouvert, et ceci pour les deux configurations. Les réponses impulsionnelles obtenues sont

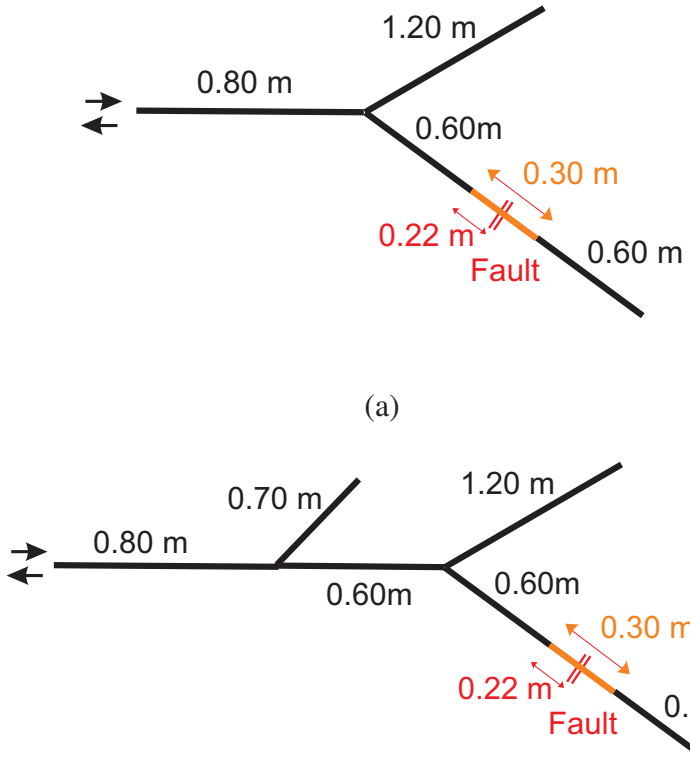

FIGURE I.8 : Les deux structures de réseaux considérées dans les mesures : (a) un réseau en Y ; (b) un réseau en 2Y. Chaque branche du réseau consiste en un cable coaxial d'impédance caractéristique 50 Ω, tandis que les sections en rouge représentent les échantillons contenant le défaut, comme illustré dans la Fig. I.7. Les terminaisons des lignes ont été adaptées ou laissées en circuit-ouvert, selon la configuration de test. Le symbole de la double flèche indique le port de test.

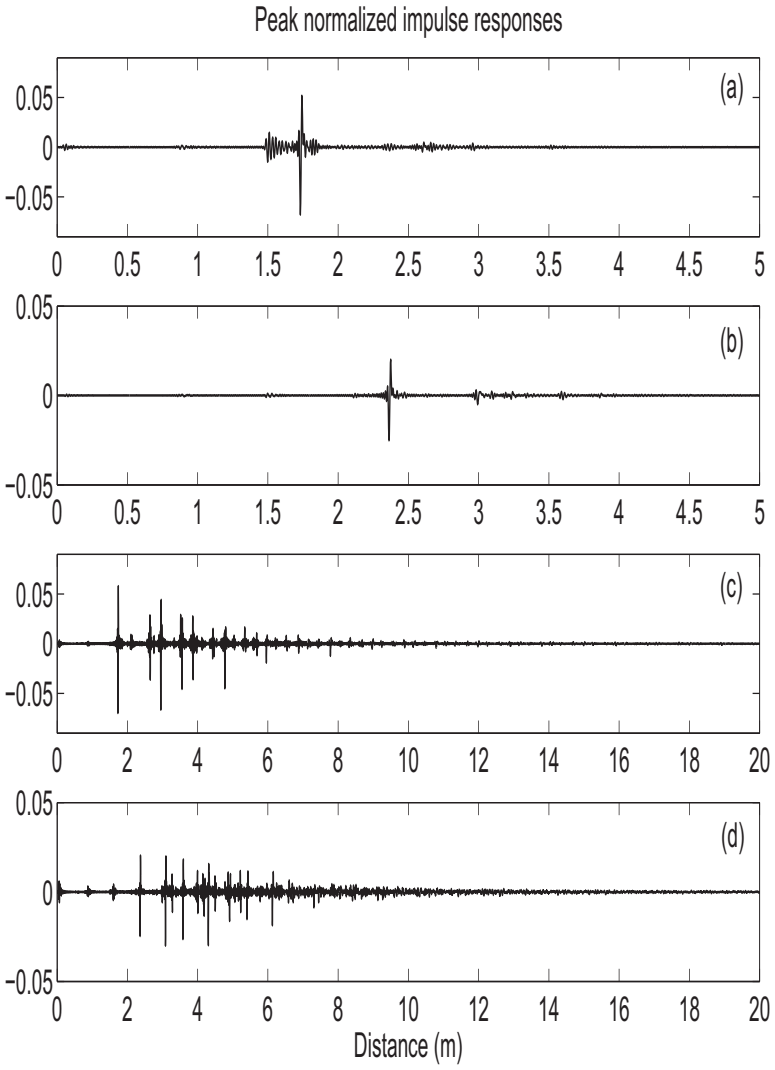

FIGURE I.9 : Les réponses impulsionnelles obtenues pour les différentes configurations : (a) un réseau en Y , avec extrémités adaptées ; (b) un réseau en 2Y, avec extrémités adaptées ; (c) un réseau en Y, avec extrémités en circuit-ouvert ; (d) un réseau en 2Y, avec extrémités en circuit-ouvert.

End loads	Bandwidth	Single Y	Double Y
Matched	200 MHz	6.1	5.1
	500 MHz	5.7	6.3
	2 GHz	6.4	6.5
Open	200 MHz	11.45	19.38
	500 MHz	10.6	12.85
	2 GHz	13.8	16.84

TABLE I.1 : Gain de détection (exprimé en dB) obtenu pour les quatres configurations introduites, pour trois valeurs de la bande passante.

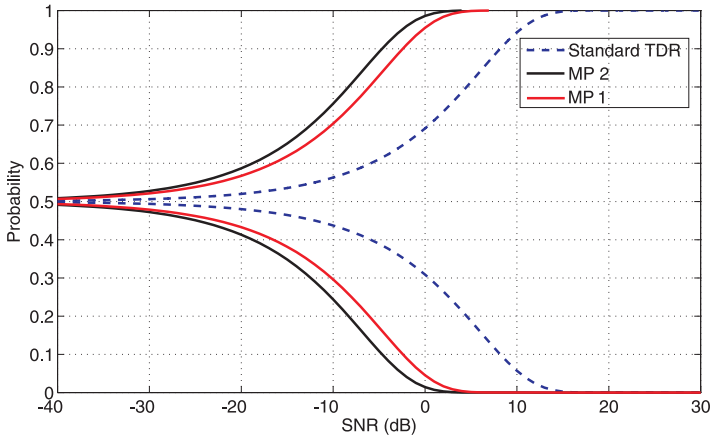

FIGURE I.10 : Probabilités de détection des deux configurations étudiées en Fig. I.8(a) and (b), avec des extrémités en circuit-ouvert, et une valeur du seuil égale à 0.5.

illustrées dans la Fig. I.9. Ces résultats suggèrent la dépendance de la réponse du système sur les conditions aux extrémités (les charges) ; si le nombre d'échos ne varie presque pas dans le cas d'extrémités adaptées, il est fortement amélioré dans le cas des extrémités en circuit-ouvert. Sous ces conditions, une structure plus complexe du réseau entraine un gain de détection plus important, comme le suggère le tableau I.1. Trois bandes passantes ont été analysées, et les résultats montrent une influence mineure de ce paramètre pour les extrémités adaptées, ou une variation de moins de 1 dB est observée, tandis que pour les autres cas de plus amples variations sont observées.

On considère dans ce qui suit les deux réseaux en 1Y et 2Y avec extrémités en circuit ouvert.

On propose de tracer les courbes de probabilités pour ces deux cas, notés respectivement MP1 et MP2. Les courbes sont tracées sur la Fig. I.10, où l'on observe une amélioration importante par rapport au cas de la TDR standard ; ces résultats valident que la complexité de la réponse du réseau a un effet positif sur les performances de la MP, contrairement aux méthodes existantes ; ceci prouve l'avantage apporté par cette méthode quant à la détection des défauts non-francs dans les réseaux filaires.

I.4 Localisation des défauts

Dans cette partie nous abordons la localisation des défauts non-francs dans les réseaux filaires, vu que la MP ne permet pas de déterminer la position du défaut à cause du manque d'origine de temps. Nous commençons d'abord par une brève description des méthodes de localisation existantes.

I.4.1 Méthodes existantes

I.4.1.1 Méthodes de réflectométrie

Les méthodes de réflectométrie déjà exposées sont utilisées souvent pour localiser les défauts dans les réseaux filaires. Dans le cas simple on dispose d'un seul port de test, servant à injecter le signal de test et récupérer le signal réfléchi pour l'analyser. Lorsque le réseau devient plus complexe (plusieurs jonctions par exemple), on a recours à plusieurs ports de test disposées aux extrémités du réseau ; il s'agit de la réflectométrie distribuée. Comme indiqué dans les sections précédentes, ces méthodes sont efficaces pour détecter les défauts francs (court-circuit et circuit-ouvert) dans les configurations simples des réseaux, comme par exemple lorsqu'il s'agit d'une simple ligne de transmission, mais sont insuffisantes une fois que le défaut est non-franc (autre types de défauts comme défaut d'isolement) ou la structure du réseau est complexe.

I.4.1.2 Méthodes itératives

Méthodes itératives : Ces méthodes sont basées sur la résolution du problème inverse : on essaie de remonter à la position du défaut en analysant la réponse du système. Généralement ces méthodes consomment du temps et une solution ne correspondant pas à la position réelle du défaut peut être trouvée (comme c'est le cas pour les algorithmes de minimisation locale).

I.4.2 Méthode de localisation proposée

La nouvelle méthode que nous proposons est une méthode distribuée non-itérative qui localise directement les défauts non-francs dans les réseaux à structure complexe. Cette méthode consiste en deux étapes : la première étant la synthèse des signaux de test en adaptant la méthode DORT (Décomposition de l'Opérateur de Retournement Temporel) à notre cas de propagation guidée, la deuxième étant l'élaboration d'un algorithme de post-traitement qui permet la localisation directe du défaut, et aussi la localisation de plusieurs défauts. Nous commençons par expliquer la méthode DORT de laquelle on se sert pour créer les signaux de test.

I.4.2.1 Méthode DORT

Cette méthode a été développée en premier dans le domaine de l'acoustique, pour la problématique de focalisation sur une cible parmi plusieurs cibles. L'idée de base de la méthode est la suivante : on considère un réseau de N transducteurs (émettant et recevant les ondes acoustiques) dans un milieu inhomogène. On suppose qu'on dispose de deux cibles (A) et (B) qui sont des diffuseurs ponctuels, avec (A) ayant la réflectivité la plus élevée. Si on injecte un signal de test à partir de chacun des transducteurs, puis on récupère les signaux réfléchis, on les inverse dans le temps et on les réinjecte une deuxième fois (ce processus est connu sous le nom de retournement temporel ; il est à la base de la DORT) et on itère ce processus un nombre suffisant de fois, on arrivera à focaliser sur le diffuseur le plus réflecteur, dans ce cas (A).

Pour focaliser sur l'autre diffuseur, la solution était d'utiliser la méthode DORT. Pour expliquer comment cette méthode fonctionne il faut d'abord définir l'Opérateur de Retournement Temporel (ORT).

I.4.2.1.1 ORT

Dans l'exemple déjà considéré, nous avons considéré un ensemble de N transducteurs qui émettent et reçoivent les signaux. L'ORT est introduit pour exprimer les signaux réfléchis en fonction des signaux injectés. Si K désigne la matrice de transfert du système, chaque élément $k_{ij}(\omega)$ de cette matrice est une fonction de transfert inter-élément : l'émetteur est l'élément numéro j et le récepteur est l'élément numéro i parmi les N transducteurs. Pour chaque fréquence, et pour l'ensemble des N transducteurs, on obtient une matrice de transfert NN. Théoriquement, vu que le milieu est réciproque, $k_{ij}(\omega) = k_{ji}(\omega)$, c'est à dire que K est symétrique.

L'ORT qu'on notera T est défini comme suit :

$$T = K * K \tag{I.23}$$

Où $*$ désigne le complexe conjugué. La symétrie de K implique que T est une matrice hermitienne et par conséquent peut être diagonalisée ; le nombre des valeurs propres non nulles est égal à celui des cibles. On a aussi démontré que dans ce cas ces valeurs propres sont proportionnelles au carré de la réflectivité des cibles. Ayant introduit l'ORT, on détaille maintenant les différentes étapes de la méthode DORT.

I.4.2.2 Etapes de la DORT

La première étape de cette méthode est la mesure de la matrice de transfert K du système : si on a N transducteurs, on envoie une impulsion temporelle depuis le transducteur i et on enregistre la réponse du système sur chacun des transducteurs ; le processus est répété N fois et la matrice K est stockée.

La deuxième étape est la diagonalisation de l'ORT. Cette opération permet d'obtenir un ensemble de valeurs et vecteurs propres ; la valeur propre la plus élevée correspond à la cible la plus réflective, et ainsi de suite.

La troisième étape est la propagation des composantes des vecteurs propres correspondant à une valeur propre choisie. En effet si on veut obtenir une focalisation sur la cible la plus réflective, on propage depuis les N transducteurs, les composantes du vecteur propre correspondant à la valeur propre la plus élevée. De même si on veut obtenir une focalisation sur la cible la moins réflective (notée (B) dans notre exemple précédent) on propage les composantes du vecteur propre correspondant à la deuxième valeur propre la plus significative.

La méthode DORT a été le point de départ dans la première phase de notre travail, qui consiste à synthétiser les signaux de test. Cependant il fallait l'adapter pour notre cas de la propagation guidée. La section suivante illustrera notre nouvelle méthode de localisation.

I.4.2.3 Critère de localisation

Vu les différences qui existent entre la propagation en espace libre et la propagation guidée, nous avons adapté la DORT à notre cas. En considérant les défauts non-francs, on doit considérer le système différence : c'est à dire la matrice K sera la différence de deux matrices : la

première, notée K_{sd}, est la matrice de transfert du système sans défaut ou système référence, et la deuxième, K_{ad}, est celle du système défectueux. On a alors

$$K = K_{ad} - K_{sd} \tag{I.24}$$

La première étape de notre méthode consiste à synthétiser des signaux de test à partir de K. Ainsi l'ORT est calculé est les valeurs et vecteurs propres sont extraites. La valeur propre la plus élevée correspond au défaut. Lorsqu'il s'agit de plusieurs défauts, le nombre des valeurs propres non nulles obtenues est égal à celui des défauts.

Pour expliquer notre méthode de localisation, nous commençons par considérer le cas d'un seul défaut, dans un réseau filaire complexe, contenant par exemple deux jonctions. Des ports de test sont placés aux extrémités de ce réseau et serviront à injecter et recevoir les signaux. Après avoir mesuré la matrice K, et extrait les valeurs propres et les vecteurs propres correspondants, nous considérons le vecteur propre correspondant à la valeur propre la plus élevée ; ses composantes constituent les nouveaux signaux de test.

Si on injecte directement ces signaux dans le réseau, vu l'existence de plusieurs jonctions, on n'arrivera pas à distinguer la position du défaut ; c'est pourquoi nous avons mis en place un algorithme de post traitement qui le fait. Introduisons tout d'abord un outil qu'on appelle diagramme ZT.

I.4.2.3.1 Diagramme ZT

Nous avons développé cet outil graphique pour observer la propagation de la tension dans le réseau. Ceci nous permet de tracer le chemin suivi par les signaux injectés et voir s'il y a une focalisation éventuelle à un certain endroit du réseau. Sur l'axe des abscisses on situe les positions dans le réseau, en commençant par une origine prédéfinie, l'une des extrémités du réseau par exemple. L'axe des ordonnées est l'axe du temps.

I.4.2.3.2 Sommation des puissances

A partir du diagramme ZT, où l'on observe la tension $v(z,t)$ en fonction de la position z et du temps t, on construit un diagramme où on somme le carré de la tension $v(z,t)$, et ceci pour tous les instants t, étant donnée une certaine position z. En d'autres termes, pour tout point du

réseau (de position z) on calcule la quantité qu'on note $p(z)$

$$p(z) = \int v^2(z,t)dt \tag{I.25}$$

Cette opération nous permet d'obtenir un diagramme que nous appellerons le diagramme de sommation de puissance. Il nous permet de bénéficier des interférences constructives observées sur le diagramme ZT à la position du défaut.

Pour les cas simples de réseaux, comme par exemple une ligne simple ou encore un réseau en Y, on observe un maximum global à la position du défaut, qui nous permet de déterminer directement cette position. Mais étant donné que nous nous intéressons aux réseaux complexes, où plusieurs discontinuités existent, les diagrammes de sommation de puissances dans ce cas présentent plusieurs maximums locaux dus au fait que les signaux interfèrent à différentes positions. Pour cela on calcule, pour tous ces maximums locaux un contraste qu'on définit comme suit.

I.4.2.3.3 Contraste

Nous avons choisi de définir le contraste comme étant le rapport entre la valeur du pic du maximum local (sur le diagramme de sommation de puissance) et celui du palier local. En effet, le diagramme présente des intervalles où l'on observe des valeurs de paliers presque stables avec des minimums et maximums locaux. Pour pouvoir calculer la valeur d'un certain palier, on extrait d'abord ces points et les points appartenant à leur voisinage dont la valeur de $p(z)$ ne contribue pas à la définition du plateau. Les points qui restent servent à calculer la valeur de ce dernier, et ensuite le contraste est calculé pour tous les maximums locaux. La position où l'on a un contraste maximal est celle correspondant à la position du défaut. L'avantage du calcul du contraste est qu'il permet aussi l'automatisation de la procédure de localisation, en vue par exemple d'une étude statistique de la méthode.

Pour résumer, l'algorithme de localisation d'un défaut dans un réseau filaire se résume comme suit :

- Mesure de la matrice de transfert du réseau référence (sans défaut).
- Mesure de la matrice de transfert du réseau sous test (éventuellement défectueux).
- Calcul de la matrice K, différence des deux matrices précédentes.
- Calcul de l'ORT et calcul des valeurs propres et vecteurs propres ; choix du vecteur propre correspondant à la valeur propre la plus élevée dans le cas d'un seul défaut. Dans le cas

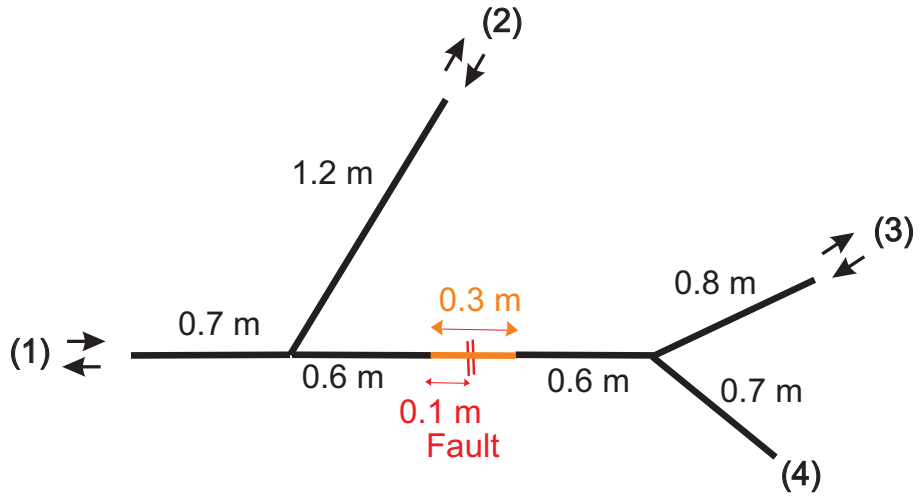

(b)

FIGURE I.11 : Réseau implémenté pour tester la méthode de localisation.

de n défauts, choix des n vecteurs correspondants aux n valeurs propres les plus significatives.

– Injection dans un modèle du système référence des composantes du vecteur propre choisi.
– Pour les différentes positions dans le réseau, construire les diagrammes de sommation de puissances.
– Extraire les maximums locaux.
– Pour chaque maximum, calculer le contraste correspondant, à partir du calcul du palier correspondant.
– La position à laquelle correspond le contraste le plus élevé est celle correspondant au défaut.

Cet algorithme sera par la suite appliqué et nous montrerons un exemple de résultat expérimental que nous avons obtenu.

I.4.3 Résultats expérimentaux

Le même matériel expérimental que celui utilisé dans la partie détection des défauts est aussi utilisé ici. Le réseau étudié est celui représenté par la Fig. I.11 : c'est un réseau en 2Y, avec trois extrémités liées aux ports de test de l'analyseur de réseau, et la quatrième extrémité adaptée. Le défaut est celui déjà étudié dans la partie détection : un défaut d'écrasement.

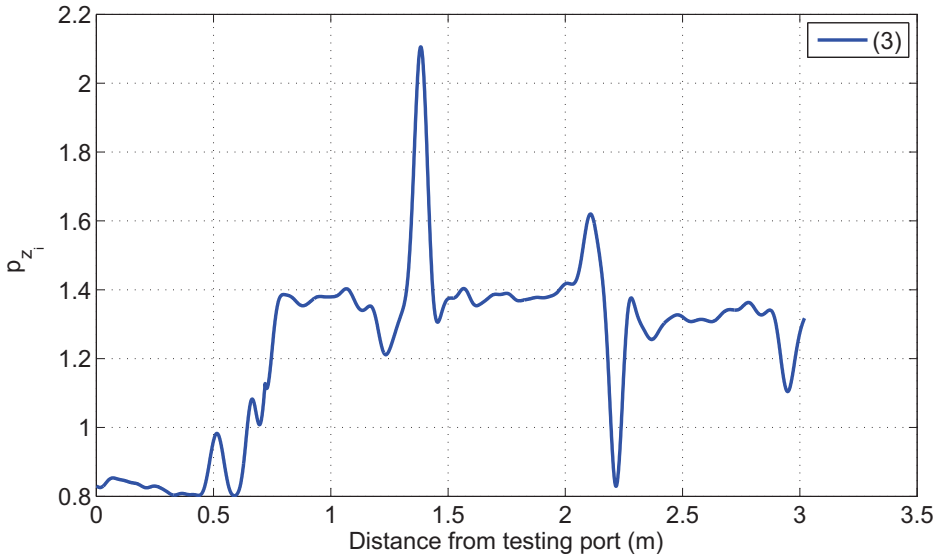

FIGURE I.12 : Le diagramme de sommation de puissances, observé entre les ports (1) et (3), pour le réseau de la Fig. I.11. On remarque un maximum à la position du défaut, situé à 1.4 m du port de test (1).

Le diagramme de sommation de puissances observé entre les extrémités (1) et (3) est représenté sur la Fig. I.12, où l'on observe un pic maximal à la position du défaut, situé à 1.4 m du port de test (1). Nous remarquons que la nouvelle méthode permet de localiser directement le défaut non-francs, sans besoin d'itérations.

I.5 Conclusion

Dans la thèse, nous avons développé des nouvelles approches dans la détection et la localisation des défauts. La MP permet l'amélioration de la détection des défauts non-francs dans les réseaux filaires à structure complexe. La méthode de localisation basée sur la DORT permet de localiser ce type de défaut dans les réseaux complexes, sans besoin d'itérations. Ces méthodes ont été validées par des simulations et des études expérimentales, dont un extrait a été présenté dans ce résumé.

Les méthodes présentées ci-dessus nécessitent une étude plus approfondie : pour la méthode de localisation nous avons présenté une étude de faisabilité, donc une étude paramétrique et expérimentale plus approfondie est nécessaire. La robustesse de cette méthode et de la MP aux

tolérances sur les mesures est aussi un aspect intéressant à observer. L'implémentation pratique de la méthode de localisation devra être inspectée spécialement lorsqu'il s'agit de systèmes à grandes dimensions dont les extrémités ne peuvent être reliées à un même appareil de mesure. Les deux méthodes doivent être examinées dans le cas des lignes de transmission multifilaires, vu qu'un grand nombre de câbles consistent en des multi-conducteurs.